

Northumbria Research Link

Citation: Rajbhandari, Sujan (2010) Application of wavelets and artificial neural network for indoor optical wireless communication systems. Doctoral thesis, Northumbria University.

This version was downloaded from Northumbria Research Link:
<https://nrl.northumbria.ac.uk/id/eprint/1933/>

Northumbria University has developed Northumbria Research Link (NRL) to enable users to access the University's research output. Copyright © and moral rights for items on NRL are retained by the individual author(s) and/or other copyright owners. Single copies of full items can be reproduced, displayed or performed, and given to third parties in any format or medium for personal research or study, educational, or not-for-profit purposes without prior permission or charge, provided the authors, title and full bibliographic details are given, as well as a hyperlink and/or URL to the original metadata page. The content must not be changed in any way. Full items must not be sold commercially in any format or medium without formal permission of the copyright holder. The full policy is available online: <http://nrl.northumbria.ac.uk/policies.html>

**Application of Wavelets and Artificial
Neural Network for Indoor Optical
Wireless Communication Systems**

Sujan Rajbhandari

Ph. D.

2009

Application of Wavelets and Artificial Neural Network for Indoor Optical Wireless Communication Systems

Sujan Rajbhandari

A thesis submitted in partial fulfilment
of the requirements of the
University of Northumbria at Newcastle
for the degree of
Doctor of Philosophy

Research undertaken in the
School of Computing, Engineering and Information Sciences

October 2009

Abstract

This study investigates the use of error control code, discrete wavelet transform (DWT) and artificial neural network (ANN) to improve the link performance of an indoor optical wireless communication in a physical channel. The key constraints that barricade the realization of unlimited bandwidth in optical wavelengths are the eye-safety issue, the ambient light interference and the multipath induced intersymbol interference (ISI). Eye-safety limits the maximum average transmitted optical power. The rational solution is to use power efficient modulation techniques. Further reduction in transmitted power can be achieved using error control coding. A mathematical analysis of retransmission scheme is investigated for variable length modulation techniques and verified using computer simulations. Though the retransmission scheme is simple to implement, the shortfall in terms of reduced throughput will limit higher code gain. Due to practical limitation, the block code cannot be applied to the variable length modulation techniques and hence the convolutional code is the only possible option. The upper bound for slot error probability of the convolutional coded dual header pulse interval modulation (DH-PIM) and digital pulse interval modulation (DPIM) schemes are calculated and verified using simulations.

The power penalty due to fluorescent light interference (FLI) is very high in indoor optical channel making the optical link practically infeasible. A denoising method based on a DWT to remove the FLI from the received signal is devised. The received signal is first decomposed into different DWT levels; the FLI is then removed from the signal before reconstructing the signal. A significant reduction in the power penalty is observed using DWT. Comparative study of DWT based denoising scheme with that of the high pass filter (HPF) show that DWT not only can match the best performance obtain using a HPF, but also offers a reduced complexity and design simplicity.

The high power penalty due to multipath induced ISI makes a diffuse optical link practically infeasible at higher data rates. An ANN based linear and DF architectures are investigated to compensation the ISI. Unlike the unequalized cases, the equalized schemes don't show infinite power penalty and a significant performance improvement is observed for all modulation schemes. The comparative studies substantiate that ANN based equalizers match the performance of the traditional equalizers for all channel conditions with a reduced training data sequence. The study of the combined effect of the FLI and ISI shows that DWT-ANN based receiver perform equally well in the present of both interference.

Adaptive decoding of error control code can offer flexibility of selecting the best possible encoder in a given environment. A suboptimal 'soft' sliding block convolutional decoder based on the ANN and a $\frac{1}{2}$ rate convolutional code with a constraint length is investigated. Results show that the ANN decoder can match the performance of optimal Viterbi decoder for hard decision decoding but with slightly inferior performance compared to soft decision decoding. This provides a foundation for further investigation of the ANN decoder for convolutional code with higher constraint length values.

Finally, the proposed DWT-ANN receiver is practically realized in digital signal processing (DSP) board. The output from the DSP board is compared with the computer simulations and found that the difference is marginal. However, the difference in results doesn't affect the overall error probability and identical error probability is obtained for DSP output and computer simulations.

Acknowledgement

The research was carried out within school of computing, engineering and information sciences, Northumbria University. I would like to express my sincere gratitude to Northumbria University for providing me a studentship to carry out the research. I would also like to thank Northumbria communication research group and intelligent modelling lab for providing necessary equipments, software and test bed.

My special thanks go to my supervisors Prof. Maia Angelova and Prof. Fary Ghassemlooy for providing me continuous support, guidance and encouragement. I would like to thank them for giving me the opportunity to undertake the study under their supervision. Without their constructive advice and reading the material without delay including this thesis, it would have been impossible to finish the project on time.

Sincere thanks also go to my colleagues in the Northumbria communication research group and intelligent modelling lab for providing excellent research environment and also for making time really enjoyable.

I would like to thank my beloved father, mother, brothers and sisters-in-law for their supports, both financially and morally. Finally special thank goes to my wife Kanchan (Puja) for her constant support, patience and encouragement throughout this work.

Declaration

I declare that the work contained in this thesis has not been submitted for any other award and that it is all my own work.

Sujan Rajbhandari

August 2009

Table of Content

Abstract	ii
Acknowledgement	iii
Declaration	iv
List of Figures	ix
List of Tables	xvi
List of Abbreviations	xvii
List of Symbols	xx
Chapter 1 Introductions	1
1.1 Research Motivations and Objectives	3
1.2 Original Contributions	10
1.3 List of Publications and Awards	11
1.3.1 <i>Refereed Journal Papers</i>	11
1.3.2 <i>Conference Papers</i>	12
1.3.3 <i>Poster</i>	14
1.4 Organization of the Thesis	14
Chapter 2 An Overview of Optical Wireless Communications	17
2.1 Introduction	17
2.2 Overview of Optical Wireless Communications.....	18
2.3 Link Configurations	21
2.4 Indoor Optical Wireless Channel	23
2.5 Optical Transmitter and Eye-Safety	26
2.6 Optical Receiver	29
2.7 Ambient Light Sources	31
2.8 Modulation Techniques.....	33
2.8.1 <i>Digital Baseband Modulation Techniques</i>	35
2.8.2 <i>Subcarrier Intensity Modulation</i>	49
2.9 Summary	50
Chapter 3 Symbol Retransmission Scheme	51
3.1 Introduction	51
3.2 Repetition Coding	52
3.3 Symbol Retransmission.....	53
3.4 Symbol Retransmission for Variable Symbol Length Modulation Schemes.....	53
3.4.1 <i>Slot Error Rate Equations</i>	56
3.5 SER for DH-PIM with Symbol Retransmission	61
3.5.1 <i>Results and Discussions</i>	62

3.6 Summary	65
Chapter 4 Convolutional Code for Indoor Optical Wireless Communications	67
4.1 Introductions	67
4.2 Convolutional Code	67
4.2.1 <i>The Transfer Function and Distance Properties of a Convolutional Code</i>	70
4.2.2 <i>Optimum Decoding of a Convolutional Code - the Viterbi Algorithm</i>	71
4.2.3 <i>Performance of Convolutional Codes</i>	72
4.3 Convolutional Coded DH-PIM	73
4.3.1 <i>Error Bound for CC-DH-PIM</i>	75
4.3.2 <i>SER Performance of CC-DH-PIM</i>	76
4.4 Convolutional Coded DPIM	82
4.4.1 <i>SER Performance of CC-DPIM</i>	83
4.5 Summary	86
Chapter 5 Artificial Light Interference and Discrete Wavelet Transform based Denoising.....	87
5.1 Introductions	87
5.2 Artificial Light Interference and Performance without Filtering.....	88
5.2.1 <i>Performance of OOK without Filtering</i>	90
5.2.2 <i>Performance of PPM without Filtering</i>	93
5.2.3 <i>Performance of DPIM without Filtering</i>	97
5.3 The Effect of FL with Electrical High-Pass Filtering	99
5.4 Introduction to Time-Frequency Analysis	101
5.4.1 <i>Wavelet Analysis</i>	102
5.4.2 <i>Continuous Wavelet Transform</i>	104
5.4.3 <i>Discrete Wavelet Transform</i>	106
5.5 DWT based Denoising	107
5.5.1 <i>Performance of OOK with DWT Denoising</i>	107
5.5.2 <i>Performance of PPM with DWT Denoising</i>	113
5.5.3 <i>Performance of DPIM with DWT Denoising</i>	116
5.6 Comparative study of DWT and HPF.....	119
5.7 Summary	121
Chapter 6 Artificial Neural Network Based Adaptive Equalizer for a Dispersive Indoor Optical Wireless Channel	123
6.1 Introduction.....	123
6.2 Diffuse Indoor Optical Wireless Channel Model.....	124
6.3 Unequalized Performance	125
6.3.1 <i>OOK</i>	125
6.3.2 <i>PPM</i>	128

6.3.3	<i>DPIM</i>	131
6.4	Equalization Techniques	135
6.5	Equalization as a Classification Problem.....	137
6.6	Introduction to Artificial Neural Network	139
6.6.1	<i>Neuron</i>	139
6.6.2	<i>ANN Architectures</i>	141
6.7	Training Network.....	143
6.7.1	<i>Backpropagation Learning</i>	143
6.8	The ANN based Adaptive Equalizer.....	144
6.8.1	<i>Equalized OOK</i>	145
6.8.2	<i>Equalized PPM</i>	152
6.8.3	<i>Equalized DPIM</i>	158
6.8.4	<i>Comparative Study of the ANN and FIR Based Equalizers</i>	160
6.9	Summary	163
Chapter 7 Discrete Wavelet Transform and Artificial Neural Network		
	Based Receiver	165
7.1	Introductions	165
7.1	OOK	166
7.2	PPM.....	169
7.3	DPIM.....	171
7.4	Summary	174
Chapter 8 Adaptive Decoding of Convolutional Code using Artificial Neural		
	Network.....	175
8.1	Introductions	175
8.2	The Structure of ANN Decoder	177
8.3	Optimization of ANN Parameters.....	179
8.3.1	<i>Window Length and Decoding Position</i>	179
8.3.2	<i>Number of Neurons</i>	181
8.3.3	<i>Training SNR</i>	181
8.3.4	<i>Training Length</i>	183
8.4	Comparative Study of ANN and Viterbi Decoder	184
8.5	Performance of ANN Equalizer and ANN Decoder in Diffuse Indoor OWC Channels.....	185
8.6	Summary	188
Chapter 9 Hardware Realization.....		189
9.1	Introductions	189
9.2	DWT Denoising in DSP.....	190
9.3	ANN Based Equalizer in DSP.....	193
9.4	Summary	195
Chapter 10 Conclusions and Future Works		196

10.1 Conclusions	196
10.2 Future Works.....	202
Appendix A Filter Coefficients of Wavelet Families [302, 303]	204
References	207

List of Figures

Figure 1.1: The summary of the challenges, the existing and the proposed solutions for indoor OWCs considered in this research. Chapter numbers where the proposed research is discussed are given in brackets and research carried out is given in bold.	9
Figure 2.1: Classification of infrared links.	21
Figure 2.2: Equivalent baseband model of an optical wireless system using IM/DD. ...	23
Figure 2.3: Optical power spectra of common ambient light sources [43].	31
Figure 2.4: Symbol mapping of different modulation techniques.	36
Figure 2.5: Transmitted waveforms for OOK: (a) NRZ, and (b) RZ ($\gamma = 0.5$).	36
Figure 2.6: PSD of OOK-NRZ and OOK-RZ ($\gamma = 0.5$) [51].	37
Figure 2.7: The block diagram of OOK system.	38
Figure 2.8: The block diagram of the matched filter based receiver for PPM scheme with soft and hard decision decoding.	41
Figure 2.9: The block diagram of the matched filter based receiver for DPIM scheme.	45
Figure 2.10: The block diagram of the matched filter based receiver for DH-PIM scheme.	46
Figure 3.1: A flow chart showing the majority decision process for $R_{rt} = 4$	55
Figure 3.2: Slot error probability of R_{rt} of three P_{se3r} against the standard slot error probability without retransmission P_{se1r} for average symbol length of 2, 4, 8 and 16.	57
Figure 3.3: SER for retransmission rate of 3, 4 and 5 against the standard slot error probability without retransmission for average symbol length of 2 and 16.	61
Figure 3.4: The system block diagram of the proposed DH-PIM symbol retransmission.	62
Figure 3.5: The predicted SER against the electrical SNR for retransmission rate of 3, 4 and 5 at a data rate of 1 Mbps for 16-DH-PIM ₂	63
Figure 3.6: (a) The SER against the electrical SNR for retransmission rate of 3, 4 and 5 at a data rate of 1 Mbps for 16-DH-PIM ₂ ; (b) the SER against the electrical SNR for retransmission rate of 3, 4 and 5 at a data rate of 1 Mbps for 16-DH-PIM ₁	64

Figure 4.1: $\frac{1}{2}$ Convolutional code encoder.	68
Figure 4.2: State Trellis diagram of an $\frac{1}{2}$ convolutional encoder.	69
Figure 4.3: State diagram of an $\frac{1}{2}$ convolutional encoder.	69
Figure 4.4: Modified state diagram.	70
Figure 4.5: A block diagram of convolutional coded DH-PIM scheme.	74
Figure 4.6: Trellis diagram of CC-DH-PIM ₂	75
Figure 4.7: Modified state diagram for CC-DH-PIM	76
Figure 4.8: The SER against the SNR for different error bounds for CC-DH-PIM ₂	77
Figure 4.9: A flow chart diagram for determining the SER of the CC-DH-PIM system.	78
Figure 4.10: The theoretical and simulation SER versus the SNR for (a) standard 8 & 16-DH-PIM ₂ and 8 & 16-CC-DH-PIM ₂ , (b) standard 8 & 16-DH- PIM ₁ and 8 & 16-CC-DH-PIM ₁	80
Figure 4.11: The theoretical SER against the SNR for 16-PPM and coded and uncoded DH-PIM _{1&2}	81
Figure 4.12: The SER against SNR for 16-CC-DH-PIM _r with constraint lengths of 3 and 7.	82
Figure 4.13: A block diagram of convolutional coded DPIM scheme.	83
Figure 4.14: The theoretical upper bound and simulation SER against the electrical SNR for 16-CC-DPIM with 0, 1 and 2 guard slot.	84
Figure 4.15: The simulated SER against electrical SNR for uncoded (standard) and coded 16-DPIM with 0, 1 and 2 GS.	84
Figure 4.16: The SER against the electrical SNR for 8, 16 & 32 DPIM and 8, 16 & 32-CC-DPIM.	85
Figure 5.1: (a) Low frequency interference component, and (b) high frequency interference component.	90
Figure 5.2: Block diagram of the OOK system.	91
Figure 5.3: NOPR and OPP to achieve a BER of 10^{-6} against data rates for OOK scheme with and without FLI.	92
Figure 5.4: The block diagram of matched filter based hard and soft decision detector for PPM in presence of FLI.	94
Figure 5.5: NOPR to achieve an SER of 10^{-6} against data rates for 4, 8 and 16-PPM hard decision decoding scheme with and without of FLI.	96
Figure 5.6: NOPR to achieve an SER of 10^{-6} against data rates of 4, 8 and 16-PPM soft decision decoding scheme with and without of FLI.	96

Figure 5.7: The block diagram of matched filter based receiver for DPIM scheme in presence of FLI.....	97
Figure 5.8: NOPR against data rates for 4, 8 and 16-DPIM schemes with and without FLI.....	98
Figure 5.9: The time frequency resolution of (a) STFT, and (b) WT.....	103
Figure 5.10: The scaling and translation to the Morlet wavelet.....	104
Figure 5.11: (a) Decomposition of a signal by DWT, and (b) the DWT decomposition process.	107
Figure 5.12: DWT based receiver for the OOK in presence of artificial light interference.....	108
Figure 5.13 : The PSD of OOK at 2 Mbps: (a) received signal with FLI, and (b) wavelet denoising. The Daubechies wavelet with 6 levels of decompositions is used.....	110
Figure 5.14 : The PSD of OOK at 200 Mbps: (a) received signal with FLI, and (b) wavelet denoising. The Daubechies wavelet with 12 levels of decompositions is used.....	110
Figure 5.15: Normalized optical power requirement against data rates for OOK modulation scheme with and without DWT denoising in the presence of the FLI.	113
Figure 5.16: Block diagram of DWT based receiver for PPM (hard and soft decoding) schemes in the presence of FLI.....	114
Figure 5.17: NOPR versus data rates for 4, 8 and 16 PPM hard decoding scheme with DWT denoising in the presence of the FLI.....	115
Figure 5.18: NOPR versus data rates for 4, 8 and 16 PPM soft decoding scheme with DWT denoising in the presence of the FLI.....	116
Figure 5.19: Block diagram of DWT based receiver for DPIM in the presence of FLI.....	117
Figure 5.20: NOPR versus data rates for 4, 8 and 16 DPIM scheme with DWT denoising in the presence of the FLI.....	118
Figure 5.21: The OPP against the decomposition level for the DWT based receiver at data rates of 20, 50, 100 and 200 Mbps.....	120
Figure 5.22: The OPP against cut-off frequencies for a HPF based receiver at data rates of 20, 50, 100 and 200 Mbps.....	120
Figure 6.1: The block diagram of the unequalized OOK system.....	126

Figure 6.2: NOPR against the normalized delay spread D_T for unequalized OOK in diffuse indoor OWC channel.....	127
Figure 6.3: Theoretical and simulated OPP for unequalized OOK system against the h_0	128
Figure 6.4: The block diagram of the unequalized PPM system with hard and soft decision decoding.....	128
Figure 6.5: NOPR against the normalized delay spread for 4, 8 and 16-PPM with hard and soft decision decoding in dispersive channel.	130
Figure 6.6: Block diagram of the unequalized DPIM system with a threshold detector.....	132
Figure 6.7: NOPR against the normalized delay spread for 4, 8 and 16-DPIM with and without guard slots in dispersive channel.....	133
Figure 6.8: NOPR against the normalized delay spread for 4, 8 and 16-DPIM(1GS) with hard and soft decoding in dispersive channel.	134
Figure 6.9: Block diagram of system with an equalizer [257].....	135
Figure 6.10: Block diagram of the linear equalizer.....	136
Figure 6.11: Structure of the decision-feedback equalizer.....	137
Figure 6.12: The schematic diagram of neuron showing inputs, a bias, weights and an output.....	139
Figure 6.13: A single layer feedforward network with 2 output neurons.....	142
Figure 6.14: Fully connected feedforward multilayer network.....	142
Figure 6.15: Neural network with feedback connection.....	142
Figure 6.16: The system block diagram of ANN based linear equalizer for indoor OW communication.....	146
Figure 6.17: ANN based linear equalizer structure.....	146
Figure 6.18: System block diagram of ANN based DFE receiver.....	146
Figure 6.19: ANN based DFE structure.....	146
Figure 6.20: The MSE against the number of iteration for ANN based equalizer (linear and DFE) for a channel with D_T of 2 at data rate of 200 Mbps.	149
Figure 6.21: NOPR versus the normalized delay spread for unequalized and ANN equalized (linear and decision feedback) OOK scheme.....	150
Figure 6.22: The simulation and predicted optical power penalty against h_0 for unequalized and equalized (DF) OOK at data rate of 200 Mbps.....	151
Figure 6.23: ANN based linear equalizer for soft and hard decoding PPM scheme. ...	153

Figure 6.24: ANN based decision feedback equalizer for soft and hard decoding PPM scheme.....	153
Figure 6.25: NOPR against the normalized delay spread D_T for unequalized and ANN based linear equalizer for PPM hard decision decoding scheme.....	154
Figure 6.26: OPP against the normalized delay spread D_T for unequalized and ANN based linear equalizer for PPM hard decision decoding scheme.	155
Figure 6.27: NOPR against the normalized delay spread D_T for unequalized and ANN based linear equalizer for PPM soft decision decoding scheme.....	156
Figure 6.28: OPP against the normalized delay spread D_T for unequalized and ANN based linear equalizer for PPM soft decision decoding scheme.	156
Figure 6.29: OPP versus the normalized delay spread D_T for ANN based linear and DF equalizers for PPM hard decision decoding scheme.....	157
Figure 6.30: ANN based linear equalizer for DPIM scheme.....	158
Figure 6.31: ANN based decision feedback equalizer for DPIM scheme.	158
Figure 6.32: NOPR versus normalized RMS delay spread for unequalized and linear ANN equalizer for DPIM (OGS) scheme.....	159
Figure 6.33: OPP against the normalized delay spread D_T for ANN based linear and DF for DPIM scheme.	160
Figure 6.34: The MSE between the actual and target outputs from the linear equalizers for (a) FIR filter equalizer and (b) ANN equalizer.	161
Figure 6.35: BER against the electrical SNR for traditional and ANN linear equalizers for OOK scheme at data rate of 200 Mbps for channel with D_T of 2 with different training lengths (TLs).	162
Figure 6.36: BER against the electrical SNR for traditional and ANN DFEs for modulation scheme at data rate of 200 Mbps for channel with D_T of 2 with different training lengths	163
Figure 7.1: Unequalized NOPR against the normalized delay spread in presence/absence of FLI with/without DWT based denoising for data rates of 40, 120 and 200 Mbps.	167
Figure 7.2: The block diagram of the DWT-ANN based receiver for OOK modulation scheme for an indoor OWC link.	167
Figure 7.3: The NOPR for OOK against the normalized delay spread with/without FLI with DWT-ANN receiver for data rates of 40, 120 and 200 Mbps.....	168

Figure 7.4: OPP versus the data rates (20-200 Mbps) for DWT-ANN based receiver OOK scheme with the normalized delay spread values of 0, 0.4, 1.2 and 2 in presence of the FLI.....	169
Figure 7.5: The block diagram of DWT-ANN based receiver for PPM hard and soft decision decoding scheme in diffuse indoor OWC in presence of FLI.	170
Figure 7.6: OPP for DWT-ANN receiver at SER of 10^{-6} against the D_T of [0, 2] for 4-PPM hard decision decoding scheme in a diffuse channel with FLI at data rates of 2 and 5 Mbps.	171
Figure 7.7: The block diagram of the DWT-ANN based receiver for the DPIM modulation scheme for effective removal of the FLI and channel equalization in an indoor OW link.	172
Figure 7.8: OPP for DWT-ANN receiver at SER of 10^{-6} against the normalized delay spread of 0.01- 2 for 4-DPIM in presence of FLI at data rates of 10, 40 and 120 Mbps.	173
Figure 7.9: OPP for DWT-ANN receiver at SER of 10^{-6} against the normalized delay spread of 0.01- 2 for 16-DPIM in presence of FLI at data rates of 10 and 40 Mbps.	173
Figure 8.1: The block diagram of discrete equivalent of communication system with convolutional encoder and decoder.	177
Figure 8.2: State transition diagram of convolutional code.	178
Figure 8.3: Schematic of ANN decoder with input codewords and output bits.	178
Figure 8.4: The BER against the SNR for an ANN decoder with a range of window lengths.	180
Figure 8.5: The BER against SNR for ANN decoder with varying number of neurons in the hidden layer.	182
Figure 8.6: The BER against the SNR for an ANN decoder with varying number of neurons in hidden layer.	182
Figure 8.7: The BER against the SNR for an ANN decoder with varying training length.	183
Figure 8.8: BER against the SNR for uncoded and convolutional coded systems with ANN and Viterbi ‘hard’ and ‘soft’ decoders in AWGN channel.	184
Figure 8.9: The block diagram of ANN based equalizer and decoder for diffuse indoor OWC channel.	185
Figure 8.10: BER against the SNR for an ANN equalizer with ANN and Viterbi ‘hard’ and ‘soft’ decoders in a dispersive channel with D_T of 1.	186

Figure 8.11: BER against the SNR for an ANN equalizer, ANN decoder with and without interleaver/deinterleaver pair in a dispersive channel with D_T of 1.....	187
Figure 9.1: Simulink diagram of the DWT based denoising	190
Figure 9.2: The block diagram of (a) DWT decomposition and (b) DWT reconstruction.	191
Figure 9.3: The received OOK signal at 50 Mbps in presence of FLI denoised using Matlab and Simulink	191
Figure 9.4: The Simulink model of DSP implementation of the DWT based denoising.	192
Figure 9.5: Square of error signal e_r between the DSP and Matlab denoised outputs against number of samples.	193
Figure 9.6 : Simulink model of ANN based DFE structure.....	194

List of Tables

Table 2.1: Comparison of radio and infrared Communication [43, 140].....	19
Table 2.2: Comparisons of LED and LD [144].....	28
Table 2.3: Laser classifications [41, 144].	28
Table 2.4: Comparisons of PIN diodes versus avalanche photodiodes.	30
Table 2.5: Symbol mapping of PPM, DPPPM, DPIM, DH-PIM, MDPIM and DAPPM for bit resolution of $M = 3$	48
Table 2.6: The average symbol length and bandwidth requirement of PPM, DPIM and DH-PIM.....	48
Table 3.1: Probability of bit error for $(n, 1)$ repetition code.	53
Table 3.2: The simulation parameters.....	62
Table 3.3: Code gain for 16-DH-PIM retransmission system at P_{se} of 10^{-4}	65
Table 4.1: The binary data, coded and uncoded DH-PIM ₂ for $M = 3$, and $\Gamma = 2$	75
Table 4.2: The simulation parameters for CC-DH-PIM _{Γ}	78
Table 5.1: Low frequency component phase values.....	89
Table 5.2: High frequency component amplitude and phase values.	89
Table 5.3: The decomposition level and the approximate cut-off frequency (MHz)....	109
Table 5.4: The NOPR to achieve a BER of 10^{-6} at a data rate of 200 Mbps for DWT based receiver with different mother wavelets.....	112
Table 5.5: The decomposition level and the approximate cut-off frequency (MHz)....	114
Table 5.6: The decomposition level γ and the cut-off frequencies (MHz) for L - DPIM.....	117
Table 6.1: Valid DPIM(1GS) 3-bit sequence.....	133
Table 6.2: The list of training algorithm for ANN.....	148
Table 6.3: ANN parameters for equalizations.....	148
Table 8.1 The simulation parameters for ANN decoder.	179
Table 9.1: The BER calculated using the Simulink model and DSP implementation. .	194
Table A.1: Filter coefficients of Daubechies wavelets	204
Table A.2: Filter coefficients of Symlets wavelets (Sym2- Sym8)	205
Table A.3: Filter coefficients of Coiflet wavelets (Coif 1- Coif 4).....	206
Table A.4: Filter coefficients of Biorthogonal Spline (Bior) wavelets.....	206

List of Abbreviations

4G	Fourth generation
ALI	Artificial light interference
ALS	Artificial light source
ANN	Artificial neural network
APD	Avalanche photodiodes
ARQ	Automatic-repeat-request
AWGN	Additive white Gaussian noise
BER	Bit error rate
bior	Biorsplines
BLW	Baseline wanders
BP	Backpropagation
CC-DH-PIM	Convolutional code DH-PIM
CC-DPIM	Convolutional coded DPIM
CCS	Code composer studio
coif	Coiflets
CWT	Continuous wavelet transform
DAPPM	Differential amplitude pulse-position modulation
dB	Decibel
db	Daubechies
DD	Direct detection
DF	Decision feedback
DFE	Decision feedback equalizer
DH-PIM	Dual header pulse interval modulation
dmey	Discrete Meyer wavelet
DPIM	digital pulse interval modulation
DPLL	Digital phase locked loop
DPPM	Differential pulse position modulation
DSP	Digital signal processing
DWT	Discrete wavelet transform
EMI	Electromagnetic interference
FDPIM	Fixed-length DPIM
FEC	Forward error control
FFT	Fast Fourier transform
FIR	Finite impulse response

FLI	Fluorescent light interference
FOV	Field of view
FSO	Free space optics
FSP	Free space photonics
FT	Fourier transform
FWHM	Full width half maximum
GB	Guard band
GDA	Gradient descent algorithm
GS	Guard slot
HPF	High pass filter
IDWT	Inverse discrete wavelet transform
IEC	International electrotechnical commission
IID	Independent, identically distributed
IM	Intensity modulation
IR	Infrared
ISI	Intersymbol interference
LAN	Local area network
LD	Laser diodes
LDPC	Low parity density code
LED	Light emitting diode
LOS	Line-of-sight
LPF	Low pass filter
MAN	Metropolitan-area network
MAP	Maximum <i>a posteriori</i>
MDPIM	Multilevel digital pulse interval modulation
ML	Maximum likelihood
MLP	Multilayer perceptron
MLSD	Maximum likelihood sequence detection
MLSE	Maximum likelihood sequence estimator
MMSE	Minimum mean-square error
MRA	Multiresolutional analysis
MSB	Significant bit
MSE	Mean square error
NEF	Noise energy function
NLOS	Non-line-of-sight
NOPR	Normalized optical power requirement

NRZ	Non-return-to-zero
OFDM	Orthogonal frequency division multiplexing
OOK	On-off keying
OPP	Optical power penalty
OW	Optical wireless
OWC	Optical wireless communication
PAPR	Peak-to-average power ratio
pdf	Probability density function
PER	Packet error rate
PIM	Pulse interval modulation
PIN	Positive-intrinsic-negative
PPM	pulse position modulation
PPM+	Pulse-position modulation plus
PSD	Power spectral density
PSK	Phase shift keying
PWT	Packet wavelet transform
QAM	Quadrature amplitude modulation
RF	Radio frequency
RMS	Root mean square
RNN	Recurrent neural network
RTDX	Real-time data exchange
RZ	Return-to-zero
SER	Slot error rate
SIM	Subcarrier intensity modulation
SNR	Signal-to-noise ratio
STFT	Short time Fourier transform
sym	Symlet
TDL	Tapped delay line
TI	Texas instrument
WAN	Wide area network
WPT	Wavelet packet transform
WT	Wavelet transform
ZFE	Zero forcing equalizer

List of Symbols

\otimes	Convolution
$\delta(\cdot)$	Dirac delta function
Φ_i	Amplitudes of odd harmonics of 50 Hz
Ψ_i	Amplitudes of even harmonics of 50 Hz
Γ_j	Amplitude of switching frequency harmonics
θ_j	Phase of switching frequency harmonics
\bar{E}_{bit}	Average energy per bit.
\bar{L}_{DPIM}	Average symbol length of DPIM
$\lfloor \cdot \rfloor$	Floor function
h_i	Discrete-time impulse response of channel
CM_j	Correlation metric
E_p	Energy of the transmitted pulse
E_{pulse}	Energy per infrared pulse
F_c	Centre frequency
$H_{LOS}(0)$	Transfer function of LOS link
I_p	Average photocurrent
\bar{L}	Average symbol length
P_{avg}	Average transmitted power
P_{avg_OOK}	Average optical power requirement for OOK
$P_{avg_PPM_hard}$	Average optical power requirement for PPM hard decoding
$P_{avg_PPM_soft}$	Average optical power requirement for PPM soft decoding
$P_{e_bit_OOK}$	Probability of bit error for OOK-NRZ
P_p	Incident optical power
P_{se_DPIM}	Probability of slot error for DPIM
$P_{se_PPM_hard}$	Probability of slot error for PPM hard decoding
P_{se-CC}	Bit error probably of convolutional code
T_{symb}	Symbol interval
b_i	Noise free channel output
$m_{high}(t)$	High frequency component of fluorescent lamp
$m_{fl}(t)$	Interference photocurrent from fluorescent lamp
m_k	Fluorescent light interference signal sample
$m_{low}(t)$	Low frequency component of fluorescent lamp
w_{ij}	Weight from the hidden node i to the node j a
y_{nh}	n^{th} level detail coefficient

η_B	Bandwidth efficiency
η_i	Quantum efficiency
σ_n	Standard deviation of the Gaussian, non-white, zero mean
Δ	Sample period
a	Constant related to RMS delay spread
$A_{\cos}(\psi)$	Effective photodetector area
a_i	Input data bits
B	Bandwidth IR transceiver
b_i	Noise free channel output
c	Velocity of light in vacuum
$C(f)$	Channel impulse response
d_{TR}	Distance between the transmitter and the receiver
d	Hamming distance
D	Delay
d_{min}	Minimum Hamming distance
D_{rms}	RMS delay spread
D_T	Normalized delay spread
E_g	Band gap energy
f	Frequency
f_c	Cut-off frequency of HPF
$G_R(f)$	Receiver filter response
$G_T(f)$	Transmitter filter response
h	Planck's constant
$H(0)$	Channel dc gain
$h(t)$	Channel impulse response
H_{LOS}	Impulse response of LOS channel
I_B	Average DC photocurrent
L	Symbol length
M	Bit resolution
N	Total number of bits over a 20 ms interval
N_0	Noise spectral density
$p(t)$	Impulse response of transmitter filter
P_{syme}	Symbol error probability
q	Charge of an electron
$Q()$	Marcum function
R	Photodetector responsivity

r	Code rate
$r(t)$	Impulse response of matched filter
R_b	Bit rate
R_{rt}	Retransmission rate
T_b	Bit duration
T_{s_DPIM}	DPIM slot duration
T_{s_PPM}	PPM slot duration
$u(t)$	Unit step function
W	Window length
w_0	Bias
y_{1h}	First level detail coefficient
y_{1l}	First level approximation coefficient
α_{opt}	Optimum threshold level
γ	Duty cycle, Decomposition level
ζ	Channel span
η_p	Power efficiency
λ	Wavelength
M	Memory
ξ	Desired (bit or slot) error probability
τ	Bit (slot) duration
$E(n)$	Cost function
$F(s, \tau)$	CWT of a signal
$d(n)$	Desired response
s	Scaling
$y(n)$	Actual response
Φ	Radiant flux
η	Learning rate
τ	Translation
ψ	Mother wavelet

Chapter 1 Introductions

Optical wireless communication (OWC), also popularly known as free space optics (FSO) or Free Space Photonics (FSP) or open-air photonics, is an optical communication technology utilizing a light propagating in free space to transmit data between two points.

The concept of light as a means of communication goes back to pre-historic time when natural light sources like sun, moon, star or artificial light sources like fire and sign languages were used for communications. The modern form of optical communications was initiated by the Alexander Graham Bell [1] in 1878. It was in fact the first form of wireless speech communication. Three decades later, wireless speech communications using the radio wave was achieved by the Reginald Fessenden [2]. The introduction of the optical fibre, improvement in semiconductor devices and discovery of laser had made modern communication possible using optical wavelength.

The first successful demonstration of a wireless local area network (LAN) by Gfeller and Bapst [3] in the IBM lab had revolutionized in-house wireless personal communications. Though their proposal made use of infrared (IR) wavelength, the present wireless LAN is dominated by radio frequency (RF) links. RF technology offer a number of unique advantages including availability of highly-sensitivity receivers, flexibility, mobility and relatively simple link set-up, that had made RF the dominating medium for communications [4]. The fact that an alternative technology was not necessary for in-house personal communication is also a cause of RF being the dominant technology until recently. However, the scenario is rapidly changing largely due to rapid growth in bandwidth demand by the end-users, the bandwidth congestion in the RF domain and licensing issue. The rapid growth of internet users, file and video sharing, audio and video broadcasting and ever increasing bandwidth demand for personal communications have placed a huge pressure on already congested bandwidth of RF systems. To satisfy the demand for higher

data rates, more complex coding, multiple antennas and higher carrier frequencies have already been introduced [4], however it is very unlikely that RF alone would be able to provide the necessary bandwidth to end-users at certain location and application within the network. For example in the last mile link the potential solution (and maybe the best option) would be to utilize the licence free optical technology. Optical systems offer what RF is lacking, the promise of theoretically unlimited bandwidth. As the advantage of optical communications in the form of optical fibre is already demonstrated, it is without a doubt that the optical wireless (OW) systems will play a significant role in personal communications. The only question is when its unfulfilled potential will be fully realized.

There has been a continuous interest from researchers and industrial sectors on application of OWC systems. The first experimental work used a full duplex IR link at a bit rate of 64 kbps [3], within a decade a higher data rate of up to 50 Mbps was reported by a number of companies including the Hitachi, IBM, Fujitsu, Hewlett-Packard, AT&T Bell, BT Labs, Motorola [5-10]. With a tracking architecture, BT Labs in 1996 reported a data rate of 1 Gbps [6, 11]. We have seen growing academic research activities as well as industrial development including the indoor OWC channel modelling [12-14], 50 Mbps diffuse links [15, 16], high speed integrated transceivers [17, 18], more power efficient modulation techniques [19-25], holographic diffusers [26-29] and a fly-eye receiver [30, 31].

The OWC is suitable for specific applications in the hospital and library environment which are sensitive to the electromagnetic interference (EMI) [32]. The IR wireless transceiver is commercially available for a number of applications including PC-PC connectivity, laptops, mobile devices, PDAs, and printers. However, the most successful application of OWC system is the IrDA for short range communications [33]. Annual shipments of IrDA transceivers are above 300 million units for two successive years and it is increasing rapidly [34]. Recently, KDDI R&D Laboratories has developed a 1 Gbit/s high-speed IR wireless data link which can replace USB connections [35]. Other specific applications of OWC include vehicle-to-vehicle wireless communications for road safety [36], passenger aircrafts [37, 38], high-speed trains [39], airports and railway stations, hospitals and medical applications [32, 40]. With such extensive applications supported by industrial and academic research, the OWC communications will have a key role in future personal communications as a complementary technology to RF.

1.1 Research Motivations and Objectives

Though fundamental concepts of RF and IR communications are similar, due to the different natures of the RF and IR signals, they possess different challenges when used for wireless applications. Spatial confinement of IR signal within a room and highly directional transmitter mean that IR systems suffer less from co-channel interference. The larger receiver area compared to the signal wavelength means the multipath fading is non-existent for IR wavelength. The adverse weather conditions in outdoor environment including solar interference, fog, rain, snow, dust particles and turbulence pose the greatest challenges to long range outdoor OWC systems. Relatively short link length in indoor environment makes indoor OWC free from such undesirable effects. However, the indoor channel poses a number of challenges; many of which are unique to the indoor environment.

One of the most sensitive apprehensions in the indoor OWC system is the eye and skin safety issue [41-45]. Due to the availability of a cheap optical transceiver, the near-IR wavelength in the range of 780-950 nm is commercially the most viable solution. The light at this wavelength behaves like visible light. The cornea and eye lens do not absorb the radiation at near-IR wavelength and it is focused into retina. The invisibility of these wavelengths to human eyes means no blinking reflex. Since retina does not have heat sensor, continuous exposure to high intensity light at these wavelengths can permanently damage retina leading to complete blindness.

The laser eye safety is classified by the International Electrotechnical Commission (IEC) [41]. The laser transmitter must be Class 1M for it to be safe when viewed by the naked eye. To be within the specifications of the maximum permissible exposure, the average optical power at 780-950 nm of radiation for pointed source should be < 1 mW [41]. This limits the link range that can be achieved. Higher permitted average optical radiation in the 1550 nm range, by almost a factor of 50, makes 1550 nm more suitable for longer link length. However, 1550 nm is not yet a practicable solution for the indoor application due to higher transceiver cost. Instead of using a pointed source like laser, wide beam area devices like LEDs can transmit higher power without being unsafe. Alternatively, holographic diffusers can be used to achieve a higher transmitter power without violating the safety guidelines [26-28, 46-49].

It is clear that the indoor optical channel is power limited and the holographic diffuser is an indirect method to transmit more power. However, it is not always necessary to pump more power to achieve higher reliability. Advanced signal processing at the transmitter and the receiver, more suitable modulation techniques and error corrections at the receiver are alternative methods to improve link performance. A number of baseband modulation techniques had been studied for the indoor OWC [19-22, 25, 50-54] each having unique characteristic. Among them, pulse position modulation (PPM) provides unparalleled power efficiency. Combining power efficient modulation techniques with the error control coding can provide a significant performance improvement in terms of reduced error probability or power requirement. Power efficiency is important not only to meet the safety standard but also to enhance battery life for the handheld devices.

The simplest method of achieving higher power efficiency is to add redundancy through repetitive retransmission of a bit or a symbol through the channel. If a bit or a symbol is repetitively transmitted for a predefined number of times, the receiver would select the bit or the symbol that is repeated the highest number of time. The symbol retransmission scheme for PPM is reported in [55-57]. Doubling the repetition rate provides an incremental signal-to-noise ratio (SNR) gain of ~ 3 dB. Combining the repetition coding with automatic-repeat-request (ARQ) protocol [58] leads to a lower complexity transceiver design with superior performance [56]. The symbol repetition scheme can be applied to other baseband modulation techniques like digital pulse interval modulation, dual header pulse interval modulation with some modification. Due to lack of symbol boundaries in these modulation schemes, the simple decoding algorithm is not applicable and error probability analysis needs to take care of not only the variable symbol length but also the symbol error probability. To the best knowledge of the author, retransmission scheme has not been reported for variable symbol length modulation scheme and the error probability analysis for such modulation scheme was carried out and reported for the first time in [59]. The slot error rate (SER) analysis supported by computer simulation is discussed in detail in this thesis. A case study is carried out for DH-PIM. However, the analysis can be applied for any variable symbol length modulation technique without modifications.

The SNR reduction to achieve a SER of 10^{-6} for retransmission scheme depends on the symbol length and ~ 3 dB reduction is achieved for DH-PIM with a retransmission rate of

four. The retransmission scheme is effective, simple to implement without the need for an additional transmitter or receiver. However, the penalty is a significant reduction in the data throughput. For example, to achieve a code gain of ~ 3 dB, the retransmission rate should be four, meaning a 300% overhead burden.

A number of more efficient error correction codes exist for digital communications. The error correction code differs from the retransmission scheme in the sense that it allows error correction at the receiver. The error correction codes can broadly be classified into the linear block code and the convolutional code. The binary error correction codes can be applied to the on-off keying (OOK). With/without modification, the convolutional and block codes can be applied to PPM [60-71]. The complexity arises when these codes need to be applied to modulation techniques with no fixed symbol boundaries. Linear block codes take a fixed number of bits as input, hence are not suitable for the variable symbol length modulations. A fixed-length DPIM (FDPIM) based on DPIM is suggested and the turbo code is applied to FDPIM [72]. Though symbol length is fixed for FDPIM, the average symbol length is significantly higher than that of DPIM. Hence the throughput that can be achieved using DPIM cannot be attained. In fact, the average symbol length of FDPIM is equal to PPM; however the advantage of such a system compared to PPM is questionable. Marker codes to correct insertion/deletion errors for differential PPM (DPPM) is investigated by Sethakaset and Gulliver [73] who had shown that such code offers ~ 3 dB improvement in SNR for 2 and 4-DPPM. The improvement is < 1 dB for 8 and 16-DPPM. The performance can be improved significantly by using concatenating marker and the Reed–Solomon codes [21]. However, the penalty paid is the throughput reduction and the bit overhead of 240% for 4-DPPM with a marker code and higher if concatenated.

Since the convolutional encoder takes serial input, it would be logical to apply the convolutional code instead of the block code for variable symbol length modulation schemes. Convolutional codes offer greater simplicity of implementation with high error correction capability. Convolutional codes for variable symbol length modulation techniques like DPIM and DH-PIM are first investigated by the author and the results are published in [74-76]. DH-PIM with a unique header pattern applied to the convolutional encoder results in a distinctive pattern. As a result, the state diagram and the error

probability for convolutional coded DH-PIM would be different from the general case. New analysis is necessary to determine the upper bound of the error probability for convolutional coded DH-PIM. In this thesis, the mathematical analysis is verified by the computer simulation using Matlab, details of which are given in the subsequent chapters.

The error correction code provides the SNR gain in presence of the additive white Gaussian noise (AWGN). However, non-Gaussian noise, unique to the indoor environment due to artificial light sources (ALSs) used for domestic lightening, is another source of interference for indoor OWC links. The ALSs have strong spectral content at the near-IR range. ALSs are periodic with a spectral content covering DC-to-MHz range depending on the type and manufacturers [77-81]. If not alleviated, the interference due to ALS is in fact the most dominating source of the system impairment [77-80, 82-86]. A receiver design based on the differential optical filtering to reduce the artificial light interference (ALI) is investigated by Moreira *et al* [87]. Photocurrents of two optical receivers, one with an optical filter and another without a filter are combined in such a way that the effect of the interference is minimized [87]. The interference cancellation differential receiver [87] is based on the assumption that the transmitted signal and the interference have different optical spectra. An alternative approach using two linear orthogonal polarisers coupled with a differential detector is suggested by Lee [88]. The polarizer method is very simple and easily applicable under the condition that the signal light is polarized. Alternatively, angle diversity techniques in which multiple sectored receivers are utilized can also be effective to combat the ambient noise [89]. All methods described above require more than one receiver with further signal processing to combine the received signal (photocurrents) from the different receivers in order to minimize the effect of ALI. The alternative approach (and the simplest method) is the combination of the optical bandpass filter and an electrical high pass filter [43, 80, 82, 90, 91] which does not require an additional photodetector. The spectral content of the florescent light drive by electronic ballast ranges to MHz and most important factor of impairment. The first-order analogue HPF is not very effective in reducing the power penalty due to florescent light interference at low data rates for OOK [51, 82]. Dickenson [92] in his study found that a digital HPF significantly improves the SNR reduction to achieve the desired error probability compared to its analogue counterpart. The limiting factor is a very high order of filter (> 5000 for a cut-off frequency of 0.5 MHz). Alternative method to remove the ALI using the discrete wavelet transform is

investigated in this research. The modulating signal and the interference are separated into different bands of frequencies using DWT; a band of signal that corresponds to the interference is removed from reconstructed signal. The study shows that DWT is not only more effective for removing ALI compared to the digital HPF, but also offers added advantage in terms of significantly reduced filter order with a simple repetitive structure for realization [93, 94].

Another key challenge that mutilates the performance of the indoor optical wireless channel is the multipath induced intersymbol interference (ISI). A diffuse indoor optical wireless channel can be modelled as a linear baseband impulse response and is completely characterised by the root mean square (RMS) delay spread and the optical path loss [95]. For a typical room, the average value of RMS delay spread for optical channel ranges from 8-12 ns. The diffuse links are more susceptible to the power penalty due to ISI, which increases exponentially with increasing the data rates. OOK is the least susceptible to ISI among the baseband modulation techniques and an irreducible bit error rate (BER) is observed at a normalized delay spread (normalized using bit duration) of > 0.6 [43, 96]. For a typical room with a delay spread of 10 ns, this leads to the highest attainable bit rate of 60 Mbps. If a compensation technique is not incorporated in the receiver, OOK reception is not feasible at this bit rate. The optimum receiver in the presence of ISI is the maximum-likelihood sequence detection (MLSD). Due to a number of complexities for practical implementation including high complexity, delay and larger memory requirement, a practical but suboptimal method using the equalization technique is often the preferred option [15, 16, 43, 67, 97-100]. The traditional equalization techniques based on the finite impulse response (FIR) filter are well studied and undoubtedly provide significant performance improvement for a number of diffuse communication channels including indoor OW channels. More recently, the adaptive equalization has been defined as a classification problem, opening new avenues for utilization of classification tools like the artificial neural network for equalizations [101-104]. ANN as an equalization tool has a number of advantages most importantly the adaptability, a nonlinear decision boundary and parallel processing capabilities. A feedforward multilayer perceptron (MLP) ANN with a supervised backpropagation training algorithm is utilized for effective channel equalization for diffuse indoor OW channels in this study. Both linear and decision feedback (DF) structures are investigated with latter offering improved performance [93, 94, 105, 106].

The performance impairment factors, the ISI and ambient light interference, are presented concurrently in diffuse indoor OWC channels. However, most researchers tend to investigate effect of these factors on the performance independently and very little study has been done on combined effects of these channel impairments [84, 86]. The performance of the equalization techniques is not well investigated in presence of the FLI with filtering. A study of the combined effect of FLI and ISI is carried out with the DWT and ANN for denoising and equalization, respectively. The results of the study are summarized in Chapter 7 and reported in [93, 94].

Adaptive decoding of error control codes can be very useful for future communication systems. The rate-adaptive error control code is a powerful technique to improve the energy efficiency of the overall system [107-109]. The rate-adaptive techniques are focused on the changing of the code-rate of the punctured convolutional code. Adaptive decoding has also had an important aspect as it will provide possibility of using different encoders at the transmitter and decoding without having detail knowledge of the encoder. In Chapter 8, it is demonstrated that an adaptive decoding of the convolutional code using ANN is possible. Though significant further study is needed to make adaptive algorithm efficient, the existence of such a scheme is verified and a number of parameters are optimized.

Finally, the DWT based denoising and ANN based equalizers are practically implemented in digital signal processing board and simulation results are verified using the output of the practical results as given in Chapter 9.

The challenges of indoor OWC systems taken into consideration in this research, the existing and the proposed solutions are summarized in Figure 1.1.

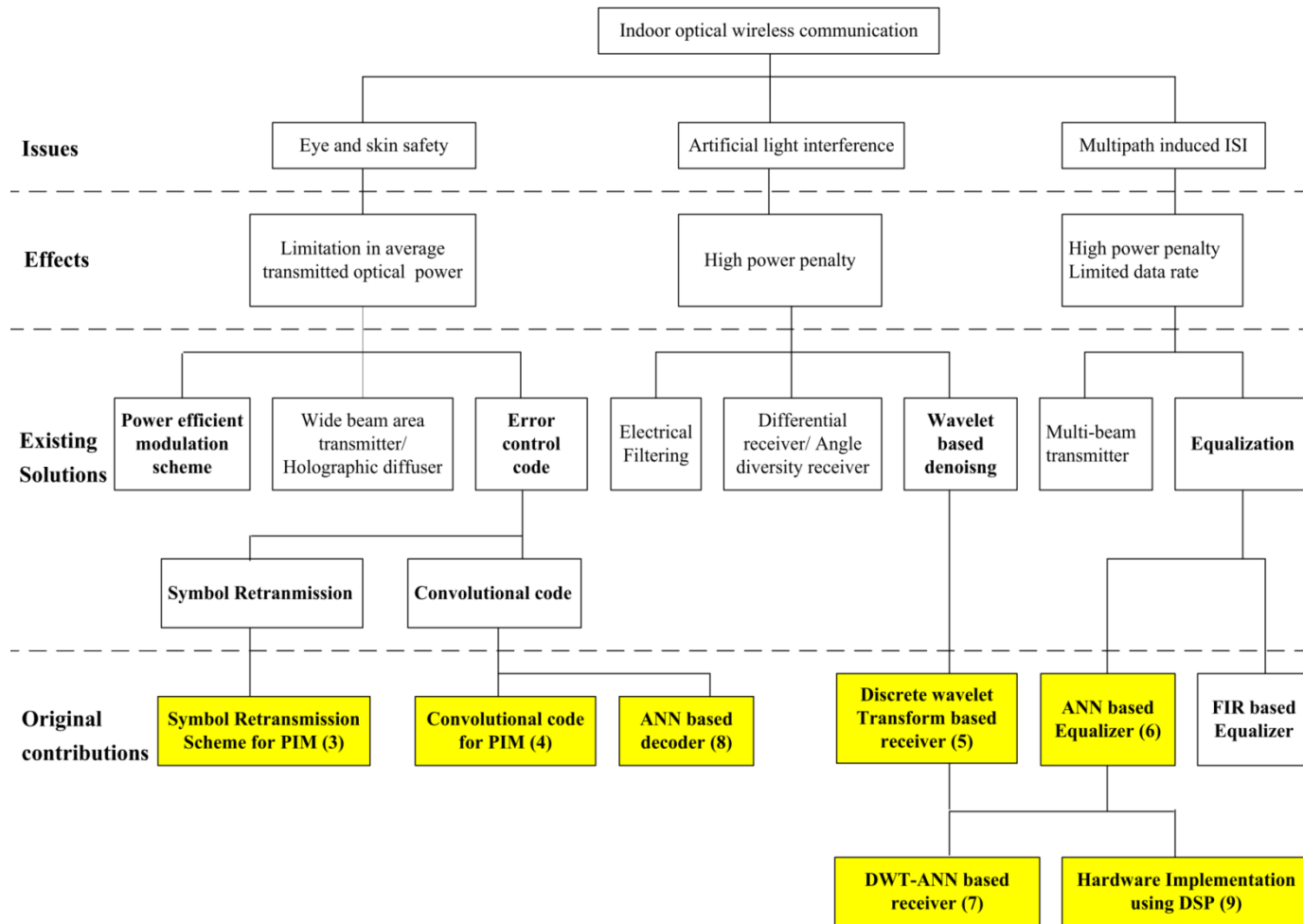


Figure 1.1: The summary of the challenges, the existing and the proposed solutions for indoor OWCs considered in this research. Chapter numbers where the proposed research is discussed are given in brackets and research carried out is given in bold.

1.2 Original Contributions

As a result of the study, the following original contributions are made:

1. Investigation of the retransmission scheme for indoor OWC schemes is carried out. Original expression for the slot error probability for the variable symbol length modulation scheme is derived and verified using computer simulation, see Chapter 3.
2. Convolutional code is applied to the variable symbol length modulation techniques of DH-PIM and DPIM. New expressions to estimate the upper limit of error probability of convolutional coded DH-PIM is derived and verified using computer simulations, see Chapter 4.
3. Investigation of ALI with the DWT based denoising is carried out for a number of modulation techniques. Comparative studies of the digital HPF and DWT are carried out showing a number of advantages of the proposed methods. The mother wavelet providing the best performance is determined, see Chapter 5.
4. Investigation of the power penalty induced due to ISI in a diffuse channel for different modulation techniques is carried out. A new soft decoding method for DPIM to reduce the effect of ISI is suggested showing improved performance, see Chapter 6.
5. Adaptive channel equalization using the ANN for a diffuse indoor OWC link is proposed and studied. Both linear and DF structures are investigated and the performance of equalizers are examined for a number of modulation techniques. The study shows the effectiveness of such equalizers to mitigate multipath induced ISI. Comparative study of the equalizer and with a traditional FIR filter based equalizer is carried out and demonstrates that the ANN based equalizer can match the performance of traditional equalizers in all channel condition with reduced training length, see Chapter 6.

6. A study of the combined effect of FLI and ISI is carried out with the DWT denoising and ANN based equalizer. The study shows that power penalty due to one of the factors is the dominating source of performance impairment. Power penalty at low data rates is mostly due to FLI. However, ISI induced power penalty causes significant impairment at higher data rates, see Chapter 7.
7. Adaptive decoding of convolutional code using the feedforward backpropagation ANN is proposed. A number of parameters including training length, decoding depth and number of neurons are optimised. Comparative studies of the decoder with optimum Viterbi decoder are examined. The performance of hard decoding using the ANN and Viterbi decoder show almost identical performance. The soft decoding of Viterbi decoder outperforms the soft decoding using ANN, however the difference is less than 0.6 dB, see Chapter 8.
8. For practical realization, the DWT based receiver and ANN based equalizer are implemented using a DSP board. Rapid prototyping of the proposed system is carried out using TMS320C6713 DSP board and Matlab/Simulink. The practical results verified the computer simulations, see Chapter 9.

1.3 List of Publications and Awards

The investigations led to the following publications and awards:

1.3.1 Refereed Journal Papers

1. S. Rajbhandari, Z. Ghassemlooy, and M. Angelova, "Effective denoising and adaptive equalization of indoor optical wireless channel with artificial light using the discrete wavelet transform and artificial neural network", *IEEE Journal of Lightwave Technology*, vol.27, no.20, pp. 4493-4500, Oct. 2009
2. S. Rajbhandari, Z. Ghassemlooy and M. Angelova, "Bit error performance of diffuse indoor optical wireless channel pulse position modulation system employing artificial neural networks for channel equalisation," *IET - Optoelectronics*, vol.3, no.4, pp. 169-179, August 2009.

3. Z. Ghassemlooy, S. Rajbhandari, and N. M. Aldibbiat, "Convolutional coded dual header pulse interval modulation for photonic wireless links" IET - Optoelectronics, vol.3, no.3, pp.142-148, June 2009.
4. S. Rajbhandari; Z. Ghassemlooy, and M. Angelova, "Performance of the wavelet transform-neural network based receiver for DPIM in diffuse indoor optical wireless links in presence of artificial light interference," IJEEEE, vol. 5, no. 2, pp.102-111, 2009.
5. S. Rajbhandari, N. M. Aldibbiat, and Z. Ghassemlooy, "Analysis and evaluation of symbol retransmission in optical wireless links employing DH-PIM", European Transaction on Telecommunications, vol. 20, no.2, pp. 217-225, 2009.
6. Z. Ghassemlooy, R. Dickenson, and S. Rajbhandari, "Wavelet transform - artificial neural network receiver with adaptive equalization for a diffuse indoor optical wireless OOK link", Mediterranean Journal of Computers and Networks, vol. 5, no. 1, pp. 1-9, 2009.

1.3.2 Conference Papers

7. S. Rajbhandari, Z. Ghassemlooy, and M. Angelova, "The efficient denoising artificial light interference using discrete wavelet transform with application to indoor optical wireless system", Tenth international symposium on Communication Theory and Application (ISCTA'09), pp. 155-160, Ambleside, UK, July 2009.
8. R. Kharel, S. Rajbhandari, K. Busawon, and Z. Ghassemlooy, "Digitization of chaotic signal for reliable communication in non-ideal channels", proceeding of International Conference on Transparent Optical Networks "Mediterranean Winter" 2008 (ICTON-MW'08), ISBN: 978-1-4244-3485-5, pp. Sa1.2 (1-6), Marrakech, Morocco, 11-13 Dec., 2008. **Invited Plenary Paper.**
9. Z. Ghassemlooy, R. Dickenson, and S. Rajbhandari, "Signal detection and adaptive equalization using wavelet transform - artificial neural network in diffuse indoor optical wireless links", XIII Congreso Internacional de Telecomunicaciones SENACITEL 2008, Valdivia, Chile, November 2008.
10. S. Rajbhandari, Z. Ghassemlooy, and M. Angelova, "Performance of DWT-ANN based signal detector/equalizer for DPIM in practical indoor optical

wireless links”, CSNDSP, ISBN: 978-1-4244-1876-3, pp. 106-109, Graz, Austria, July 2008.

11. S. Rajbhandari, Z. Ghassemlooy, and M. Angelova, "Signal detection and adaptive equalization using a discrete wavelet transform – artificial neural network for OOK indoor optical wireless links", ICEE 2008, Tehran, Iran, 13-15 May 2008, Paper No. 2808.
12. Z. Ghassemlooy, and S. Rajbhandari, "Performance of diffused indoor optical wireless links employing neural and adaptive linear equalizers," **Invited paper**, 6th ICICS, Singapore, 10-13 Dec. 2007, Paper No. P0455, 1-4244-0983-7/07.
13. Z. Ghassemlooy, W.O. Popoola, S. Rajbhandari, M. Amiri, and S. Hashemi, "A synopsis of modulation techniques for wireless infrared communication," **Invited paper**, Intern. Conf. on Transparent Optical Networks - Mediterranean Winter (ICTON-MW'07), Sousse, Tunisia, 6-8 Dec. 2007.
14. S. Rajbhandari, Z. Ghassemlooy and M. Angelova, "The Performance of PPM using neural network and symbol decoding for diffused indoor optical wireless links", 9th International conference on Transparent Optical Networks (ICTON2007), pp.161-164, Rome, Italy.
15. S. Rajbhandari, Z. Ghassemlooy, and M. Angelova, "Performance of OOK with ANN equalization in indoor optical wireless communication system," The 8th annual Postgraduate Symposium on the convergence of Telecommunications, Networking & Broadcasting (PGNET 2007), ISBN 1-9025-6016-7, Liverpool, UK, pp 86-90, June 2007.
16. S. Rajbhandari., Z. Ghassemlooy, N. Aldibbiat, M. Amiri, and W.O. Popoola, "Convolutional coded DPIM for indoor non-diffuse optical wireless link”, The 7th IASTED International Conferences on Wireless and Optical Communications (WOC 2007), ISBN 978-0-88986-659-1, Montreal, Canada, pp. 286-290, May-Jun. 2007.
17. N. Aldibbiat, S. Rajbhandari and F. Ghassemlooy, "Convolutional coded DPIM for indoor optical wireless links”, LCS2006, UCL, London, 2006.
18. S. Rajbhandari, Z. Ghassemlooy, and N.M. Aldibbiat, "Performance of convolutional coded dual header pulse interval modulation in infrared links “, Proceeding of the 6th annual postgraduate symposium on the convergence of

telecommunications, networking and broadcasting (PGNET), ISBN 1-9025-6013-9, pp 227-231 Liverpool , UK, June 2006.

1.3.3 Poster

19. Rajbhandari, S., Angelova, M., and Ghassemlooy, Z.: “Wavelet transform and artificial neural network for digital signal detection and equalization in optical wireless communication”, UK GRAD Program Yorkshire & North East Hub, Poster Competition & Network Event, York, UK, 7 March 2008, Poster No. 48.
20. "Application of neural network and wavelets for digital signal detection and equalization in indoor optical wireless system" Northumbria University-CEIS research seminar, 9 May 2007.

1.4 Organization of the Thesis

The thesis is divided into ten chapters. The first chapter provides the summary of the research undertaken with motivation and objectives. The literature review of indoor OWC systems is summarised in Chapter 2. The building blocks of indoor OWC systems, the transmitter, the receiver devices and the optical channel are described in details along with some of the key challenges. The synopsis of baseband modulation techniques is given which provides the platform for discussion in subsequent chapters. The retransmission scheme to improve the performance of indoor OWC systems is given Chapter 3. The decoding algorithm using the majority decision scheme for retransmission system is outlined and the slot error probability for a variable symbol length modulation scheme is derived for retransmission rates of 3, 4 and 5. The mathematical analysis of error probability is verified using computer simulation, details of which are given in the chapter.

Convolutional codes for variable symbol length modulation schemes like DPIM and DH-PIM are subject of study of Chapter 4. The derivation of upper bound for error probability of a $\frac{1}{2}$ rate convolutional encoder with a constraint length of 3 and a Viterbi decoder is outlined in the chapter. The chapter provides SER of convolutional coded DPIM and DH-PIM generated using computer simulation and compared with the

theoretical upper bounds. Finally comparative studies of a number of modulation techniques are also given.

A novel denoising method based on the DWT to reduce the effect of ALI in the indoor OWC system is proposed in Chapter 5. The electrical model of fluorescent lamps driven by electronic ballasts is described briefly followed by power penalties incurred due to the FLI for OOK, PPM and DPIM. The chapter also provides an overview of the continuous and discrete wavelet transform. The concept of DWT based denoising is discussed in detail and supported by study of the optical power requirement and optical power penalty to achieve a slot/bit error probability of 10^{-6} for OOK, PPM and DPIM in presence and absence of FLI with DWT based denoising. Finally, a comparative study of the DWT and high pass filtering is carried out and the advantage of DWT is highlighted.

The effect of multipath induced ISI in the indoor OWC system is investigated in Chapter 6. The power penalties in channels with a normalized delay spread range of 0-1 is reported showing an exponential growth in the power penalty with increasing delay spread for all modulation techniques. The concept of equalization as classification problem is described followed by the introduction to ANN as a classification tool. The architecture and working principle of the linear and DF equalizers are considered and the performance of such equalizers is examined for OOK, PPM and DPIM in a channel with a normalized delay spread of [0, 2]. Optical power penalty is calculated for unequalized and equalized systems to demonstrate the effectiveness of ANN based equalizer. Comparative studies of the traditional equalizer based on a FIR filter and ANN are also summarised in the chapter.

The combined effect of FLI and ISI due to multipath propagation is explored in Chapter 7. Both DWT denoising and ANN equalizer are implemented at the receiver to mitigate the effect of FLI and ISI, respectively. Computer simulations are carried out to study the combined effect under different conditions for a number of modulation techniques and the findings are reported.

Chapter 8 proposes a new adaptive decoder using ANN for $\frac{1}{2}$ rate convolutional code with a constraint length of 3. A number of advantages of the suggested system are outlined followed by a comparative study with the optimum Viterbi decoder. ANN

parameters are optimised to obtain the best performance. Both hard and soft decoding schemes are taken into consideration for the decoder.

Chapter 9 reports the result of practical implementation of the proposed DWT-ANN receiver. Computer simulation as outlined in Chapters 5, 6 and 7 are verified by practical implementation using a TMS320C6713 DSP board, a code composer studio (CCS) and Matlab/Simulink.

The final chapter of the thesis summarizes the research undertaken and the results of the investigation. Concluding remarks are drawn based on the discussion on the thesis and future recommendations are provided.

Chapter 2 An Overview of Optical Wireless Communications

2.1 Introduction

Light had been used in communication since pre-historic times. People used smoke and light to transmit information. Invention of telephone and telegraph made the transfer of data and voice through a cable possible. With demonstration of Marconi in 1901 to transmit radio wave from the Isle of Wight to Tugboat 18 miles away, new horizon in the field of communication opened and grew rapidly. Historically, the very first form of 'wireless' speech communication was achieved at optical wavelengths in 1878 [110]. The optical wireless communication was first demonstrated by Alexander Graham Bell in the late nineteenth century who called it photophone. However, it wasn't until the invention of the laser, some new semiconductor devices and optical fibre in the 1960s that optical communications finally began getting some real attention. F.R. Gfeller and U. Bapst suggested the use of IR wireless in-house communication in 1979 [3] which started a new era of indoor OWC.

Though basic system model for in-house OWC was first proposed in 1979 [3], the extensive studies of channel capacity, channel modelling as well as modulation techniques were done mostly in the late nineties [11, 96, 99, 111, 112]. A number of modulation techniques with certain distinctive features have been proposed. OOK, PPM, differential PPM (DPPM) [52], DPIM [51], DH-PIM [25], differential amplitude pulse-position modulation (DAPPM) [21], edge position modulation [20, 53, 113] and subcarrier modulations [114, 115] are some of the most popular modulation techniques, though variations of these modulation techniques do exist [116]. The modulation techniques are briefly introduced in the chapter with the OW channel model, optical transmitter and receiver, challenges in the implementation for the personal communication and possible existing solutions. Proposed new solutions would be discussed in subsequent chapters. This chapter gives the overview of the OWC with main focus on indoor application. The overview of the OWC is given in Section 2.2, followed by most popular link configurations in Section 2.3. The indoor OW channel is

briefly summarised in Section 2.4. Optical transmitter and optical receiver is the subject of the Section 2.5 and 2.6 respectively. Ambient light sources and their possible affect on OWC are explored in Section 2.7. Section 2.8 provides overview of the modulation techniques that are investigated in this study and finally the chapter is concluded by a summary.

2.2 Overview of Optical Wireless Communications

The increasing popularity of files and video sharing and the possibility of digital radio and TV broadcast over the internet have already put a huge bandwidth demand on the personal communication systems. Though there has been a continuous growth in capacity of the typical LAN and wide area network (WAN) due to deployment of fiber optics, there has not been such development in metropolitan-area network (MAN) [117]. The fourth generation (4G) communication systems promises to support multiple applications and a higher bandwidth per user (more than 100 Mbps) for both indoor and outdoor applications [118]. However, the bandwidth per end-user is limited at most to a few Mbps in existing communication systems because of the bottleneck imposed by the use of copper cables or RF wireless links at the last mile. The gap between wired and wireless data rates continues to grow, with RF systems lagging by a significant factor [119]. Although, higher RF frequencies (beyond 60 GHz) have been suggested to overcome the bandwidth bottleneck per user, the cost is too high and therefore is required a huge reduction in cost before the end users will benefit from the potential wide bandwidth [11, 42]. In this scenario, the OWC has a part to play in wider 4G vision [4, 120, 121].

One logical solution to the bandwidth congestion problem and the ‘last mile access’ bottleneck, is to move across to the optical domain and take advantage of what has already been achieved in the fibre backbone. Fibre-to-the-home is already a common concept in developed countries providing end-to-end high bandwidth links. Expansion of fibre to the homes in some cases may not be the best solution, considering the cost and deployment [122-124]. An alternative option would be to depot OWC technology, which offers a wide bandwidth, security and compatibility with the existing optical fibre backbone [20, 125]. In fact FSO can be consider as the extension of the fiber optics for last mile [126].

Whilst the IR technology is currently overshadowed by the plethora of RF schemes for wireless networking in the home and office applications, it still has significant potential when bandwidth demand is high. Cheaper transceiver cost, quick deployment, relatively easy link set-up and compatibility with the existing optical fibre communication systems have made OWC an attractive alternative in places where fibre is rather difficult to deploy [42, 125, 127]. OWC systems have found its application in multitude of communication systems ranging from the terrestrial and deep space communications [128-130], airports and railway stations, hospitals, medical applications [32, 40], aircrafts [37], vehicle-to-vehicle wireless communication for road safety [36] and high-speed trains [39]. There had been a rapid industrial growth of application of both indoor and outdoor OW systems [125, 131, 132]. The outdoor OW links is already providing a commercial application in backbone long-haul communications using line-of-sight (LOS) links at data rates of more than 2.5 Gbps per wavelength [133, 134]. However, progress and development in the indoor application is relatively slow because of lack of mobility. However, the scenario is changing quickly largely due to the bandwidth congestion in the RF domain. Installation of optical hotspots in public buildings (rail way stations, airports, etc.) providing data rates in the range of GHz is already commercially available. The future office design will include high speed optical hotspot points in specific locations and for particular applications [4]. Recently a growing interest has been observed in using white LED lamp that can transmit broadband via the same light that illuminates the room [135-139].

Table 2.1: Comparison of radio and infrared communications [43, 140].

Property	Radio	Infrared	Implication for IR
Bandwidth regulated	Yes	No	Approval not required world-wide compatibility
Passes through walls	Yes	No	Inherently secure carrier reuse in adjacent rooms.
Multipath fading	Yes	No	Simple link design
Multipath dispersion	Yes	Yes	Problematic at high data rates
Path loss	High	High	
Dominant noise	Other users	Background	Short range
Average power proportional to	$\int f_e(t) ^2 dt$	$\int f_o(t) dt$	$f_e(t)$ and $f_o(t)$ are the electrical and optical input signals with high peak-to-average ratio.

The key differences of the radio wave and IR links are given in Table 2.1. Compared to the radio wave communications; optical communications provide a number of advantages for the wireless applications. IR offers a huge unregulated bandwidth which can readily be utilized. On the other hand, the radio wave is already congested with little room for expansion and is getting more expensive for license. Unlike the radio wave, the optical transmitter can emit highly directive beam and hence can have interference-free small cell offering high data rate within close proximity without a need for multiple access. The optical system can provide highly localized radiation foot print as light cannot penetrate opaque objects. The high directivity and spatial confinements gives the optical channels very high security against the eavesdropping. Another key advantage of the IR communication system is its immunity to EMI and can be used in environments like hospital and library where interference must be minimized. Due to large area photodetector, the OW links are not affected by multipath fading. Since the photodetector absorbs the waves separately and averages the incoming energy, the destructive interference is not possible. In addition to the gigabit-per-second data-transfer rate, relatively low cost and small size transceiver also favours the application of the IR in indoor applications.

The key challenge in application of the IR for indoor applications is the potential eye-safety issue. The collimated light beam entering the eye is focused in retina. The eye is insensitive to the IR ray and hence does not induce blink reflex to the invisible light and since retina has no pain sensor, the invisible light can permanently damage the retina. The maximum power that can be transmitted is limited by eye-safety regulations. The LOS links are very susceptible to blocking probability and does not allow mobility, and complex tracking system may be necessary. Though diffuse system is less susceptible to blocking, multipath propagation leads to high path loss and ISI leading to high power penalty [6, 43, 44]. The background radiations from both natural and artificial source act as noise at receiver and if proper technology is not incorporate at the receiver; this would limit the range of the system. In addition, the IR receiver sensitivity is significantly lower than that of radio channels as the detector responds linearly with the incident power and hence the system is more susceptible to path loss.

Both IR and RF have advantages and disadvantages and it would be too early to predict that IR system would dominate the indoor personal communication. It would rather be a hybrid of the IR-RF system that would be the most suitable for the applications as the

IR system provide unparallel bandwidth while RF system can provide flexibility and mobility. It would be more likely that the two system works in complementary manner, the preference depending upon the applications [4, 43, 119, 141].

2.3 Link Configurations

A number of topologies can be adopted for the effective communication for different indoor environments and applications. The topologies employed for various designs can be classified according to 1) the degree of directionality of transmitter and receiver and 2) the existence of the LOS path between the transmitter and the receiver [6, 43, 142]. Different link configurations of the IR links are given in Figure 2.1. For the directed LOS, there must be an unobstructed path between the transmitter and the receiver for an uninterrupted communication. The transmitter has very narrow beam and receiver has narrow field of view (FOV) resulting in a minimum path loss and rejection of the ambient light. The directed LOS links can achieve the maximum data rate and the data rate is limited only by the photodetector capacitance [143]. However, the LOS is suitable only for specific applications due to blocking and shadowing probability and lack of mobility. Tracking option is often incorporated in the transmitter and the receiver to allow for mobility to the system.

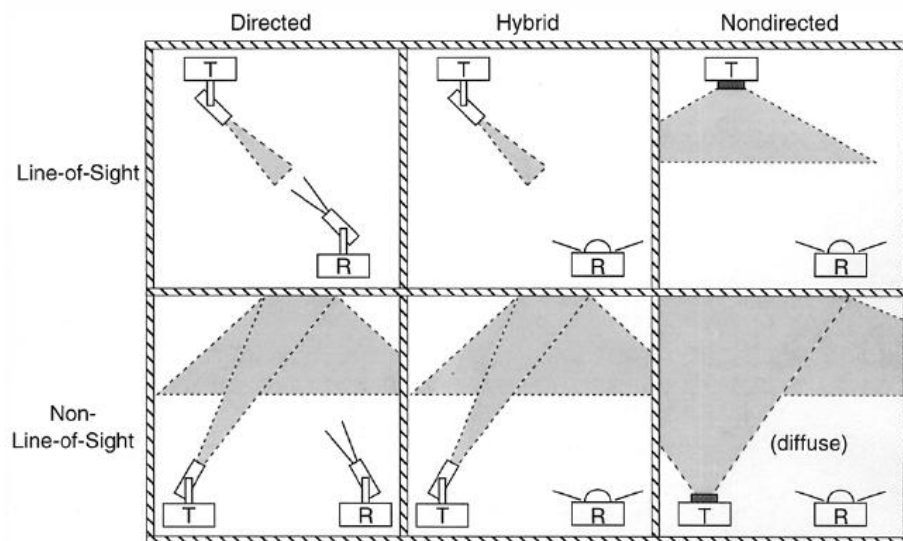


Figure 2.1: Classification of infrared links.

In the non-directed LOS, a broader coverage area and mobility is achieved by using a wide beam transmitter and wide FOV receivers. This set-up eases the strict hardware set-up to maintain uninterrupted path between the transmitter and the receiver in directed LOS. However, path loss is higher and the link is prone to blocking. In hybrid LOS systems, either the transmitter or the receiver has a wide FOV, while the other element has a narrow FOV. A typical hybrid LOS system uses ceiling mounted transmitters that illuminate the wide area.

Like in directed LOS links, the transmitter has a narrow angle emission and the receiver has a narrow FOV for directed non-LOS links. However, to overcome any obstacles between them, the transmitter is aimed at a reflective surface so that the first reflection can reach the receiver. In addition to overcoming barrier, the information signal is received after a single reflection, which minimizes the multipath dispersion [141]. However, the alignment is problematic due to highly directional transmitter and receiver. The hybrid system incorporates either a wide beam transmitter or a narrow FOV receiver or vice versa. This relaxes the need for strict alignment between the transmitter and the receiver. Though blocking probability can be significantly reduced using the link design, the system is affected by multipath propagation.

One of the most attractive link configurations is the non-directed and non-LOS (diffuse) link as there is no need for accurate alignment between transmitter and receiver and also the system can provide the flexibility in terms of mobility. The typical configuration proposed in Geffer [3] consists of a wide beam transmitter pointed towards the ceiling where beam undergo multiple reflection before it is collected by wide FOV receiver. The system displays excellent mobility, low blocking probability and easy link set-up. Possible mobility within certain periphery makes diffused link more suitable for portable applications. However, the path loss is very high, in the range of 120-130 dB for a typical configuration [6] and the ultimate unequalized bit rate is limited to 260 Mbps due to high ISI cause by multipath propagation [3, 144].

Quasi-diffuse link is often preferred in indoor environment as the system can provide low probability of the blocking and high mobility without a high path loss. In the quasi-diffuse link, multiple transmitters with narrow beam width is directed in different directions and multiple receiver with narrow FOV focusing in different directions can be utilised for collecting the radiation [127, 145, 146]. The quasi-diffuse system

requires lower transmitter power, has a lower path loss and reduced multipath dispersion compared to the wide beam transmitter [125].

2.4 Indoor Optical Wireless Channel

Intensity modulation with direct detection (IM/DD) is the only practicable method of communication because of the cost and complexity [43]. The transmitted optical power of the source $x(t)$ is directly varied by changing the drive current according to the modulating signal. The receiver employs a photodetector. The photocurrent $y(t)$ of the photodetector is directly proportional to instantaneous power incident upon it, i.e. proportional to the square of received electric field. The model is shown in Figure 2.2 where R is the photodetector responsivity, $h(t)$ is the baseband channel impulse response and $n(t)$ is the signal independent shot noise, modelled as AWGN.

The equivalent baseband model of an optical wireless link can be summarised by:

$$y(t) = Rx(t) \otimes h(t) + n(t); \quad (2.1)$$

where symbol \otimes denotes the convolution.

There is a major difference between the RF and the optical links. The channel input is non-negative value as the instantaneous optical power is non-negative. i.e.

$$x(t) \geq 0. \quad (2.2)$$

The average transmitted optical power P_{avg} is given by:

$$P_{avg} = \lim_{T \rightarrow \infty} \frac{1}{2T} \int_{-T}^T x(t) dt; \quad (2.3)$$

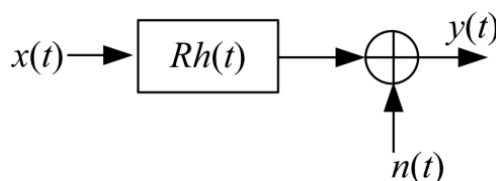


Figure 2.2: Equivalent baseband model of an optical wireless system using IM/DD.

rather than the usual time-average of $|x(t)|^2$ used RF system. However, the SNR is defined in terms of the electrical power:

$$SNR = \frac{R^2 H^2(0) P_{avg}^2}{R_b N_0}; \quad (2.4)$$

where N_0 is the noise spectral density and $H(0)$ is the channel DC gain given by:

$$H(0) = \int_{-\infty}^{\infty} h(t) dt. \quad (2.5)$$

The source of noise is the ambient light, emanating from both the natural and artificial sources. The IR and visible background noise gives rise to the shot noise, which can be modelled as additive, white, Gaussian, and independent of $x(t)$ [7]. In the presence of intense ambient light, which is usually the case, shot noise is the dominant noise source in a typical diffuse receiver. Even if little or no ambient light is present, the dominant noise source is the receiver preamplifier noise, which is also signal independent and Gaussian [147]. If I_B is the average DC photocurrent in the photodetector generated by the shot noise, the single-sided power spectral density (PSD) N_0 is given by [82]:

$$N_0 = 2qI_B; \quad (2.6)$$

where q is the charge of an electron.

As large area photodetector is employed in optical communication system compared to the wavelength of the carrier, the multipath fading is not present. But the temporal dispersion of the received signal due to multipath propagation is a problem [144]. In short distance LOS links, multipath dispersion is seldom a problem and LOS links channel are often modelled as a linear attenuation and delay [95]. The optical LOS links are considered as non-frequency selective and the path loss depends on the square of distance d_{TR} between the transmitter and the receiver. The detected radiant flux Φ at the receiver also depends on the effective photodetector area $A\cos(\psi)$. The transfer function of LOS link $H_{LOS}(0)$ can be simplified to [20] :

$$H_{LOS}(0) = \frac{A\cos(\psi)}{d_{TR}^2}. \quad (2.7)$$

The attenuation in a diffuse channel is difficult to predict since it is dependent on a multitude of factors, such as room dimensions, the reflectivity of the ceiling, walls and objects within the room, and the position and orientation of the transmitter and receiver, window size and place and other physical matters within a room. There are different attempts to accurately characterise the indoor optical channel [14, 95, 96, 111, 148-165]. Mathematically, the impulse response of the optical wireless channel is calculated by integrating the power of all the components arriving at the receiver after multipath propagation [149]. The response of a LOS link is an impulse with the delay due to the propagation path. The received signal in case of the non-LOS links consists of various components arriving from different path, the path-length of these components differ in proportion to the room design, hence there is broadening of the pulse. The distribution of the channel gain in decibel (dB) for the LOS component follows a modified gamma distribution, and the channel gain in dB for LOS channels including all reflections follows a modified Rayleigh distribution for most transmitter–receiver distances [14].

The first channel model proposed by Barry *et al* [153] evaluates the impulse response of an arbitrary room with Lambertian reflectors. This method calculates the multiple reflections of the signal based on recursive algorithm. However, the model is applicable for a specific room configuration and does not take account of shadowing and furniture layout. More efficient simulation model for indoor channel is proposed by Lomba *et al* [111, 151] considering multiple reflection of the signal. The simulation efficiency is improved by ‘time-delay agglutination’ and ‘time and space indexed tables’ procedures. Iterative site-based model was suggested by Carruthers *et al* [95, 150] to simulate the effect of multipath reflections in the receiver. The study suggested that channels LOS paths must be modelled separately from those fully diffuse channels with no such path. A new approach was taken by López-Hernández *et al* [163] to develop efficient simulation of the channel by slicing into time steps rather than into a number of reflections. The indoor optical channel is modelled as parallel combination of LOS and diffuse paths and analytical model is introduced by Jungnickel *et al* [148]. Most of the channel models described above are based on the Monte-Carlo Ray tracing algorithm and Lambert’s model of reflection. However, the use of Phong’s model can lead to different impulse response for the same channel with respect to Lambert’s model when surfaces present a high specular component [157]. The impulse response can be modelled by decomposing signal into primary and higher-order reflections [149]. The gamma probability density function is used for the matching function of the primary

reflection impulse response. Impulse response of the higher order reflections is simulated using spherical model. The analysis shows that the bandwidth characteristics are dominated by the response of the primary reflection. Though many models had been proposed and studied for simulating impulse response of indoor IR channel, by far the most used in simulation is the ceiling bounce model introduced by Carruthers and Kahn [95] because of its excellent matching with the measured data and simplicity of the model. The multipath IR channels are characterized by only two parameters, optical path loss and RMS delay spread. This method came up with a closed form expression for the impulse response assuming the transmitter and the receiver to be co-located in planes parallel to the floor and directed towards the ceiling. The accuracy of the ceiling model can be improved by modifying the expression for delay spread [156, 166]. In this study, channels with a range of delay spreads are considered. Since modified ceiling bounce model differ from the model introduced by Carruthers and Kahn [95] only on the calculation of the delay spread and both use same expression for $h(t)$, it is in fact irrelevant to discuss the difference of the model here. The detail of the ceiling bounce model is given in Chapter 6 of this thesis.

2.5 Optical Transmitter and Eye-Safety

The optical transmitter converts an electrical signal to an optical signal. A variety of light sources are used for optical transmission mainly semiconductor laser diodes (LD) and LED. The output optical intensity of these devices is approximately linearly proportional to drive current. The LEDs are constructed of direct band gap semiconductors [167] and the central wavelength λ of the emitted photons is given by [167]:

$$\lambda = \frac{hc}{E_g} ; \quad (2.8)$$

where h is Planck's constant , c is the velocity of light in vacuum and E_g is the band gap energy.

LEDs are based on the principal of spontaneous emission and LD operates on stimulation emission. So a population inversion needs to be created to operate an LD,

which means the LD must properly be biased for its operation. LDs are highly coherent and the spectral width is much smaller than LED. However, the operating cost is much higher because of complexity in circuiting. The physical structure and physics of these device are beyond the scope of this thesis and interested reader can refer to [144, 167, 168]. Only brief comparisons of the LD and the LED are provided for indoor OW applications.

The comparisons of the LED and the LD are given in Table 2.2. The use of these devices in optical communication depends on many factors, namely speed of operation, age factor and the cost. The emission spectra of an LED are much broader than that of an LD. The full width half maximum (FWHM) of the LD can be as low as 0.1 nm in contrast to the LED which can have FWHM 20 nm or more. Due to the stimulated emission, the recombination time constant of LD is much lower than that of the LED, allowing high speed of operation for LDs. In fact, the LDs can operate in gigahertz range while LEDs are limited to a megahertz range [45, 144]. LDs are pointed devices and because of coherency and high intensity of the emitted radiation, the LD might not be safe for indoor applications without the beam being diffused to ensure the safety. The holographic diffuser [26, 46] and integrating sphere diffusers can be used for making the transmitted power eye-safe [48, 169]. LEDs, on the other hand, radiate in a wide angle and are generally considered to be eye-safe. Wide transmitted beam in LEDs make them more suitable for non-directed links [12]. Also due to simplicity in drive circuit and cost factors, LEDs are more suitable for low cost indoor applications with limited data rates. LED suffers from low electrical-to-optical conversion efficiency, low modulation bandwidths, broad spectral width leading to the difficulty in rejection of the ambient light at the receiver [144]. The nonlinearity in output power due to the temperature fluctuation and ageing factor is more pronounced in LDs.

Human eye is a very sensitive tissue and could be damaged by extreme conditions. The cornea and lens are transparent to the visible and near-IR wavelengths. High intensity light entering within these wavelengths could permanently damage the eye as the light is focused on to the retina and retina has no pain sensor. Since IR wavelength is invisible light, eye cannot provide blinking reflex and hence laser operating at near-IR wavelength are potentially hazardous. Since low cost optoelectronics components are available at the range of 780-950 nm wavelength, they are more suitable for low cost indoor application. However, only a limited link range can be achieved at these

wavelengths due to eye-safety. The eye-safety regulation limits the average power to be less than 1mW [41]. On the other hand, laser beams at 1550 nm wavelength are absorbed by the cornea and lens and do not focus onto the retina, hence they are potentially safe [170]. The permitted average optical radiation in 1550 nm wavelength is much higher (Table 2.3) compared to the 800 nm range. Hence larger link length can be achieved in 1550 nm. Moreover, operating in the wavelength can provide additional advantages like compatibility with the fibre optics and higher receiver sensitivity [170].

Table 2.2: Comparisons of LED and LD [144].

Characteristics	LED	LD
Optical spectral width	25-100 nm	0.1 to 5 nm
Modulation bandwidth	Tens of kHz to hundreds of MHz	Tens of kHz to tens of GHz
Special circuitry required	None	Threshold and temperature compensation circuitry.
Eye safety	Considered Eye safe	Must be rendered eye safe
Reliability	High	Moderate
Cost	Low	Moderate high

Table 2.3: Laser classifications [41, 144].

Category	Wavelength			
	650nm (Visible)	880nm (Infrared)	1310nm (Infrared)	1550nm (Infrared)
Class 1	$\leq 0.2\text{mW}$	$\leq 0.5\text{mW}$	$\leq 8.8\text{mW}$	$\leq 10\text{mW}$
Class 2	0.2-1mW	N/A	N/A	N/A
Class 3A	1-5mW	0.5-2.5mW	8.8-45mW	10-50mW
Class 3B	5-500mW	2.5-500mW	45-500mW	50-500mW

2.6 Optical Receiver

The optical receiver collects light and converts the incident light into electrical current. Photodiodes normally operate in reverse biased condition and if the incident photons have sufficient energy, they will generate free electron-hole pairs. The drift and diffusion of these carriers constitute the photocurrent. The basic steady-state operation of a solid-state photodiode can be modelled by the expression [144].

$$I_p = q\eta_i \frac{P_p}{h\nu}; \quad (2.9)$$

where I_p is the average photocurrent, η_i is the quantum efficiency of the device, P_p is the incident optical power, ν frequency and $h\nu$ is the photon energy. The ratio of the electrical current I_p generated to the incident optical power P_p indicates the conversion efficiency of the device and is known as the responsivity R . Rearranging (2.9), the responsivity R of the photodiode is given by [144]:

$$R = \frac{I_p}{P_p} = \frac{q\eta_i}{h\nu}. \quad (2.10)$$

Two types of medium- and large-area silicon photodiodes are widely available: ordinary positive-intrinsic-negative (PIN) photodiodes and avalanche photodiodes (APDs). The main limiting factor for use of these devices in wireless communication is the junction capacitance of the devices. Large area photodiodes are used in the optical wireless receiver to collect as much transmitted light as possible, which leads to high capacitance and slow speed of operations. The sensitivity improves as the photodiode area reduces because of the correspondingly lower capacitance. However, small-area photodiodes incur a greater coupling loss due to the small aperture they present to the incoming beam, so a careful trade-off between these factors is necessary to optimize the final performance [7].

Though structurally very similar, working principle of the PIN photodiode and APD are different. The incident light is absorbed in the intrinsic region of PIN photodiode producing free carriers which are collected in junction to produce photocurrent. The APD works on the principle of the avalanche multiplication that when accelerated free carriers collide with lattice generates more carriers. As a result, APDs have a

photocurrent gain of greater than unity, while PIN photodiodes are fixed at unit gain [144].

Table 2.4 shows the comparison of PIN photodiodes and APDs. APDs are favoured in direct detection optical receivers when there is little ambient-induced shot noise, as their internal gain helps to overcome preamplifier thermal noise, which increases the receiver SNR [41]. However, APD has non-linear behaviour; as a result addition circuitry is necessary to improve the performance. This increases the cost and lowers the system reliability [38]. PIN photodiodes are commonly used in the indoor OWC due to lower cost, tolerance to wide temperature fluctuations, linear response over a wide range and operation with an inexpensive low-bias voltage power supply [38]. PIN receivers are about

10 to 15 dB less sensitive than APD receivers [42]. Increasing the transmitter power and using larger receiver lens diameter can compensate the reduced sensitivity of these receivers [42]. The better internal gain of APDs increases the SNR but APDs are expensive and need high operating voltages. To increase the efficiency of the system, the transmitter should work in the range of 900 nm as the photo-response of silicon PIN is peak at this value, and fall sharply in the wavelength above this value [37].

Table 2.4: Comparisons of PIN diodes versus avalanche photodiodes.

Characteristic	PIN photodiode	Avalanche photodiode
Modulation bandwidth	Tens of MHz to tens of GHz	Hundreds of MHz to tens of GHz
Photocurrent gain	1	10^2 - 10^4
Special circuitry required	None	High Bias voltage and temperature compensation circuitry
Linearity	High	Low
Cost	Low	Moderate to high

2.7 Ambient Light Sources

The ambient light source (both natural and artificial) has optical spectrum in both the operating line-width of 830 nm and 1550 nm. The photocurrent generated by the ambient lights act as a noise source in the receiver, which degrades the performance. The average combined power of the ambient light results in the photodetector generating a DC background photocurrent I_B that gives rise to shot noise $n(t)$ which is the dominant noise source in optical wireless systems [44]. The shot noise due to ambient light is independent of the signal and can be modelled as a white Gaussian [43, 82] with one-sided PSD N_0 given by (2.6). The main sources of ambient light are sunlight, incandescent lamps and fluorescent lamps. The optical spectrum of the ambient light is shown in Figure 2.3. The spectra have been scaled to have equal maximum value, and the longer wavelength region of the fluorescent lamp spectrum has been amplified by a factor of 10 in order to make it clearly visible. The sunlight is typically the strongest source of noise and represents an unmodulated source of ambient light with a very wide spectral width and a maximum PSD located at ~ 500 nm. Sunlight produces the highest levels of background current and is the major source of shot noise at the receiver photodiode. The background current due to artificial illumination is only few tens of μA , well below that produced by sunlight which could be as high as 5 mA [171].

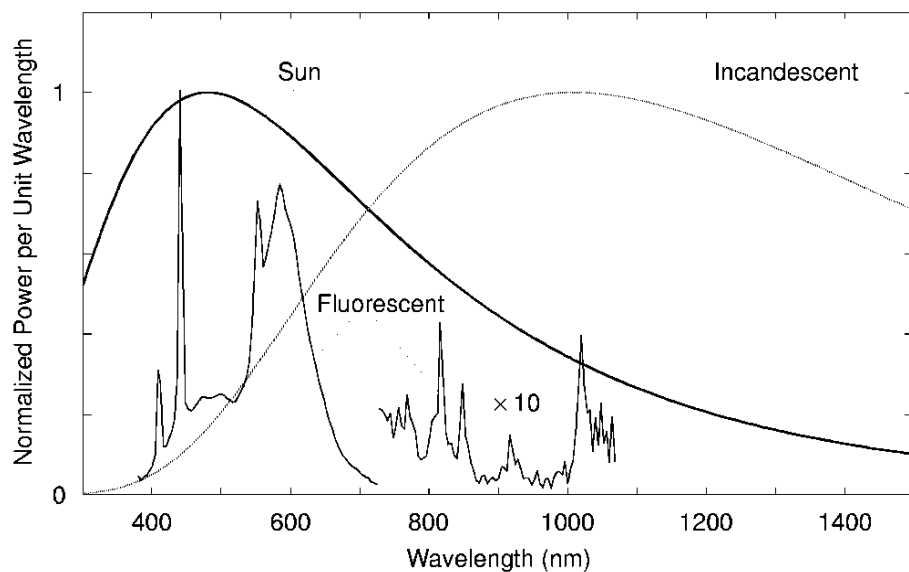


Figure 2.3: Optical power spectra of common ambient light sources [43].

Moreira *et. al* [77, 79] carried out extensive measurements of a variety of ambient light sources and produced a model to describe the interference signal. Boucouvalas [81] also carried out similar measurements, which included a number of consumer products which use IR transmission. Along with experimental characterization of ambient light sources, a significant amount of work has been done on analyzing the effect of ambient light interference (ALI) on the link performance [78, 80, 82, 84, 86, 87, 172, 173].

All artificial ambient light sources are modulated, either by the mains frequency or, in the case of some fluorescent lamps, by a high frequency switching signal. Incandescent lamps have a maximum PSD around 1 μm , and produce an interference signal which is a near perfect sinusoid with a frequency of 100 Hz [79]. Only the first few harmonics carry a significant amount of energy and interference effect can be effectively reduced by using a HPF [78, 79, 87]. The interference produced by fluorescent lamps driven by the conventional ballasts is distorted sinusoidal and extending up to 20 kHz [79]. The interference can be effectively reduced using a HPF of with a cut-off frequency of 4 kHz even at a low data rate of 1 Mbps and does not cause a significant degradation in performance [78].

The interference produced by the fluorescent lamps driven by the electronic ballasts is the most serious source of performance degradations. The spectrum of the interference depends on the switching frequency. However all models exhibit components at the switching frequency and at harmonics of that frequency. Harmonics of the switching frequency can extend into the MHz range, and therefore present a much more serious impairment to optical wireless receivers. The interference can be modelled using a high frequency component and low frequency component and due to significant spectral component at high frequencies, even the HPF does not provide significant improvement in the performance for different modulation schemes even at higher data rates (> 10 Mbps) [78, 80].

Other noise source like IR audio headphone transmitters and TV remote control unit can be sources of the noise as the operating wavelengths of these equipments coincide with OW transceiver [81].

A significant effort has been made for design of receiver to reduce the effect of the ambient light in the receiver [80, 81, 87-89, 143]. The most obvious method is the

combination of an optical bandpass filter and an electrical HPF. In order to remove the RF interference arising from ambient light sources, a HPF is often inserted in the receiver chain, prior to decision thresholding. However, with baseband modulation schemes such as OOK, this causes a baseline wander (BLW) [91]. The daylight optical filter can remove significant amount of out-of-band light noise. However, a large proportion of spectrum of ambient light overlaps with the operating wavelength of OW transceiver at 870 nm and 1500 nm introducing interference. The use of a differential receiver to cancel the interference was suggested by Barry [174]. A different approach to reduce the interference is taken by Moreira *et al* [87] in which they have utilized the combination of the differential receiver and optical filter. The technique can be applied to any type of ALI, incandescent light and fluorescent light with and without electronic ballasts, or any combination of them [87]. A differential detector coupled with two orthogonal linear polarisers can be effective in the removing time-varying interference. The method is simple and very useful for overcoming the interference due to ambient-noise light [88]. Angle diversity receiver technique takes advantage of the directionality of the light source. Due to the directional nature of both the signal and noise, the SNR depends on: i) on the position, orientation and radiation pattern of the signal and noise sources; and ii) on the position, orientation and FOV of the receiver [89, 175]. In his work, multiple receivers with a narrow FOV for focusing in different direction are utilised instead of a single receiver with a wide FOV. The receiver operates by estimating the SNR seen by each sector and combines them in order to maximise the SNR.

2.8 Modulation Techniques

A number of modulation techniques have been proposed and thoroughly analysed in literature for indoor OWC systems. Because of the constraint imposed to maximum average radiation due to eye-safety and power efficiency to improve the battery life of handheld device, the transmitted power should in fact be as low as possible. Limitations on power favours modulation with high peak to mean power characteristics like PPM with a short pulse duration. The main metrics against which a particular modulation technique is assessed are the reliability of the transmission, the bandwidth efficiency and the power efficiency it offers under typical noise and multipath conditions.

- i) *Transmission Reliability*: A modulation technique should be able to provide a minimum acceptable error-rate in adverse possible conditions. The modulation should be able to provide resistance to the ISI and variations in the data signal DC component [125]. A long absence of ‘zero to one’ transition may be problematic as the clock recovery by a digital phase locked loop (DPLL) might not be feasible [176]. Moreover, multiple consecutive high pulses should be avoided, since the resulting IR signal would be distorted by the HPF in the receiver [177]. In addition, the modulation technique should be resistant to a number of factors such as the phase jitter due to variations of the signal power, pulse extensions due to diffusion component larger time constant and pulse distortion due to near field signal clipping [20, 125].
- ii) *Power Efficiency*: The transmitted optical power is limited as a result of eye and skin safety requirement [42, 43] and for battery powered optical wireless gadgets the power consumption needs to be minimised as well. These factors make the power efficiency of a particular modulation technique the most important consideration. As such, different signalling schemes are usually compared in terms of the required average optical power (or SNR) to achieve a desired error performance at given data rate. The power efficiency η_p of a modulation scheme is given by the average power required to achieve a given BER at a given data rate [44]. Mathematically, η_p is defined as [20]:

$$\eta_p = \frac{E_{pulse}}{\bar{E}_{bit}} ; \quad (2.11)$$

where E_{pulse} is the energy per infrared pulse and \bar{E}_{bit} is the average energy per bit.

- iii) *Bandwidth Efficiency*: Although the optical carrier theoretically can be considered as having ‘unlimited bandwidth’, the other constituents (the photodetector area, multipath channel) in the system limit the amount of bandwidth that is practically available for a distortion-free communication system [42]. Also the ensuing multipath propagation in diffuse link/non-directed LOS limits the available channel bandwidth [149]. This also makes the bandwidth efficiency a prime metric. The bandwidth efficiency η_B is defined as [20]:

$$\eta_B = \frac{R_{bit}}{B} ; \quad (2.12)$$

where R_{bit} is the achievable bit rate and B is the bandwidth of the IR transceiver. The relationship bandwidth and power efficiencies depend on the average duty cycle γ given by [20]:

$$\eta_p = \frac{\eta_B}{\gamma} . \quad (2.13)$$

- iv) *Other Considerations:* Implementation simplicity is another design requirement when considering a modulation scheme. The cost of implementing a very complex modulation scheme might render the scheme unfeasible irrespective of its power/bandwidth efficiency. Other indices against which modulation schemes are compared and evaluated are resilience to interference from the artificial ambient light sources and the channel induced dispersion as well as power contained at and near DC.

Significant number of modulation techniques had been proposed for indoor optical wireless channel. The modulation techniques can broadly be classified into two groups: baseband and subcarrier schemes.

2.8.1 Digital Baseband Modulation Techniques

For the signalling schemes in this class, the data has not been translated to a much higher carrier frequency prior to intensity modulation of the optical source. Thus a significant portion of the signal power is restricted to the DC region. Signal mapping of different baseband modulation schemes utilised in this study is given in Figure 2.4 and described in details below.

2.8.1.1 OOK

OOK is the most reported modulation techniques for IM/DD in optical communication. This is apparently due to its simplicity. A bit one is simply represented by an optical pulse that occupies the entire or part of the bit duration while a bit zero is represented by

the absence of an optical pulse (see Figure 2.5). Both the return-to-zero (RZ) and non-return-to-zero (NRZ) schemes can be applied. In the NRZ scheme, a pulse with duration equal to the bit duration is transmitted to represent 1 while in the RZ scheme the pulse occupies only the partial duration of bit. Figure 2.5 shows the single mapping of OOK-NRZ and OOK-RZ with a duty cycle $\gamma = 0.5$ for average transmitted power of P_{avg} . Hence, the envelop for OOK-NRZ is given by:

$$p(t) = \begin{cases} 2P_{avg} & \text{for } t \in [0, T_b) ; \\ 0 & \text{elsewhere} \end{cases} \quad (2.14)$$

where T_b is the bit duration.

The electrical PSDs of the OOK-NRZ and OOK-RZ ($\gamma = 0.5$) assuming independently identically distributed (IID) one and zeros are given by [178]:

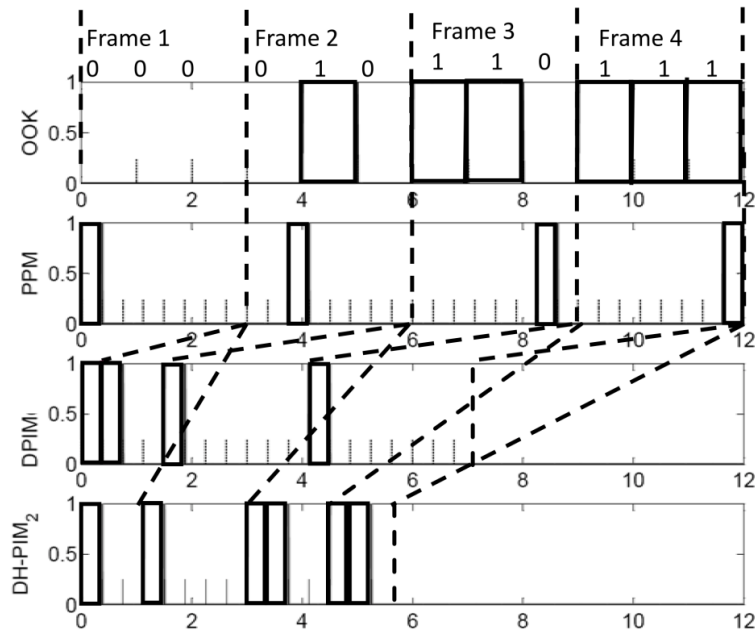


Figure 2.4: Symbol mapping of different modulation techniques.

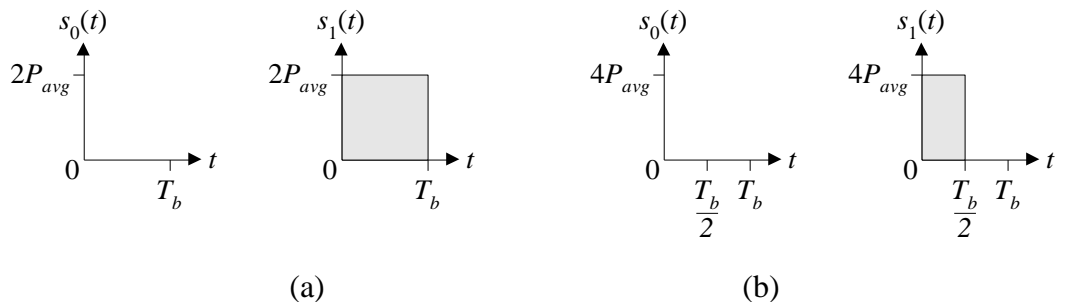


Figure 2.5: Transmitted waveforms for OOK: (a) NRZ, and (b) RZ ($\gamma = 0.5$).

$$S_{OOK-NRZ}(f) = (P_{avg}R)^2 T_b \left(\frac{\sin \pi f T_b}{\pi f T_b} \right)^2 \left[1 + \frac{1}{T_b} \delta(f) \right]; \quad (2.15)$$

$$S_{OOK-RZ(\gamma=0.5)}(f) = (P_{avg}R)^2 T_b \left(\frac{\sin \pi f T_b}{\pi f T_b} \right)^2 \left[1 + \frac{1}{T_b} \sum_{n=-\infty}^{\infty} \delta\left(f - \frac{n}{T_b}\right) \right]; \quad (2.16)$$

where $\delta(\cdot)$ is the Dirac delta function.

The PSDs of OOK-NRZ and OOK-RZ ($\gamma = 0.5$) are plotted in Figure 2.6. The power axis is normalized to the average electrical power multiplied by the bit duration $(P_{avg}R)^2 T_b$ and the frequency axis is normalized to the bit rate R_b ($1/T_b$). For baseband modulation techniques, the bandwidth requirement is generally defined as the span from DC to the first null in the PSD of the transmitted signal. As expected, OOK-RZ ($\gamma = 0.5$) has twice the bandwidth requirement of OOK-NRZ, since the pulses are only half as wide. The OOK-NRZ has power efficiency η_p of 2 and bandwidth efficiency η_B of 1. The OOK-RZ has the same η_p as OOK-NRZ however η_B depends on the duty cycle γ . The bandwidth efficiency η_B for $\gamma = 1/4$ is very low, with a value of 0.25. Furthermore, RZ does not support sample clock recovery at the receiver because it allows a long low signal without any 0 to 1 transition [20]. Therefore, bit stuffing is necessary which further decreases η_B . Both OOK-NRZ and OOK-RZ have significant power content at DC and low frequencies, making difficulties in removing the noise imposed by artificial sources of ambient light. The penalties imposed when the high pass filtering is imposed in such system are known as BLW.

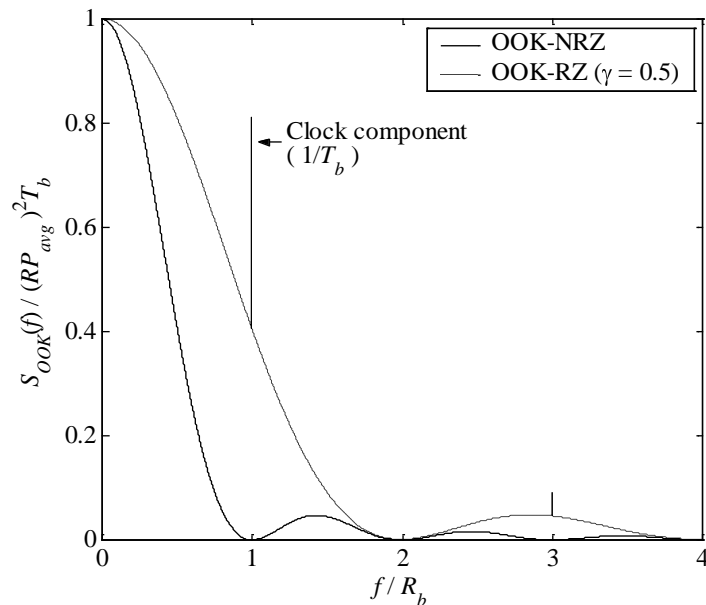


Figure 2.6: PSD of OOK-NRZ and OOK-RZ ($\gamma = 0.5$) [51].

The system block diagram of OOK-NRZ system with a matched filter based receiver is given in Figure 2.7. The binary data $a_i \in \{0, 1\}$; $i = 1, 2 \dots$ is passed through a transmitter filter $p(t)$ with a unit-amplitude impulse response of one bit duration T_b to convert it to a continuous signal. Hence, the output of the transmitting filter $s(t)$ is

$$s(t) = \sum_{i=-\infty}^{\infty} a_i p(t - iT_b). \quad (2.17)$$

The continuous electrical signal $s(t)$ is converted to an optical signal using typical LEDs or LDs and the optical signal is transmitted through the channel. The output of the transmitter filter is scaled by the peak detected signal photocurrent $2P_{avg}$ where P_{avg} is the average transmitted optical signal power. The signal independent shot noise $n(t)$ is added to the signal, which is modelled as white and Gaussian, with a single-sided power spectral density N_o [82]. The receiver front incorporates a photodetector, which converts incident optical signal to photocurrent. To account for the effect of photodetector on the received signal, the received signal is scaled by the photodetector responsivity R taken to be unity in the thesis. Hence the detected signal $z(t)$ is:

$$z(t) = R[x(t) + n(t)]. \quad (2.18)$$

For the AWGN without channel distortion, the optimal receiver is the maximum likelihood (ML) receiver. ML receiver involves continuous-time filter with an impulse response $r(t)$, which is matched to the transmitted pulse shape $p(t)$, followed by a sampler and a threshold detector [43]. The output of the matched filter is sampled at the end of each bit period and a binary ‘one’ or ‘zero’ is assigned to the sampled value depending upon the amplitude being greater than or less than the threshold value. The impulse response of the matched filter $r(t)$ and the sampled output y_i of the matched filter are given by:

$$r(t) = \frac{p(-t)}{\sqrt{E_p}}; \quad (2.19)$$

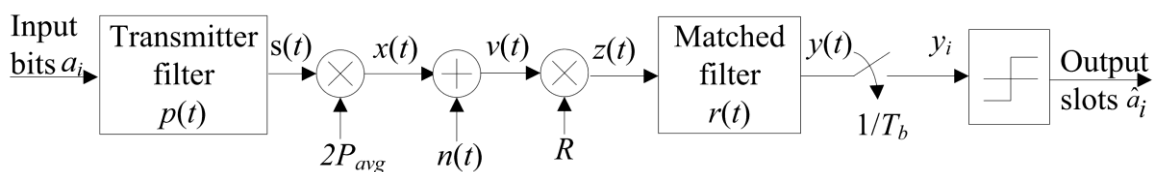


Figure 2.7: The block diagram of OOK system.

$$y_i = z(t) \otimes r(t)|_{t=iT_b}; \quad (2.20)$$

where the symbol \otimes denotes convolution and E_p is the energy of the transmitted pulse:

$$E_p = \begin{cases} (2RP_{avg})^2 T_b & \text{for } a_i = 1 \\ 0 & \text{otherwise} \end{cases}. \quad (2.21)$$

For the IID binary data, the optimum threshold level α_{opt} , which minimises the probability of error, lies midway between expected one and zero levels [179]. Thus,

$$\alpha_{opt} = RP_{avg}\sqrt{T_b}. \quad (2.22)$$

Hence, the probability of bit error for OOK-NRZ is given by [44]:

$$P_{be_OOK} = Q\left(\frac{RP_{avg}\sqrt{T_b}}{\sqrt{N_0/2}}\right); \quad (2.23)$$

where $Q(\cdot)$ is the Q -function, $Q(\vartheta) = \frac{1}{\sqrt{2\pi}} \int_{\vartheta}^{\infty} e^{-\frac{\omega^2}{2}} d\omega$.

Since average energy per bit E_b is given by:

$$E_b = \frac{E_p}{2} = 2 (RP_{avg})^2 T_b; \quad (2.24)$$

Thus equation (2.23) can be expressed as:

$$P_{e_bit_OOK} = Q\left(\sqrt{\frac{E_b}{N_0}}\right). \quad (2.25)$$

In the OOK-RZ formatting, the average energy per bit is increased by a factor of $1/\gamma$. Hence in an AWGN channel, OOK-RZ signaling requires $5\log\gamma$ (dB) of optical power less than the OOK-NRZ data format to achieve the same level of bit error performance. However, the penalty will be in term of the bandwidth requirement which increases by a factor of γ .

To reduce the BER, a number of forward error controls can be applied [66]. In diffuse optical links, the multipath induced dispersion limits the achievable data rate. For instance, a data rate of 100 Mbps is not feasible with OOK signalling within a channel having a normalised delay spread of 0.6 [95]. For OOK to perform optimally in a multipath channel, the maximum likelihood sequence detector (MLSD) should be adopted. However, the implementation of such detector is not practical because of its complexity and the prohibitive processing time. A sub-optimal but practical approach would be to use an equalizer. Employing a decision feedback equaliser (DFE) with the OOK makes the hitherto unfeasible 100 Mbps data rate a possibility even in the most dispersive channel as reported in [95]. Various other equalization techniques have been proposed for OOK scheme and their detailed analysis are available in [43, 95, 149] and references there in. The error control code and equalization techniques will be discussed further in subsequent chapters in the thesis. OOK-NRZ is used for all study and OOK will be used to represent OOK-NRZ unless stated otherwise.

2.8.1.2 PPM

PPM is an orthogonal baseband modulation technique well researched in optical communications for its superior power efficiency compared to any other baseband modulation techniques [84]. This factor makes it well suited for handheld devices, where lower power consumption is one of the key factors. It finds commercial application in point-to-point communication like IrDA, laptop, palmtop etc. An L -PPM symbol consists of a single pulse of one slot duration within L ($= 2^M$, where bit resolution $M > 0$ is an integer) possible time slots with the remaining slots being empty (see Figure 2.4 for the detail symbol mapping). Information is encoded within the position of the pulse and the position of the pulse corresponds to the decimal value of the M -bit input data. In order to achieve the same throughput, PPM slot duration T_{s_PPM} is shorter than the OOK bit duration T_b by a factor L/M i.e.

$$T_{s_PPM} = \frac{T_b M}{L}. \quad (2.26)$$

Hence the PPM symbol sequence is given by [116, 180]:

$$x(t) = LP_{avg} \sum_{k=0}^{L-1} c_k p\left(t - \frac{kT_{symp}}{L}\right); \quad (2.27)$$

where c_k is the PPM symbol sequence, $T_{symp}(= T_b M)$ is the symbol interval.

Unlike OOK, PSD of PPM has zero DC values for all M [181]. This provide increased resistance to BLW over DC schemes and permits the use of higher cut-on frequencies when using high-pass filtering to reject the interference produced by artificial sources of ambient light [80].

The block diagram of the matched filter based receiver for PPM scheme is given in Figure 2.8. The PPM encoder converts M -bit binary data sequence input bits $\{a_i ; i = 1.. M\}$ into one of the possible L symbols. The PPM symbols are passed to a transmitter filter $p(t)$ which has a unit amplitude rectangular impulse response with a duration of one slot T_{s_PPM} . The output of the transmitter filter is scaled by the peak detected signal photocurrent LP_{avg} . The channel noise $n(t)$ is added to the modulated signal. The received signal is scaled by the photodetector responsivity R at the receiver. The detected signal $z(t)$ is passed to the unit energy matched filter with an impulse response $r(t)$ matched to $p(t)$.

In the AWGN channel, two decoding algorithms can be used for the PPM signals:

- i. Hard decision decoding using a threshold detector.
- ii. Soft decision decoding using a maximum *a posteriori* (MAP) or maximum likelihood detector.

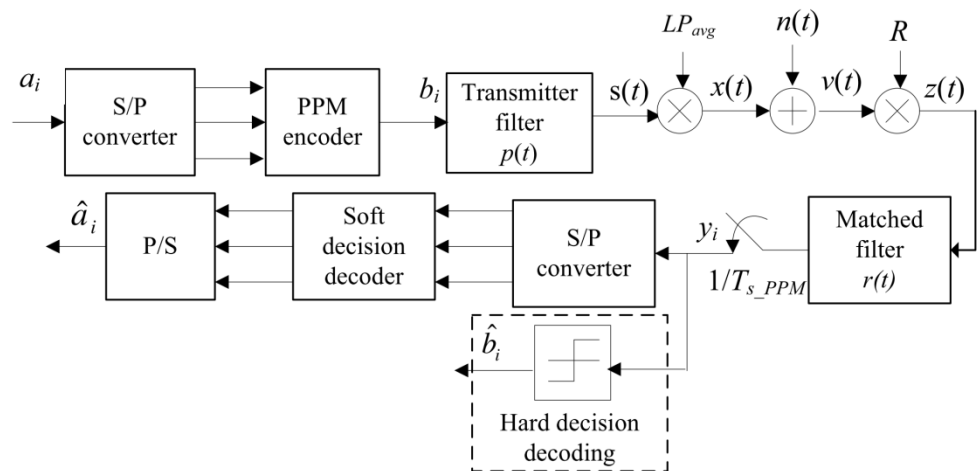


Figure 2.8: The block diagram of the matched filter based receiver for PPM scheme with soft and hard decision decoding.

For the hard decision decoding scheme, the filter output is sampled at the end of each slot, and a “one” or a “zero” is assigned depending on whether the signal is above or below the threshold level at the sampling instant. For the ‘soft’ decision scheme, a block of L samples are passed to a soft decision detector, which assigns a one to the slot which contains the largest sample and zeros to the remaining slots. In the soft decoding, the threshold value is not necessary as the decision is made based on the relative values of the slot within a symbol. This method of decoding is optimal for systems in which AWGN is the dominant noise source and there is no channel distortion [179].

Since the peak output of the matched filter when a pulse is transmitted is $\sqrt{E} = LRP_{avg}\sqrt{T_s}$ and 0 for the empty slot, the slot error probability for hard decision is given by [44, 84]:

$$P_{se_PPM_hard} = \frac{1}{L} Q\left(\frac{LRP_{avg}\sqrt{T_s} - \alpha}{\sqrt{N_0/2}}\right) + \frac{(L-1)}{L} Q\left(\frac{\alpha}{\sqrt{N_0/2}}\right); \quad (2.28)$$

where α is the threshold level. Since the probabilities of empty slots and a pulse are not equal, a threshold value of $\alpha = \sqrt{E}/2$ is not optimum. The probability is a complicated function of the signal and noise powers, and the order L . Nonetheless, for low probability of error, the $\alpha = \sqrt{E}/2$ is very close to the optimum value and (2.28) can be simplified to:

$$P_{se_PPM_hard} = Q\left(\sqrt{\frac{E}{2N_0}}\right); \quad (2.29)$$

Note that E is the energy of a symbol, which encodes $\log_2 L$ bits of data. Hence, the average energy per bit E_b is given by [179]:

$$E_b = \frac{E}{\log_2 L}. \quad (2.30)$$

On simplification, (2.30) can be written as:

$$E_b = L(RP_{avg})^2 T_b. \quad (2.31)$$

The average optical power requirement to achieve a given BER for L -PPM hard decoding and soft decoding systems are, respectively given by [43, 44]:

$$P_{avg_PPM_hard} = \sqrt{\frac{4}{L \log_2 L}} P_{avg_OOK} ; \quad (2.32)$$

$$P_{avg_PPM_soft} = \sqrt{\frac{2}{L \log_2 L}} P_{avg_OOK} ; \quad (2.33)$$

where P_{avg_OOK} is the average optical power requirement for OOK. From (2.33), it is apparent that to achieve similar error performance, PPM requires an average power lower than that required by OOK by a factor of $\sqrt{(0.5L \log_2 L)}$. Since most of the indoor optical channels are power limited (rather than bandwidth limited), then PPM schemes with $L > 2$ would be a desirable option. In fact, 4-PPM is the signalling format adopted by the IrDA in their serial physical layer at a data rate of 4 Mbps.

Symbol and slot synchronization as well as the multipath induced ISI are the limiting factors in the performance of the PPM schemes. In diffuse links, the incurred power penalty due to the ISI is higher than that of the OOK signalling, because of smaller slot durations. The descriptions of MLSD as well as the DF and the linear equalizers applied to reduce the power penalty due to multipath propagation and the performance of the equalized and unequalized L -PPM can be found in [67, 84, 97-99, 181, 182].

A number of variations of PPM have been proposed for the indoor OWC. In order to avoid consecutive pulses, PPM plus (PPM+) was proposed in [20] where a redundant low chip is inserted after each high chip. Though PPM+ improves the reliability; it further decreases the bandwidth efficiency. Other variations of PPM are multiple PPM (MPPM) and overlapping PPM, the performance of which is reported in [116, 183, 184]. The differential PPM (DPPM) improves the power efficiency as well as bandwidth efficiency or the throughput by removing all the empty slots that follow a pulse in a PPM symbol [52, 185]. The average number of slots per symbol in DPPM $\bar{L}_{DPPM} = (L + 1)/2$ is almost half that of PPM. This provides possibility for improving the data throughput or bandwidth efficiency [52]. With every DPPM symbol ending with a pulse, there exists an inherent symbol synchronization capability. On the AWGN channel, for any given L , DPPM has a slightly higher power requirement but a much lower bandwidth requirement compared with PPM. A MAP detector scheme to overcome the ISI due to multipath propagation is suggested in [185] with significant performance improvement and more than 10 dB less power requirement than the hard decision. Performance of DPPM with concatenated coding in diffuse channel is reported

in [22] in which a combination of marker and Reed–Solomon codes is used to correct insertion/deletion errors.

Combination of the PPM with the pulse amplitude modulation can be used to improve the data throughput, bandwidth capacity and peak-to-average power ratio (PAPR). A number of such variations had been suggested including DAPPM [21, 186], multiple pulse amplitude and position modulation [54, 187].

2.8.1.3 Pulse Interval Modulation

In pulse interval modulation, information is encoded by inserting empty slots between two pulses. The simplest method is to use DPIM [24, 50, 51]. DPIM is an anisochronous modulation technique, in which each block of $M (= \log_2 L)$ input data bits $\{d_i, i = 1, 2, \dots, M\}$ is mapped to one of L possible symbols $\{s(n), 0 < n \leq L\}$ of different length. A symbol is composed of a pulse of one slot duration followed by a series of empty slots, the number of which is dependent on the decimal value of the M -bit data stream being encoded (see Figure 2.4). DPIM can be used to achieve either higher bandwidth efficiency or power efficiency compared to PPM by varying the value of L . For a fixed average bit rate and fixed available bandwidth, improved average power efficiency can be achieved when using higher bit resolution (i.e. higher M) compared to PPM [51]. Unlike PPM schemes where both slot and symbol synchronisations are the requirement, DPIM also offers a built-in symbol synchronisation capability.

Since symbol length in DPIM is variable, slot duration T_{s_DPIM} is chosen in such a way that the mean symbol length is equal to the time taken to transmit the same number of bits using fixed symbol (frame) length schemes such as OOK and PPM. T_{s_DPIM} is given as [12]:

$$T_{s_DPIM} = \frac{T_b M}{\bar{L}_{DPIM}} ; \quad (2.34)$$

where \bar{L}_{DPIM} is the average symbol length of DPIM.

$$\bar{L}_{DPIM} = \frac{2^M + 1}{2}. \quad (2.35)$$

The system block diagram of the matched filter based receiver for DPIM system is shown in Figure 2.9. The DPIM encoder maps each block of $\log_2 L$ input bits to one of L possible symbols, each different in length. The symbols are passed to a transmitter filter, which has a unit-amplitude rectangular impulse response $p(t)$, with a duration of one slot T_{s_DPIM} . The output of the transmitter filter is scaled by the peak detected signal photocurrent $\bar{L}_{DPIM} P_{avg}$. Shot noise $n(t)$ is then added to the signal. The receiver consists of a photodetector of responsivity of R followed by a unit energy matched filter with an impulse response $r(t)$, which is matched to $p(t)$. The filter output is sampled at the end of each slot period, and a one or zero is assigned depending on whether the signal is above or below the threshold level at the sampling instant. Though suboptimal, a threshold level is set to $\alpha = RP_{avg} \sqrt{\bar{L}_{DPIM} T_b \log_2 L} / 2$, which is midway between expected one and zero levels, can be used for simplification of the receiver.

In contrast to PPM, DPIM has a variable symbol length. As a result, an error in a symbol not only affects the symbol itself but also the preceding symbols. Therefore it is difficult to localise an error to a particular symbol. Consequently the error performance simply cannot be described in terms of BER. In such cases the error performance is best described in terms of SER P_{se} and packet error rate (PER) P_{pe} . For non-dispersive channel, the SER for the DPIM system with matched filter based receiver and threshold level set in the middle of the energy of the pulse and zero is given by [51]:

$$P_{se_DPIM} = Q \left(\sqrt{\frac{E}{2N_0}} \right); \quad (2.36)$$

where E is the energy of a symbol and is given by $\sqrt{E} = \bar{L}_{DPIM} RP_{avg} \sqrt{T_{s_DPIM}}$.

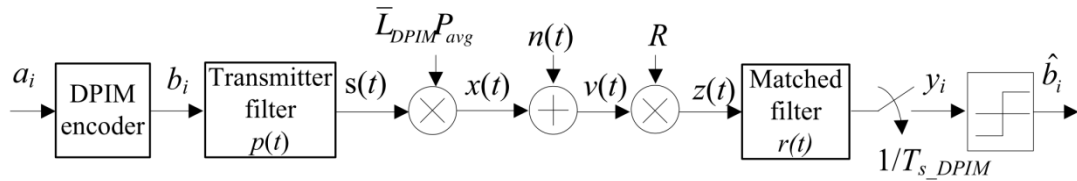


Figure 2.9: The block diagram of the matched filter based receiver for DPIM scheme.

Unlike the case of PPM, the PSD of DPIM has a significant DC and low frequency components [50, 188]. Hence, DPIM system suffers from the BLW effects when the HPF is used [91, 189]. In order to avoid symbols with a zero time slot between the adjacent pulses, an additional guard slot (GS) of one or more time slots may be added to each symbol immediately following the pulse. Adding one or more guard slots also provides immunity to the multipath induced ISI for moderately dispersive channel [190]. For highly dispersive channel, equalization schemes must be incorporated to achieve a reasonable SER. The performance of the DPIM system with an equalizer is evaluated in [51, 191] and it is found that zero-forcing DFE provides significantly better performance compared to the DPIM with guard slots.

A further improvement in throughput and capacity can be achieved by implementing a more complex baseband modulation techniques like the DH-PIM $_{\Gamma}$ [25]. The n^{th} symbol $\mathbf{X}_n(h_n, d_n)$ of a DH-PIM $_{\Gamma}$ sequence is composed of a header $h_n \in \{H_0, H_1\}$ initiating the start of a symbol and a number of empty information slots d_n . Depending on the most significant bit (MSB) of message \mathbf{a}_i , one of two possible symbol headers of equal duration $T_h = (\Gamma + 1)T_s$, where $\Gamma > 0$ is an integer, could be considered, header H_0 and H_1 for MSB of “0” and “1”, respectively. The value of $d_n \in \{0, 1, \dots, 2^{M-1} - 1\}$ is simply the decimal value of \mathbf{a}_i or its 1’s complement when a symbol starts with H_0 and with H_1 , respectively [112]. A guard slot $T_g \in \{(0.5 \Gamma + 1)T_s, T_s\}$ corresponding to $h_n \in \{H_0, H_1\}$ is used in DH-PIM $_{\Gamma}$ symbol. The header pulses have dual functions of symbol initiation and built-in symbol synchronization. The average symbol length \bar{L}_{DH-PIM} and slot duration T_{S_DH-PIM} of DH-PIM $_{\Gamma}$ are given by [112] :

$$\begin{aligned} \bar{L}_{DH-PIM} &= \frac{(2^{M-1} + 2\Gamma + 1)}{2} ; \\ T_{S_DH-PIM} &= \frac{2M}{(2^{M-1} + 2\Gamma + 1)R_b} ; \end{aligned} \quad (2.37)$$

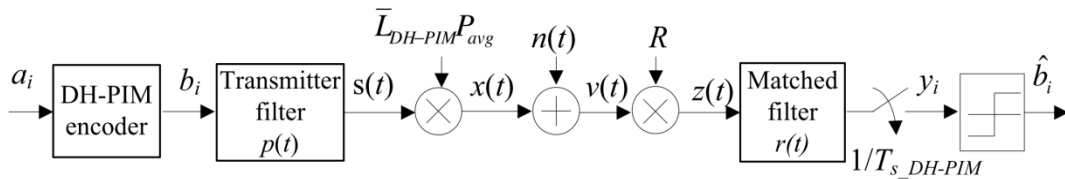


Figure 2.10: The block diagram of the matched filter based receiver for DH-PIM scheme.

DH-PIM $_{\Gamma}$ average symbol length can be reduced by a proper selection of Γ , thus offering improved transmission throughput and bandwidth requirements compared to the DPIM, DPPIM and PPM schemes [25].

A system block diagram of DH-PIM $_{\Gamma}$ scheme is given in Figure 2.10. An M -bit binary input sequence $\mathbf{a}_i = \{a_1, a_2 \dots a_M\}$, is first converted into DH-PIM $_{\Gamma}$ symbol format \mathbf{b}_i before being applied to a transmitter filter $p(t)$ with a unit-amplitude impulse response of one slot duration T_{s_DH-PIM} . The output of the transmitter filter is scaled by the peak detected signal photocurrent $\bar{L}_{DH-PIM} P_{avg}$, where \bar{L}_{DH-PIM} is the average symbol length of DH-PIM symbols. Like in other systems, AWGN $n(t)$ is added to the signal before being detected by a photodetector at the receiver. Received signal is scaled by R to account the photodetector responsivity. The output of the optical receiver $z(t)$ is applied to a matched filter, followed by a sampler (sampling at the slot rate $f_s = 1/T_{s_DH-PIM}$) and a threshold detector to regenerate the DH-PIM $_{\Gamma}$ sequence $\hat{\mathbf{b}}_i$.

In the non-dispersive channel, the matched filter based receiver with the receiver sampling rate equal to the slot rate is used. Assuming H_0 and H_1 are equally likely, the slot error probability of the DH-PIM $_{\Gamma}$ for a LOS link configuration is given by [112]:

$$P_{se_DH-PIM} = \frac{1}{4\bar{L}_{DH-PIM}} \left[(4\bar{L}_{DH-PIM} - 3\Gamma) Q\left(\frac{\mu\alpha R P_{avg}}{\sqrt{N_0 R_b}}\right) + 3\Gamma Q\left(\frac{\mu(1-\alpha) R P_{avg}}{\sqrt{N_0 R_b}}\right) \right]; \quad (2.38)$$

where $\mu = \sqrt{32M\bar{L}_{DH-PIM}/9\Gamma^2}$, α is the threshold level and P_{avg} is the average received optical power.

The symbol mapping of the baseband modulation techniques discussed so far is summarised in Table 2.5. The average symbol length and bandwidth requirement for these modulation techniques are listed in Table 2.6. DH-PIM $_{\Gamma}$ offers a higher bit rate compared to the DPIM and PPM and requires less bandwidth with higher average optical power requirements [25, 192]. For the same order of bit resolutions, the DH-PIM $_2$ provide improved resistance to multipath induced ISI [193] and equalization can significantly improved the error performance [194]. Since DH-PIM $_{\Gamma}$ symbol has a significant DC and low frequency components compared to the DPIM and PPM [195], the DH-PIM $_{\Gamma}$ has higher power penalty due to HPF for lower cut-off frequencies [85].

Table 2.5: Symbol mapping of PPM, DPPPM, DPIM, DH-PIM, MDPIM and DAPPM for bit resolution of $M = 3$.

OOK	8-PPM	8-DPPM	8-DPIM	8-DH-PIM₂
000	10000000	1	1	100
001	01000000	01	10	1000
010	00100000	001	100	10000
011	00010000	0001	1000	100000
100	00001000	00001	10000	110000
101	00000100	000001	100000	11000
110	00000010	0000001	1000000	1100
111	00000001	00000001	10000000	110

Table 2.6: The average symbol length and bandwidth requirement of PPM, DPIM and DH-PIM.

Modulation Scheme	PPM	DPIM	DH-PIM
Average symbol Length	2^M	$\frac{(2^M + 3)}{2}$	$\frac{(2^{M-1} + 2\Gamma + 1)}{2}$
Bandwidth requirement normalised to NRZ-OOK	$\frac{R_b 2^M}{M}$	$\frac{R_b (2^M + 3)}{2M}$	$\frac{R_b (2^{M-1} + 2\Gamma + 1)}{\Gamma M}$

Other baseband modulation techniques based on the multilevel pulse amplitude modulation and PIM also exist. For further discussion, one can refer to [19, 21, 23, 54, 185]. The focus of this study is not to approve or disapprove effectiveness of particular modulation techniques for indoor OWC links, rather to apply some of the advanced signal processing to mitigate the adverse channel effect in indoor OWC for existing modulation techniques.

2.8.2 Subcarrier Intensity Modulation

The subcarrier intensity modulation in optical communications follows from techniques such as multiple carrier modulation in radio communication. Optical subcarrier modulation operates by combining one or multiple RF carriers called subcarriers, and using this composite RF signal $m(t)$ to modulate the intensity of an optical source [196, 197]. Prior to this, the data stream is pre-modulated on the subcarrier frequencies using evolved modulation schemes such as phase shift keying (PSK), quadrature amplitude modulation (QAM) [198]. During one symbol duration $m(t)$ is given by:

$$m(t) = \sum_{j=1}^{N_s} A_j g(t) \cos(\omega_{cj}t + \theta_j); \quad (2.39)$$

where N_s is the number of subcarriers, $g(t)$ is the rectangular pulse shape function, $\{\omega_{cj}\}_{j=1}^{N_s}$ is the angular frequency and $\{A_j\}_{j=1}^{N_s}$ is the peak amplitude of each subcarrier. At the receiver, a direct detection is employed followed by a standard RF demodulator to extract the data. For a single SIM, the electrical filter used at the receiver must have the same bandwidth as OOK signalling if quadrature-PSK is used. For BPSK modulated subcarrier the bandwidth requirement is twice that of OOK. For multiple SIM, the bandwidth requirement apparently increases by a factor of N .

Since each subcarrier contained in $m(t)$ is sinusoidal with both positive and negative values, to modulate the intensity of the LD (or an LED) without clipping, the amplitude of this composite signal must always be greater than the threshold current. A DC offset must therefore be added to $m(t)$ in order to meet this requirement. Consequently, subcarrier modulation schemes are less power efficient than pulse modulation techniques. For instance in an AWGN limited direct LOS IR communication link, using a single-SIM with either BPSK or QPSK results in 1.5 dB more optical power compared to the OOK [20]. Additionally, the optical modulation depth must be such that the optical source operates within its dynamic range. SIM can also be implemented with the subcarrier signals made orthogonal to one another to achieve orthogonal frequency division multiplexing (OFDM) [114, 115]. This is particularly interesting as it can be easily implemented via IFFT/FFT in available signal processing chips [43, 196]. By ensuring that each subcarrier transmits at relatively low data rates, the need for an equalizer can be avoided while maintaining the same aggregate data rate. It also offers a

greater immunity to near DC noise from the fluorescent lamps [43, 196]. However with a DC offset, a multiple SIM results in a $10\log N$ (dB) increase in optical power requirement compared with a single subcarrier. Also, multiple SIM suffers from both inter-modulation and harmonics distortions due to the inherent optical source non-linearity.

2.9 Summary

The infrared wireless communication in indoor environment has attracted a considerable research interest in the past decade. It gained a quick popularity due to availability of huge unregulated bandwidth and many other advantages over the RF links. Moreover, the availability of low cost receiver and transmitter makes it suitable for indoor communication. The infrared communication has its own challenges. The average optical power that can be transmitted is limited by the eye safety reason, so the link budget should be properly managed and the background ambient light introduce shot noise to the system. With IrDA already in successful operation and supported by industrial and academic research, some of these problems are resolved. The infrared wireless system as a complementary to RF system for wireless connectivity is a very promising technology. The infrared offers virtually unlimited licence free bandwidth, low transceiver cost and electromagnetic interference free operation.

Significant works have been done in the investigation of intensity modulation, direct detection baseband modulation techniques. The most popular modulation techniques are OOK due to its simplicity in the implementation and PPM for unparallel power efficiency. Other modulation techniques like DPIM and DH-PIM can either provide improved bandwidth efficiency (increase throughput) or improved power efficiency. However there is always a trade-off between the bandwidth and the power. This study has proposed a number of advanced techniques to mitigate the adverse channel effect for indoor OWC. Due to space limitation, performances of only few baseband modulation schemes are investigated. However, the techniques proposed in the study should in fact be equally applicable to other modulation techniques.

Chapter 3 Symbol Retransmission Scheme

3.1 Introduction

The key advantage of the digital communication system is the possibility to recover exact replica of the transmitted message in a given channel conditions. Since the message is binary, having either zero or one state, error occurs if a binary zero is received when a binary one is transmitted or vice versa. The error probability in the received signal depends on the noise level which is quantified using the SNR. The error probability in the system is measured in terms of the BER and there is a direct relationship between the SNR and BER. If the BER performance of any communication system is below the acceptable level, it is necessary to increase the transmitter power, which in turns increases SNR of the system. Ironically, the maximum transmitted optical power in indoor OW applications is limited due to the ocular safety reasons [41, 43]. Furthermore, indoor OW channel links performance degrades significantly due to the ambient light interference [78, 80]. Hence an alternative method to improve the reliability is sought out. One option is to use the error control code methods. Following Shannon famous paper on the relationship between the channel capacity and the SNR [199], a number of codes providing a low error probability in a given channel condition had been proposed. The basic concept in the error control code is to add redundancies in the transmitted data, and use the redundancy to detect and correct errors in the received data.

Significant work has been done in the field of error control coding, a number of very powerful codes including the turbo code [200] and the low parity density code (LPDC) [201] have been proposed. In this chapter existing codes have been applied to different environments to assess the performance of the indoor OW channel. The simplest form of the error control code is the repetition code in which multiple copies of the same message are transmitted and the receiver makes the decision based on the most repeated symbol. In this chapter, the error performance of the repetition coding for different modulation techniques is reported. The analytical calculation of slot error probabilities are given followed by computer simulations. The error correction repetition coding for

error detection is introduced in Section 3.1 followed by the symbol retransmission scheme in Section 3.2. The mathematical analysis and simulation results for the symbol retransmission scheme for DH-PIM modulation are presented in Section 3.3 and Section 3.4, respectively. The summary of the chapter is given in the final section.

3.2 Repetition Coding

The simplest form of error correct code is the repetition coding in which a bit is repetitively transmitted a predefined number of times i.e. the $(n, 1)$ repetition code, where n is odd, is obtained by repeating the input bit n times. The decoding at the receiver is done by the majority decoding rule [201]. If the majority of the received bits is “0”, then decode a “0”, otherwise decode a “1”. For example, for a $(5, 1)$ repetition code, if there are three or more “1” in the received codeword, the decoder will select “1”. Otherwise the decoder selects “0”. Since the minimum Hamming distance D_{hm} of a $(n, 1)$ repetition code is n , the system can detect $(n - 1)$ errors and correct $\lfloor (n - 1)/2 \rfloor$ errors, where $\lfloor x \rfloor$ is the largest integer less than or equal to x . Hence, the decoder will introduce errors if more than half of the received bits are in error.

The bit error probability in a coded system can be calculated by summing all probabilities that more than half of the received bits are in error. The probability $P(i, n)$ that exactly i bits are in error out of n bits is given by:

$$P(i, n) = \binom{n}{i} p^i (1 - p)^{n-i}; \quad (3.1)$$

where p is the probability of error in each random bit.

Then the BER P_e^n of a $(n, 1)$ repetition code is:

$$P_e^n = \sum_{i=\kappa+1}^n \binom{n}{i} p^i (1 - p)^{n-i}; \quad (3.2)$$

where $\kappa = \lfloor (n - 1)/2 \rfloor$.

The bit error probabilities for different code rates and different BERs are listed in Table 3.1. The improvement in the BER performance is at the cost of reduced throughput and implementation complexity. BER performance improves with increasing the repetition rate but throughput of the system reduces accordingly.

Table 3.1: Probability of bit error for $(n, 1)$ repetition code.

Input BER	Output BER			
	code (3,1)	code (5,1)	code (7,1)	code (9,1)
10^{-2}	2.98E-4	9.851E-6	3.417E-7	1.219E-8
10^{-3}	2.998E-6	9.985E-9	3.492E-11	1.256E-13
10^{-4}	3.000E-8	9.998E-12	3.499E-15	1.260E-18
10^{-5}	3.000E-10	1.000E-014	3.500E-19	1.260E-23
10^{-6}	3.000E-12	1.000E-017	3.500E-23	1.260E-28

3.3 Symbol Retransmission

A symbol retransmission technique, in which each symbol is retransmitted for a predefined number of times, is suggested for PPM scheme [55-57]. This technique can easily be implemented in the FPGA and offers an incremental SNR gain of ~ 3 dB with doubling the code repetition rate [55]. Similar techniques can be applied to other modulation techniques like DPIM and DH-PIM. However, due to lack of fixed symbol boundaries in DPIM and DH-PIM, the analysis of error probability should take care of the variable symbol length as well as the probability of the symbol error. The slot error probability of PPM can be derived simply from symbol error probability due to fixed symbol length [57].

The analysis of slot error probability for variable symbol length modulation techniques is discussed below. For the verification of analysis, computer simulation is carried out for DH-PIM scheme.

3.4 Symbol Retransmission for Variable Symbol Length Modulation Schemes

For practical purpose, retransmission rates must be three or greater as the retransmission rate of two will not provide any performance gain. In the case of retransmission rate of two, the receiver compares two symbols and selects the first symbol rather than requesting a retransmission. However, the downside is that one cannot determine which symbol is the correct; therefore this procedure is not recommended for practical applications. In the case of three symbols retransmission, if an error occurs in only one

symbol, the remaining two symbols are the same. The receiver can select one of two symbols as the valid symbol. In this way, a slot error confined to one symbol can be detected and corrected. Slot errors appearing in more than one symbol could be detected and corrected by increasing the symbol retransmission rate, but this is not practical due to the reduced data throughput.

Consider a modulation scheme with retransmission rate R_{rt} where $R_{rt} = 1, 3, 4$ or 5 . The retransmission rate R_{rt} is achieved by transmitting a symbol $x(t)$ repetitively R_{rt} times. At the receiver, a majority decision mechanism is applied to the received sequence, i.e. the receiver selects the symbol that is repeated the highest number of times from a group of received symbols. For the case where more than one symbol are different but are repeated the same number of times, the receiver can arbitrarily select one of them as no mechanism exists to point out the correct symbol. The majority decision algorithm for $R_{rt} = 4$ is shown in Figure 3.1. Here, each symbol $x(t)$ is transmitted four times and the received group of symbols are $y_r(t) = \{y_1(t), y_2(t), y_3(t), y_4(t)\}$.

The decoded symbol y is correct as long as it is equal to x (in what follows hereafter, x and y will replace $x(t)$ and $y(t)$ for simplicity). As can be seen from Figure 3.1, probability $P(y_r = y_i)$ depends on the equality of the received symbols. Symbols equality $y_i = y_j$ for all $i, i \neq j$ depends two factors: (i) the probability of the received symbol being error-free and/or (ii) the error(s) slot position. Thus, in the mathematical analysis both the probabilities of slot error and equality of erroneous symbols are taken into consideration. For the calculation of slot error probability, following assumptions are made: a) all the possible symbols are equi-probable, b) the probabilities of occurrence of errors in all slots and symbols are equal and c) the occurrence of error in two or more slots within the same symbol is very low.

At the receiver when decoding, comparisons are carried out at the symbol level, therefore the symbol error probability P_{syne} is determined and is given by [25]:

$$P_{syne} = 1 - (1 - P_{se})^{\bar{L}}; \quad (3.3)$$

where P_{se} is the probability of slot error and \bar{L} is the average symbol length. The detailed derivation of SER calculation for R_{rt} of 3, 4 and 5 is described below. In the following derivations, $P(x)$ denotes the probability of the event x , $P_{syne}(m, n)$ denotes the

probability of occurring errors in exactly n symbols out of m symbols, P_{neq} and P_{nuneq} are the probability of n symbols being equal and unequal, respectively, P_{nm} and P_n are the dummy variables denoting error probability due to m symbols being equal out of n erroneous symbols and the total symbol error probability due to error in n symbols.

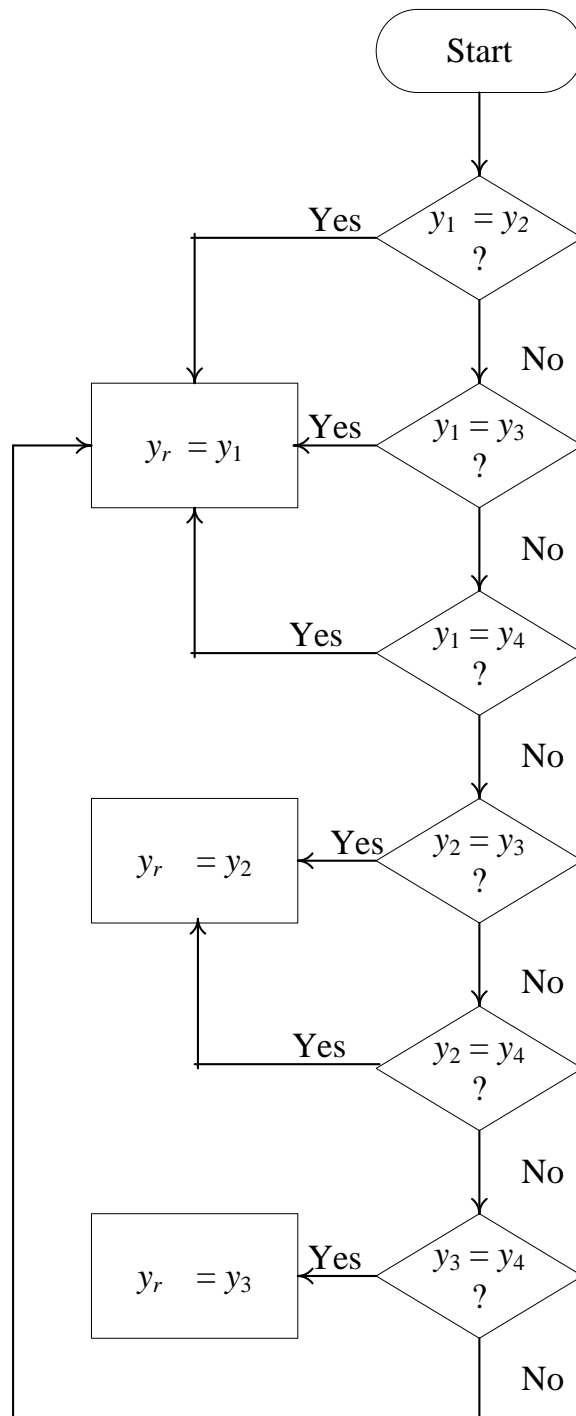


Figure 3.1: A flow chart showing the majority decision process for $R_{rt} = 4$.

3.4.1 Slot Error Rate Equations

Case 1: Three symbol retransmission ($R_{rt} = 3$)

The decoded symbol will have an error if one of the following conditions is true:

1.
$$P_1 = P_{syne}(3,3) = P_{syne}^3. \quad (3.4)$$

- 2.

- (a)
$$P_{22} = P_{2eq}P_{syne}(3,2) = \frac{1}{L} \left[\frac{3!}{2!} P_{syne}^2 (1 - P_{syne}) \right]. \quad (3.5)$$

- (b)
$$P_{21} = \frac{2}{3} P_{2uneq}P_{syne}(3,2) = \frac{2}{3} \left(1 - \frac{1}{L} \right) \left[\frac{3!}{2!L} P_{syne}^2 (1 - P_{syne}) \right]. \quad (3.6)$$

The total probability of symbol error for R_{rt} of 3 is the summation of (3.4), (3.5) and (3.6) given as:

$$P_{syne3r} = P_{syne}^3 + \frac{1}{L} \left[\frac{3!}{2!} P_{syne}^2 (1 - P_{syne}) \right] + \frac{2}{3} \left(1 - \frac{1}{L} \right) \left[\frac{3!}{2!L} P_{syne}^2 (1 - P_{syne}) \right]. \quad (3.7)$$

On simplification, (3.7) is given by:

$$P_{syne3r} = P_{syne}^2 \left[\frac{1}{L} + 2 \right] - P_{syne}^3 \left[\frac{1}{L} + 1 \right]. \quad (3.8)$$

By substituting (3.3) into (3.8) the SER for $R_{rt} = 3$ is given as:

$$P_{se3r} = 1 - \left[1 - \left(P_{syne}^2 \left[\frac{1}{L} + 2 \right] - P_{syne}^3 \left[\frac{1}{L} + 1 \right] \right) \right]^{1/L}. \quad (3.9)$$

The slot error probability for $R_{rt} = 3$ in (3.9) shows the dependencies of average symbol length \bar{L} and symbol error probability P_{syne} . Since P_{syne} can be calculated from slot error probability P_{se} as given in (3.3), P_{se3r} can theoretically be calculated if the average symbol length as well as P_{se} is known. At low values of P_{syne} , the higher order of P_{syne} can be neglected and hence P_{se3r} is proportional to the square of P_{syne} . Such simple relationship between P_{se3r} and the average symbol length \bar{L} does not exist. It can only be safe to say that P_{se3r} is inversely proportional to \bar{L} . Figure 3.2 shows the relation of the P_{se3r} against the standard P_{se1r} without retransmission for average symbol length of 2, 4, 8 and 16. For same valued of P_{se1r} , the values of P_{se3r} decreases with increasing values of \bar{L} , clearly demonstrating the inverse relationship between P_{se3r} and \bar{L} . The non-linear relationship between P_{se3r} and P_{se1r} is also clear from the figure and as expected from (3.9) the second order of P_{se1r} is dominating factor in the curves.

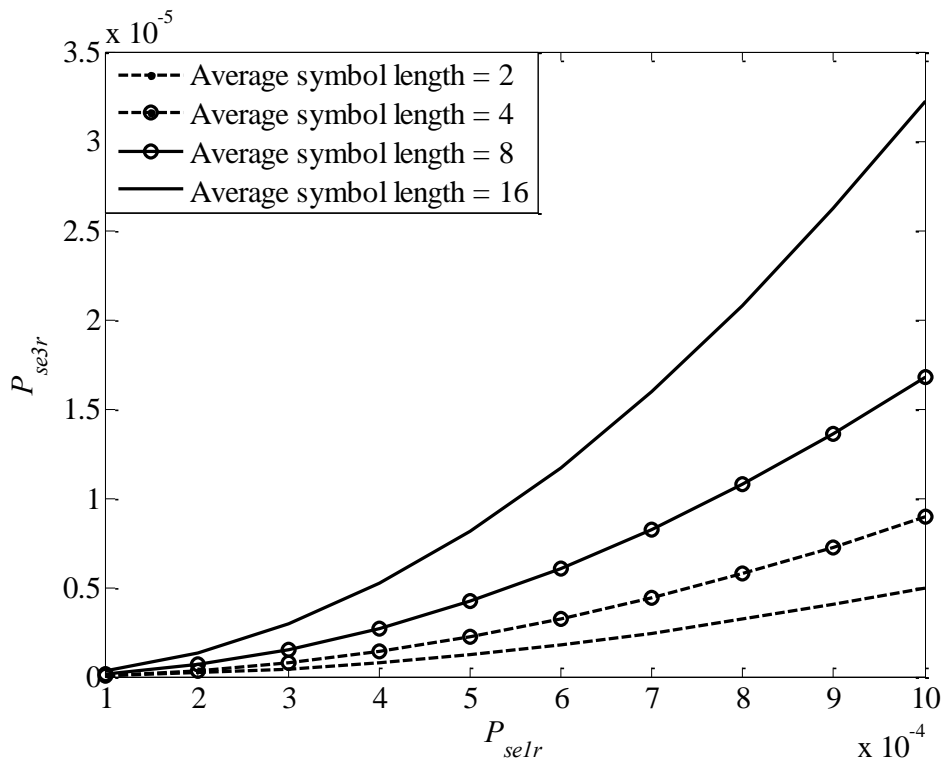


Figure 3.2: Slot error probability of R_{rt} of three P_{se3r} against the standard slot error probability without retransmission P_{se1r} for average symbol length of 2, 4, 8 and 16.

Case 2: Four symbol retransmission ($R_{rt} = 4$)

The conditions for a decoded symbol to be erroneous for $R_{rt} = 4$ are given below:

1.
$$P_4 = P_{syne}(4,4) = P_{syne}^4. \quad (3.10)$$

2.

(a)
$$P_{33} = P_{3eq}P_{syne}(4,3) = \frac{1}{\bar{L}^2} P_{syne}(4,3). \quad (3.11)$$

(b)
$$P_{32} = P_{2eq}P_{syne}(4,3) = \frac{3\bar{L}(1-\bar{L})}{\bar{L}^3} P_{syne}(4,3). \quad (3.12)$$

(c)
$$P_{31} = \frac{3}{4} P_{3uneq}P_{syne}(4,3). \quad (3.13)$$

Hence the symbol error probability due to an error occurring in three symbols is given by:

$$P_3 = \left[\frac{1}{\bar{L}^2} + \frac{3\bar{L}(1-\bar{L})}{\bar{L}^3} + \frac{3}{4} \left\{ \frac{1}{\bar{L}^2} + \frac{3\bar{L}(1-\bar{L})}{\bar{L}^3} \right\} \right] P_{syne}(4,3). \quad (3.14)$$

3.
$$P_{22} = \frac{1}{2} P_{2eq}P_{syne}(4,2). \quad (3.15)$$

The symbol error probability obtained by summation of (3.10), (3.14) and (3.15) is given by:

$$P_{syne4r} = \frac{3P_{syne}^2}{\bar{L}} + P_{syne}^3 \left(3 - \frac{3}{\bar{L}} - \frac{2}{\bar{L}^2} \right) + P_{syne}^4 \left(\frac{2}{\bar{L}} - 2 \right). \quad (3.16)$$

Thus, the SER for $R_{rt} = 4$, P_{se4r} is given by:

$$P_{se4r} = 1 - \left[1 - \frac{3P_{syne}^2}{\bar{L}} + P_{syne}^3 \left(3 - \frac{3}{\bar{L}} - \frac{2}{\bar{L}^2} \right) + P_{syne}^4 \left(\frac{2}{\bar{L}} - 2 \right) \right]^{1/\bar{L}}. \quad (3.17)$$

As in case of retransmission rate of 3, the slot error probability for the retransmission rate of 4 depends on the average symbol length and symbol error probability P_{syne} . The second order of P_{syne} is dominating terms that determine the P_{se4r} . The coefficient of the second power of P_{syne} in (3.9) is $\left[\frac{1}{\bar{L}} + 2 \right]$ and has values between 2 and 3 as $1 \leq \bar{L} < \infty$. However, coefficient of the second power of P_{syne} in (3.17) is $3/\bar{L}$, values of which can be 0 to 3. This shows that P_{se4r} is always less than P_{se3r} except for $\bar{L} = 1$, in which case both can have same values.

Case 3: Five symbol retransmission ($R_{rt} = 5$)

For R_{rt} of 5 the decoded symbol will be error-free if at least three symbols are received correctly. However, an error will occur in the decoded symbol if one of the following conditions applies.

1.
$$P_{45} = P_{syne}(5,5) = P_{syne}^5. \quad (3.18)$$

- 2.

- (a)
$$P_{41} = \frac{4}{5} P_{3uneq} P_{syne}(4,5) = \frac{4}{5} \left[\frac{\bar{L}(\bar{L}-1)(\bar{L}-2)(\bar{L}-2)}{\bar{L}^4} \right] P_{syne}(4,5). \quad (3.19)$$

- (b)
$$P_{42} = (1 - P_{4uneq}) P_{syne}(4,5). \quad (3.20)$$

Hence the probability of selecting erroneous symbols due to an error occurring in any of 4 symbols is given by:

$$P_4 = \left[\frac{4}{5} \frac{\bar{L}(\bar{L}-1)(\bar{L}-2)(\bar{L}-2)}{\bar{L}^4} + 1 - \frac{\bar{L}(\bar{L}-1)(\bar{L}-2)(\bar{L}-2)}{\bar{L}^4} \right] \frac{5!}{3!2!} P_{syne}^3 (1 - P_{syne})^2. \quad (3.21)$$

3.

$$(a) \quad P_{33} = P_{3eq}P_{syne}(5,3) = \frac{1}{\bar{L}^2}P_{syne}(5,3). \quad (3.22)$$

$$(b) \quad P_{32} = \frac{1}{2}P_{2eq}P_{syne}(5,3) = \frac{3\bar{L}(\bar{L}-1)}{2\bar{L}^3}P_{syne}(5,3). \quad (3.23)$$

Hence,

$$P_3 = \left[\frac{3}{2\bar{L}} - \frac{1}{2\bar{L}^2} \right] \frac{5!}{3!2!} P_{syne}^3 (1 - P_{syne})^2. \quad (3.24)$$

Summing (3.18), (3.21) and (3.24) and with further simplification, the symbol error rate for $R_{rt} = 5$, P_{syne5r} is given by:

$$P_{syne5r} = \left(\frac{15}{\bar{L}} - \frac{5}{\bar{L}^2} \right) P_{syne}^3 + \left(4 - \frac{24}{\bar{L}} - \frac{1}{\bar{L}^2} + \frac{6}{\bar{L}^3} \right) P_{syne}^4 + \left(-3 + \frac{9}{\bar{L}} + \frac{6}{\bar{L}^2} - \frac{6}{\bar{L}^3} \right) P_{syne}^5. \quad (3.25)$$

Thus, the slot error rate for $R_{rt} = 5$ is given by:

$$P_{se5r} = 1 - \left[1 - \left(\frac{15}{\bar{L}} - \frac{5}{\bar{L}^2} \right) P_{syne}^3 + \left(4 - \frac{24}{\bar{L}} - \frac{1}{\bar{L}^2} + \frac{6}{\bar{L}^3} \right) P_{syne}^4 + \left(-3 + \frac{9}{\bar{L}} + \frac{6}{\bar{L}^2} - \frac{6}{\bar{L}^3} \right) P_{syne}^5 \right]^{1/\bar{L}}. \quad (3.26)$$

Unlike the previous cases, (3.26) has no second order coefficients of P_{syne} indicating the possibility of lower error probability. Secondly, the lowest power of P_{syne} is P_{se5r} shows dependency on first and second powers of \bar{L} .

The comparative study of the slot error probabilities for retransmission rates R_{rt} of 3, 4 and 5 with average symbol lengths \bar{L} of 2 and 16 is given in Figure 3.3. The figure clearly demonstrates the performance improvement in terms of lower error probability for retransmission schemes. R_{rt} of 3 and 4 offers significantly less improvement compared to that of 5. Unlike cases of R_{rt} of 3 and 5, slot error probabilities for $R_{rt} = 4$ show little variation over \bar{L} of 2 and 16. For R_{rt} of 3 and 5, smaller values of \bar{L} offer lower error probabilities.

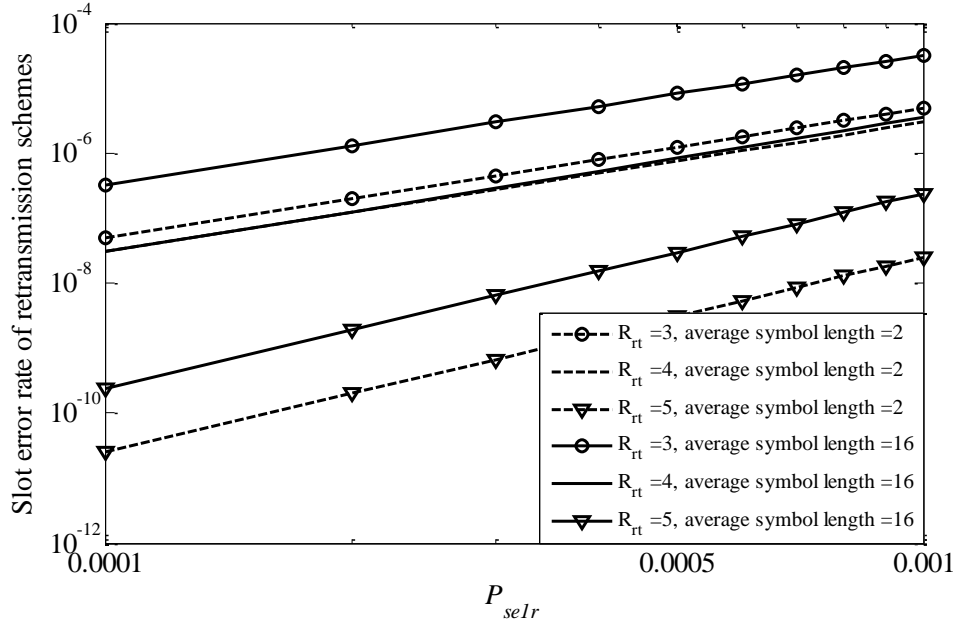


Figure 3.3: SER for retransmission rate of 3, 4 and 5 against the standard slot error probability without retransmission for average symbol length of 2 and 16.

3.5 SER for DH-PIM with Symbol Retransmission

The system block diagram for the symbol retransmission scheme for DH-PIM scheme is depicted in Figure 3.4. The input binary data b_k is first converted to its equivalent DH-PIM symbol x_k . The retransmission encoder duplicates x_k ‘ r ’-times, and its output symbol sequence x_{rk} is applied to the optical transmitter. Assuming the noise signal $n(t)$ being white and Gaussian, the received signal is $z(t) = [x(t)+n(t)]$. At the receiver the output of photodetector is passed through a matched filter, the output of which is sampled at the slot rate T_s^{-1} , prior to being applied to the threshold detector to regenerate the transmitted DH-PIM symbol stream, \bar{z}_k . The function of retransmission decoder is reverse of the retransmission encoder; the only difference is that the encoder outputs $\{x_{1k} \dots x_{rk}\}$ are identical whereas the decoder outputs $\{y_{1k}, \dots, y_{rk}\}$ are not. The output of the decision circuit y_k is an approximation of transmitted symbol x_k based on the received DH-PIM sequence $\{y_{1k}, \dots, y_{rk}\}$ following the algorithm described in Figure 3.1. The output from decision devices is converted to binary data \hat{b}_k using DH-PIM decoder. To determine SER, x_k and y_k are compared slot-by-slot. It is possible to determine the BER by comparing b_k and \hat{b}_k . However, for a variable symbol length modulation scheme such as DH-PIM, PER is the preferred option, which is directly calculated from the SER [51].

3.5.1 Results and Discussions

To verify the mathematical analyses derived in Section 3.4.1, the proposed system is simulated in Matlab based on the block diagram given in Figure 3.4. All the important system parameters adopted for simulation are given in Table 3.2. The theoretical results for the SER for 16-DH-PIM₂ for different retransmission rates, is displayed in Figure 3.5. The performance of different code can be compared using the code gain which is defined as the difference in SNRs for the uncoded and the code systems to achieve the same error probability. It is observed that at low values of P_{se} the code gains for R_{rt} of 3 and 4 are very close. This can be explained with reference to (3.17) and (3.26) where it is shown that P_{serr} depends on the second and higher powers of P_{se} , with the latter having a negligible contribution in P_{serr} as P_{se} decreases. The marginal improvement in the code gain for R_{rt} of 4 compared to R_{rt} of 3 is mainly due to a large coefficient of P_{se}^2 in (3.17). Since the coefficient of P_{se}^3 is negative in (3.9) and positive in (3.17), the difference in the code gain is larger at lower values of SNR compared with the higher values. In case of P_{se5r} , the dominant term is P_{se}^3 , therefore, the code gain increases as P_{se} decreases compared with R_{rt} of 3 and 4.

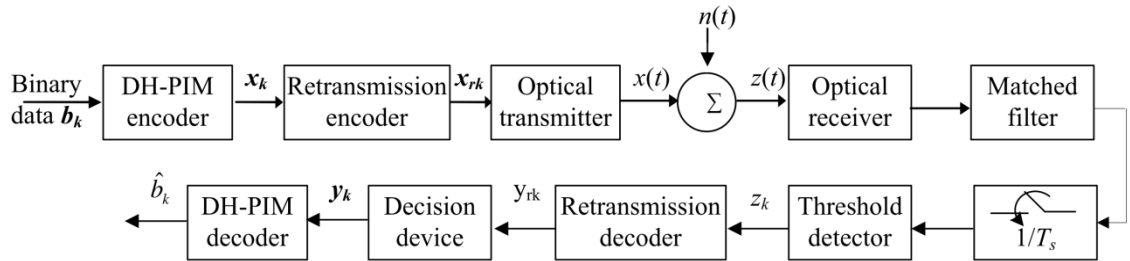


Figure 3.4: The system block diagram of the proposed DH-PIM symbol retransmission.

Table 3.2: The simulation parameters.

Parameter	Value
Γ	1 and 2
M	3, 4 and 5
Detector responsivity R	1 A/W
Ambient induced shot noise current I_b	200 μ A
Bit rate R_b	1 Mbps
Retransmission rate R_{rt}	3, 4 and 5

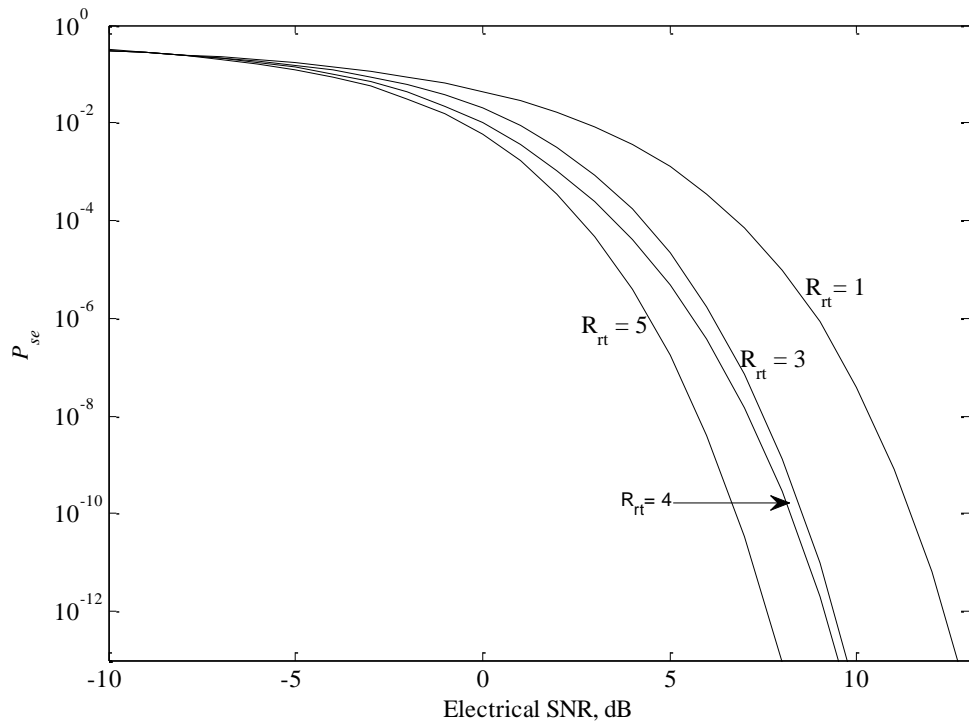
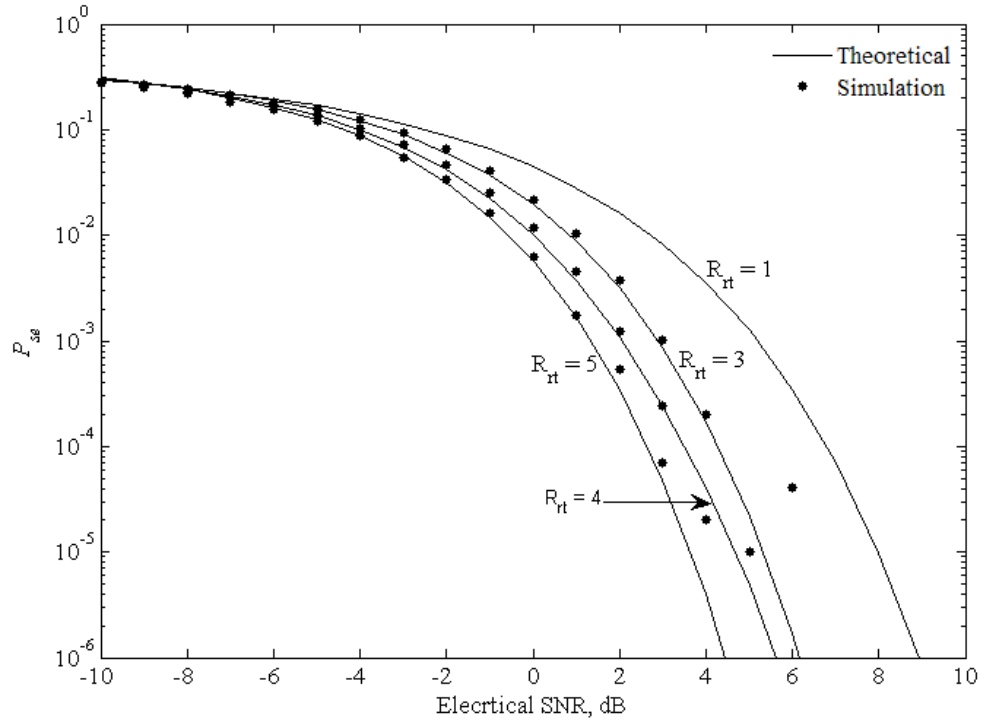
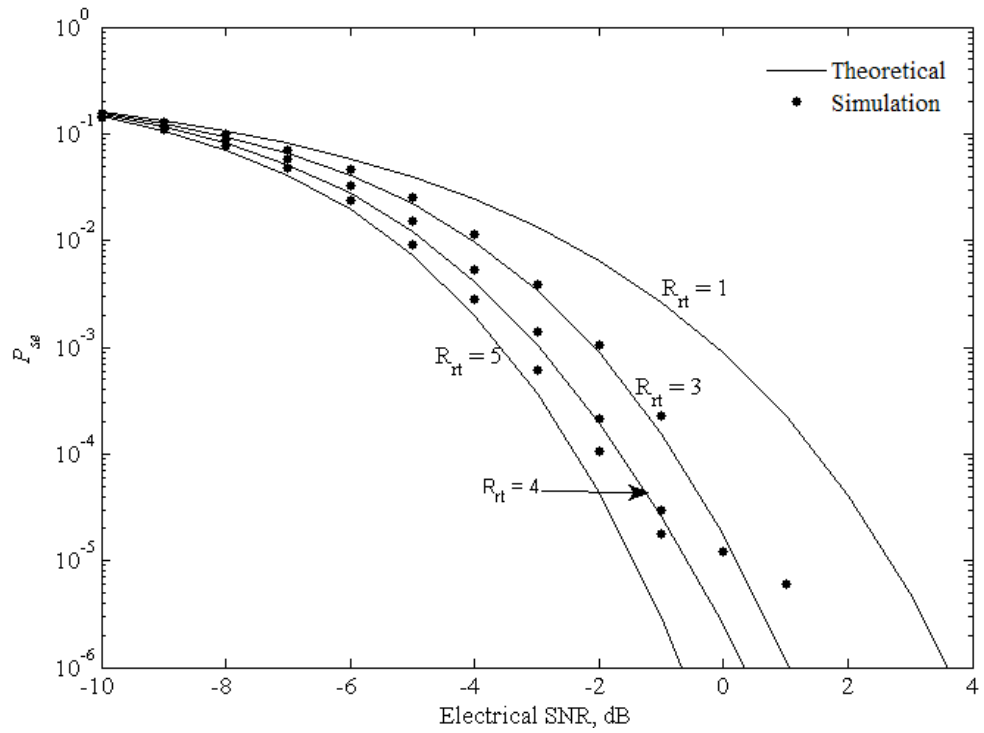


Figure 3.5: The predicted SER against the electrical SNR for retransmission rate of 3, 4 and 5 at a data rate of 1 Mbps for 16-DH-PIM₂.

Figure 3.6 shows the theoretical and Monte-Carlo simulation results for the SER against the electrical SNR for different retransmission rates at a data rate of 1 Mbps for 16-DH-PIM_{1&2}. Although in the analysis it is assumed that the error per symbol is limited only to one slot, it is observed that the simulation and theoretical results match closely up to P_{se} of 10^{-3} . The divergence between the predicted and simulated result at lower P_{se} is due to computational power as the number of symbols generated for each case is only 10^4 . At very high values of P_{se} there is little or no code gain that improves with decreasing P_{se} . As expected, increasing the rate of retransmission will decrease the SNR requirements to achieve a certain SER at the cost of reduced system data throughput and increased system complexity. At a P_{se} of 10^{-5} , the SNR code gains for DH-PIM₂ are 3.6, 4.3 and 5.2 dB for R_{rt} of 3, 4 and 5, respectively compared with R_{rt} of 1. The SNR for DH-PIM₁ gain drops to 2.4, 3.3 and 4.2 dB for R_{rt} of 3, 4 and 5, respectively. This drop in the SNR gain is mainly attributed to the symbol header composed of three slots with a pulse of half slot duration.



(a)



(b)

Figure 3.6: (a) The SER against the electrical SNR for retransmission rate of 3, 4 and 5 at a data rate of 1 Mbps for 16-DH-PIM₂; (b) the SER against the electrical SNR for retransmission rate of 3, 4 and 5 at a data rate of 1 Mbps for 16-DH-PIM₁.

Table 3.3: Code gain for 16-DH-PIM retransmission system at P_{se} of 10^{-4} .

DH-PIM Γ	Code gain (dB)		
	$R_{rt} = 3$	$R_{rt} = 4$	$R_{rt} = 5$
$\Gamma = 2, M = 3$	2.72	3.35	4.38
$\Gamma = 2, M = 4$	2.57	3.27	4.18
$\Gamma = 2, M = 5$	2.33	3.20	3.90
$\Gamma = 1, M = 3$	2.48	3.28	4.11
$\Gamma = 1, M = 4$	2.26	3.16	3.86
$\Gamma = 1, M = 5$	2.07	2.93	3.59

Table 3.3 illustrates the code gain for 16-DH-PIM_{1&2} retransmission system at error probability of P_{se} of 10^{-4} for R_{rt} of 3, 4 and 5 and M equal to 3, 4 and 5. The SNR code gain decreases as M increases, which is due to the fact that the average length of a symbol increases with M , thus resulting in a higher probability of symbol error. This can be explained with reference to (3.9), (3.17) and (3.26), in which it is shown that the probability of slot error for the retransmission case P_{serr} not only depends on the P_{se} but also on the average symbol length where symbols with a longer length will encounter higher probability of slot error per symbol.

3.6 Summary

The probability of errors for symbol retransmission with variable symbol length was evaluated. Detailed mathematical analysis was presented to derive the slot error probabilities for different retransmission rates. The analysis showed the dependencies of the error probability of retransmission schemes to the symbol error probabilities and average symbol length. The performance improves for higher retransmission rate, however longer symbol length significantly reduces the gain. A case study was provided for DH-PIM scheme to verify the analysis. The slot error probabilities for different retransmission rate were calculated using the mathematical analysis and Monte-Carlo

simulation. Computer simulation results show excellent match with the theoretical analysis confirming the results. A code gain of more than 2 dB can be achieved for a retransmission rate of 3 at P_{se} of 10^{-4} . Further code gain can be obtained if the retransmission rate is increased. Code gains of more than 3 dB and 4 dB have been obtained at P_{se} of 10^{-4} for retransmission of 4 and 5 respectively for all cases. Code gain also depends on the average number of slots per symbol. Hence, the code gain decreases with increases in the bit resolution. The code gain for DH-PIM₁ is about 0.2-0.3 dB less compared to the DH-PIM₂ for same bit resolution and P_{se} . Though analysis is verified only for the DH-PIM system, it is expected that it will equally be valid for all modulation techniques with variable length like DPPM and DPIM.

Chapter 4 Convolutional Code for Indoor Optical Wireless Communications

4.1 Introductions

Though the repetition code offers an improvement in the error performance, the penalty in terms of reduced throughput is huge. The challenge is to design an efficient code which can detect the maximum number of errors with a minimum overhead and complexity. A number of efficient codes which can broadly be classified into the linear block code and convolutional code exists in the literature. More recently, turbo code [200] and the LDPC [202] with performance close to the Shannon limit are extensively studied [203-206]. These codes can be applied to OOK and PPM modulation schemes with/without simple modifications due to fixed symbol boundaries [60-71]. The complexity arises when these codes need to be applied to variable symbol length modulation techniques. Linear block codes take a fix number of input bits and add redundant bits based on the predefined algebraic equations. Block codes are not suitable for the variable symbol length modulation techniques like DPIM and DH-PIM modulation schemes. The convolutional encoder which accepts a serial input can be applied to the modulation schemes with a variable symbol length. Though turbo codes are parallel concatenation of recursive systematic convolutional code [41], it cannot be applied to variable length modulation schemes as the turbo codes are essentially block codes due to the application of interleaver. Thus the use of convolutional codes is the best option.

4.2 Convolutional Code

The source information bit stream is generally independent and identically-distributed (IID) random data, thus it is not possible to check the validity of the received sequence. The concept of the error control code is to add redundant bits that are dependent on the information bits, where dependencies are exploited at the receiver to detect and correct

errors in the received codewords. In block codes k symbols are used to produce blocks of n symbols (where $n > k$). On the other hand, a convolutional code operates in continuous streams of data, hence is more suitable for variable length modulation schemes in indoor OWC systems. Convolutional code is the preferred option over the block codes in practice due to its performance superiority as well as using widely available soft decoding algorithms [201].

Convolutional codes are forward error control (FEC) codes. The convolutional encoder can be viewed as finite state machine consisting of M -stage shift register with prescribed connections to n modulo-2 adders. A k -bit input sequence applied to an encoder produces an n -bit output sequence and hence the code rate $r = k/n$. A typical $1/2$ rate encoder is shown in Figure 4.1. The input data to the encoder are shifted along a shift register of length M . The n -bit output of the modulo-2 adder is transmitted through the channel, where the transmitted bits sequence $\{x_{1k}\}$ and $\{x_{2k}\}$ are not independent but depend on a number of the n -bit input sequence. A symbol (K, n, k) is used throughout the thesis to represent a convolutional encoder with a code rate of k/n and constraint length $K = M + 1$.

The convolutional encoder can be represented by a generator representation, a tree diagram representation, a state diagram representation and the Trellis diagram representation. The generator representation shows the hardware connection of the shift register to the modulo-2 adder. A “1” represents a connection and a “0” represents no connection. The encoder in Figure 4.1 can be represented as:

$$\begin{aligned} g_1 &= [1 \ 1 \ 1] \\ g_2 &= [1 \ 0 \ 1]; \end{aligned} \tag{4.1}$$

where the subscripts 1 and 2 denote the corresponding output terminals.

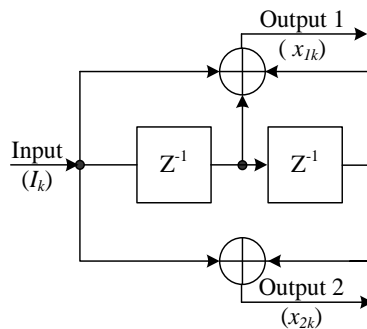


Figure 4.1: $1/2$ Convolutional code encoder.

The Trellis diagram is more popular and more instructive than a tree diagram. Since the convolutional code encoder is a finite state machine and the output of the encoder depends on the input and the state of encoder, it can also be represented by a state diagram. Considering the $\frac{1}{2}$ encoder shown in Figure 4.1, the shift registers can be in any of the four possible states: 00, 10, 01 and 11. The Trellis transition diagram and the state diagram of the $\frac{1}{2}$ encoder is given in Figure 4.2 and Figure 4.3, respectively. A dotted line in the graph indicates that the input bit is 1 and the solid line indicates that the input bit is 0.

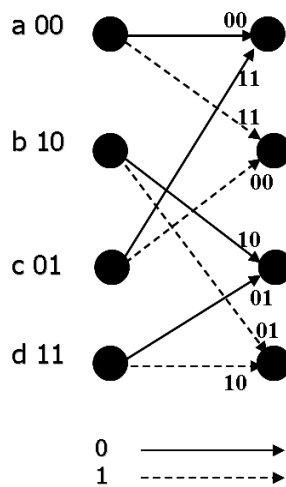


Figure 4.2: State Trellis diagram of an $\frac{1}{2}$ convolutional encoder.

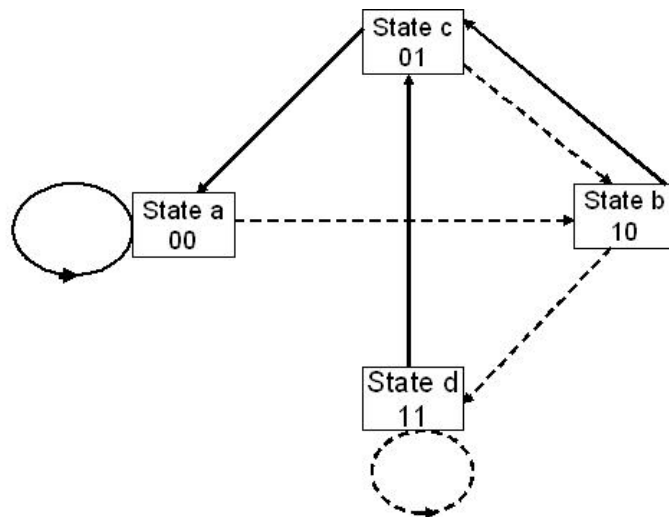


Figure 4.3: State diagram of an $\frac{1}{2}$ convolutional encoder.

4.2.1 The Transfer Function and Distance Properties of a Convolutional Code

The error correction capabilities of a convolutional code depend on the decoding method and on the Hamming distance properties. It is difficult to ascertain the exact error detection and correction capabilities of a convolutional code. However, indication can be obtained by the block code concept where the error correction capabilities depend on the minimum Hamming distance D_{hm} between the valid codewords [207]. D_{hm} can be stated from its tree diagram. Alternatively, the distance properties of a convolutional encoder can be obtained from the state diagram. For simplicity, the state diagram of Figure 4.3 is modified and given in Figure 4.4. The exponent of D on each branch gives the Hamming weight of the encoder output corresponding to those branches. The exponent of I is the Hamming weight of corresponding branch and the exponent of L is always equal to one as the length of each branch is one. Using the diagram, which consists of five nodes, the four state equations can be written as:

$$\begin{aligned} X_b &= D^2LIX_a + LIX_c \\ X_c &= DLX_b + DLX_d \quad ; \\ X_d &= DILX_b + DLIX_d \\ X_e &= D^2LX_c \end{aligned} \quad (4.2)$$

The transfer function of the code $T(D)$ is defined as $T(D)=X_e/X_a$. Solving (4.2) gives:

$$T(D, L, I) = \frac{D^5L^3I}{1 - DLI(1 + L)}. \quad (4.3)$$

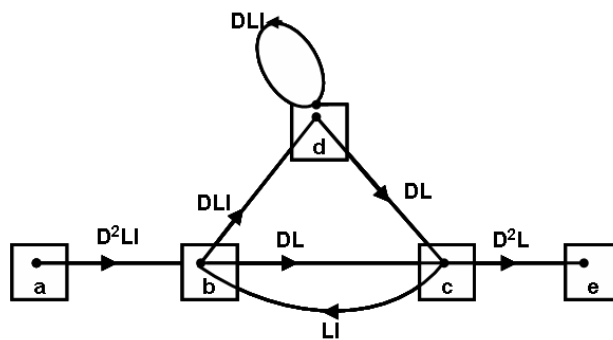


Figure 4.4: Modified state diagram.

Using the series expansion of $(1 - DLI(1 + L))^{-1}$, (4.3) leads to:

$$T(D, L, I) = D^5L^3I + D^6L^4I^2(1 + L) + D^7L^5I^2(1 + L)^2 + \dots \quad (4.4)$$

From (4.4) one can make the following observation on the Trellis diagram [207].

1. There is no path at a distance of 0, 1, 2, 3 or 4 from the all zero path.
2. There is a single path that has a distance of 5 from the all zero path. It differs from the all zero path in one input bit and converges to the all zero path in the third branch (L^3).
3. There are two paths having a distance of 6. Both of them differ from the all zero path by two inputs (I^2) and one converges to the all zero path in the fourth (L^4) branch and the other in fifth branch (L^5). And so on.

So D_{hm} of the above mentioned encoder is five, which means that the two errors in the received sequences are correctable. A problem with the convolutional coding is the possibility of errors propagation, which may lead to catastrophic error propagation unless the encoder state transition is chosen properly. If there is another state apart from state zero, having a zero-weight returning loop, a finite number of errors could be translated to infinite number of decoding errors, causing catastrophic error propagation [179, 208].

4.2.2 Optimum Decoding of a Convolutional Code - the Viterbi Algorithm

Since the convolutional encoder is a finite-state machine, the optimum decoder is the maximum likelihood sequence estimator. The convolutional code can be decoded by choosing a path in the code tree whose code sequence differs from the received sequence in the fewest number of places. Equivalently, one can use the Trellis representation. The Viterbi algorithm utilizes the Trellis diagram to compute the path metrics [209]. A metric for a particular path is defined as the Hamming distance between the coded sequence represented by that path and the received sequence. At each node the path having lower metric is retained and the other path is discarded. The paths that are retained are called the survivors. If both paths entering a node have the same metrics, either of them is chosen randomly. The Viterbi algorithm can be summarized as [209]:

- 1) Starting at level $j = M$, where $M = K-1$ is the encoder memory, compute the metric for each path entering the state and store the survivor path and its metric for each state.
- 2) Increment j by 1. Compute the metric for all the paths entering each state by adding the metric of the incoming branches to the metric of the connecting from the survivor. Store the path and metric having the lower metric.
- 3) If level $j < L+M$, where M is the length of incoming message, repeat step 2. Otherwise stop.

4.2.3 Performance of Convolutional Codes

To determine the probability of error for the convolutional code, without loss of generality it is assumed that all input bits are zero. Consider a node with a Hamming distance of d . If d is odd, the path can correct $\frac{1}{2}(d+1)$ number of errors, otherwise incorrect path will be selected. Therefore, the probability of selecting incorrect path is [179]:

$$P(d) = \sum_{k=(d+1)/2}^d \binom{d}{k} p^k (1-p)^{d-k} ; \quad (4.5)$$

where p is the probability of occurrence of error in a bit. If d is even, incorrect path is selected when the number of errors is greater than $d/2$. If the number of errors is $d/2$, there is $1/2$ probability of selecting the incorrect path. So the probability of selecting incorrect path is:

$$P(d) = \sum_{k=d/2+1}^d \binom{d}{k} p^k (1-p)^{d-k} + \frac{1}{2} \binom{d}{0.5d} p^{d/2} (1-p)^{d/2} . \quad (4.6)$$

The upper bound for the bit error probably P_{se-CC} for the convolutional code is given by [179]:

$$P_{se-CC} < \sum_{d=d_{free}}^{\infty} \beta_d P(d) ; \quad (4.7)$$

where β_d is the coefficients of expansion of derivative of $T(D,I)$, evaluated at $I = 1$.

Using (4.7) the upper bound for (3, 1, 2) encoder described above is given by:

$$P_{se-CC} < \sum_{d=5}^{\infty} 2^{(d-5)}(d-4)P(d) . \quad (4.8)$$

Instead of using (4.5) and (4.6) for the $P(d)$, one can use the upper bound $P(d) < [4p(1-p)]^{1/2}$ and the expression for upper bound P_{se-CC} is given by [179, 207]:

$$P_{se-CC} < \left. \frac{\partial T(D,I)}{\partial I} \right|_{I=1, D=\sqrt{4p(1-p)}} . \quad (4.9)$$

Substituting the derivative of (4.4) into (4.9) results in:

$$P_{se-CC} < \sum_{d=5}^{\infty} 2^{(d-5)}(d-4) \left(\sqrt{4p(1-p)} \right)^d . \quad (4.10)$$

One of the attractive features of convolutional coding is that soft decisions could be used. All above derivatives are valid for hard decisions. A further 2.5 dB is gained for $10^{-6} < P_b < 10^{-2}$ when soft decision is employed .

4.3 Convolutional Coded DH-PIM

The system block diagram of the convolutional coded DH-PIM_T (CC-DH-PIM_T) scheme is given in Figure 4.5. The block diagram differs from Figure 2.10 as a convolutional encoder and the Viterbi decoder are implemented at the transmitter and the receiver respectively. The DH-PIM_T sequence $\{b_i\}$ is applied to the convolutional encoder to generate a coded sequence $\{b_{ci}\}$. The CC-DH-PIM symbol b_{ci} is passed through a transmitter filter $p(t)$, scaled by the peak detected signal photocurrent

$\bar{L}_{DH-PIM}P_{avg}$. AWGN $n(t)$ is added to the transmitted signal $s(t)$ before being detected by a photodetector at the receiver. The output of the optical receiver $z(t)$ is applied to a matched filter $r(t)$, followed by sampler and a threshold detector to regenerate the coded DH-PIM sequence \hat{X}_c . Detail descriptions of each block of transmitter and receiver for DH-PIM are given in Chapter 2, Section 2.8.1.3. A ‘hard’ decision Viterbi decoder is applied $\{\hat{b}_{ci}\}$ to estimate the non-coded DH-PIM symbol sequence \hat{b}_i .

When DH-PIM $_{\Gamma}$ sequence is fed into a (3, 2, 1) convolutional encoder with the state diagram shown in Figure 4.1, an exclusive pattern is generated because of the unique header patterns followed by a number of empty slots. For illustration purposes, DH-PIM $_2$ is taken and the symbol structure of DH-PIM $_2$ is given in Table 4.1. A DH-PIM $_2$ symbol is composed of one of two headers $H_0 = [100]$ and $H_1 = [110]$, followed by a number of empty slots corresponding to the decimal value of the input bit sequence [25]. H_0 and H_1 will produce new header sequences of [11 10 11] and [11 01 01], respectively provided that the encoder initial state is ‘a’. The encoder is normally at state ‘a’ after each symbol since there are two zeros at the end of each DH-PIM $_{\Gamma}$ symbol except for the symbol with a decimal equivalent of $2^M - 1$. For symbols with the decimal equivalent of $2^M - 1$, after a symbol is being generated, the encoder will be in the state ‘c’ and a different header patterns of [00 10 11] and [00 01 01] will be assigned to the current symbol, as symbols follow either path 3 or 4 in the Trellis diagram in Figure 4.6. Thus, CC- DH-PIM $_{\Gamma}$ symbols with four headers and a limited number of possible paths will have different transfer function and error probability, which is investigated in the following Section.

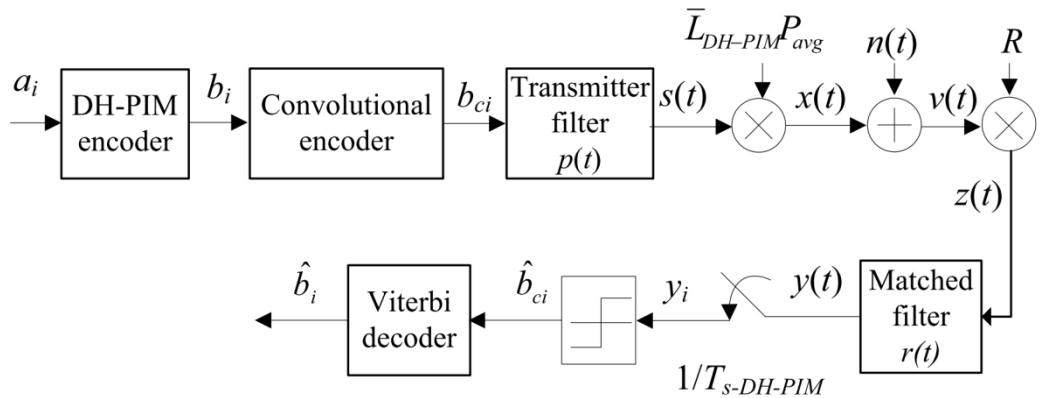


Figure 4.5: A block diagram of convolutional coded DH-PIM scheme.

Table 4.1: The binary data, coded and uncoded DH-PIM₂ for $M = 3$, and $\Gamma = 2$.

Binary data ($M = 3$)	DH-PIM ₂	CC-DH-PIM ₂	CC-DH-PIM ₂ preceded by 2^M-1
000	100	11 10 11	00 10 11
001	100 0	11 10 11 00	00 10 11 00
010	100 00	11 10 11 00 00	00 10 11 00 00
011	100 000	11 10 11 00 00 00	00 10 11 00 00 00
100	110 000	11 01 01 11 00 00	00 01 01 11 00 00
101	110 00	11 01 01 11 00	00 01 01 11 00
110	110 0	11 01 01 11 00	00 01 01 11
111	110	11 01 01	00 01 01

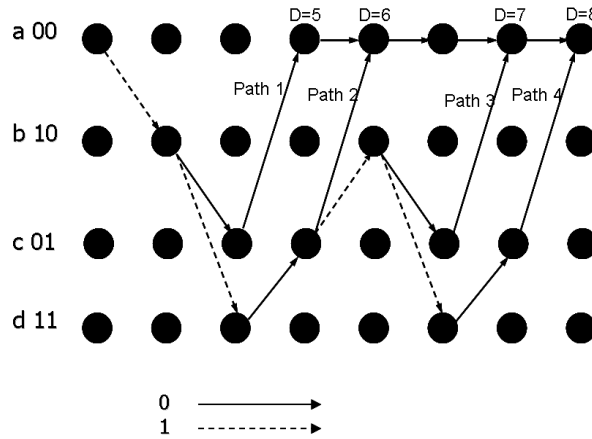


Figure 4.6: Trellis diagram of CC-DH-PIM₂.

4.3.1 Error Bound for CC-DH-PIM

As mentioned above, because of the unique header pattern, it is not difficult to verify that there is no state transition going via loop of state ‘ d ’ in Figure 4.4. So the state diagram of Figure 4.4 needs to be modified to Figure 4.7. One can observe that the two state diagrams are very similar except the self-loop at the state ‘ d ’ is not present in the modified state diagram. As the consequence, the signal flow equations are modified into the followings:

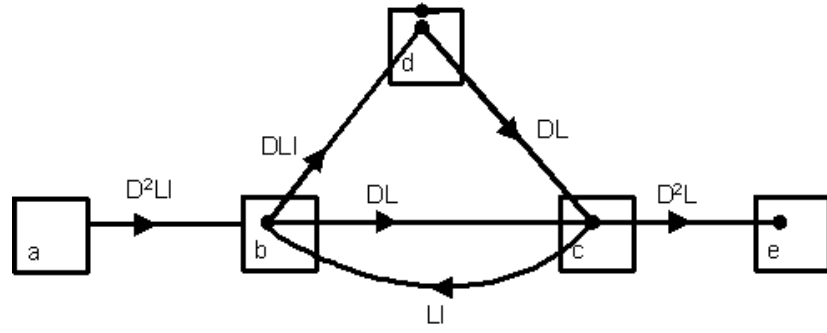


Figure 4.7: Modified state diagram for CC-DH-PIM

$$\begin{aligned}
 X_b &= D^2LIX_a + LIX_c \\
 X_c &= DLX_b + DLX_d \\
 X_d &= DILX_b \\
 X_e &= D^2LX_c.
 \end{aligned} \tag{4.11}$$

Solving the above equations results in the following transfer function:

$$T(D, L, I) = \frac{D^5L^3I(1 + DLI)}{1 - DL(1 + DLI)}. \tag{4.12}$$

The upper error bound also needs to be modified according to the transfer function and the modified upper bound is given by:

$$P_{se-CC} < P(5) + 4P(6) + 9P(7) + 20P(8); \tag{4.13}$$

where $P(d)$ is given by (4.6) and (4.7).

4.3.2 SER Performance of CC-DH-PIM

The comparative studies of upper error bounds (given by (4.8) and (4.10) for a general convolutional encoder and (4.13) for CC-DH-PIM_Γ) can be a good measure to find the effectiveness of convolutional code for DH-PIM_Γ. Figure 4.8 shows the predicted SER performance against the SNR for (4.8), (4.10) and (4.13) for 16-DH-PIM₂. For an SER $\leq 10^{-6}$, the upper bound for CC-DH-PIM_Γ and the general upper bound almost overlap, diverging at lower values of SNR. Since the upper bound for CC-DH-PIM_Γ is always

less than or equal to the upper bound for its counterparts, it is expected that it should give similar or even improved SER performance compared to the other convolutional coded modulation schemes such as OOK for the same value of uncoded SER. This is because CC-DH-PIM_Γ has fixed header patterns that limit the number of possible paths in the Trellis diagram. As a result, the expansion coefficient β_d of (4.7) is different for the CC-DH-PIM_Γ. The coefficients of 3rd and 4th terms of (4.10) and (4.13) are (12, 32) and (9, 20), respectively. Although the first two terms are the dominating terms in determining the error bound at lower SER values, the contribution of other terms cannot be neglected for higher SER values. Hence, the error bounds (4.10) and (4.13) will have noticeable differences at higher uncoded SER values. In other words, as the number of possible paths decreases, the probability of error decreases. This is because there is only a finite set of paths to choose from, thus making the decoding process much simpler.

For DH-PIM_Γ scheme, a (3, 1, 2) convolutional encoder and the Viterbi algorithm with the ‘hard’ decoding is utilized. Assuming an ideal channel with single-sided PSD $N_0 = 2qI_B$ and $I_b = 200 \mu\text{A}$, the proposed CC-DH-PIM_Γ system is simulated using Matlab. The simulation parameters used and the flow chart for determining the error rates for the CC-DH-PIM are given in Table 4.2 and Figure 4.9, respectively.

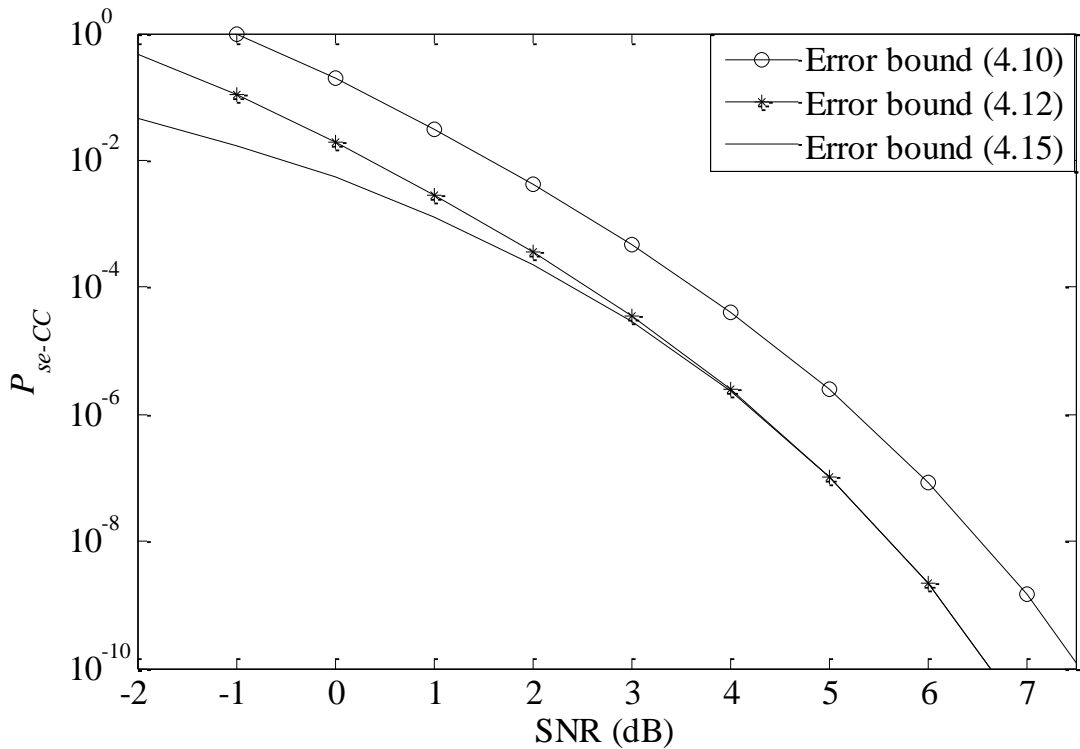


Figure 4.8: The SER against the SNR for different error bounds for CC-DH-PIM₂.

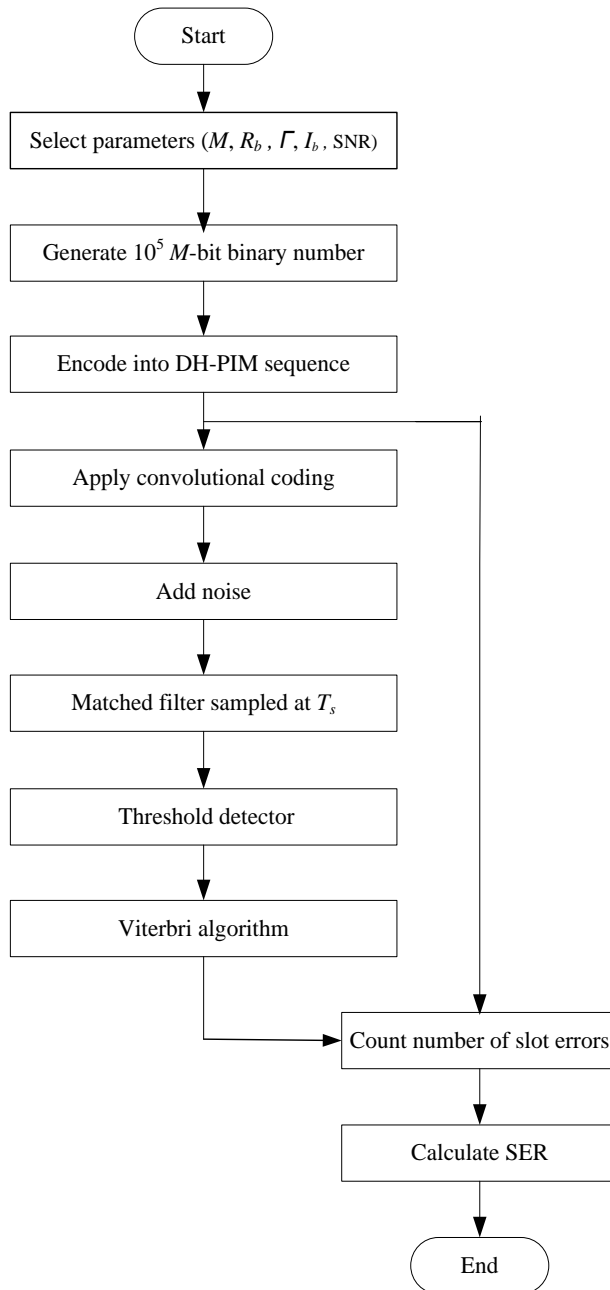


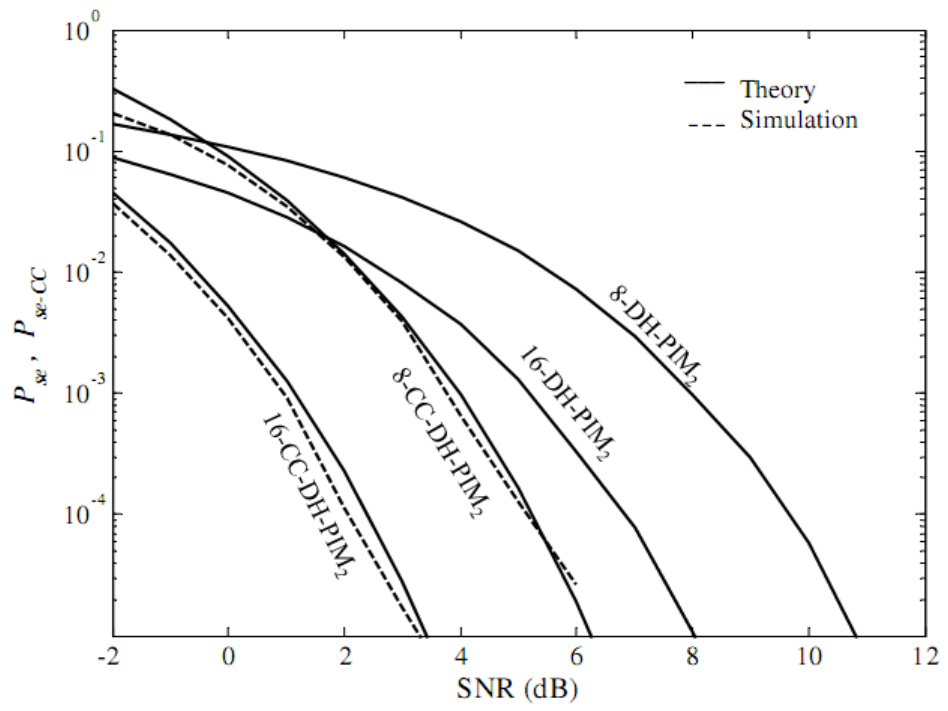
Figure 4.9: A flow chart diagram for determining the SER of the CC-DH-PIM system.

Table 4.2: The simulation parameters for CC-DH-PIM $_{\Gamma}$.

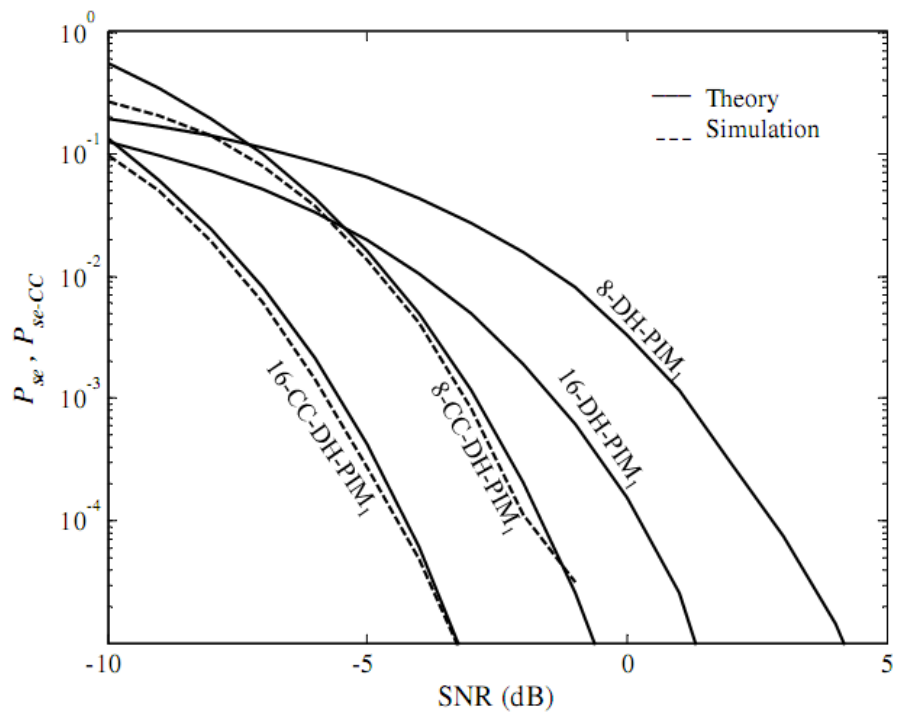
Parameters	Values
M	3 and 4
Γ	1 & 2
Detector responsivity R	1 A/W
Background noise current I_b	200 μ A
Threshold level k	0.5
Pulse duty cycle	100 %

Figure 4.10 provides the predicted and simulated results for SER performance for the standard DH-PIM_{1&2} and CC-DH-PIM_{1&2} schemes for $M = 3$ and 4. For $P_{se} < 10^{-2}$ the predicted and simulated curves for the CC-DH-PIM_Γ match each other reasonably well. Since it is somewhat difficult to ascertain the exact Hamming distance for the convolutional code in the theoretical analysis, only the upper bound is considered. The simulated SER performance is very close to the upper bound, but is always less than or equal to it. The code gain decreases with the SNR and at very low values of SNR (or SER > 0.1) the code gain is negative. At higher values of SER, introducing coding contributes to more correlated errors from the uncorrelated random errors [210], thus giving rise to additional errors and hence degrading the error performance. A code gain of more than 4 dB is observed for P_{se} of 10^{-4} compared to the standard DH-PIM₂ scheme for $M = 3$ and 4, respectively. To achieve a certain SER, the SNR required decreases as M increases. This is expected since the SER of uncoded DH-PIM scheme decreases with M [112]. A difference of almost ~3 dB in the SNR is observed at the P_{se} of 10^{-4} for M of 3 and 4. Similarly in the case of DH-PIM₁ scheme, a code gain of more than ~4 dB is observed at a SER of 10^{-4} .

Detailed comparison of the SER performance of the standard DH-PIM_Γ with other modulation schemes is given in [112]. Here the comparison of the CC-DH-PIM_Γ (upper bound) to the standard DH-PIM_Γ and PPM schemes is made, see Figure 4.11. CC-DH-PIM₁ offers the best performance compared to the uncoded PPM and DH-PIM₁, as expected. However, the Trellis coded PPM scheme does outperform all other coded modulation schemes including the CC-DH-PIM₁. It is expected that the coded PPM offers the least optical power requirement compared to the uncoded PPM. The performance of 16-CC-DH-PIM₂ is very close to that of the standard 16-DH-PIM₁. The SER of the 16-CC-DH-PIM₂ runs almost parallel to the standard 16-DH-PIM₁, 16-CC-DH-PIM₂ requiring just more than 0.5 dB of SNR to achieve the same SER performance. To achieve a SER of 10^{-6} , 16-CC-DH-PIM₁ requires ~5 dB lower SNR compared to the standard DH-PIM₁, while 16-DH-PIM₂ requires ~4 dB more SNR compared to the 16-CC-DH-PIM₂. The reduction in SNR means a reduction in the transmitted power to achieve the same error probability. Note that a reduction of 3 dB in SNR is equivalent to half the transmitter power. The gain in SNR could be used to increase the link length or trade for performance.



(a)



(b)

Figure 4.10: The theoretical and simulation SER versus the SNR for: (a) standard 8 & 16-DH-PIM₂ and 8 & 16-CC-DH-PIM₂, and (b) standard 8 & 16-DH-PIM₁ and 8 & 16-CC-DH-PIM₁.

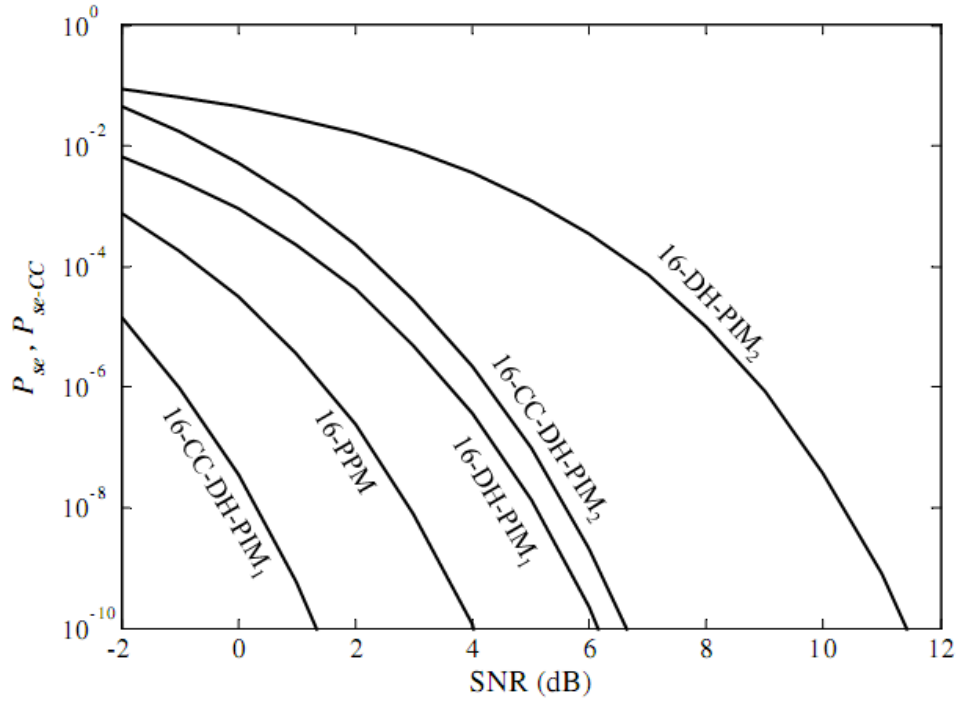


Figure 4.11: The theoretical SER against the SNR for 16-PPM and coded and uncoded DH-PIM_{1&2}.

The performance of the CC-DH-PIM _{Γ} system can further be enhanced by increasing the constraint length, which results in increased code gain but at the cost of increased system complexity. Thus, there exists a trade-off between complexity and performance. A $\frac{1}{2}$ rate convolutional encoder with a constraint length of 7, which are readily available, is used to assess the performance of different CC-DH-PIM _{Γ} systems. Simulated P_{se} performance of 16-CC-DH-PIM _{Γ} with a generator of (133, 171) in octal number is depicted in Figure 4.12. Also shown for comparison is P_{se} of 16-DH-PIM _{Γ} and 16-CC-DH-PIM _{Γ} . The best SER performance is observed for CC-DH-PIM _{Γ} with a constraint length K of 7 for $P_{se} \leq 10^{-2}$. At $P_{se} = 0.005$, P_{se} curves of CC-DH-PIM _{Γ} with K of 3 and 7 intersect, indicating no code gain with higher values of constraint length. However, at $P_{se} \leq 10^{-3}$, there is a marked improvement in the performance when using a longer constraint length. An additional ~ 2 dB code gain can be achieved at an SER of 10^{-5} using an encoder with $K = 7$ compared to the encoder with $K = 3$. This additional code gain can be used to increase the link range in indoor OWC system.

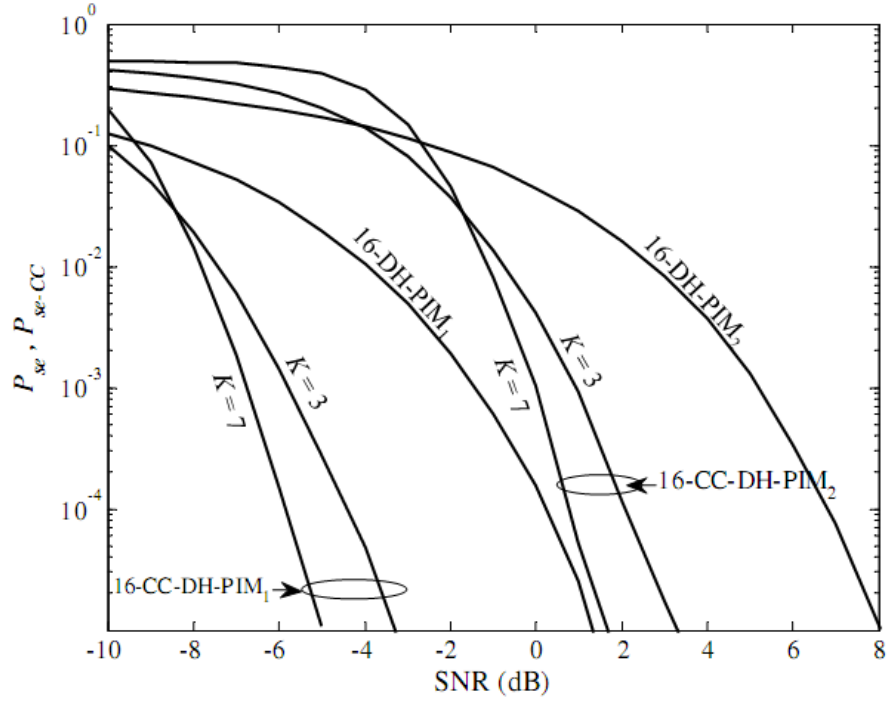


Figure 4.12: The SER against SNR for 16-CC-DH-PIM_Γ with constraint lengths of 3 and 7.

4.4 Convolutional Coded DPIM

DPIM is a pulse time modulation technique with variable symbol length like DH-PIM_Γ. Unlike DH-PIM_Γ, DPIM symbols have no header patterns and hence the error bounds given by (4.8) and (4.10) can be used for theoretical analysis. A block diagram of typical convolutional coded DPIM (CC-DPIM) scheme is given in Figure 4.13. Notice the similarities in the block diagram of the convolutional coded DH-PIM and DPIM. The DPIM sequence $\{b_i\}$ is applied to the convolutional encoder to generate coded sequence $\{b_{ci}\}$. The $\{b_{ci}\}$ is applied to the transmitter filter and scaled by $\bar{L}_{DPIM}P_{avg}$ before transmitted through a channel. At the receiver, a Viterbi decoder is applied to $\{\hat{b}_{ci}\}$ to estimate the transmitted DPIM sequence $\{\hat{b}_i\}$.

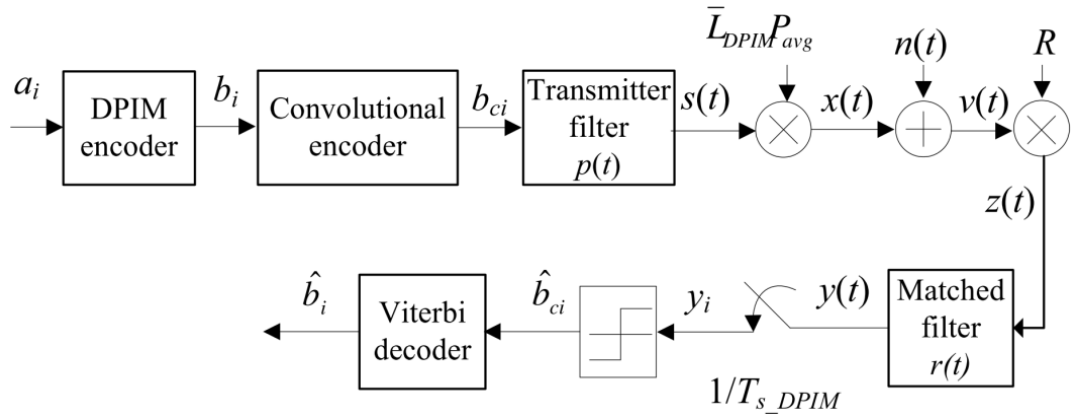


Figure 4.13: A block diagram of convolutional coded DPIM scheme.

4.4.1 SER Performance of CC-DPIM

Unlike DH-PIM_Γ, DPIM does not have a unique header pattern and hence the upper bound given by (4.10) can be used to estimate the error probability of coded system. The theoretical analysis and simulation results of probability of slot error for 16-CC-DPIM for guard bands of 0, 1 and 2 is given in Figure 4.14. Because most of symbols have at least two empty slots at the end of the symbol, the memory is cleared and hence a Hamming distance of 5 is the dominating term in calculating the upper bounds. Hamming distances of 6 and 7 have effects on the performance when P_{se} is low. Hamming distances higher than 7 have very small effects, therefore, only the first three terms of the expansion of (4.10) are taken into account when calculating the upper bound.

Because of the difficulty to ascertain an exact Hamming distance for convolutional coding, there is no simple exact expression for the first-event error probability and union bound given by (4.10) needs to be utilised for theoretical calculations and thus, the error bound is the only method to judge the performance of a convolutional encoder. Computer simulation is expected to produce P_{se} close to but less than the upper bound. The simulation results and the theoretical upper bound for the SER of 16-CC-DPIM for $M = 4$ are in close match with difference of less than 0.5 dB for all cases. As expected, DPIM with 2 GS displays the best performance requiring ~ 0.5 dB and ~ 1 dB lower SNR compared to the CC-DPIM with 0 and 1 GS at $P_{se} = 10^{-4}$, respectively as uncoded DPIM(2GS) also outperforms the DPIM(0GS) and DPIM(1GS).

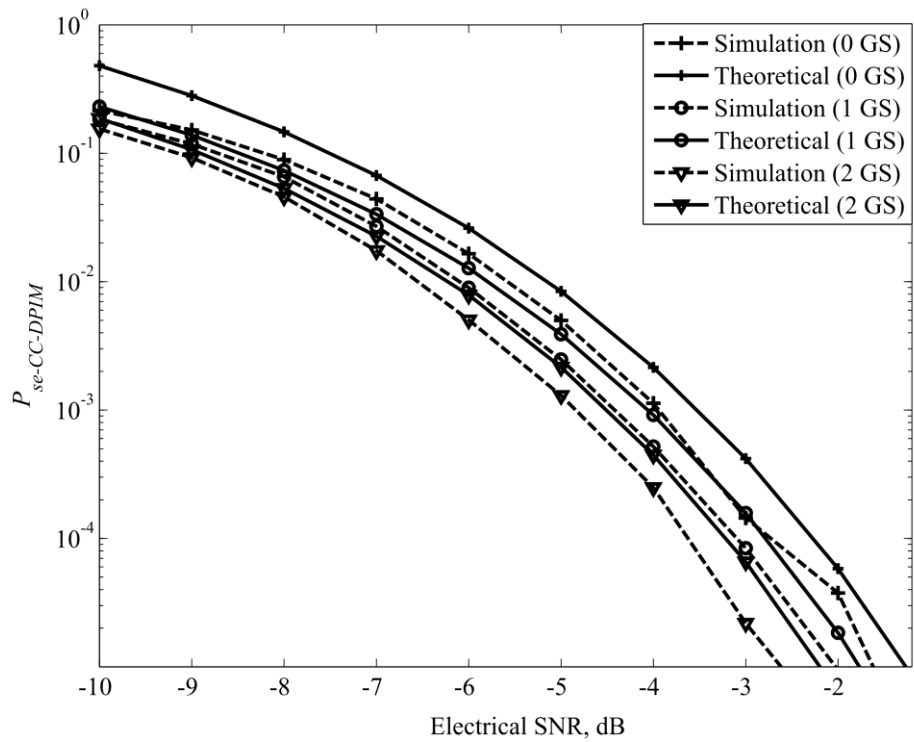


Figure 4.14: The theoretical upper bound and simulation SER against the electrical SNR for 16-CC-DPIM with 0, 1 and 2 guard slot.

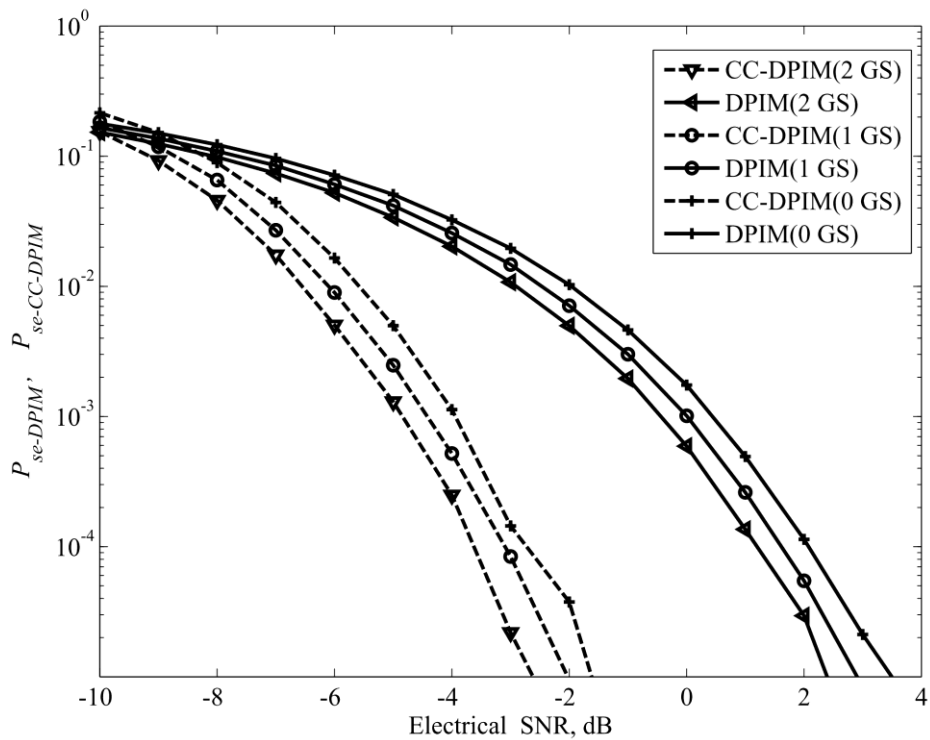


Figure 4.15: The simulated SER against electrical SNR for uncoded (standard) and coded 16-DPIM with 0, 1 and 2 GS.

Applying convolutional coding to the DPIM system improves the performance of system by reducing the SNR required to achieve certain SER. Figure 4.15 compares the SER performance of uncoded and coded 16-DPIM. CC-DPIM gives a code gain of ~ 4 dB at $P_{se} = 10^{-4}$ compared to the standard DPIM for all guard slots. At $P_{se} = 10^{-4}$, CC-DPIM (2 GS) requires only SNR of 3.6 dB, ~ 0.5 dB and ~ 1 dB less compared to the uncoded DPIM(2GS), CC-DPIM(1GS) and CC-DPIM(0GS), respectively.

The effects of changing the bit resolution M on the slot error rate performance of CC-DPIM is depicted in Figure 4.16. CC-DPIM shows code gains of ~ 5 and ~ 4.4 dB for $M = 5$ and 3, respectively, compared to the uncoded DPIM. At $P_{se} < 10^{-2}$, 8 and 16-CC-DPIM outperform the uncoded 16 and 32-DPIM with a code gain of ~ 2 dB and ~ 1 dB at P_{se} of 10^{-4} , respectively. At lower values of P_{se} , 16-CC-DPIM outperforms the standard 32-DPIM.

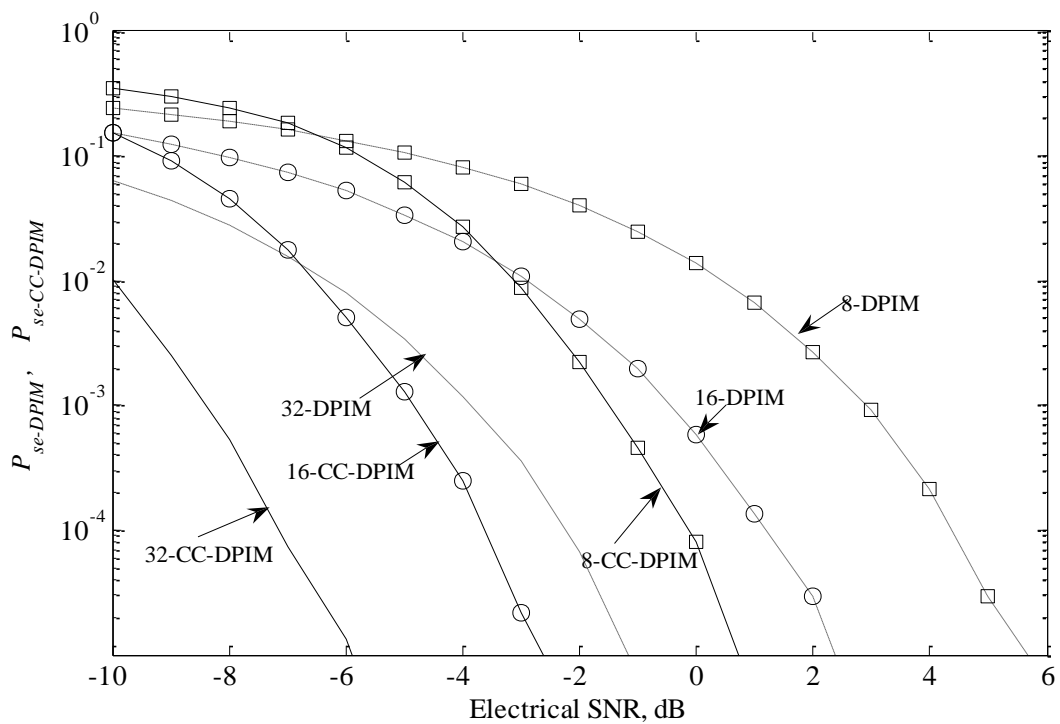


Figure 4.16: The SER against the electrical SNR for 8, 16 & 32 DPIM and 8, 16 & 32-CC-DPIM.

4.5 Summary

In this chapter, the mathematical analysis and simulation results for $\frac{1}{2}$ rate convolutional code with an (3, 1, 2) encoder was studied for DPIM and DH-PIM_r. The analysis for the DH-PIM employing the Viterbi 'hard' decision decoding was presented. Because the CC-DH-PIM has only finite paths in the Trellis diagram, the upper bound for error probability was modified. Simulation results were compared with the modified error bound for the CC-DH-PIM showed a good match indicating that the mathematical analysis was correct. CC-DH-PIM provided an improvement in the system performance and a code gain of more than 4 dB was achieved for SER of less than 10^{-4} compared to the uncoded DH-PIM for $M = 3$ and 4, respectively. At higher SER, there was a negative code gain, suggesting unworthiness of applying error control coding for very noisy channel. As SER decreases, the code gain also improves and at a very low SER, the curve of SER verses SNR for coded and uncoded DH-PIM runs parallel. It was observed that 16-CC-DH-PIM₁ can outperform 16-PPM but the Trellis coded PPM is the best in term of SNR required achieving desired SER. A further improvement in system performance was realized using encoder of a constraint length of 7. The (7, 1, 2) CC-DH-PIM showed improved performance than the (3, 1, 2) at the cost of system complexity. The improvement in the error performance of course was achieved at the cost of the reduced transmission throughput compared with the uncoded case. Similar improvement for the DPIM was also observed for different guard slots. A code gain of more than 4 dB was observed in all cases when convolutional code was applied to DPIM. CC-DPIM(2GS) showed improved SER performance over CC-DPIM(0GS) and CC-DPIM(1GS).

Chapter 5 Artificial Light Interference and Discrete Wavelet Transform based Denoising

5.1 Introductions

The error control codes reduce the bit error probability in the presence of AWGN. However, in addition to the AWGN, periodic and deterministic form of noise due to the artificial light sources also exists in indoor optical wireless channels. ALI has potential to degrade the performance severely. Fluorescent lamps emit strongly at a spectral band of 780–950 nm overlapping with cheap optical transceiver components. Electronic ballasts driven fluorescent lamps have electrical spectrum contents that range up to MHz making such lamps potentially serious impairment to IR links [43, 79, 80].

The potential solution to reduce the effect of the fluorescent light interference (FLI) is to use a high pass filter (HPF). Selections of modulation techniques also affect the link performance in presence of FLI [78]. The modulation scheme like PPM with a low spectral content at or near DC level provides immunity to the FLI. On the other hand, OOK with a high spectral content near the DC region is more likely to be affected by the FLI and the power penalty without HPF would be much higher. Digital HPFs provide improved performance compared to its analogue counterpart. However, the HPF filter introduces another type of ISI known as the BLW that mainly affect modulation techniques with strong frequency components near the DC region [80, 91]. In this chapter, an alternative approach to HPF based on the discrete wavelet transform (DWT) is introduced. Using the DWT, the signal is separated into different frequency bands to ensure that interference and modulating signals are effectively separated. Band of frequencies corresponding to the interference are removed from the signal and hence the reconstructed signal in theory can be free from FLI. Since the spectral content of the FLI and the modulating signal overlaps for baseband modulation schemes, there would

certainly be a power penalty compared to the ideal channel. It is expected that the power penalty corresponding to the signal with a low DC component would be much lower. Hence three modulation techniques; OOK, PPM and DPIM are studied and their power penalties due to FLIs are simulated when employing the DWT.

5.2 Artificial Light Interference and Performance without Filtering

The background radiation both from the artificial and natural light can cause serious performance degradation in indoor OW links. A number of artificial light sources have different interfering patterns. The incandescent lamps produce almost perfect sinusoidal interference at the harmonics of 100 Hz. The fluorescents lamps produce a periodic interference and its characteristics depend on the type of the lamp [78-80]. The fluorescent lamps driven by conventional ballasts are distorted harmonics and have spectral components at multiples of the 50 Hz extending up to 20 kHz. The interference produced by fluorescent lamps driven by electronic ballasts pose the most severe problem as the interfering harmonics extend up to 1 MHz.

Fluorescent lamps driven by electronic ballasts can be modelled using a high frequency $m_{high}(t)$ and a low frequency $m_{low}(t)$ components of the photocurrent at the receiver. Thus, the zero mean periodic photocurrent $m_{fl}(t)$ due to the fluorescent lamp is given as [77, 79]:

$$m_{fl}(t) = m_{low}(t) + m_{high}(t); \quad (5.1)$$

where

$$m_{high}(t) = \frac{I_B}{A_2} \sum_{j=1}^{22} \Gamma_j \cos(2\pi f_{high} j t + \theta_j); \quad (5.2)$$

$$m_{low}(t) = \frac{I_B}{A_1} \sum_{i=1}^{20} [\Phi_i \cos(2\pi(100i - 50)t + \varphi_i) + \Psi_i \cos(2\pi 100i t + \phi_i)]; \quad (5.3)$$

where Φ_i and Ψ_i are the amplitudes of the odd and even harmonics of 50 Hz mains signal, respectively, Γ_j and θ_j are the amplitude and phase of the harmonics, f_{high} is the electronic

ballast switching frequency, A_2 is the constant relating the interference amplitude to I_B . For detailed description and parameter values refer to [79]. The typical values for m_{low} and m_{high} are given in Table 5.1 and Table 5.2. For the f_{high} of 37.5 kHz, there are 750 cycles of high frequency component per cycle (20 μ S) of the low frequency component. With I_B set at 2 μ A, one complete cycle of the low frequency component and three complete cycles of high frequency components of the interference photocurrent are shown in Figure 5.1.

Table 5.1: Low frequency component phase values.

i	ϕ_i (rad)	ϕ_i (rad)	i	ϕ_i (rad)	ϕ_i (rad)
1	4.65	0	11	1.26	6.00
2	2.86	0.08	12	1.29	6.17
3	5.43	6.00	13	1.28	5.69
4	3.90	5.31	14	0.63	5.37
5	2.00	2.27	15	6.06	4.00
6	5.98	5.70	16	5.49	3.69
7	2.38	2.07	17	4.45	1.86
8	4.35	3.44	18	3.24	1.38
9	5.87	5.01	19	2.07	5.91
10	0.70	6.01	20	0.87	4.88

Table 5.2: High frequency component amplitude and phase values.

J	Γ_j (dB)	θ_j (rad)	j	Γ_j (dB)	θ_j (rad)
1	-22.2	5.09	12	-39.3	3.55
2	0	0	14	-42.7	4.15
4	-11.5	2.37	16	-46.4	1.64
6	-30.0	5.86	18	-48.1	4.51
8	-33.9	2.04	20	-53.1	3.55
10	-35.3	2.75	22	-54.9	1.78

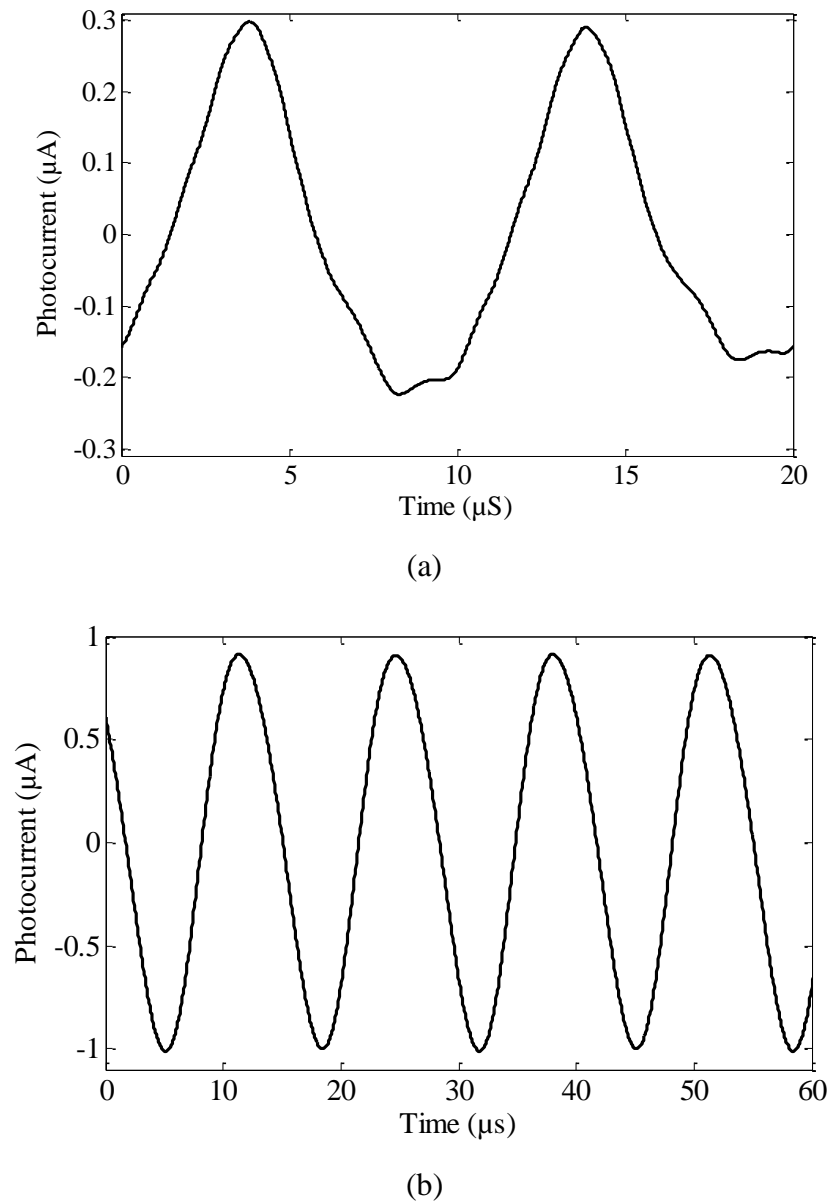


Figure 5.1: (a) Low frequency interference component, and (b) high frequency interference component.

5.2.1 Performance of OOK without Filtering

In this section, the performance of OOK is analysed in the presence of FLI without any filtering. The block diagram of the OOK system under consideration is shown in Figure 5.2. A matched filter based receiver is considered here without any form of filtering. The matched filter based OOK system for indoor OWC is described in Section 2.8.1.1. The difference here lies in the channel noise. In addition to signal independent shot noise $n(t)$, the fluorescent light induced photocurrent $m_{fl}(t)$ is also added to the modulated signal.

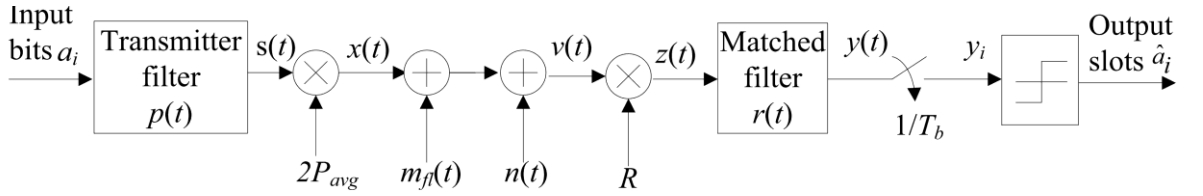


Figure 5.2: Block diagram of the OOK system.

Considering a linear system, the bit error probability of OOK P_{be_OOK} in the presence of the FLI can be calculated by separately treating the FLI and modulating signal at the input to the matched filter. The sampled output at the output of the matched filter due to the OOK signal is $2RP_{avg}\sqrt{T_b}$ for binary ‘1’ and 0 for binary ‘0’. The output of the matched filter due to the FLI signal, sampled at the end of each bit period, is given as [80]:

$$m_k = m_{fi}(t) \otimes r(t) \Big|_{t=kT_b}. \quad (5.4)$$

Since the interfering signal is periodic, the error probability can be estimated by calculating P_{be_OOK} over the period of interference and averaging over the periods [78]. By considering every slot over a 20 ms interval (i.e. one complete cycle of $m_{fi}(t)$) and averaging, the P_{be_OOK} in the presence of the AWGN is given by [51, 80]:

$$P_{be_OOK} = \frac{1}{N} \sum_{k=1}^N Q \left(\frac{RP_{avg}\sqrt{T_b} + m_k}{\sqrt{N_0/2}} \right) + Q \left(\frac{RP_{avg}\sqrt{T_b} - m_k}{\sqrt{N_0/2}} \right); \quad (5.5)$$

where N is the total number of bits over a 20 ms interval.

For the comparisons of different modulation schemes under different channel conditions, the optical power penalty (OPP) and normalized optical power requirement (NOPR) are considered here. Let the desired (bit or slot) error probability for the system be ξ , then OPP and NOPR are defined as:

- (a) **Normalized optical power requirement (NOPR):** The NOPR of a system is calculated by normalising the optical power required to achieve the error probability of ξ in the interfering channel with that of OOK system at 1 Mbps in an ideal AWGN channel without interference,

$$\text{NOPR} = \frac{\text{Optical power required to achieve } \xi}{\text{Optical power required to achieve } \xi \text{ for OOK @1 Mbps in ideal channel}} \quad (5.6)$$

(b) **Optical power penalty (OPP):** The OPP of a system is calculated by normalising the optical power required to achieve the error probability of ξ in the interfering channel with that of ideal AWGN channel without interference (other system parameters like the modulation type, bit rate remains the same),

$$\text{OPP} = \frac{\text{Optical power required to achieve } \xi}{\text{Optical power required to achieve } \xi \text{ in an ideal AWGN channel}} \quad (5.7)$$

In this study, the error probability of 10^{-6} is taken as standard and used in all the calculation of OPP and NOPR hereafter.

The performance of OOK system with a matched filter in the presence of the FLI is simulated. The NOPR and OPP against the data rates are given in Figure 5.3. Also shown is the NOPR for OOK in the absence of interference. The NOPR in absence of the interference increases linearly with the logarithm of data rates (note the logarithmic scale in X-axis). However, NOPR in the presence of the FLI are almost constant for the all data rates with a variation of < 1 dB. Since the FLI is the dominating factor of the interference, the bit error probability is governed by the photocurrent due to the FLI and hence results in very high OPPs. The OPP for data rates of 1, 10, 100 and 200 Mbps in presence of FLI are 16.6, 11.6, 7.1 and 6 dB, respectively.

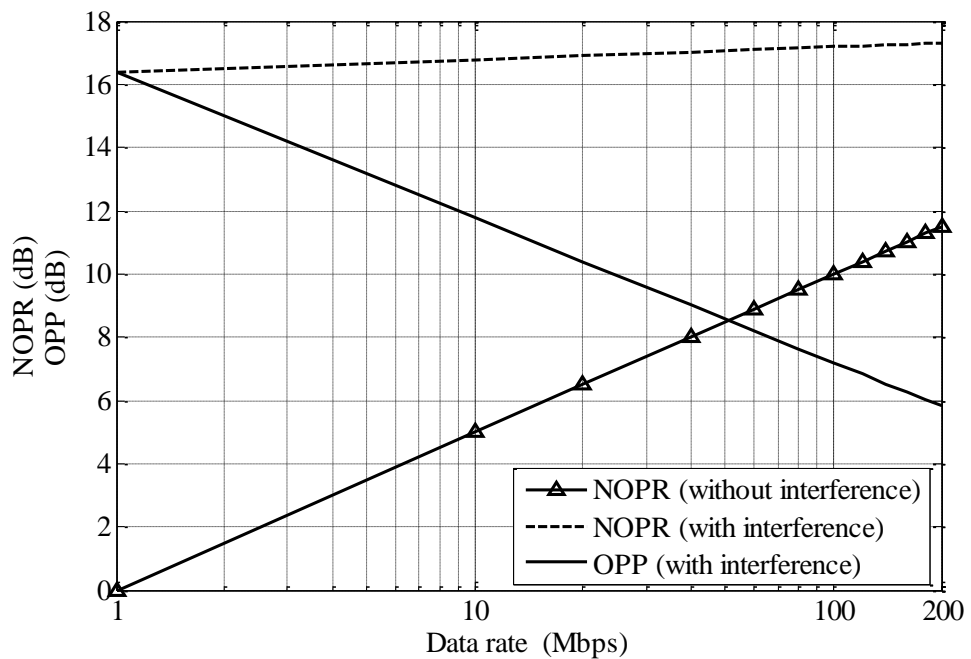


Figure 5.3: NOPR and OPP to achieve a BER of 10^{-6} against data rates for the OOK scheme with and without FLI.

5.2.2 Performance of PPM without Filtering

In this section, the performance of PPM system under the influence of the FLI is investigated. Since PPM can be considered to be a block code with minimum hamming distance of one, both ‘hard’ and ‘soft’ decoding is possible. Although the later is computationally complex compared to the former, it offers SNR gain of more than 1.5 dB in a LOS link and higher gains in non-LOS Links [43]. In PPM employing a simple L -input comparator, ‘soft’ decision decoding is carried out by finding a correlated matrix with the highest average amplitude. Consider a block code with N possible combinations ($N = L$ for PPM). Following the similar approach taken in [211] and taking into consideration that optical system has no negative energy, the received sequence r_j is given by:

$$\begin{aligned} r_j &= \sqrt{E} + n_j && \text{if } j^{\text{th}} \text{ bits is 1;} \\ r_j &= n_j && \text{if } j^{\text{th}} \text{ bits is 0;} \end{aligned} \quad (5.8)$$

where n_j represents the zero mean AWGN and E is the energy per bit and $j = 1, \dots, N$.

The decoding aims to find N dimensional vector with elements given by:

$$CM_j = \sum_{j=1}^N c_{ij} r_j ; \quad (5.9)$$

where c_{ij} denotes the bit in the j^{th} position of the i^{th} code word and $i = \{1, \dots, N\}$. Hence $c_{ij} = \{0, 1\}$ depending upon the bit corresponding to 0 and 1 respectively. Since a PPM symbol contains only one pulse, the value of CM_i depends only on the non-zero bit of the i^{th} code word. Thus, the ‘soft’ decoding can be carried out by assigning “1” to the bit with highest amplitude and “0” to the remaining bits. To clarify the concept, consider 4-PPM with received symbol $\mathbf{r} = \{r_1, r_2, r_3, r_4\}$. Then CM is given by:

$$CM = \begin{bmatrix} 1 & 0 & 0 & 0 \\ 0 & 1 & 0 & 0 \\ 0 & 0 & 1 & 0 \\ 0 & 0 & 0 & 1 \end{bmatrix} [r_1 \ r_2 \ r_3 \ r_4] = \begin{bmatrix} r_1 \\ r_2 \\ r_3 \\ r_4 \end{bmatrix}. \quad (5.10)$$

Since the values $CM_i = r_j$ for $i = j$, selecting a codeword corresponding to the maximum value of CM_i is equivalent to assigning “1” to the bit with the highest amplitude.

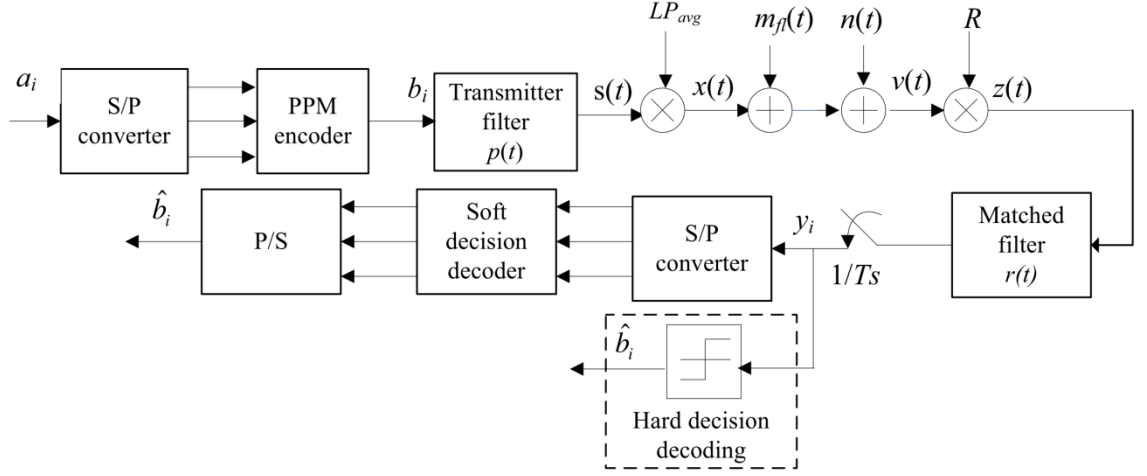


Figure 5.4: The block diagram of the matched filter based hard and soft decision detectors for PPM in presence of FLI.

The block diagram of the matched filter based hard and soft detectors for PPM in presence of FLI is given in Figure 5.4. The PPM encoder converts M -bit binary data sequence input bits $\{a_i ; i = 1.. M\}$ into one of the possible L symbols. The PPM symbols are passed to a transmitter filter which has a unit amplitude rectangular impulse response $p(t)$, with the duration of one slot T_{s-PPM} . The output of the transmitter filter is scaled by the peak detected signal photocurrent LP_{avg} . The FLI $m_{fl}(t)$ is added, along with the shot noise $n(t)$. Detail of the soft and hard decision decoding schemes are described in Section 2.7.1.2. Though suboptimal, a threshold level of $\alpha = RP_{avg}\sqrt{LT_b \log_2 L}/2$, which is midway between expected one and zero levels, is utilized for hard decision decoding.

Following the similar approach taken for the OOK, the SER for hard decision PPM can be calculated and is given as [51]:

$$P_{se_PPM_hard} = \frac{1}{N} \sum_{k=1}^N \frac{1}{L} Q \left(\frac{P_{avg}\sqrt{LT_b \log_2 L}/2 + m_k}{\sqrt{N_0/2}} \right) + \frac{(L-1)}{L} Q \left(\frac{P_{avg}\sqrt{LT_b \log_2 L}/2 - m_k}{\sqrt{N_0/2}} \right); \quad (5.11)$$

where N is the total number of slots over a 20 ms interval and m_k is given by (5.4) with sampling time taken as T_{s-PPM} .

For the probability of error for PPM with the ‘soft’ decoding scheme, the union (upper) bound is utilized and is given by [80]:

$$P_{se_PPM_soft} = \frac{1}{N} \sum_{k=1}^{N/L-1} \sum_{j=1}^L \sum_{\substack{k=1 \\ k \neq j}}^L Q \left(\frac{P_{avg} \sqrt{LT_b \log_2 L} + m_{iL+j} - m_{iL+k}}{\sqrt{N_0}} \right). \quad (5.12)$$

To investigate the effect of the FLI for the PPM scheme, a number of simulations are carried out at different data rates for different bit resolutions. The NOPR to achieve a SER of 10^{-6} for 4, 8 and 16-PPM hard decision decoder is given in Figure 5.5. Unlike the ideal cases, the variations in the NOPR for the channel with FLI are small indicating that the FLI is the main source of performance impairment. The NOPR increases with the data rate for all cases, however the increment is less than 1 dB for 16-PPM and 2 dB for 4-PPM. The OPP can be calculated by subtracting NOPR in the presence of interference to the NOPR without interference. The OPP is the least for 16-PPM and also decreases with data rates for all bit resolutions. The OPP at 200 Mbps is ~ 3 dB for 16-PPM and almost 0.5 dB higher for 8-PPM and a further ~ 0.5 dB penalty occurs for 4-PPM. The OPP for PPM system is significantly lower compared to the OOK for all data rates due to smaller slot duration of PPM.

The NOPR against data rates for the 4, 8 and 16-PPM with the soft decision decoding with and without the FLI is shown in Figure 5.6. Compared to the hard decision decoding, significant performance improvements can be achieved using soft decoding. In fact, the NOPR for the PPM with and without interference are almost identical for data rate > 20 Mbps. The performance improvement at higher data rates is due to the reduced variation of the FLI signal over the duration of one symbol. In soft detection, it is the values of the FLI samples relative to other samples within the same symbol which is important, rather than the absolute values. This leads to lower probability of symbol error, thus reducing the power penalty [43].

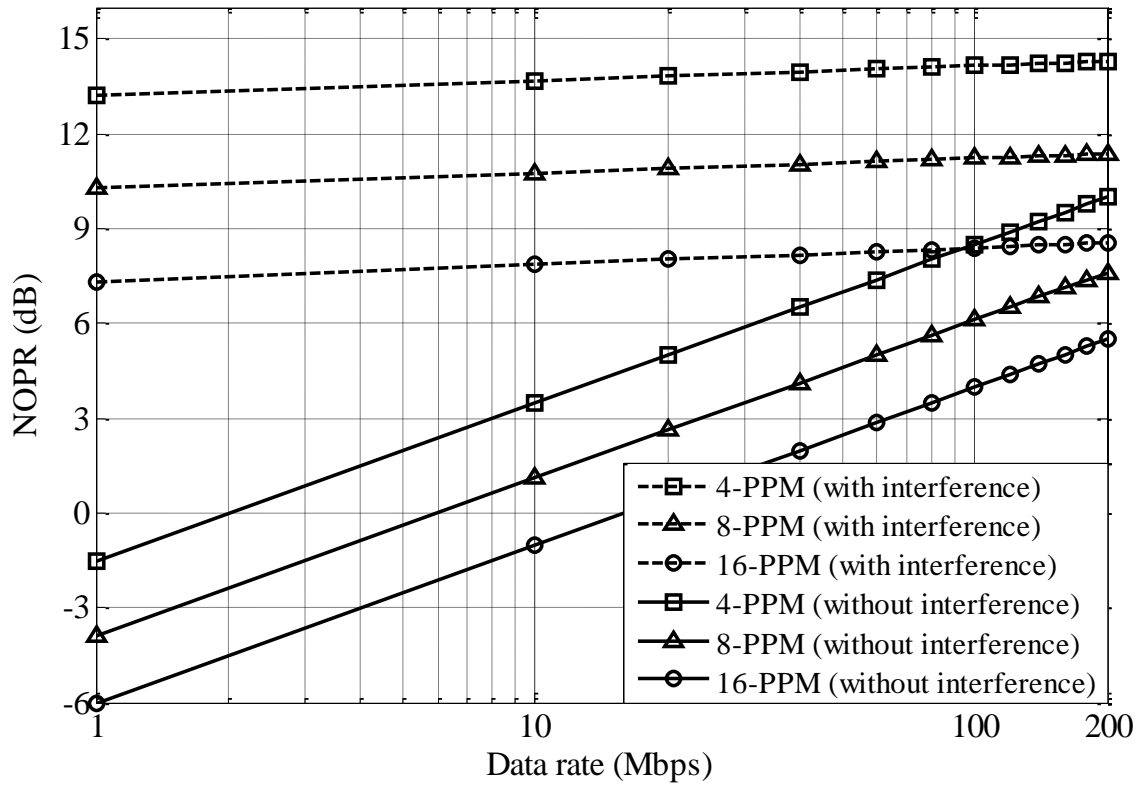


Figure 5.5: NOPR to achieve an SER of 10^{-6} against data rates for 4, 8 and 16-PPM hard decision decoding scheme with and without of FLI.

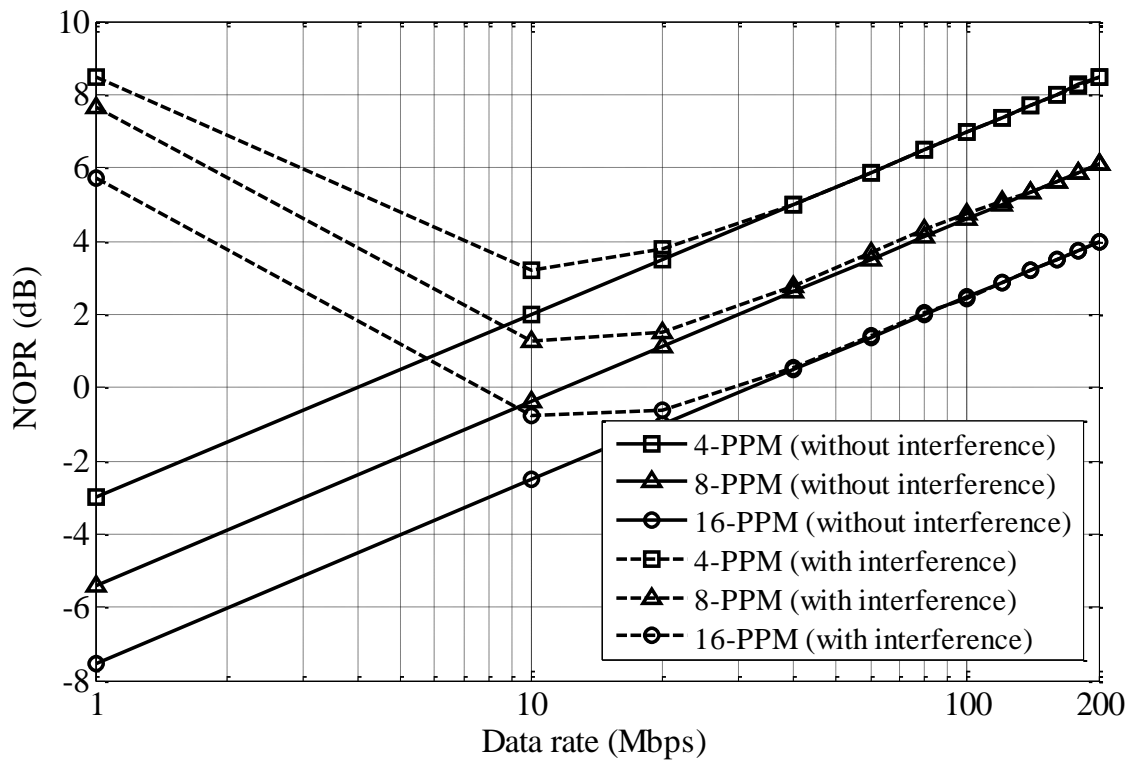


Figure 5.6: NOPR to achieve an SER of 10^{-6} against data rates of 4, 8 and 16-PPM soft decision decoding scheme with and without of FLI.

5.2.3 Performance of DPIM without Filtering

The system block diagram of the matched filter based receiver for DPIM system under consideration is shown in Figure 5.7. Detailed descriptions of each block of the DPIM system is given in Section 2.7.1.3, the only difference is on the addition of FLI photocurrent $m_{fl}(t)$, which is added to the modulated signal along with the shot noise $n(t)$. The receiver consists of a photodetector of responsivity of R followed by a unit energy matched filter with an impulse response $r(t)$, which is matched to $p(t)$ and threshold detector. For the simplification, a suboptimal threshold level of $\alpha = RP_{avg}\sqrt{L_{avg}T_b \log_2 L/2}$ is utilised throughout the chapter.

For the theoretical calculation of the average probability of slot error for DPIM in presence of the FLI, a approach similar to OOK and PPM with a hard decision decoding can be taken and the average probability of slot error for DPIM is given as [51]:

$$P_{se_DPIM} = \frac{1}{N} \sum_{k=1}^N \frac{1}{L_{avg}} Q \left(\frac{P_{avg} \sqrt{L_{avg} T_b \log_2 L/2 + m_k}}{\sqrt{N_0/2}} \right) + \frac{(L_{avg} - 1)}{L_{avg}} Q \left(\frac{P_{avg} \sqrt{L_{avg} T_b \log_2 L/2 - m_k}}{\sqrt{N_0/2}} \right); \quad (5.13)$$

where N is the total number of slots under consideration, and L_{avg} is the average number of slots per symbol for DPIM.

The theoretical performance of DPIM system in presence of the FLI is given in [51].

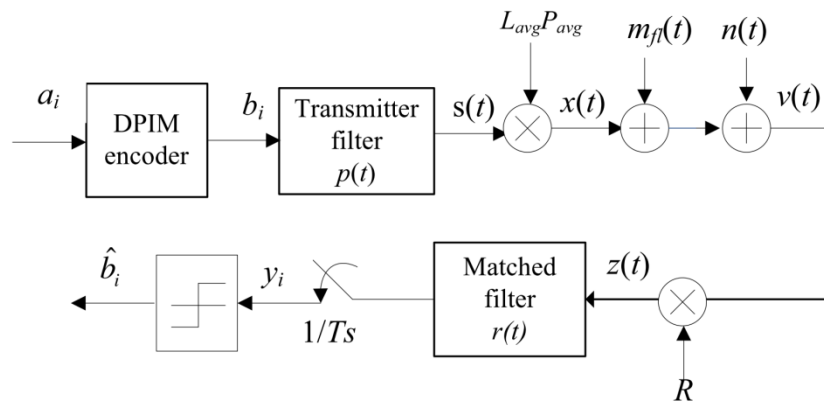


Figure 5.7: The block diagram of matched filter based receiver for DPIM scheme in presence of FLI.

In this study, computer simulations are carried out to calculate the error probability of the DPIM system in presence of the FLI. The NOPRs to achieve a SER of 10^{-6} for 4, 8 and 16-DPIM under the constraint of the FLI for a range of data rates is shown in Figure 5.8. As in the previous cases for the OOK and PPM with a hard decision detector scheme, there is little variation in the NOPR for data rates from 1-200 Mbps indicating the dominant noise source being the FLI. The NOPRs for 4-DPIM are ~ 15.3 dB and ~ 16.4 dB at 1 Mbps and 200 Mbps, respectively which are 1 dB higher and 2 dB lower for OOK and 4-PPM for respective data rates. As in the case of the PPM ‘hard’ decoding system, the OPPs are the minimum for the 16-DPIM and increase with the decreasing bit resolutions. DPIM has power penalties which are slightly higher than those of PPM with the hard decoding ranging from 14.6 – 16 dB at 1 Mbps to 4.5 – 5.4 dB at 200 Mbps.

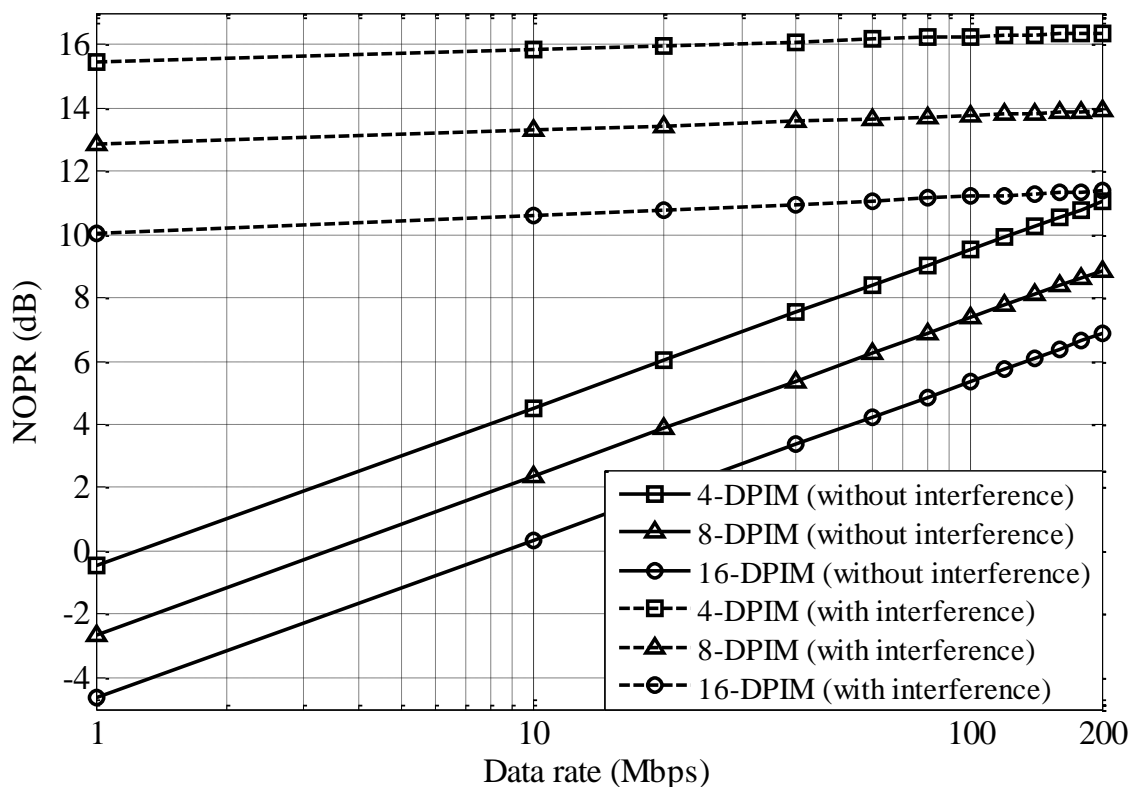


Figure 5.8: NOPR against the data rates for 4, 8 and 16-DPIM schemes with and without FLI.

5.3 The Effect of FL with Electrical High-Pass Filtering

In order to reduce the effect of the low frequency noise signal due to the FLI, a HPF is incorporated at the receiver in indoor OW systems. However, a sequence of pulses that are passed through a HPF exhibits a variation in the nominal zero level. This variation introduces a form of ISI in baseband modulation techniques like OOK, DPIM and is known as BLW. The detail analysis of BLW effect and performance of different modulation techniques in presence of the FLI with HPF is reported in [51, 78, 80, 83, 90, 91, 172, 189]. This section provides a review of the performance of the different modulation techniques under the constraint of FLI with high pass filtering

To analyse the effect of HPF in the absence of FLI, the discrete-time equivalent impulse response of the cascaded transmitter filter, receiver filter and HPF are calculated. The resulting impulse response c_j decays rapidly to zero with time, hence it can be truncated without significant loss of accuracy [80]. The BER is then approximated using the truncated length J . The BER is calculated by averaging the error rate over all possible symbol sequences of length J .

Assuming OOK, the discrete time equivalent impulse response, truncated to have a duration of J bit periods, is given as [80]:

$$c_j = \begin{cases} p(t) \otimes r(t) \otimes g(t) |_{t=jT_b}, & 1 < j < J \\ 0, & \text{otherwise} \end{cases} \quad (5.14)$$

where $g(t)$ is the impulse response of HPF.

Let a_j denotes a transmitted bit sequence of length J , the average bit error probability for OOK system for the J^{th} bit is given by [51, 80]:

$$P_{be_OOK} = \frac{1}{2^J} \sum_{a_j \in \{0,1\}^J} Q \left(\frac{2RP_{avg} |a_j \otimes c_j|_{j=J}}{\sqrt{\sigma_n}} \right); \quad (5.15)$$

where σ_n is the standard deviation of the Gaussian, non-white, zero mean, shot noise samples at the matched filter output, given as [83, 172]:

$$\sigma_n = \sqrt{\frac{N_0}{2} \frac{(1 - e^{-2\pi f_c T_b})}{2\pi f_c} \frac{1}{T_b}}; \quad (5.16)$$

where f_c is the cut-off frequency of HPF. To calculate the BER of OOK-NRZ in presence of the FLI with HPF, the superposition principle is applied and the BER is averaged over all possible sequences. The sampled output due to the FLI signal after passing through the matched filter and the HPF is given by:

$$m_j = m(t) \otimes r(t) \otimes g(t) |_{t=jT_b}. \quad (5.17)$$

The sampled output due to J^{th} bit is given by (5.15) and the overall output signal is superposition of the c_j and m_j . Hence, the overall probability of error is found by averaging over M bits and J sequences [51, 80]:

$$P_{be_OOK} = \frac{1}{2M \cdot 2^J} \sum_{k=1}^M \sum_{a_j \in \{0,1\}^J} \left[Q \left(\frac{2RP_{avg} |a_j \otimes c_j|_{j=J} + m_k}{\sigma_n} \right) + Q \left(\frac{2RP_{avg} |a_j \otimes c_j|_{j=J} - m_k}{\sigma_n} \right) \right]. \quad (5.18)$$

By applying similar approach to the other modulation techniques, the BLW effect and the performance in presence of the FLI signal with HPF can be evaluated [51, 80, 91, 189]. The following results are summary of the analysis and evaluation given in [51].

DPIM is more resistant to BLW than OOK and PPM is the most resistant to the effects of BLW. This superiority of PPM is due to the fact that unlike other baseband modulation techniques, PPM contains only a small proportion of its power around the DC value. The higher orders of DPIM and PPM shows greater robustness to BLW as the bandwidth requirement increases with the order and consequently, there is less power below the cut-off frequency as a fraction of the total power. The performance of the OOK, DPIM and PPM in presence of the FLI with HPF is evaluated in [51, 78, 80]. HPF is not effective in reducing the effect of FLI for OOK at a bit rate less than 10 Mbps. Even at 100 Mbps, a power penalty is reduced only to ~ 3 dB compared to the channel without FLI. The HPF provides a significant improvement in performance for the PPM system even at 1 Mbps. At 10 Mbps, the power penalty for PPM with the hard decoding is reduced to ~ 1 dB and at 100 Mbps the power penalty is virtually zero. Like in the case of OOK, the HPF offers no power reduction at a data rate of 1 Mbps for DPIM. Significant improvement can be achieved at higher bit rate for the DPIM system; At 100 Mbps, high pass filtering is very effective, thus resulting in the average OPP of less than 1 dB compared to the same bit rate without interference.

5.4 Introduction to Time-Frequency Analysis

It is important to have time as well as frequency information of signal as many characteristics of the signal can be revealed only in time or frequency. The earliest work on the time-frequency transformation was done by Joseph Fourier. He showed that it is possible to represent a periodic signal by linear combination of harmonics of the sinusoidal function. The Fourier transform (FT) is by far the most extensively used time-frequency analysis till today because of its simplicity and existence of extensive analytical solution. However, FT of a signal gives the frequency components of the signal but fails to provide the information when these frequencies occur. FT of a signal has meaning only if the signal is time invariant. Hence, to analyse the transient phenomenon, different time-frequency mapping tools that are localised in time are used.

One simple way to analyse a nonstationary signal having a transient phenomenon is to divide the signal into small segments in time, within which the signal can be considered to be stationary. The approach is called windowed FT or short time FT (STFT). In STFT analysis, the signal is divided into many equal segments in time. The segments are small enough to ensure the signal within a segment can be considered to be stationary. The FT in the particular time window is carried out and the window slides along the signal to analyse another segment. Properly selected window for STFT analysis can give the true time-frequency representation of the signal. However, a constant window width causes the Heisenberg Uncertainty problem, well known in quantum physics. Uncertainty problem states that one cannot know the exact time-frequency representation of a signal, i.e. one cannot know what spectral components exist at what instances of times [212]. What one can know is the time intervals in which certain band of frequencies exist, which is a resolution problem. Narrow windows give good time resolution, but poor frequency resolution. Wide windows give good frequency resolution, but poor time resolution. Hence, care should be taken in selecting the window size as wide windows may violate the condition of stationarity [213]. Hence, the best method to analyze nonstationary signal is to use a variable window length and this is done by the wavelet analysis.

5.4.1 Wavelet Analysis

FT or STFT are not a very useful tool for analysing nonstationary signals or signals with the abrupt changes. The problem in analysing such signals in the Fourier domain is due to the sinusoidal base and the fixed resolution of the STFT which give rise to the uncertainty in the analysis [214]. By having a non-sinusoidal base for the analysis and taking a flexible approach in the window size, it is possible to condense the information in both the time and the frequency [215]. A base, known as the mother wavelet, well localised in times is selected and it is dilated or condensed without changing the actual shape to analyse the signal. The dilated wavelet is used to analyse low frequency components and compressed wavelet is used to analyse high frequency components or the transient behaviour of the signal. It is equivalent to a mathematical microscope as compressing the wavelet is equivalent to increasing the magnification of the microscope, thus enabling one to see the greater details of the signal [213].

To understand the time-frequency resolution of WT and STFT consider their time-frequency mapping as shown in Figure 5.9. Each rectangular box (both in STFT and WT) has a fixed area. Each box represents an equal portion of the time-frequency plane, but giving different proportions to time and frequency. The widow is fixed in both time and frequency in STFT offering fixed time-frequency resolutions. The window in WT is not constant. A small window considers short intervals of time but provides poor frequency resolution. A big window is less precise about time but more precise about frequency [215]. A big window is used for low frequencies and smaller windows for high frequencies in WT. At low frequencies, the height of the boxes are shorter, hence provide better frequency resolution but their widths are longer giving poor time resolution. At higher frequencies the width of the boxes decreases, i.e. the time resolution gets better, and the heights of the boxes increase, i.e. the frequency resolution gets poorer [216].

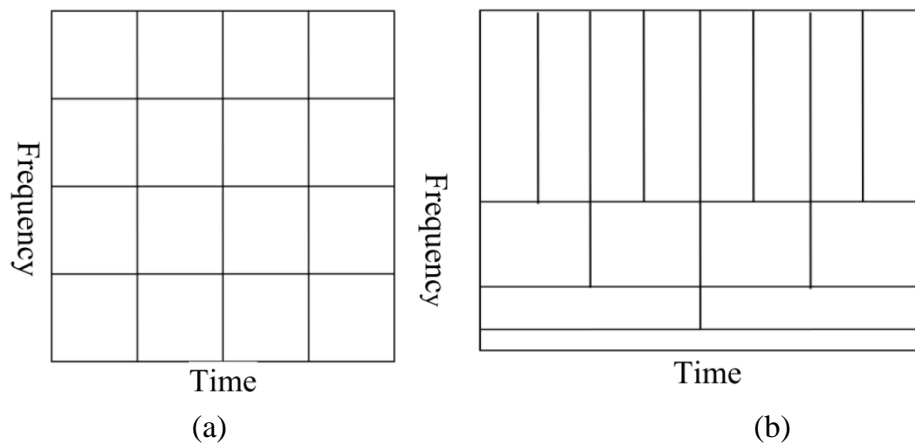


Figure 5.9: The time frequency resolution of (a) STFT, and (b) WT.

The WTs have proved to be very useful and effective in analyzing wide varieties of signals because of time-frequency localization. The fact that wavelets have the unconditional basis property for a variety of function classes implies that if one knows very little about the signal, the wavelet basis is usually a reasonable choice [217, 218]. The WT has a number of useful properties most importantly the non-linear soft-thresholding which is near optimal for statistical estimation and signal recovery and coefficient vector truncation which is near optimal for data compression [219, 220]. Best example of real application of WT is storage of fingerprints by FBI. The new digital picture compression JPEG-2000 is also based on the principle of WT [221]. Though WT is best known for image processing, denoising [222] and compression [223, 224] and has wide applicability in diverse fields like mathematics of time-series analysis [225], medicine, physics [226-230], feature extraction tools for pattern reorganisation tasks [231], communication engineering [232] and so on. In the field of communication engineering, wavelet packet transform (WPT) is proposed for multiple accesses technique [233, 234], modulation techniques as an alternative to the subcarrier modulation [235, 236], symbol synchronisation [237], signal estimation [229], CDMA system [238], channel characterisation [215, 239], adaptive denoising [240], mitigate ISI [214], channel equalization [223, 224, 238, 241] and traffic analysis [240].

5.4.2 Continuous Wavelet Transform

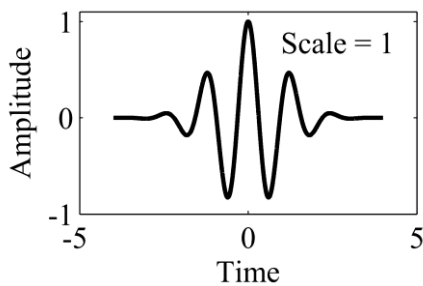
A continuous wavelet transform (CWT) decomposes signals over dilated and translated mother wavelet $\psi(t)$. A mother wavelet is well localised in time and frequency and have zero mean:

$$\int_{-\infty}^{\infty} \psi(t)dt = 0. \quad (5.19)$$

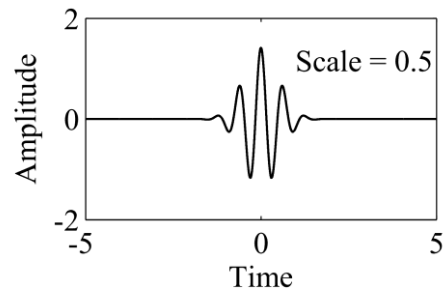
The family of mother wavelets is normalised using the norm $\|\psi_{s,\tau}(t)\| = 1$. The family of wavelets is obtained by scaling ψ by s and translating by τ as below:

$$\psi_{s,\tau}(t) = \frac{1}{\sqrt{s}} \psi\left(\frac{t-\tau}{s}\right). \quad (5.20)$$

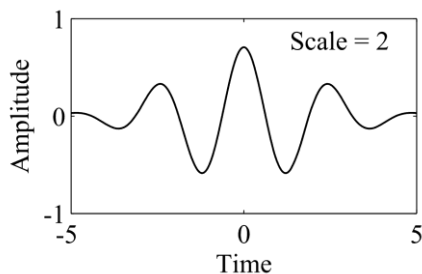
To scale a wavelet means to stretch or dilate. As the wavelet is stretched in the horizontal axis, it is squashed in vertical direction to ensure that the energy contained within the scaled wavelets is the same as the original mother wavelet [242]. The translation moves the wavelet along the x-axis. The scaling and translation operations are demonstrated in Figure 5.10 for a Morlet wavelet [215].



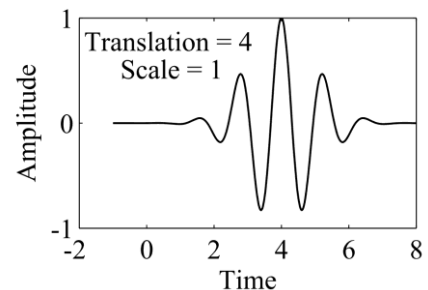
(a) Mother wavelet



(b) Wavelet scaled by 0.5 (compressed)



(c) Wavelet scaled by 2 (dilated)



(d) Wavelet translated by 4.

Figure 5.10: The scaling and translation to the Morlet wavelet.

The scale in the wavelet analysis is similar to the scale used in maps [214]. The high scales correspond to global information of a signal whereas low scales correspond to detailed information about the signal. The scale is inversely proportional to the conventional frequency, so low scale relates to the high frequency and vice versa. If $s \gg 1$, the window $\frac{1}{\sqrt{s}}\psi\left(\frac{t-\tau}{s}\right)$ is large and WT reacts mainly to low frequencies. If $s \ll 1$, the window $\frac{1}{\sqrt{s}}\psi\left(\frac{t-\tau}{s}\right)$ is small and WT reacts mainly to high frequencies. Hence the wavelet transform is represented by the scale and time as opposed to the time and frequency in Fourier transform. The relation between scale and frequency is defined as [242, 243]:

$$s = \frac{F_c \cdot \Delta}{f}; \quad (5.21)$$

where Δ is the sample period, f is the frequency and F_c is the center frequency of a wavelet in Hz defined as approximate measure of the oscillatory nature of the basis function at its centre.

The CWT of signal f and reconstruction formula are given by [244, 245]:

$$F(s, \tau) = \int_{-\infty}^{\infty} f(t) \frac{1}{\sqrt{s}} \psi^* \left(\frac{t-\tau}{s} \right) dt ; \quad (5.22)$$

$$f(t) = \frac{1}{C_\psi} \int_{-\infty}^{\infty} d\tau \int_0^{\infty} \frac{ds}{s^2} F(s, \tau) \frac{1}{\sqrt{s}} \psi \left(\frac{t-\tau}{s} \right) ; \quad (5.23)$$

where $*$ denotes a complex conjugate and C_ψ depends on the wavelet. The success of the reconstruction depends on this constant called the admissibility constant, in order to satisfy the following admissibility condition [246].

$$0 < C_\psi = \int_{-\infty}^{\infty} |\hat{\psi}(\omega)|^2 \frac{d\omega}{\omega} < \infty ; \quad (5.24)$$

where $\hat{\psi}(\omega)$ is the FT of $\psi(t)$.

5.4.3 Discrete Wavelet Transform

CWT unmixes parts of the signal that exist at the same instants, but at different scales, giving highly redundant CWT coefficients [215]. The redundancy requires significant amount of commutation time without adding any valuable information. CWT has an unmanageable infinite number of coefficients. CWT have no analytical solutions for most functions and they can be calculated only numerically [247]. The redundant coefficients in CWT can be removed by sampling both the scale and the time at dyadic (power of two) scales, thus leading to discrete wavelet transform (DWT) [213]. DWT provides sufficient information both for the analysis and synthesis of the original signal, with a significant reduction in the computation.

The DWT is calculated by applying the concept of the multiresolutional analysis (MRA) [248]. The practical implementation of the MRA can be done using a filter bank [244]. The process involves using successive application of low-pass $g(n)$ and high-pass $h(n)$ filters and down sampling by two [248]. The high-pass parts generally have no significant information about the signal and hence they are not decomposed any further. However, the low-pass parts are further decomposed into two bands until a satisfactory level of information is obtained. Figure 5.11 represents processing of splitting spectrum using the filter band and corresponding wavelet decomposition tree with the approximation and detail coefficients. The first level of approximation y_{1l} and detail y_{1h} coefficients are given by [215]:

$$y_{1h}(k) = \sum_n y(n) g(2k - n); \quad (5.25)$$

$$y_{1l}(k) = \sum_n y(n) h(2k - n). \quad (5.26)$$

The high-pass and low-pass filters satisfy the condition of the quadrature mirror filter, i.e. the sum of the magnitude response of filters is equal to one for all frequencies. The approximation coefficients can further be decomposed into different DWT coefficient levels with a maximum level of $\log_2 L$, where L is the signal length. The original signal can be reconstructed by following the inverse of decomposition process or by using [92]:

$$x'(n) = \sum_k (y_{kh}(n) \cdot g(2k - n)) + (y_{kl}(n) \cdot h(2k - n)). \quad (5.27)$$

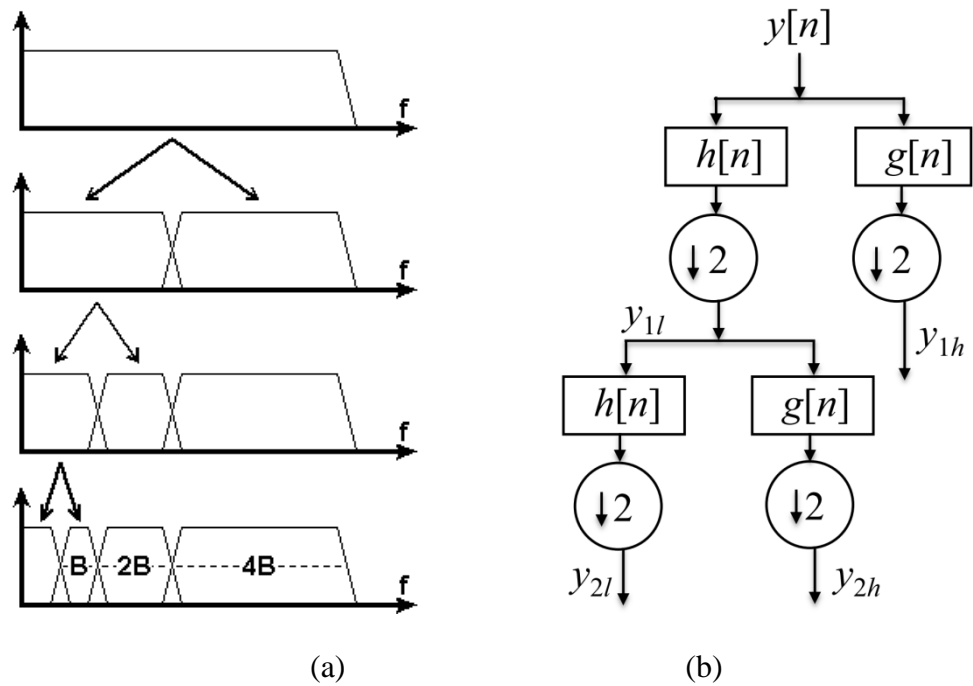


Figure 5.11: (a) Decomposition of a signal by DWT, and (b) the DWT decomposition process.

5.5 DWT based Denoising

Since FLI causes significant performance degradation, an effective measure to reduce the effect of the interference is sought. A filter is designed based on the DWT and the effect of the FLI is minimized at the receiver. The working principal and the performance of DWT based receiver for different modulation schemes are described below.

5.5.1 Performance of OOK with DWT Denoising

The receiver design based on the DWT for the OOK system is given in Figure 5.12. Comparison to the receiver structure in Figure 5.2 shows that the two structures are similar except for the wavelet denoising block. The wavelet denoising involves the decomposition of the signal $y(n)$ into different DWT levels, processing the DWT coefficients and reconstruction.

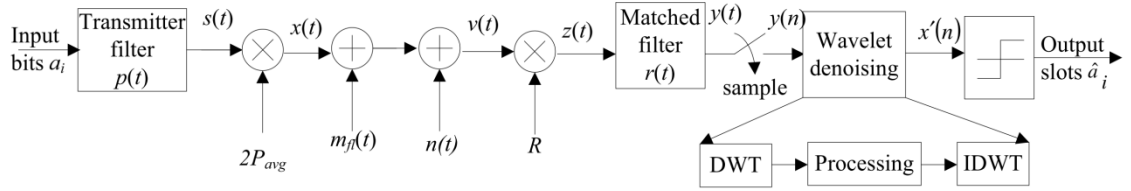


Figure 5.12: DWT based receiver for the OOK in presence of artificial light interference

The first level of decomposition involves splitting signal $y(n)$ into lowpass and highpass signals as given by (5.25) and (5.26), respectively. The second stage divides the lowpass band signal y_{1l} further to lowpass y_{2l} and bandpass y_{2h} components. Filtering and decimation process is continued until the required level is reached. The task here is to separate the interference and modulating OOK signal in the DWT domain and remove the interfering signal from the reconstructed signal. Since the FLI signal has most of its spectral contents at a low frequency region, the received signal is decomposed until the DWT coefficients of interfering signal are concentrated on the approximation coefficients. For the removal of the interfering signal from the received signal, the approximation coefficients which correspond to the interfering signal are then made equal to zero so that the reconstructed signal is free from the interfering signal i.e.

$$y_{\gamma h}(k) = 0. \quad (5.28)$$

where γ is the number of the decomposition levels. The signal is then reconstructed back using the inverse of the decomposing process as given by (5.27).

DWT decomposes the signal in the logarithmic scale; therefore it is difficult to define a precise band of frequencies that correspond to the lowest level of approximations. On the other hand, due to the spectral overlapping of the interfering signal and modulating signal, it is difficult to precisely define the cut-off frequency that would provide the optimal performance. Hayes [51] set the cut-off frequency that results in the least BLW effect. However, the definition of such precise cut-off frequency is not possible using the DWT. Therefore, the number of the decomposition level γ is calculated in such a way that the lowest level of approximation signal is within 0.5 MHz range to make the cut-off frequency F_c approximately equal to 0.5 MHz (except for a data rate < 20 Mbps, for which the cut-off frequency is taken as 0.3 MHz). The cut-off frequency is chosen as 0.5 MHz as previous studies showed that it provides near optimal performance in

presence of FLI for a digital HPF [92]. The decomposition level and approximated cut-off frequency F_c at different data rates are given in Table 5.3. The number of decomposition level γ is calculated using the following expressions:

$$\gamma = -\lfloor \log_2(T_b \times F_c) \rfloor; \quad (5.29)$$

where $\lfloor . \rfloor$ is the floor function. It is to be noted here that the cut-off frequency varies with the data rate and decompositions level.

Table 5.3: The decomposition level and the approximate cut-off frequency (MHz).

Data Rate (Mbps)	OOK	
	Decomposition Level γ	f_c (MHz)
10	5	0.31
20	6	0.63
40	7	0.63
60	7	0.94
80	8	0.63
100	8	0.78
120	8	0.94
140	9	0.55
160	9	0.63
180	9	0.70
200	9	0.78

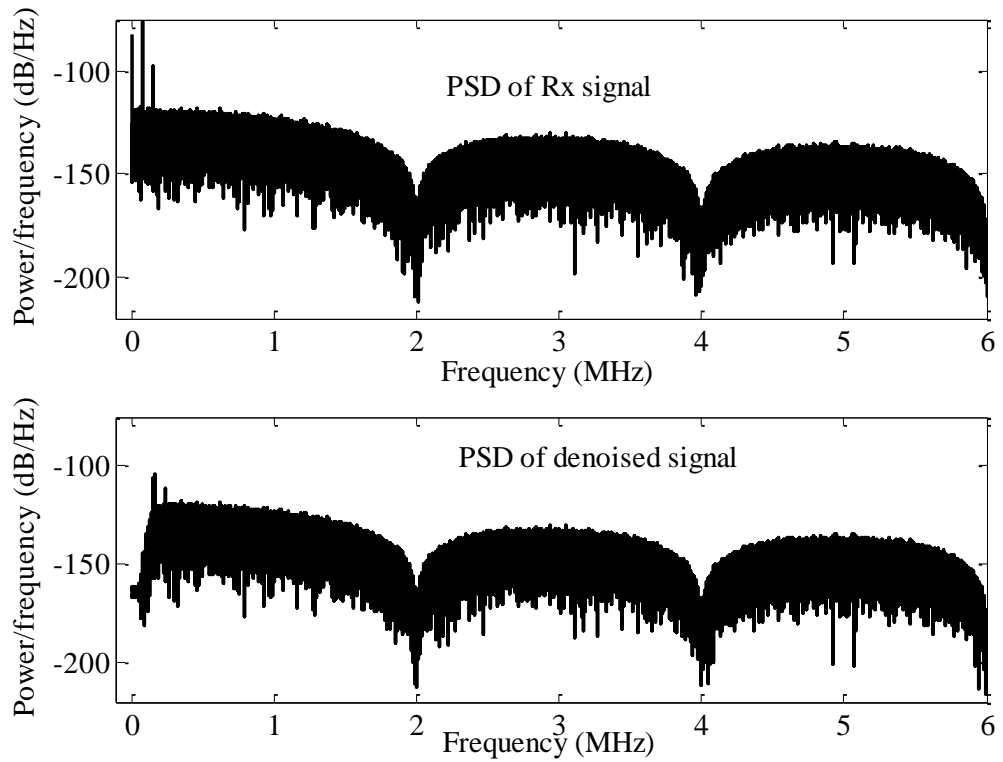


Figure 5.13 : The PSD of OOK at 2 Mbps: (a) received signal with FLI, and (b) wavelet denoising. The Daubechies wavelet with 6 levels of decompositions is used.

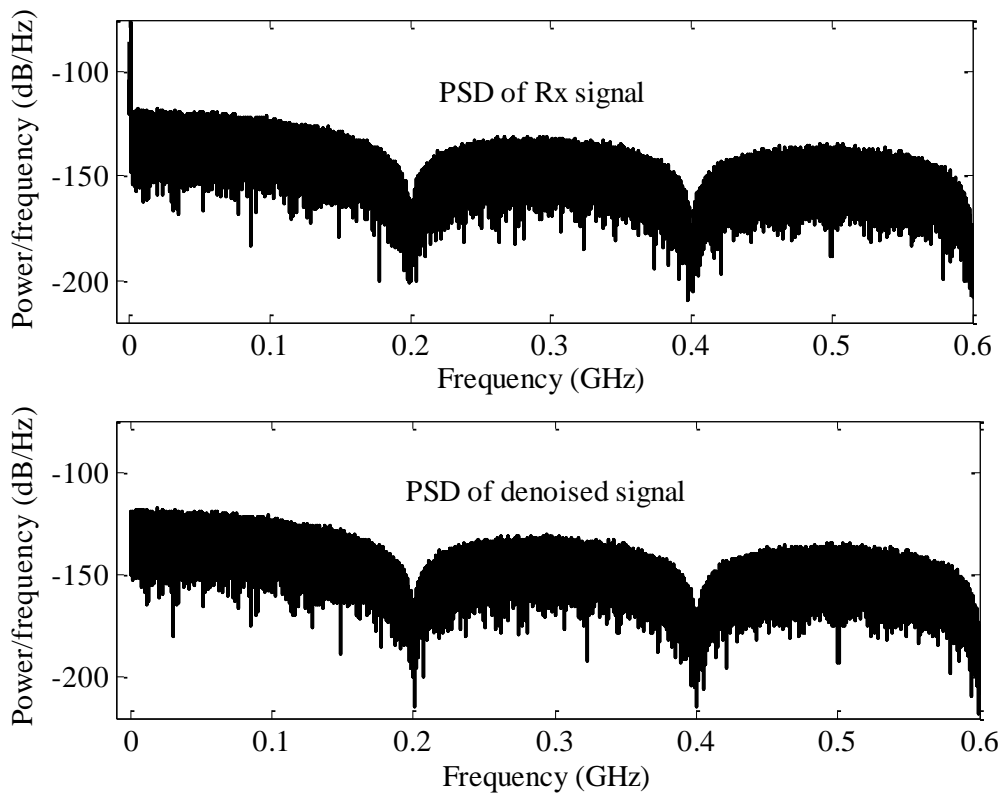


Figure 5.14 : The PSD of OOK at 200 Mbps: (a) received signal with FLI, and (b) wavelet denoising. The Daubechies wavelet with 12 levels of decompositions is used.

The PSD of the OOK signal at 2 Mbps corrupted by FLI and its denoised version using DWT are shown in Figure 5.13. The Daubechies wavelet (db8) is used for the analysis with 6 levels of decompositions and the photocurrent due to interference is arbitrarily made four times that of the signal. For clarity, the received signal is assumed to be free from the AWGN as the focus is on the effect of FLI. The PSD of the denoised signal shows that there are no significant changes at frequencies > 0.5 MHz compared to the PSD of the received signal. A significant portion of the spectral content at < 0.3 MHz is removed (the approximated cut-off frequency is 0.31 MHz) with no DC contents. Because of the spectral overlap between the signal and interference (both having high DC and low frequency components), it is not possible to remove the interference without losing the significant portion of signal, thus leading to increased power penalties. Hence the task here is to make the power penalty as low as possible. The PSD of the received and denoised signals at a higher bit rate of 200 Mbps are shown in Figure 5.14. Unlike the 2 Mbps case (see Figure 5.13), there is not much change in the PSD of received and denoised signals on a large scale. However, at a closer look there is a significant change in PSD at < 0.3 MHz. Hence a significant amount of information is retained even with the wavelet denoising and it is expected that the power penalty would not be as high as at that of 2 Mbps case. With this observation, one can conclude that the signal with a low PSD at or near the DC region can provide an enhanced immunity to the FLI.

DWT offers flexibility in the analysis where different mother wavelets could be adopted. The NOPRs linked to different mother wavelets are listed in Table 5.4. Only selected mother wavelets from the Daubechies (db), Symlet (sym), discrete Meyer wavelet (dmey), biorsplines (bior) and Coiflets (coif) families with the best and the worst performance are listed. The filter coefficients of the families of wavelet are given in Appendix C. The Haar wavelet (db1) and the db8 show the worst and best performance, respectively followed closely by the db10 and sym9. Hence in all simulation results discussed hereafter, the db8 is used for DWT denoising.

The NOPR for OOK schemes with DWT denoising in the presence of the FLI is shown in Figure 5.15. Also shown is the NOPR for the ideal channel without interference. Since no improvement can be achieved below the data rates of 10 Mbps, such rates are not considered here. Since OOK is very susceptible to BLW, only low normalized cut-off frequencies (normalized to sampling rate) are possible, which are not effective in

reducing the interference. At data rates above 10 Mbps, the DWT is very effective in reducing the interference. At a bit rate of 10 Mbps, DWT offer a reduction of ~ 5.5 dB in NOPR compared to the system without filtering. Higher reduction of ~ 7.4 dB is observed at 40 Mbps. However, this still leaves an OPP of ~ 1.6 dB compared to the same bit rate without interference. The OPP is further reduced at higher data rates with a value of ~ 1.2 dB at 200 Mbps.

Table 5.4: The NOPR to achieve a BER of 10^{-6} at a data rate of 200 Mbps for DWT based receiver with different mother wavelets.

Mother Wavelets	SNR (dB)	NOPR (dB)
db1	22.01	15.7
db2	20.9	15.2
db5	16.1	12.9
db8	15.2	12.3
db10	16.2	12.8
Coif2	16.6	13.0
Coif5	15.4	12.4
Sym3	17.2	13.3
Sym4	15.7	12.6
Sym7	15.3	12.4
dmey	15.7	12.6
Bior2.2	16.7	13.1

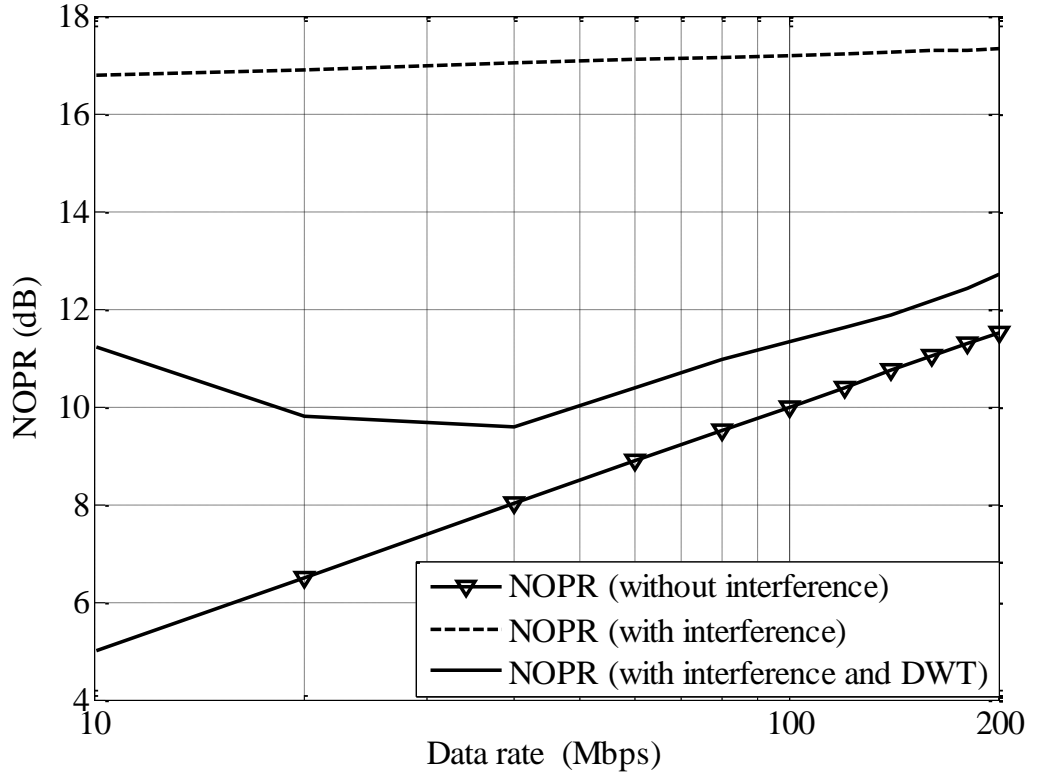


Figure 5.15: Normalized optical power requirement against data rates for OOK modulation scheme with and without DWT denoising in the presence of the FLI.

5.5.2 Performance of PPM with DWT Denoising

The block diagram of the wavelet based receiver for PPM system with hard and soft decision decoding schemes in presence of the FLI is shown in Figure 5.16. As in case of OOK, the sampled output of the matched filter $y(n)$ is denoised using the DWT. Since the sampling time at the output of the matched filter is based on the slot durations of PPM T_{s_PPM} , the decomposition level γ is modified according to:

$$\gamma = -\lceil \log_2(T_{s_PPM} \times F_c) \rceil; \quad (5.30)$$

The desired cut-off frequency F_c is taken as 0.5 MHz except for a data rate of 1 Mbps in which a lower value of $F_c = 0.3$ MHz is utilized. The number of decomposition level γ and approximate cut-off frequencies for different data rates for L -PPM is given Table 5.5.

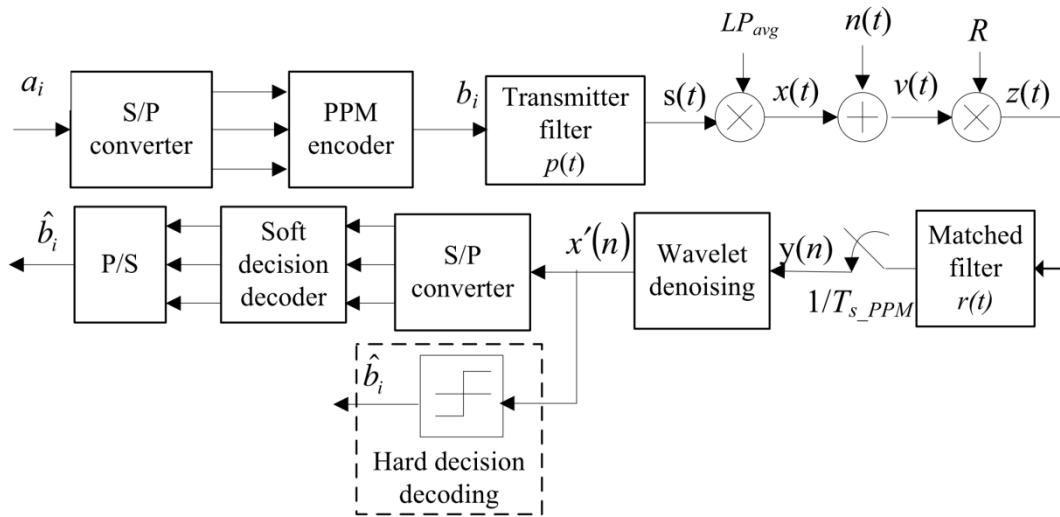


Figure 5.16: Block diagram of DWT based receiver for PPM (hard and soft decoding) schemes in the presence of FLI.

Table 5.5: The decomposition level and the approximate cut-off frequency (MHz).

Data Rate (Mbps)	4-PPM		8-PPM		16-PPM	
	Level	f_c (MHz)	Level	f_c (MHz)	Level	f_c (MHz)
1	2	0.5	3	0.33	3	0.5
10	5	0.63	5	0.83	6	0.63
20	6	0.63	6	0.83	7	0.63
40	7	0.63	7	0.83	8	0.63
60	7	0.94	8	0.63	8	0.94
80	8	0.63	8	0.83	9	0.63
100	8	0.78	9	0.52	9	0.78
120	8	0.94	9	0.63	9	0.94
140	9	0.55	9	0.73	10	0.55
160	9	0.63	9	0.83	10	0.63
180	9	0.70	9	0.94	10	0.70
200	9	0.78	10	0.52	10	0.78

In this study, both hard and soft decision decoding schemes are considered. However, the OPP at the soft decision decoding is almost zero without any filtering at data rates > 20 Mbps (Figure 5.5). The soft decoding with DWT denoising is considered only for data rate of < 20 Mbps. For the hard decision decoding, the threshold level α is set midway between one and zero levels in the absence of any BLW, given as [51, 189]:

$$\alpha = RP_{avg}\sqrt{LT_b \log_2 L} \left(\frac{1}{2} - \frac{1}{L} \right). \quad (5.31)$$

The NOPR to achieve an error probability of 10^{-6} with DWT denoising for 4, 8 and 16-PPM with the hard decision decoding scheme for data rate range of 1-200 Mbps is demonstrated in Figure 5.17. With reference to Figure 5.5, it is clear that DWT denoising shows marked reduction in the NOPR (~ 10.7 dB, 12.1 dB and 12.4 dB for 4, 8 and 16 PPM respectively) at a data rate of 1 Mbps. Since PPM has no DC component and with a low PSD at low frequencies, a higher cut-off frequency can be tolerated without BLW effect. Hence DWT offers improvement even at low frequencies for PPM scheme. Above a data rate of 10 Mbps for 4-PPM and 5 Mbps for the 8 and 16-PPM, the DWT based denoising completely eliminates power penalties due to FLI.

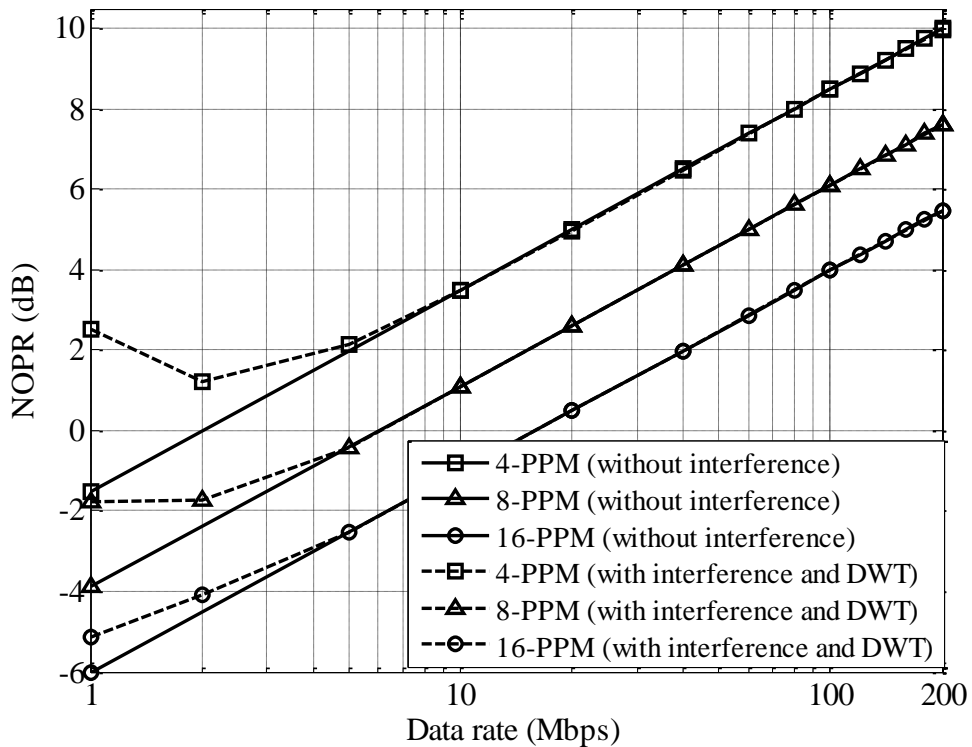


Figure 5.17: NOPR versus the data rates for 4, 8 and 16 PPM with the hard decoding scheme with DWT denoising in the presence of the FLI.

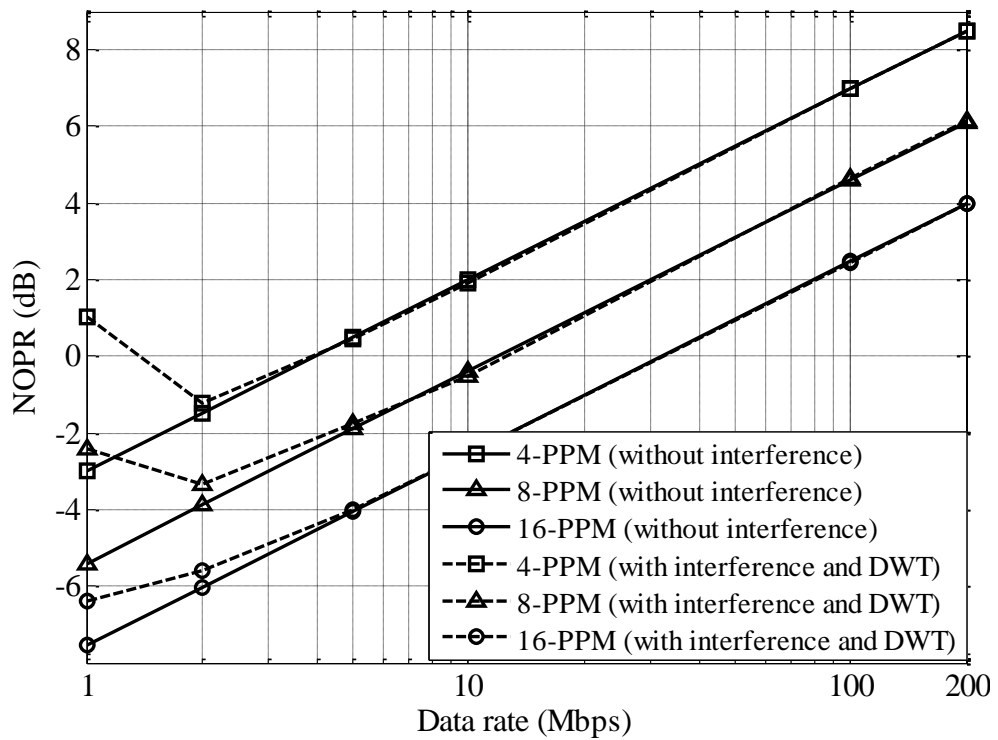


Figure 5.18: NOPR versus the data rates for 4, 8 and 16 PPM with the soft decoding scheme with DWT denoising in the presence of the FLI.

The NOPR to achieve an error probability of 10^{-6} with DWT denoising for 4, 8 and 16-PPM with the soft decision decoding scheme for a data rate range of 1-200 Mbps is given in Figure 5.18. Comparing Figure 5.6 and Figure 5.18, DWT offer no improvement above a data rate of 20 Mbps as PPM with the soft decoding is immune to the FLI. DWT provides a significant improvement even at 1 Mbps with the power penalties of ~ 4 dB, ~ 2.9 dB and ~ 1 dB for 4, 8 and 16 PPM, respectively compared to the same bit rate with no interference. The power penalties without DWT are 11.45 dB and 13.1 dB, which show the effectiveness of DWT. At 10 Mbps without DWT denoising, FLI results in power penalties of 1.1 to 2.1 dB. These power penalties are completely eliminate by DWT denoising.

5.5.3 Performance of DPIM with DWT Denoising

The DWT based denoising receiver for DPIM system in presence of the FLI is shown in Figure 5.19. Like cases of PPM and OOK, the receiver incorporates a matched filter and a sampler followed by the DWT based denoising. The wavelet denoising section removes the FLI from the received signal and the denoised signal is sliced to convert it

to binary DPIM symbols. The threshold level α is set midway between one and zero levels in the absence of any filtering and is given as [51, 189]:

$$\alpha = RP_{avg} \sqrt{L_{avg} T_b \log_2 L} \left(\frac{1}{2} - \frac{1}{L_{avg}} \right); \quad (5.32)$$

where L_{avg} is the average symbol length of DPIM.

The number of decomposition level γ can be calculated using (5.30) by replacing T_{s_PPM} by slot duration of the DPIM T_{s_DPIM} . The decomposition level γ and cut-off frequencies for DPIM scheme are given in Table 5.6.

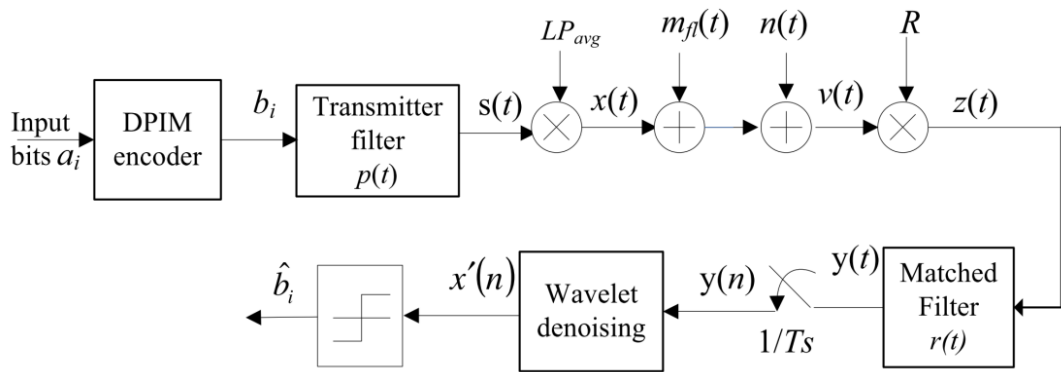


Figure 5.19: Block diagram of DWT based receiver for DPIM in the presence of FLI.

Table 5.6: The decomposition level γ and the cut-off frequencies (MHz) for L -DPIM.

Data Rate (Mbps)	4-DPIM		8-DPIM		16-DPIM	
	Level	f_c (MHz)	Level	f_c (MHz)	Level	f_c (MHz)
10	4	0.78	4	0.94	5	0.66
20	5	0.78	5	0.94	6	0.66
40	6	0.78	6	0.94	7	0.66
60	7	0.59	7	0.70	7	1.00
80	7	0.78	7	0.94	8	0.66
100	7	0.98	8	0.59	8	0.83
120	8	0.59	8	0.70	8	1.00
140	8	0.68	8	0.82	9	0.58
160	8	0.78	8	0.94	9	0.66
180	8	0.88	9	0.53	9	0.75
200	8	0.98	9	0.59	9	0.83

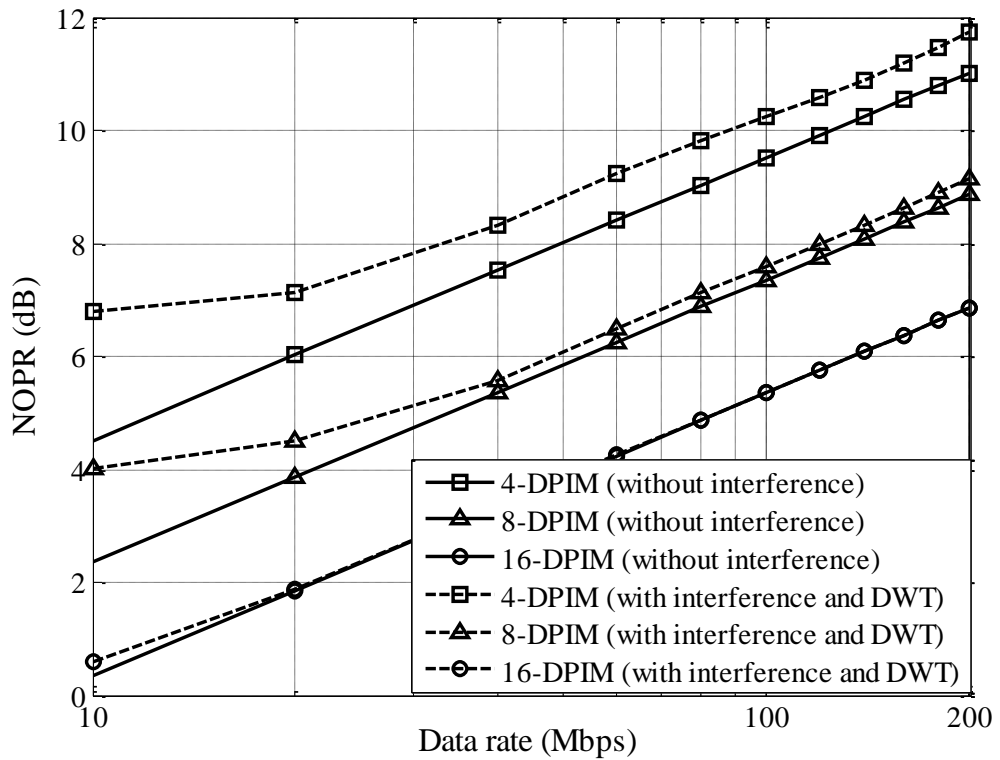


Figure 5.20: NOPR versus the data rates for 4, 8 and 16 DPIM schemes with DWT denoising in the presence of the FLI.

The NOPR to achieve a SER of 10^{-6} with DWT denoising for 4, 8 and 16-DPIM at a data rate range of 1 - 200 Mbps is given in Figure 5.20. Comparing the performance of OOK scheme in Figure 5.15 and PPM with the hard decision scheme in Figure 5.17, it can be observed that performance of DPIM with DWT is intermediate between OOK and PPM. Low order DPIM show performance similar to OOK with constant optical power penalties compared to the ideal case. However, higher order of DPIM shows almost zero power penalties. The phenomenon is due to progressive reduction of the DC and low frequency components with increasing bit resolutions. Compared to performance without FLI, the power penalties with DWT are ~ 0.7 dB at a data rate > 40 Mbps, which reduces to 0.4 dB for 8-DPIM. The power penalties is completely reduced to zero by DWT for 16-DPIM at data rate > 20 Mbps.

5.6 Comparative study of DWT and HPF

This section provides the comparative study of the DWT and HPF. Both schemes are designed to reduce the effect of the FLI. Due to the spectral overlapping of the modulating signal and interference, it is in fact impossible to reduce the effect of FLI without incurring power penalties especially for modulating techniques with a high DC component. Since OOK has the highest DC and low frequency components, it suffers most adversely from the application of the filtering. Hence the task here is to design high-quality denoising techniques with reduced complexity and minimal information loss. A case study for OOK with HPF and DWT denoising is presented as it gives good indication of the effectiveness of the techniques. It is easy to conclude that a filtering technique that provides the least power penalty is the best for other modulation techniques as well because OOK suffers the most severely from BLW. Since the digital HPF shows significantly improved performance compared to its analogue counterpart, this study is limited to the digital HPF. For the performance of the OOK and other modulation techniques with the analogue HPF, refer to [51, 78, 80].

The OPPs against the decomposition level γ for DWT for data rates of 20, 50, 100 and 200 Mbps is given in Figure 5.21. The OPPs for different filter cut-off frequencies and for the same data rates for HPF are given in Figure 5.22. For DWT the lowest threshold level is at $\gamma = 9$ for 200 Mbps. Since DWT decomposes signal in a logarithmic scale, the value of γ at which OPP is the minimal increases by one when the data rate doubles. In case of the HPF, the optimum cut-off frequency is ~ 0.2 MHz for all data rates. Note, it is not possible to define a precise cut-off frequency for DWT (as only the integer value of γ is permissible). The results shown in Figure 5.21 and Figure 5.22 indicate that the wavelet based receiver, with no parameter optimization, displays similar or better performance compared to the best achieved with the HPF. This makes the denoising process faster and more convenient.

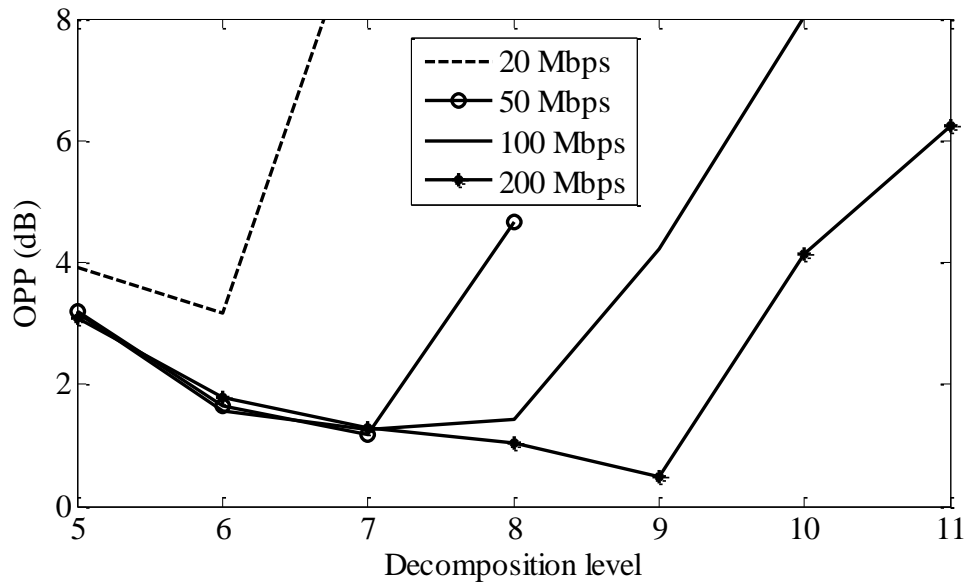


Figure 5.21: The OPP against the decomposition level for the DWT based receiver at data rates of 20, 50, 100 and 200 Mbps.

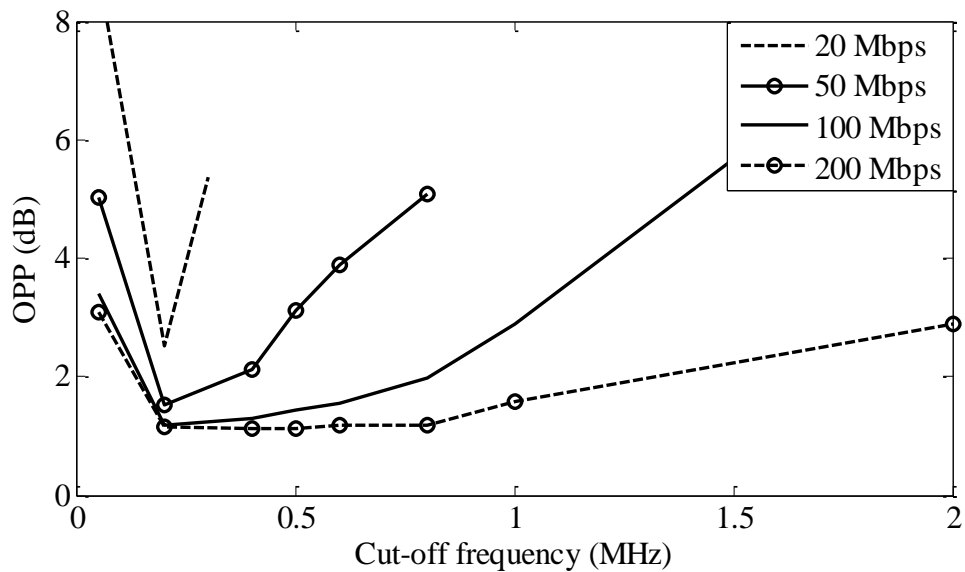


Figure 5.22: The OPP against cut-off frequencies for a HPF based receiver at data rates of 20, 50, 100 and 200 Mbps.

In addition to the performance improvement, a key advantage of the DWT is the reduced system complexity. For the optimum performance, the value of decomposition level γ varies from 6-9 (see Figure 5.22). For the input signal length of n , the total number of floating point operations (only multiplication is taken into consideration here) for the first level of decomposition is nJ . For the second stage, the length of input

signal is $n/2$ and the total number of operations is $nJ/2$ and so on. Hence, the DWT requires a maximum of $2nJ$ operations for analysis and synthesis meaning the maximum number of floating point operations is $4nJ$. Since $J = 15$ for Daubechies 8 'db8', the maximum number of the operations is $60n$. For a HPF of order L , the total number of floating point operations is $nL/2$. At a data rate of 200 Mbps and with f_c of 0.2 MHz the filter order L is 2148, thus illustrating much reduced complexity of the DWT. Moreover, the realization of the DWT is also simpler compared to the HPF as a repetitive structure is used at each level of analysis and synthesis. Hence only a 15th order filter is required to realize for the DWT compared to a filter of 2148 orders for the HPF.

5.7 Summary

The effect of FLI to a number of baseband modulation techniques was investigated in this chapter. The normalized optical power requirement for all modulation schemes with threshold detection was almost constant irrespective of the data rate indicating the dominance source of interference being FLI. Compared to the optical power requirements without interference, power penalties decrease as the data rate increases. Unlike hard decision decoding scheme, soft decision decoding for PPM showed a significantly higher resistance to the FLI. In fact the power penalty for PPM with the soft decision decoding was zero above a data rate of 20 Mbps.

A new method based on DWT was employed as an effective tool to reduce the effect of FLI. The received signal corrupted by FLI was separated into different bands of frequencies. The objective was to separate the modulating and interfering signal into different bands using DWT decomposition. Band of signals corresponding to interference was then removed and the signal was reconstructed for detection. With proper selection of decomposition level, it was possible to make the reconstructed signal free from interference. However, due to spectral overlap between the modulating and the interfering signals, a significant content of the modulating signal was removed from the received signal which leads to OPPs. The performance of OOK, PPM and DPIM were evaluated in the presence of FLI with DWT denoising. The study showed that DWT is very effective in reducing the effect of FLI. DWT offers a reduction of ~ 5.5 dB in NOPR at 10 Mbps and higher reduction of ~ 7.4 dB is observed at 40 Mbps. The optical power penalty for OOK is less than ~ 1.6 dB for the data rate > 40 Mbps. DWT

eliminates the fluorescent light induced power penalties for PPM hard decision decoding above data rate of 10 Mbps for all bit resolutions. Unlike the case of OOK, DWT even offer reduction in power penalties at a data rate of 1 Mbps for PPM system. Since PPM with the soft decision decoding scheme showed significant resistance to FLI, DWT offered reduction in NOPR at data rates < 20 Mbps and no improvement beyond 20 Mbps. The performance of DPIM with DWT denoising showed the characteristic intermediate between OOK and PPM hard decision scheme. Lower order of DPIM showed performance akin to OOK with almost a constant OPP above 40 Mbps. However, higher order of DPIM showed a null OPP above the data rate of 20 Mbps.

Comparative studies of the DWT denoising and HPF revealed that DWT can match the best performance achieved with the HPF. Besides performance improvement, DWT offers reduced system complexity, simplicity in design and flexibility. With results that had been obtained in this study, it is conclusive that DWT is very effective denoising tool for reducing the effect of FLI in indoor optical wireless channel.

Chapter 6 Artificial Neural Network Based Adaptive Equalizer for a Dispersive Indoor Optical Wireless Channel

6.1 Introduction

Though directed LOS links require the least optical power and offers high data rates in excess of 1 Gbps, the links are more susceptible to blocking, restrict user mobility and require complex tracking systems [11]. Hybrid LOS systems provide mobility to a certain degree, but are less power efficient and suffer from blocking. Non-directed non-LOS (diffuse) topologies provide mobility and are less susceptible to blocking; hence it is the preferred option for indoor applications. However, diffuse links suffer from the multipath induced ISI, thus limiting the maximum achievable data rates, for example $260 \text{ Mbps.m.s}^{-1}$ for a typical indoor OW system [3]. ISI also results in an additional power penalty that increases exponentially with the data rate [43].

For highly dispersive channels, the power penalty associated with multipath propagation becomes critical at high data rates. Unless a compensation technique is incorporated in the receiver, the power penalty makes the system practically infeasible. The traditional method is to use a compensation filter with an impulse response inverse to that of the channel impulse response. Both the linear and the decision feedback equalizers are effective for reducing the effect of ISI in indoor applications, with the later displaying slightly improved performance [179, 249]. Since the transmission channel parameters are not known in advance and the physical channel is time varying, the adaptive algorithms are the preferred option. In this scenario a training sequence is transmitted to approximate channel characteristics, and is used at the receiver to adjust equalizer's parameters accordingly. The equalizing algorithm assumes that the channel is linear,

however dispersion induced by the channel is nonlinear in nature [103]. The received signal at each sampling instant may be considered as a nonlinear function of the past values of the transmitted symbols. Hence, if the channel is non-stationary, the overall channel response becomes a nonlinear dynamic mapping [103]. Thus, in a time-varying environment, the equalization based on the filter is the non-optimum classification strategy as filters have a linear decision boundary [250, 251]. Therefore the optimum strategy would be to have a nonlinear decision boundary. Recently, several equalizers based on the multilayer perceptrons (MLP) and the recurrent neural networks with a nonlinear decision boundary have been studied for adaptive equalization [250, 252-255]. In this chapter, the performance of the MLP for equalization in indoor OW links is studied. The linear and decision feedback structures are investigated and results are presented.

6.2 Diffuse Indoor Optical Wireless Channel Model

A survey of the channel models that had been investigated for indoor OWC channel is given in Section 2.4. In this section, the expression for the ceiling bounce model that will be utilized throughout the thesis would be described. In the ceiling bounce model, the multipath IR channel is characterized by only two parameters; the optical path loss and the RMS delay spread D_{rms} . The impulse response $h(t)$ of the ceiling bounce model is given by [95]:

$$h(t, a) = \frac{6a^6}{(t + a)^7} u(t); \quad (6.1)$$

where $u(t)$ is the unit step function, $a = 2H_c/c$, H_c is the height of the ceiling above the transmitter and receiver and c is the velocity of light. The parameter ‘ a ’ is related to D_{rms} as:

$$D_{rms}(h(t, a)) = \frac{a}{12} \sqrt{\frac{13}{11}}. \quad (6.2)$$

For a more realistic channel model with multiple reflections, ‘ a ’ needs to be modified. For the un-shadowed and shadowed channels the expressions for ‘ a ’ are given by [95]:

$$a(\text{unshad.}) = 12\sqrt{11/13} (2.1 - 5.0s + 20.8s^2)D_{rms}(h_1(t)); \quad (6.3)$$

$$a(\text{shad.}) = 12\sqrt{11/13} (2.0 + 9.4s)D_{rms}(h_1(t)); \quad (6.4)$$

where $h_1(t)$ is one bounce impulse response and s is defined as the ratio of the horizontal transmitter-receiver (TR) separation to the TR diagonal, the latter being defined as the length of the segment of the line between the transmitter and the receiver.

Another important parameter that is used for study of performance at different data rates in a dispersive channel is the normalized delay spread D_T , which is a dimensionless parameter defined as:

$$D_T = \frac{D_{rms}}{T_b}. \quad (6.5)$$

6.3 Unequalized Performance

6.3.1 OOK

The block diagram of an unequalized OOK system is given in Figure 6.1. Except for the channel in Figure 6.1 considered to be dispersive with an impulse response of $h(t)$, the OOK system is identical to system given in Figure 2.7. The optical signal $x(t)$ is then subjected to the multipath distortion, hence the channel output $\varphi(t)$ in the absence of noise is given by:

$$\varphi(t) = x(t) \otimes h(t); \quad (6.6)$$

where the symbol \otimes denotes convolution. The receiver front consists of the unit energy filter $r(t)$, followed by a sampler and a threshold detector detail of which can be found in Section 2.7. The input signal to the matched filter is given by:

$$z(t) = R[\varphi(t) + n(t)]. \quad (6.7)$$

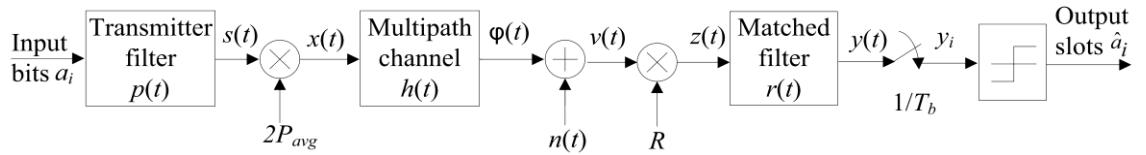


Figure 6.1: The block diagram of the unequalized OOK system.

The system can be modelled using the discrete time model and the discrete-time impulse response h_i of the cascaded system (the transmitter filter, channel and the receiver filter) is given as [96]:

$$h_i = p(t) \otimes h(t) \otimes r(t)|_{t=iT_b}; \quad (6.8)$$

with the normalization $\sum_i h_i = 1$ and sampling times are shifted to maximize the zero-sample h_0 . Unless the channel is non-dispersive, h_i contains a zero tap, a single precursor tap (with the largest magnitude) and possibly multiple postcursor taps. On a non-dispersive channel, the optimum sampling point, i.e. the point which minimises the probability of error, occurs at the end of each bit period T_b . However, on a dispersive channel, the optimum sampling point changes as the severity of ISI changes. The receiver filter output y_i corresponding to the penultimate bit, in the absence of noise, is given by:

$$y_i = 2RP_{avg} \mathbf{a}_i \otimes h_i|_{i=\zeta}; \quad (6.9)$$

where ζ is the number of channel taps and $\mathbf{a}_i = \{a_1, a_2 \dots a_\zeta\}$ is the ζ bit sequence.

The BER is approximated by averaging over all possible bits sequence of length ζ , and is given by [153]:

$$P_e = \frac{1}{2^\zeta} \sum_{i \in s_0} Q\left(\frac{RP_{avg}\sqrt{T_b} - y_i}{\sqrt{N_0}}\right) + \frac{1}{2^\zeta} \sum_{i \in s_1} Q\left(\frac{y_i - RP_{avg}\sqrt{T_b}}{\sqrt{N_0}}\right); \quad (6.10)$$

where s_0 and s_1 correspond to bit “0” and “1”, respectively.

The unequalized NOPR for OOK to achieve a BER of 10^{-6} in a diffuse channel with D_T of [0, 1] is given in Figure 6.2. The simulations are carried out for a data rate of 200 Mbps though the data rate (bit duration) used is irrelevant as the RMS delay spread is normalized to bit duration. For theoretical NOPR, the reader can refer to [51] and for

the power penalty using a five pole Bessel filter with a 3-dB cut-off frequency of $0.6/T_b$ filter refer to [96]. The NOPR in this chapter are entirely based on computer simulations.

It is clearly apparent from Figure 6.2 that the unequalized NOPR of OOK increases exponentially with D_T . A NOPR of 3 dB is incurred when D_T is ~ 0.24 . When D_T is 0.51, the NOPR is ~ 18 dB beyond which the target BER of 10^{-6} is practically impossible to achieve with a reasonable optical power.

The OPP in an unequalized system can be approximated using the worst-case bit sequences, consisting of a single one bit preceded and followed by a long string of zeros and the OPP at a low BER can be approximated using [96]:

$$\text{unequalised OPP (dB)} = 10\log_{10} \left[\frac{Q^{-1}(2^\xi \xi)}{(2h_0 - 1)Q^{-1}(\xi)} \right]. \quad (6.11)$$

The simulation and predicted (using (6.11)) OPPs for the OOK against the h_0 are given in Figure 6.3. There is a close match between the theoretical and simulated results for a range of h_0 . The OPP increases with the decreasing value of h_0 . This is expected for a channel with severe ISI where h_0 reduces.

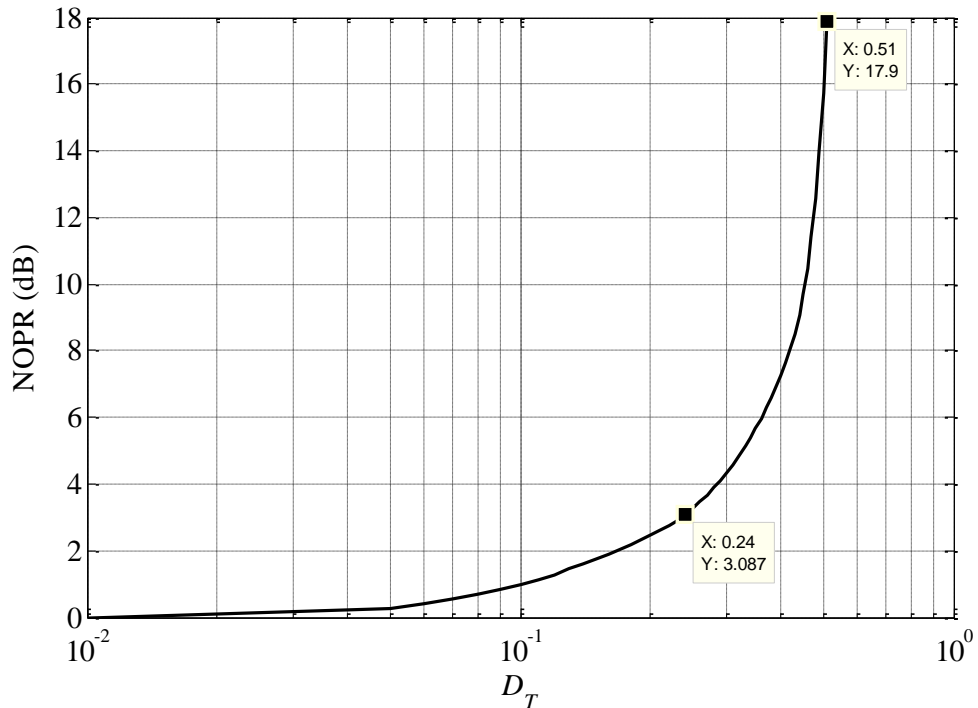


Figure 6.2: NOPR against the normalized delay spread D_T for unequalized OOK in a diffuse indoor OWC channel.

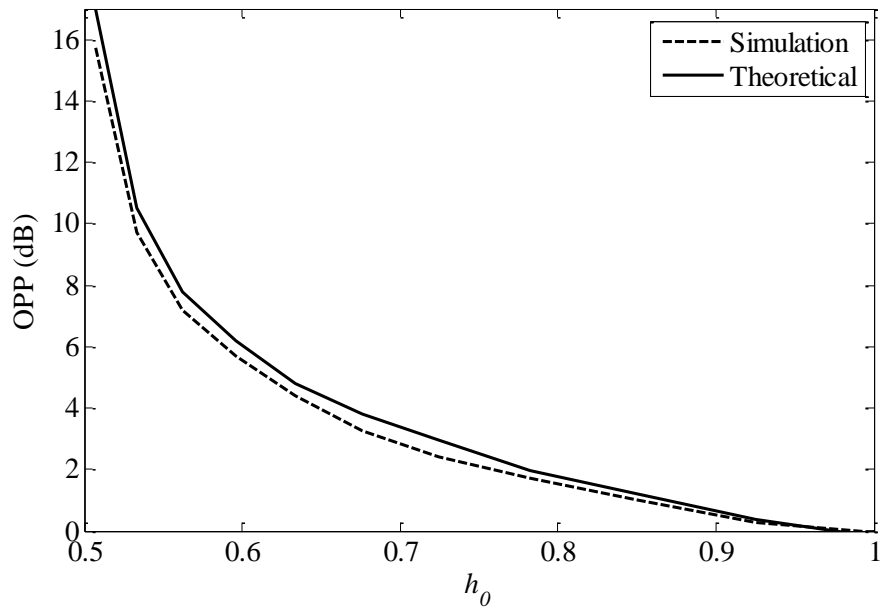


Figure 6.3: Theoretical and simulated OPPs for the unequalized OOK system against the h_0 .

6.3.2 PPM

The block diagram of the unequalized PPM system with both hard and soft decision decoding schemes is given in Figure 6.4. The detailed descriptions of the matched filter based receiver for the PPM system including the soft and hard decision decoding schemes are discussed in Section 2.8.1.2. The key difference here is the channel, which is dispersive with the impulse response of $h(t)$. The output of the matched filter is sampled and either a hard decision decoding or a soft decision decoding can be applied.

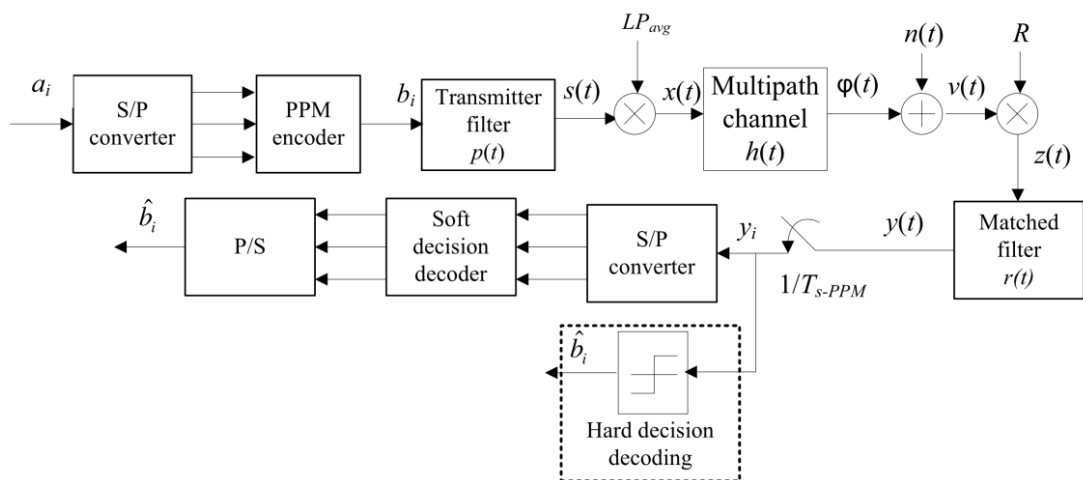


Figure 6.4: The block diagram of the unequalized PPM system with hard and soft decision decoding schemes.

To calculate the SER for the PPM hard decoding system, one need to consider all possible combination of the PPM symbols within the channel span ζ , calculate the slot error probability of individual slot and average over the entire channel span. Hence the slot error probability of PPM is given by:

$$P_{se_PPM_hard} = \frac{1}{2^\zeta} \sum_i \frac{1}{L} Q \left(\frac{y_i + \alpha_{opt}}{\sqrt{N_0/2}} \right) + \frac{(L-1)}{L} Q \left(\frac{\alpha_{opt} - y_i}{\sqrt{N_0/2}} \right); \quad (6.12)$$

where α_{opt} is the optimum threshold level. Unlike OOK, α_{opt} does not lie in the middle of the zero and one level due to unequal probability of occurrence of the empty slots and pulses. In fact α_{opt} is a complicated function of the bit resolution and the discrete-time impulse response h_i . An iterative approach to calculate the optimum threshold level α_{opt} and approximate $P_{se_PPM_hard}$ is taken in [51]. The iterative approach requires a significant computationally time, thus not practical for $\zeta > 20$ [51]. In this work a constant threshold level α_{th} is utilized which is given by:

$$\alpha_{th} = 0.5 - 0.25 \sum_{i=1}^{\infty} h_i. \quad (6.13)$$

The summation $\sum_{i=1}^{\infty} h_i$ provides the estimation of the energy of pulse that is spread to its adjacent pulses due to the dispersion. For a LOS link, the summation is zero and hence $\alpha_{th} = 0.5$. The dispersive channel will have a non-zero summation value. The value of α_{th} in a dispersive channel is less than 0.5. Assuming that one occurs in slot q of each symbol, the average symbol error probability for unequalized PPM soft decoding is given by [51, 181]:

$$P_{symbol_PPM_soft} = \frac{1}{2^\zeta} \sum_{i=1}^{\zeta} \sum_{\substack{p=1 \\ p \neq q}}^L Q \left(\frac{y_{(i-1)L+q} - y_{(i-1)L+p}}{\sqrt{N_0}} \right). \quad (6.14)$$

Computer simulations are carried out to determine the NOPR to achieve a SER of 10^{-6} for unequalized 4, 8 and 16-PPM with the soft and hard decision decoding schemes and are given in Figure 6.5. The threshold level given by (6.13) is used for the hard decision decoding. Also shown is the NOPR for OOK for comparisons. The soft decision decoding shows much improved performance compared to the hard decision decoding for all range of D_T and for all bit resolutions. The higher order PPM shows sharp

increment in the NOPR with increasing D_T for both soft and hard decision decoding schemes. This is due to the decrease in slot duration with the increase order for PPM, effectively increasing the ISI. For example, for $D_T > 0.19$, 4-PPM(hard) offers lower NOPR to achieve a SER of 10^{-6} compared to the 16-PPM(hard). For the soft decision decoding, the intersection point for 4-PPM and 16-PPM is ~ 0.24 . It can also be observed that OOK offer the least power penalty compared to all orders of the PPM(hard) for highly dispersive channel ($D_T > 0.27$) and 4-PPM (soft) offers the least power requirement for higher D_T values. The soft decision scheme offers improved resistance to ISI and difference in the OPPs for the soft and hard decoding increases with D_T . The difference in NOPR for the soft and hard decision decoding schemes increases from 1.5 dB at $D_T = 0$ to ~ 8.5 dB at $D_T = 0.4$ for 4-PPM with the soft decoding always requiring lower NOPR. The difference is even higher for 8 and 16-PPM with a noticeable difference of ~ 12.5 dB at $D_T = 0.23$ for 16-PPM. This clearly demonstrates the advantage of the soft decision decoding over the hard decision decoding in diffuse channel.

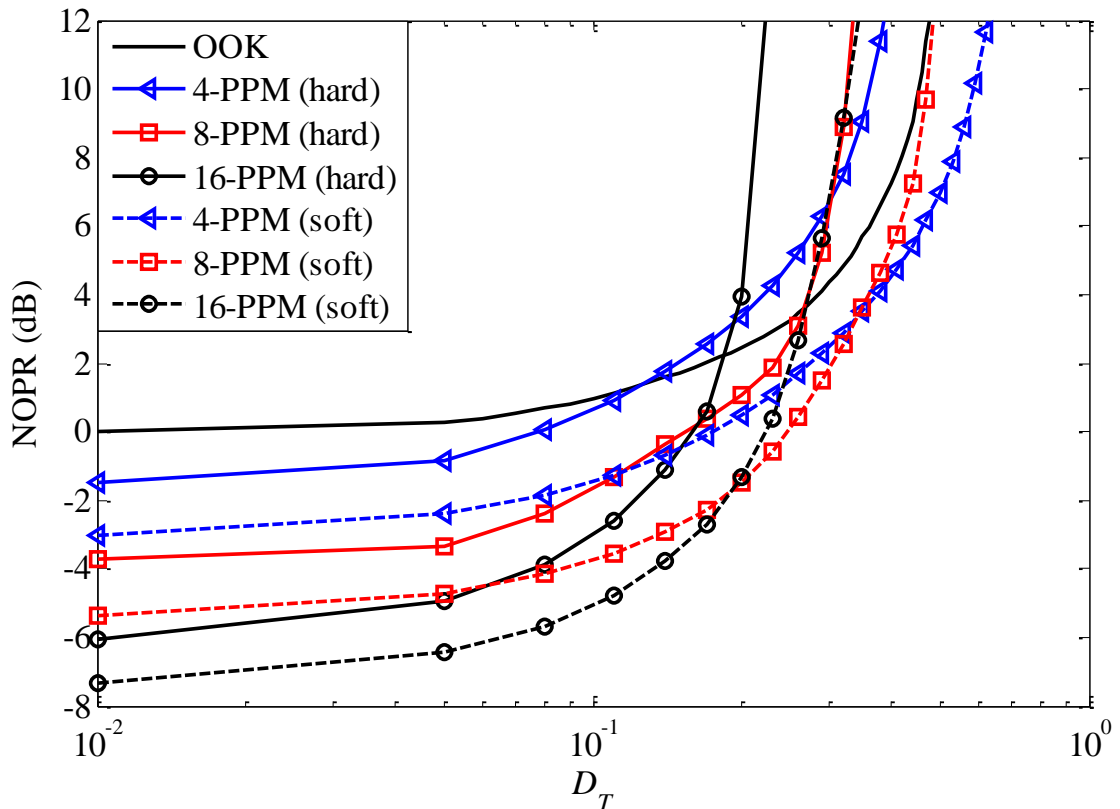


Figure 6.5: NOPR against the normalized delay spread for 4, 8 and 16-PPM with hard and soft decision decoding schemes in a dispersive channel.

6.3.3 DPIM

The block diagram of the matched filter based receiver for unequalized DPIM system is given in Figure 6.6. The matched filter based DPIM system is described in Section 2.8.1.3, hence is not repeated here. The only difference lies in the channel, which is considered to be dispersive. The channel output of the system in Figure 6.6 can be calculated using (6.6) and replacing T_b by the sampling time of DPIM in (6.8) gives the system impulse response. The output of the matched filter is sampled and sliced to generate the DPIM sequence.

Similar to OOK and PPM schemes, for calculation of the error probability all possible DPIM sequences of at least ζ slots are generated. The SER is approximated by averaging over all possible slot sequences of length ζ and is as follows:

$$P_{se_DPIM} = \frac{1}{2^\zeta} \sum_i^{2^\zeta} \frac{1}{L_{DPIM}} Q\left(\frac{y_i + \alpha_{opt}}{\sqrt{N_0/2}}\right) + \frac{(\bar{L}_{DPIM} - 1)}{L_{DPIM}} Q\left(\frac{\alpha_{opt} - y_i}{\sqrt{N_0/2}}\right). \quad (6.15)$$

Additional empty slot(s), immediately following a pulse, can be added to DPIM symbol to increase the immunity to the ISI due to multipath propagation [190]. The addition of the guard slots complicates the SER calculations and cannot easily be expressed in a concise form. For further discussion on the SER of DPIM(1GS), refer to [51]

The NOPR for unequalized DPIM system with zero and one guard slot in the diffuse channel is shown in Figure 6.7. The NOPR in this study is solely calculated using the Monte Carlo simulations. With no guard slots, the threshold level is set at half the energy level as it provides the near optimum error probability. However, for the optimum performance using one guard, the threshold level should be adjusted for different D_T . NOPR using (6.15) is reported in [51]. The difference with the result in [51] may appear as optimization is not carried out in this study. In this study, the threshold level for the DPIM(1GS) is calculated using (6.13). As in case of the PPM system, the NOPR for the DPIM increases more sharply for the higher order of the bit resolution due to smaller slot duration as the bit resolution increases. OOK shows the least NOPR for $D_T > 0.2$ compared to DPIM(0GS). The DPIM(1GS) scheme offers significantly improved performance compared to DPIM(0GS) especially at higher values of D_T . When decoding DPIM with a guard slot, if a pulse is detected then the

next slot is automatically assigned a zero. Since the adjacent slots to a pulse are the most affected by ISI, this approach of adding guard slot(s) provides a significant resistance to the ISI [190]. Expectedly, the optical power gain obtained using the guard slot increases with increasing D_T . The 4-DPIM(1GS) and 8-DPIM(1GS) offer lower NOPR compared to the OOK for all range of D_T .

In case of the DPIM with one or more guard slots, there can only be limited number of valid DPIM sequence. For example, the valid 3-bit sequence for DPIM(1GS) are given in Table 6.1. The valid DPIM(1GS) sequences do not contain two consecutive ones. Ignoring all zero sequence, it can be observed that bit sequences are orthogonal like in PPM symbol and hence there is possibility of soft decision decoding. However due to presence of all zero sequence in DPIM(1GS), a soft decision decoding approach applicable to PPM scheme need to be modified. In this study, a hybrid of soft and hard decision decoding for DPIM(1GS) is proposed. To explain the hybrid approach, the slot values (in bold) that must precede or proceed to make valid DPIM(1GS) sequence is also given in Table 6.1. In the case that no slot values given in bold means both pulse and empty slots are possible. Close look at this table reveals that all valid sequences have either 000 or 010 sequence. This unique pattern in valid DPIM(1GS) sequence can be exploited for the decoding. Considering central bit b_i is to be decoded, the hybrid decoding approach can be carried out using the following algorithm:

if $b_i > \text{threshold} \ \&\& \ b_i > b_{i-1} \ \&\& \ b_i > b_{i+1}$

$$\hat{b}_i = 1$$

else $\hat{b}_i = 0$

$$(6.16)$$

end.

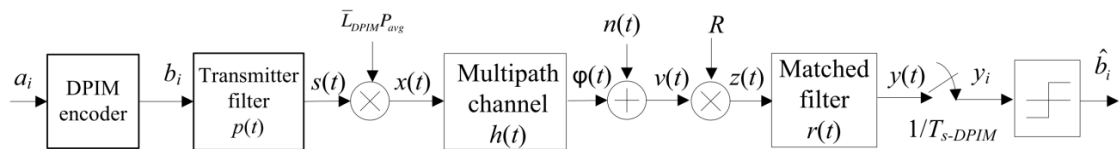


Figure 6.6: Block diagram of the unequalized DPIM system with a threshold detector.

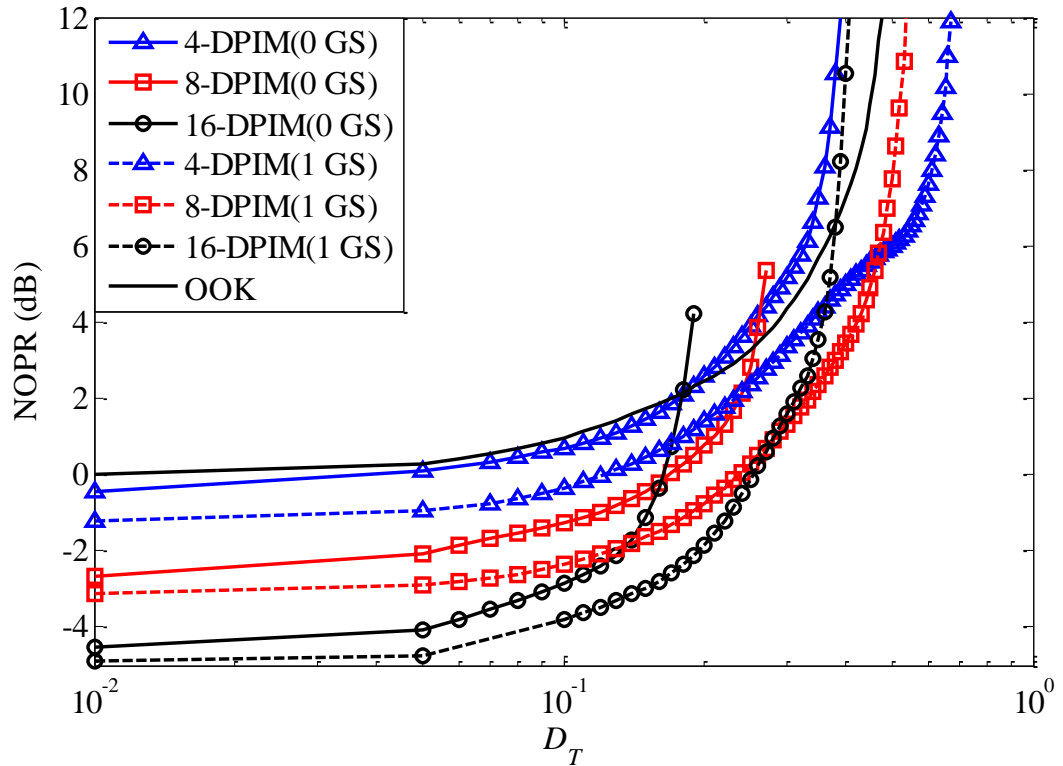


Figure 6.7: NOPR against the normalized delay spread for 4, 8 and 16-DPIM with and without guard slots in a dispersive channel.

Table 6.1: Valid DPIM(1GS) 3-bit sequence.

000
0010
010
0100

This literally means to assign a value of one to the slot with the highest amplitude if one or more slots within a 3-bit sequence have amplitudes greater than the threshold value. In a dispersive channel, since the adjacent slot contributes the maximum ISI, this simple algorithm can be effective in reducing the power penalty as in case of soft decision decoding PPM. Increasing guard slots can lead to further reduction in the power penalty at the cost of reduced throughput.

The NOPR against the normalized delay spread for 4, 8 and 16-DPIM(1GS) with hard and soft decoding schemes in a dispersive channel is given in Figure 6.8. The soft decoding here refers to the decoding based on the algorithm given in (6.16). The threshold level for the hard decoding is calculated using (6.13). However, the threshold level of $h_0/2$ is used for the soft decoding. Though importance of soft decoding is not noticeable for $D_T < 0.1$, a significant reduction in NOPR can be achieved using the soft decoding for a highly dispersive channel. Soft decoding 16-DPIM offers 0 and ~ 13.7 dB reduction in NOPRs compared to the hard decoding for D_T of 0 and 0.4, respectively. In 8-DPIM, the reductions in NOPRs are 0 and ~ 15.5 dB for D_T of 0 and 0.55, respectively. Lesser gain is achieved for 4-DPIM. The soft decoding can be applied to completely eliminate the power penalty in a less dispersive channel.

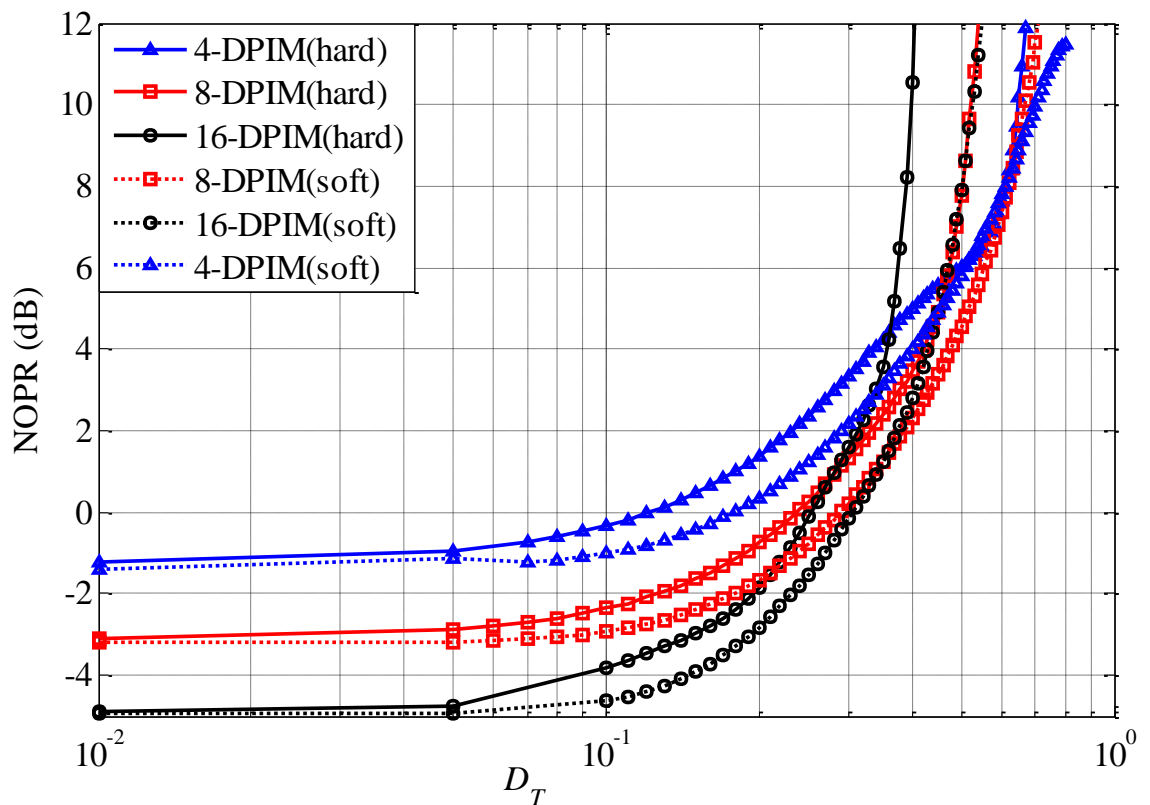


Figure 6.8: NOPR against the normalized delay spread for 4, 8 and 16-DPIM(1GS) with hard and soft decoding schemes in a dispersive channel.

6.4 Equalization Techniques

As explained in the Section 6.3, a significant power penalty incurs due to the ISI in a diffuse channel, which makes such a scheme practically less attractive particularly at higher data rates (i.e. > 10 Mbps). A number of solutions exist to reduce the effect of the ISI, with the optimum solution being the MLSD scheme [256], where data sequences are selected to minimize the Euclidean distance. However, practical implementation of MLSD is rather complex since the complexity increases exponentially with memory of the channel. Additionally, for modulation schemes with non-fixed symbol boundaries (DPIM and DPPM), MLSD scheme is not a practically viable option. Moreover, a simpler equalizing structures based on the FIR digital filter performs well and performance close to that of MLSD can be attained for indoor OWC channels [43, 249].

The block diagrams of the structure of a linear equalizer for the zero ISI at the sampling instant are given in Figure 6.9 and Figure 6.10, respectively. The receiver filter response $G_R(f)$ is generally matched to the transmitter filter response $G_T(f)$, i.e. $G_R(f) = G_T^*(f)$. For zero ISI at the sampling instant, the frequency response $G_e(f)$ of the equalizer should be inverse of the channel impulse response $C(f)$ [257]. i.e.:

$$G_e(f) = \frac{1}{C(f)}. \quad (6.17)$$

Since ISI caused by the channel is limited to a finite number of symbols, the practical channel equalizer is an FIR filter. Since the ISI is zero at the sampling instant, such a filter is called the zero forcing equalizer (ZFE). The structure of the channel equalizing filter is given in Figure 6.10. The tap weights C_n can be obtained by solving a simultaneous $2L+1$ equations as [258]:

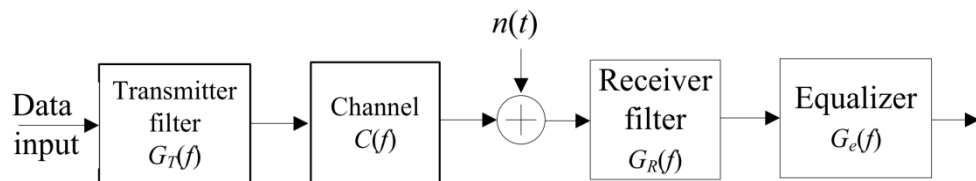


Figure 6.9: Block diagram of system with an equalizer [257].

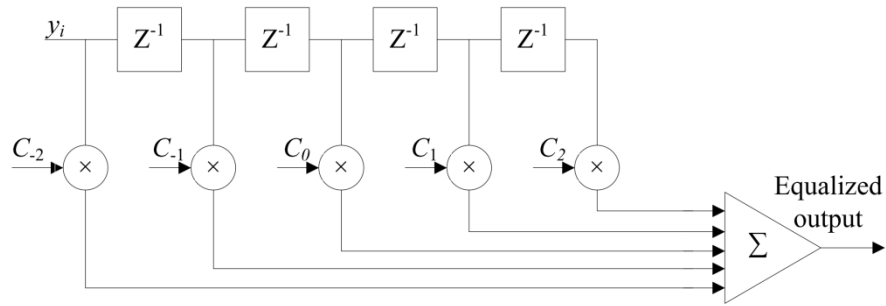


Figure 6.10: Block diagram of the linear equalizer.

$$\begin{bmatrix} y_0 & y_{-L+1} & \cdots & y_{-L} & \cdots & y_{-2L+1} & y_{-2L} \\ y_{L-1} & y_0 & \cdots & y_{-L+1} & \cdots & y_{-2L} & y_{-2L+1} \\ \vdots & \vdots & & & & & \\ y_L & y_{L-1} & \cdots & y_0 & \cdots & y_{-L+1} & y_{-L} \\ \vdots & \vdots & & & & & \\ y_{2L-1} & y_{2L-2} & \cdots & y_{L-1} & \cdots & y_0 & y_{-1} \\ y_{2L} & y_{2L-1} & \cdots & y_L & \cdots & y_1 & y_0 \end{bmatrix} \begin{bmatrix} C_{-L} \\ C_{-L+1} \\ \vdots \\ C_0 \\ \vdots \\ C_{L-1} \\ C_L \end{bmatrix} = \begin{bmatrix} 0 \\ 0 \\ \vdots \\ 1 \\ \vdots \\ 0 \\ 0 \end{bmatrix} \quad (6.18)$$

A major drawback of the ZFE is that it ignores the presence of additive noise which may result in a significant noise enhancement. This can be understood by noting that the equalizer filter response is the inverse of the channel response so the equalizer places large gain where $C(f)$ is small, boosting the noise in process. An alternative is a channel equalizer with the optimization based on the minimum mean-square error (MMSE) criterion [257]. The MMSE equalizer relaxes the zero ISI condition and selects a channel equalizer characteristic so that the combined power in the residual ISI and the additive noise at the output of the equalizer are minimized.

A significantly poor performance due to the noise enhancement can be observed using a linear equalizer for channels having a spectral null. In such cases, a nonlinear equalizer where the previously detected symbols are feedback to detect the present symbol can be implemented. A generalized structure of a DFE is given in Figure 6.11. The feedforward filter can be a fractionally spaced with adjustable tap coefficients and the feedforward filter is symbol spaced [249].

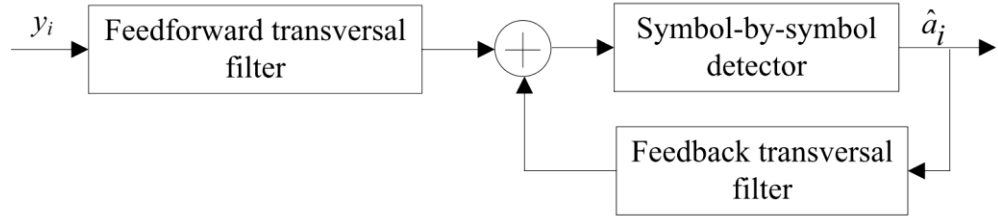


Figure 6.11: Structure of the decision-feedback equalizer.

Significant amount of research work have been reported on the performance of the DFEs for different modulation techniques in diffuse indoor OW links [43, 52, 67, 96-99]. DFEs are effective in mitigating ISI in indoor OW channels with a BER performance close to that of the MLSD [96]. Since transmission channel parameters are not known in advance and the physical channel is time varying; adaptive algorithms are the preferred option for equalization. In this scenario a training sequence is transmitted to approximate the channel characteristics, and is used at the receiver to adjust the equalizer's parameters accordingly. The adaptive algorithm is adopted throughout this chapter.

6.5 Equalization as a Classification Problem

Consider a baseband communication system as shown in Figure 6.1. The discrete received signal is given by:

$$y_i = \sum_{n=0}^{\zeta} h_n a_{n-i} + n_i = b_i + n_i ; \quad (6.19)$$

where b_i is the noise free channel output, n_i is the AWGN, and h_n is the channel taps given by the ceiling bounce model.

The J^{th} order equalizer has J taps with equally spaced delay τ for symbol space equalizer, where τ is the bit duration for OOK and the slot durations for other modulation techniques. The channel output can be written in vector form as:

$$\mathbf{Y}_i = [y_i \ y_{i-1} \ \dots \ y_{i-J+1}]^T; \quad (6.20)$$

where T represents the transpose operation. Hence the channel has J -dimensional observation space. Depending on the output vector \mathbf{Y}_i , the equalizer tries to estimate the transmitted sequence $\{\mathbf{a}_i\}$. In other words, the equalizer classifies the receiver vector \mathbf{Y}_i into one of the two classes: binary zero and binary one. The current and past $J + \zeta$ number of the transmitted symbols affect the classification decision of the equalizer. Hence, for a channel with an impulse response length of $\zeta + 1$, the possible combination of binary channel input sequence is [103, 250]:

$$\mathbf{a}_i = [a_i \ a_{i-1} \ \dots \ a_{i-\zeta-J+1}]^T. \quad (6.21)$$

The total number of the possible combinations of a_i is $n_s = 2^{J+\zeta}$. The corresponding noise free channel output vector referred to as the desired channel state is given by:

$$\mathbf{b}_i = [b_i \ b_{i-1} \ \dots \ b_{i-J+1}]^T. \quad (6.22)$$

The desired channel output state can be partitioned into two classes $\{0, 1\}$ according to the binary values of the transmitted symbol \mathbf{a}_i as [103, 250]:

$$\begin{aligned} \hat{\mathbf{a}}_i^+ &= \{\mathbf{b}_i | \mathbf{a}_{ik} = +\mathbf{1}\}; \\ \hat{\mathbf{a}}_i^- &= \{\mathbf{b}_i | \mathbf{a}_{ik} = -\mathbf{0}\}; \end{aligned} \quad (6.23)$$

where state $\hat{\mathbf{a}}_i^+$ corresponds to the input binary value of “1” and $\hat{\mathbf{a}}_i^-$ corresponds to the input binary value of “0”. The output of the channel clusters around the desired noise free outputs. The equalization problem is hence forming a decision boundary that corresponds to the transmitted symbol. Therefore, determining the values of the transmitted symbol with the knowledge of the observation vectors is basically a classification problem. Thus channel equalization is equivalent to partitioning of the J -dimensional channel output vectors into two decision regions.

The linear decision boundary may be utilized when the patterns are linearly separable. However, practical channels are not linearly separable and hence a linear boundary region on such channel is not the optimal. In general, the optimal decision boundary is nonlinear and the realization of the nonlinear decision boundary can be achieved by using ANN with a nonlinear transfer function.

6.6 Introduction to Artificial Neural Network

ANN is a mathematical and computer model which is loosely based on the biological neural networks. ANN, with a nonlinear statistical modelling capacity, is extensively used for modelling complex relationships between inputs and outputs and for pattern classification. Although introduced in 1948 [259], the extensive studies of ANN started only in the early eighties after important theoretical results related to ANN were attained. Now ANN finds its application in diverse areas such as the computing [260], medicine [261-263], finance [264], control system [265], statistical modelling [266], engineering [267].

ANN consists of simple processing units, neurons (or cells) interconnected in predefined manner. The neurons communicate by sending signals to each other. A neuron is limited to functionality of classifying only linearly separable classes [268]. However, ANN with many neurons can perform a complicated task like pattern classification, nonlinear mapping. In fact, ANN with sufficient number of neurons are universal approximators [269].

6.6.1 Neuron

Each neuron in the ANN does a simple task of modifying the input(s) by some predefined mathematical rule. The neuron has N inputs $\{ x_i : i = 1, \dots, N \}$, a weight w_i associating with each inputs and an output y . There may be additional parameter w_0 known as the bias which can be thought as weight associated with a constant input x_0 always set to 1. The functional block diagram of a neuron is shown in Figure 6.12.

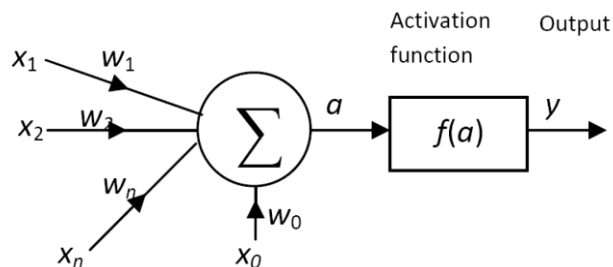


Figure 6.12: The schematic diagram of neuron showing inputs, a bias, weights and an output.

The intermediate output a can be calculated mathematically as:

$$a = \sum_i w_i x_i; \quad (6.24)$$

where $i=0, \dots, N$ if there is a bias and $i=1, \dots, N$ otherwise.

The output y is a function of the activation a and is given by:

$$y = f(a) . \quad (6.25)$$

The activation or transfer function $f(\cdot)$ depends on the application but is generally differentiable. Some popular activation functions are described below.

- (i) *Linear Function*: Defined as $y = ma$. For $m = 1$, the function is known as an identity function as the output is the exact copy of input.
- (ii) *Binary Threshold Function*: limits the activation to 1 or 0 depending on the net input relative to some threshold function. Considering a threshold level of θ , the output is given by:

$$y = \begin{cases} 1 & \text{if } a \geq \theta \\ 0 & \text{if } a < \theta \end{cases} . \quad (6.26)$$

- (iii) *Sigmoid Function (logistic and tanh)*: are commonly used activation functions for nonlinear processing and pattern classification. The output of the log-sigmoid function is a continuous function in the range of 0 to 1 defined as:

$$y = \frac{1}{1 + e^{-a}} . \quad (6.27)$$

The tan-sigmoid function is a variation of the log-sigmoid function as output ranges from -1 to +1, given by:

$$y = \tanh(a) . \quad (6.28)$$

6.6.2 ANN Architectures

The neurons can be interconnected in different and complex manners. The simplest way is to arrange neurons in a single layer. However there are other topologies, the most common are described below briefly.

- i. Single layer feedforward network:* It contains only an output layer connected to an input layer (Figure 6.13). The number of neurons in each layer varies depending on the number of inputs and outputs requirement for a particular application, but the network is strictly feedforward, i.e. signal flows from the input layer to the output layer only. Single layer networks are limited in capacity because of classification capability in linearly separable classes [268].
- ii. Multilayer feedforward network:* In order to extract the higher order statistics of data, higher number of neurons and layers are necessary [270]. Hence multilayer networks with capability of forming complex decision regions is utilised in different application. Provided there is a sufficient number of neurons a 2-layer ANN can be used as a universal approximator mapping any input-output data set [269]. Figure 6.14 shows a fully connected 2-layer network. Every multilayer network consists of (i) an input layer with no processing taking place, thus not counted as part of a network layer, (ii) a hidden layer and (iii) an output layer.
- iii. Recurrent neural network (RNN):* Unlike multilayer network, here the output is feedback to the input layer as shown in Figure 6.15. The network is very useful in time-series prediction. The training is more difficult in the recurrent network because of its chaotic behaviour [271]. Elman and the Hopfield networks are common recurrent network architecture [271].

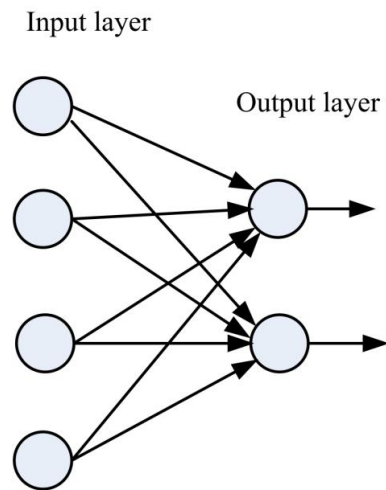


Figure 6.13: A single layer feedforward network with 2 output neurons.

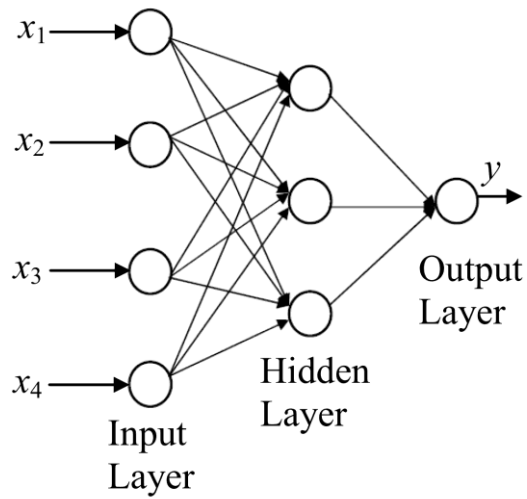


Figure 6.14: Fully connected feedforward multilayer network.

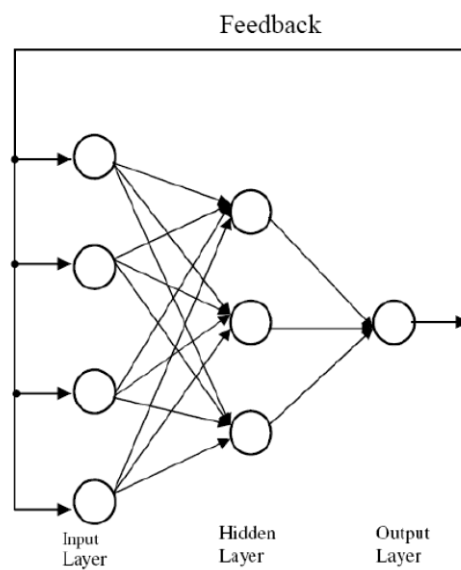


Figure 6.15: Neural network with feedback connection.

6.7 Training Network

The training of ANN is accomplished by providing ANN with the input and desired output data sets. The ANN can adjust its free parameters (weights and bias) based on the input and the desired output to minimize the cost function $E(n)$ (difference between the desired response $d(n)$ and actual response $y(n)$ of the network). The training process depends on two factors: a training data set and a training algorithm. The training data set should be representative of the task to be learnt. A poorly selected training set may increase the learning time. The training algorithm requires a minimization of the cost function. The convergence of cost function to the local minima instead of the global minimum has been an issue and algorithms based on the adaptive learning rate can improve the learning rate as well as a convergence to the global maximum [272, 273].

The learning can be classified into supervised and unsupervised learning. In supervised learning, the network is provided with an input-output pair that represents the task to be learnt. The network adjusts its free parameters so that the cost function is minimized. In unsupervised learning or self-organisation, the desired response is not present and the network is trained to respond to clusters of pattern within the input. In this paradigm the ANN is supposed to discover statistically salient features of the input population [274].

In this study, multilayer feedforward ANN is used for adaptive channel equalization for the indoor OWC. The supervised learning is more suitable of the equalization as the training sequence can be used to approximate channel more accurately. A popular supervised training algorithm known as the backpropagation (BP) is described below.

6.7.1 Backpropagation Learning

The BP supervised learning algorithm is the most popular training algorithm for multilayer networks. It adjusts the weight of ANN to minimize the cost function $E(n)$:

$$E(n) = \|d(n) - y(n)\|^2 . \quad (6.29)$$

BP algorithm performs a gradient descent on $E(n)$ in order to reach a minimum. The weights are updated as:

$$w_{ij}(n + 1) = w_{ij}(n) - \eta \frac{\partial E(n)}{\partial w_{ij}(n)} ; \quad (6.30)$$

where w_{ij} is the weight from the hidden node i to the node j and η is the learning rate parameter. The performance of the algorithm is sensitive to η . If η is too small, the algorithm takes long time to converge and if η is too large, the system may oscillate causing instability [270]. Hence adaptive learning rates are adopted for faster convergence [272, 273].

The BP can be summarised as [275]:

Step 1: Initialize the weights and thresholds to small random numbers.

Step 2: Present the input vectors, $x(n)$ and desired output $d(n)$.

Step 3: Calculate the actual output $y(n)$ from the input vector sets and calculate $E(n)$.

Step 4: Adapt weight based on (3.8).

Step 5: Go to step 2.

6.8 The ANN based Adaptive Equalizer

All practical channels are non-ideal in nature (i.e. introducing phase and amplitude distortions), thus resulting in the ISI. The effect of the channel is minimized at the receiver by incorporating an equalizer. Since practical channels are time-varying and channel parameters are not known in advance, an adaptive equalizer having a tapped delay line (TDL) with adjustable coefficients is preferred [179]. The current and past values of the received signals are linearly weighted by the equalizer coefficients and summed to produce an output. However, the distortion caused by a dispersive channel is nonlinear in nature in the most practical situations. Hence, the received signal at each sampling instant may be considered as a nonlinear function of the past values of the transmitted symbols [103]. Furthermore, channels are nonstationary; the overall channel response becomes a nonlinear dynamic mapping. On such channels, these equalizers exhibit poor performance [103, 252] and ANN with a nonlinear mapping capability has been proposed showing improved performance [103, 252, 276-280]. Fundamentally, the equalization problem is defined as a classification problem and ANN is employed for the classification [103, 250].

Since the channel parameters are not known in advance, the adaptive algorithm in which equalizing filter coefficients are adjusted using a training sequence is often the preferred model. The ANN based equalizer proposed here hence is an alternative to the adaptive linear and DF equalizers based on the traditional FIR digital filters. Both the linear and DF structures are investigated for equalization in a diffuse indoor OWC channel. The effectiveness of the ANN equalizer for a number of modulation schemes is discussed below.

6.8.1 Equalized OOK

The ANN based adaptive linear equalizer structure for OOK system is shown in Figure 6.16. The structure is similar to Figure 6.1, except for the receiver part. Since the matched filter based receiver is non-optimum for a dispersive channel where a significant power penalty incurs, it is replaced by an ANN based receiver in Figure 6.16. The received signal is sampled at the data rate R_b . The sample outputs are passed through a feedforward filter and ANN for equalization. The output of the ANN is sliced using a threshold value of 0.5 to generate a binary zero or one.

The detailed structure of the feedforward filter and an ANN based equalizer is shown in Figure 6.17. The sampled output y_i is passed through a TDL of length J . The output vector from the TDL is fed in to the ANN for classifications. For the effective use of ANN as an equalizer, ANN is first trained by transmitting a number of known OOK symbols. The ANN parameters are then adjusted to make the difference between the desired output and the ANN output as small as possible. The BP training algorithm is given in Section 6.7. Once the network is trained, it can be used as an equalizer.

The DF structure based on the ANN is shown in Figure 6.18 and Figure 6.19. The detected signals are fed back to the ANN equalizer through a feedback TDL of length K . The nonlinear structure due to the feedback filter provides enhanced performance compared to the linear structure. In this DF structure, the previously detected signal is fed back to ANN. The basic idea of the feedback structure is that if previously detected symbols are known, with appropriate weighting, the ISI contributed by these symbols can be cancelled out. One of the key problems of the DF structure is the possibility of error propagations as the detector error is feedback to the system.

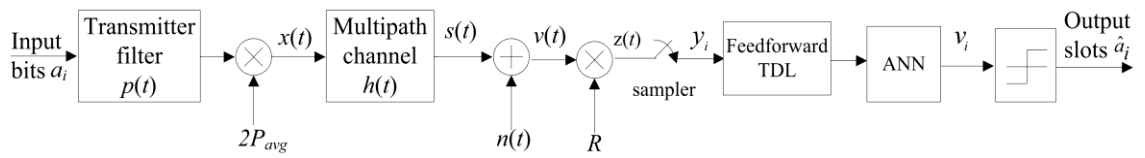


Figure 6.16: The system block diagram of ANN based linear equalizer for indoor OW communication.

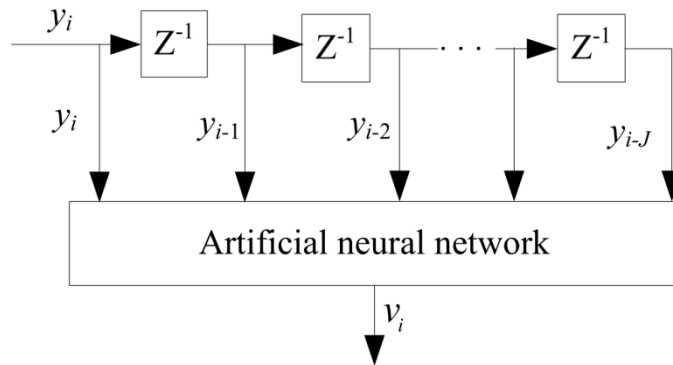


Figure 6.17: ANN based linear equalizer structure.

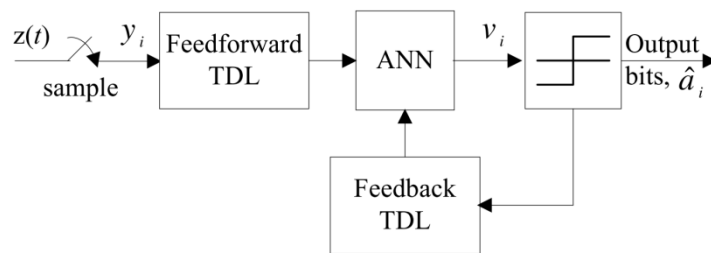


Figure 6.18: System block diagram of ANN based DFE receiver.

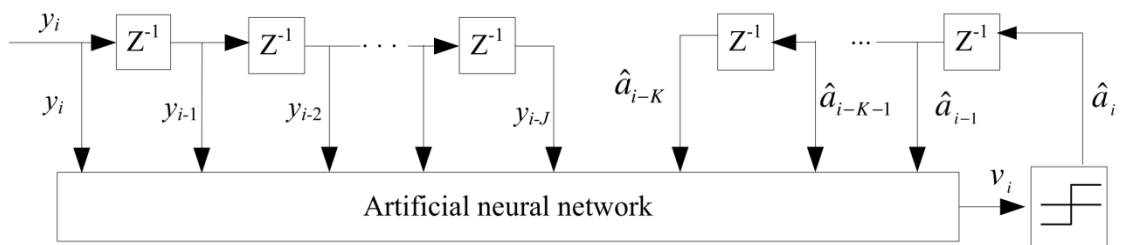


Figure 6.19: ANN based DFE structure.

These are open questions: what should be the size of the network? What architecture should be chosen? How many layers should be in the network? There are not satisfactory answers to these questions nor a predefined rule. The number of neurons in the input and output layers depends on the input vector and the desired outputs. However, the number of hidden layers and neurons can be varied. Increasing the hidden layers results in increased system complexity and the training time; however too few neurons may result in an unsatisfactory performance. The goal of optimising ANN is to find an architecture which takes less time to train, less storage requirement and less complexity without performance degradation. There are two major approaches for designing an optimal network structure: (i) build a larger network and prune the number of neurons with reduced connections, and (ii) start with a small network and neurons and continue to grow until the desired level of performance is achieved [281].

Theoretically there is no reason for using more than two hidden layers; practically the ANN structure with a single hidden layer is sufficient. Using two hidden layers rarely improves the model, and it may introduce a greater risk of converging to a local minima of cost function [282]. If sufficient neurons in a hidden layer are used, then it is not necessary to use more than one hidden layer [283]. Due to the risk of converging to the local minima, a single hidden layer is utilized with sufficient number of neurons. Theoretically, it is difficult to determine the exact number of neurons required in the hidden layer. Hence in this study, six neurons in the hidden layer is utilized as simulation results have shown that it could provide near optimum results for all range of delay spread for all modulation techniques, though the number of neurons can be reduced for a less dispersive channel.

Another key issue in applying the ANN in supervised learning method is the learning algorithm. Although the philosophy of all training algorithms is the same; to minimize the cost function; they differ in the algorithm to obtain the minimization of cost function. Some training algorithms converge faster, but require larger memory space while some guarantee convergence to the global minimum of cost function [272]. The training algorithms available in Matlab 7.4.0 are listed in Table 6.2. For the comparative study, a 2-layer ANN with six and 1 neurons in the hidden and output layers, respectively is selected. The SNR is chosen as 24 dB for all simulation with a different combination of transfer functions. For each training algorithm, a total of 9 simulations are carried out and the average time required for successful training is calculated and

listed in the second column of Table 6.2. The Levenberg-Marquardt algorithm requires the least time to train whereas the variable learning rate (traingdx) requires the longest time. However, it is to be noted that the memory requirements for the Levenberg-Marquardt algorithm is larger than for any other algorithms [284]. Another key factor in selecting the training algorithm is the performance evaluation under different conditions. The BER performance for a range of SNRs and the channel delay spreads are simulated for training algorithms requiring a training time of < 3 second. It is found that the scaled conjugate gradient algorithm provides the most consistence performance with improved performance compared to the Levenberg-Marquardt in a highly dispersive channel. Based on the optimization discussed above, a feedforward backpropagation ANN with the parameters given Table 6.3 is chosen for the all the simulations hereafter.

Table 6.2: The list of training algorithm for ANN.

Training algorithm	Average training time (second)
Levenberg-Marquardt	1.88
BFGS algorithm	7.00
Variable learning rate	4.2
Resilient backpropagation	2.64
Scaled conjugate gradient	2.83
Conjugate gradient with Powell/Beale restarts	3.07
Fletcher-Powell conjugate gradient	3.90
Polak-Ribière conjugate gradient	2.46

Table 6.3: ANN parameters for equalizations.

Parameters	Values
ANN type	Feedforward BP MLP
Number of hidden layer	1
Transfer functions (hidden layer)	Log-sigmoid
Transfer functions (output layer)	Linear
Training length	1000
Training algorithm	Scaled conjugate gradient

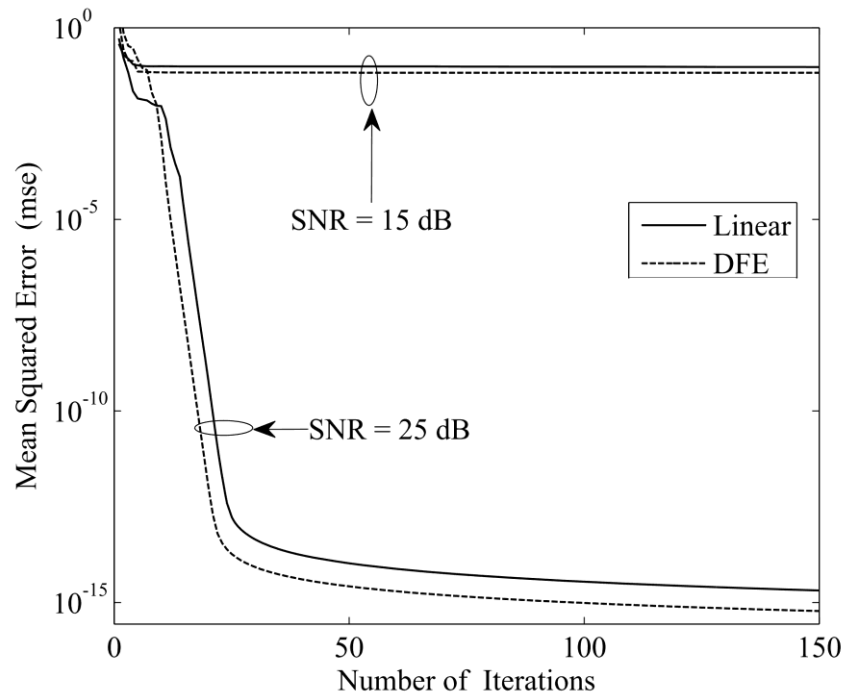


Figure 6.20: The MSE against the number of iteration for ANN based equalizer (linear and DFE) for a channel with D_T of 2 at data rate of 200 Mbps.

For comparative study of the linear and DF equalizers, the mean square error (MSE) while training, can give a clear indication of the relative performance of the equalizers. MSEs against the number of iterations for the linear and the DF structures for OOK with a D_T value of 2 are given in Figure 6.20. All the simulation parameters for both equalizers were kept the same and the error propagation in the DF equalizer is not taken into considerations. It is obvious that lower MSE values are hard to obtain at lower SNR values (i.e. 15 dB) as the AWGN is the dominant source of noise indicating the possibility of higher BER. MSE at a SNR value of 25 dB is significantly low for both structures, thus illustrating successful training and improved performance. For both SNR values, the DF structure shows slightly lower MSEs compared to that of the linear equalizer, thus signifying the possibility for improved performance. The training is effectively accomplished after 50 iterations for the SNR value of 25 dB since no significant changes to the MSE are observed.

The trained ANN can be used for the adaptive equalization in dispersive channels. The NOPR for the ANN based linear and DF equalizers for a range of D_T are shown in Figure 6.21. Also shown is the NOPR for the unequalized case for a matched filter based receiver. The DF scheme offers the least NOPR for all range of D_T closely followed by the linear case. Unlike the unequalized system where the irreducible NOPR

can be observed at $D_T > 0.5$, the equalized cases do not show such case even for $D_T = 2$ for both linear and DF equalizers. The linear and DF schemes show identical performance for $D_T < 1$ varying only at $D_T > 1$. At lower D_T values, typically < 0.01 , the equalizers show no improvement in the performance. However, the effectiveness of the equalizer in reducing the NOPR becomes apparent with increasing D_T . The optical power gain achieved with the equalizer increases as the channel became more dispersive. For example, DFE yields NOPR reduction of ~ 0.8 dB and ~ 6 dB for D_T of 0.1 and 0.4, respectively. Compared to the LOS ($D_T = 0$) case, the OPP for D_T of 2 is ~ 6 dB for DFE, OPP increases with D_T . Two factors have contributed to the power penalty: (i) ever presence of the residual ISI particularly when channel is highly dispersive and (ii) incorrect decisions being feedback to ANN [179].

It is not possible to predict the exact OPP for the adaptive DFE as the equalizer parameters are adjusted based on the training sequence. Since adaptive ANN has been used, the weight and the bias of ANN are difficult to predict, which in turn give rise to difficulty in predicting the exact impulse response of the ANN. The expression for estimation of OPPs for the unequalized and ZF-DFE are given in [96] in which the expression for the ZFE is derived by using the polynomial curve fitting method and OPPs are given by [96]:

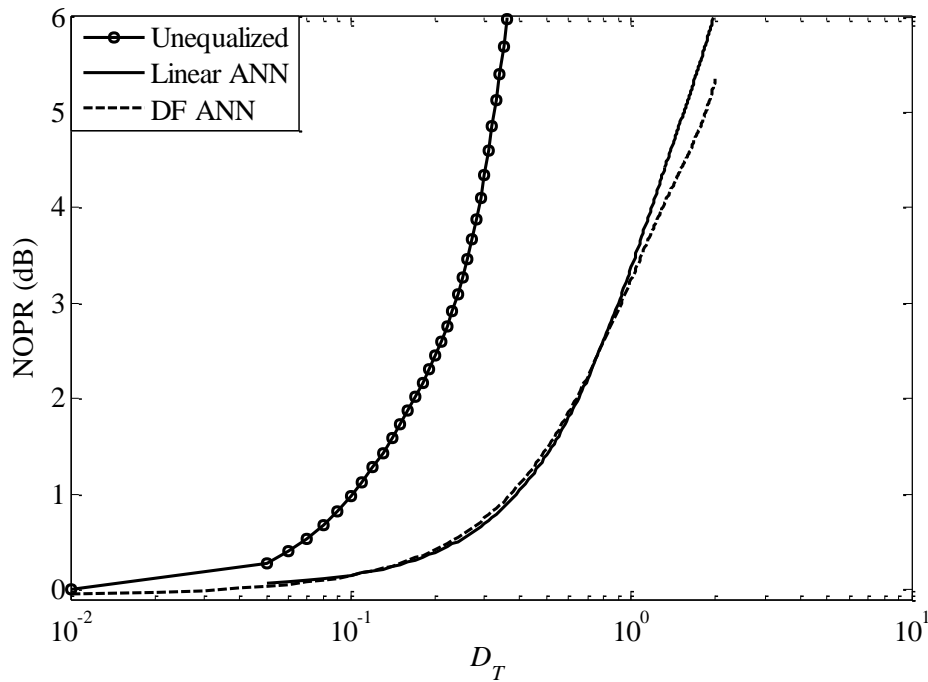


Figure 6.21: NOPR versus the normalized delay spread for unequalized and ANN equalized (linear and decision feedback) OOK schemes.

$$\text{DFE OPP (dB)} = 3(h_0^{-1} - 1). \quad (6.31)$$

Equations (6.11) and (6.31) suggest that there is a strong relation between the OPPs and h_0 for the unequalized and equalized systems. The predicted and simulated OPPs against h_0 for the DFE and unequalized systems at a data rate of 200 Mbps are given in Figure 6.22. The OPPs for both equalized and unequalized OOK have a similar profile showing an exponential growth while decreasing h_0 . As expected, the slope for the equalized system is much reduced compared to the unequalized system. The predicted results using (6.31) matches the simulated results only for a less dispersive channel ($h_0 > 0.6$) and the clear deviation in the curve appears for $h_0 < 0.6$. For a highly dispersive channel, it is not feasible to predict OPP using only h_0 as the residual ISI in the equalized system can expand beyond a bit duration. Since the indoor OW channel shows an exponential decay in the impulse response, the residual ISI decrease exponentially. By observing the trend of the OPP, it is found that OPP can be predicted with a high degree of accuracy if an impulse response taps of h_0 and h_1 are considered. The following expression provides a better estimation of OPP, which is found using curve fitting method.

$$\text{DFE OPP (dB)} = -10 \log_{10}(h_0 + 0.3h_1). \quad (6.32)$$

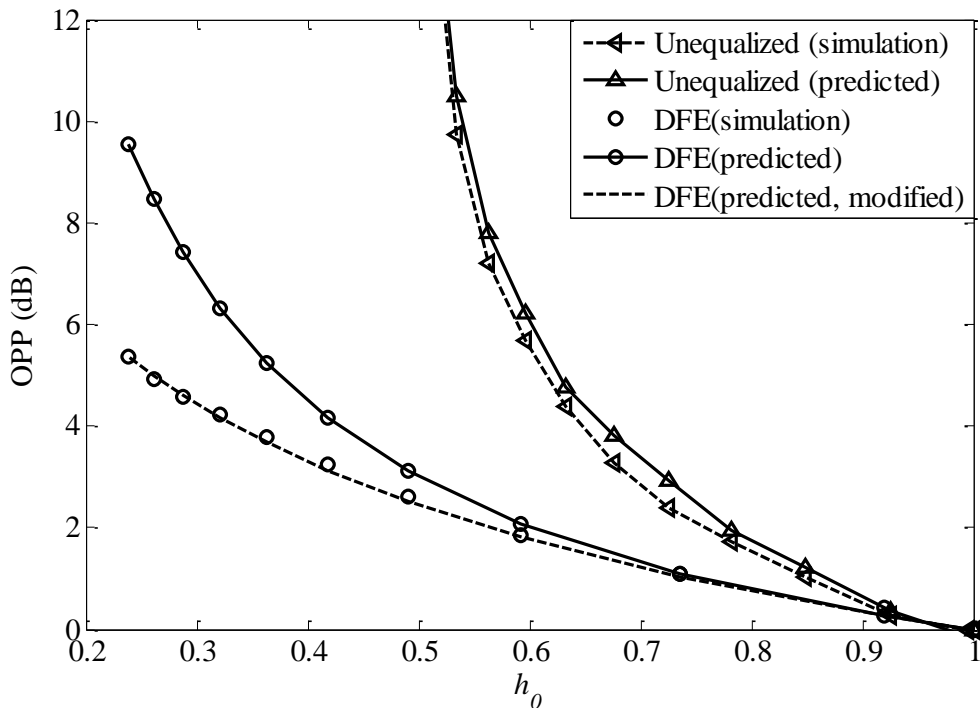


Figure 6.22: The simulation and predicted optical power penalty against h_0 for unequalized and equalized (DF) OOK systems at a data rate of 200 Mbps.

Since the channel impulse response is exponentially decaying, the effect of h_1 is much reduced compared to h_0 in the OPP and hence h_1 is scaled by 0.3. The scaling factor is found by a trial and error method and OPP for the modified expression in (6.32) is given in Figure 6.22. It can be observed that (6.31) and (6.32) provide identical OPPs for $h_0 > 0.6$. However, the modified expression provides a close match to the simulated results for a highly dispersive channel. A further channel component beyond h_1 might be necessary to consider to predict the exact OPP if the channel becomes dispersive.

6.8.2 Equalized PPM

The adaptive linear and DF equalization structures for the PPM schemes for both hard and soft decision decoding schemes are shown in Figure 6.23 and Figure 6.24, respectively. The received PPM signal is sampled at $1/T_{s-PPM}$ which is passed to the ANN through a TDL for equalization. The structure of the linear equalizer for the PPM scheme is essentially similar to that of the OOK equalizer. A trained ANN is used for the channel equalization. The hard or soft decision decoding schemes can be carried out to the equalized output for regeneration of PPM symbols. Similar to the OOK, a threshold value of 0.5 is used for the hard decoding scheme. However, in the soft decision decoding, the entire slots within the symbol are compared and a slot with the maximum amplitude is assigned one and all other slots are automatically set to zero. The DF structure for hard decision decoding is simple to implement as the hard decision output can be directly feedback to the ANN (Figure 6.24). However, the DF is difficult to implement for soft decision decoding as the receiver has to buffer a PPM symbol before making a decision. The delay in the decoding means a soft decision output cannot be feedback to ANN. One simple approach is to feedback the hard decision output as shown in Figure 6.24. The key issue for the soft decision decoding is the feedback of the hard decision. As a result, the error in the hard decision tends to propagate. Thus, a significant performance improvement is difficult to achieve using soft decision decoding compared to the hard decision though complexity increased significantly as both hard and soft decision decoding is necessary at the receiver.

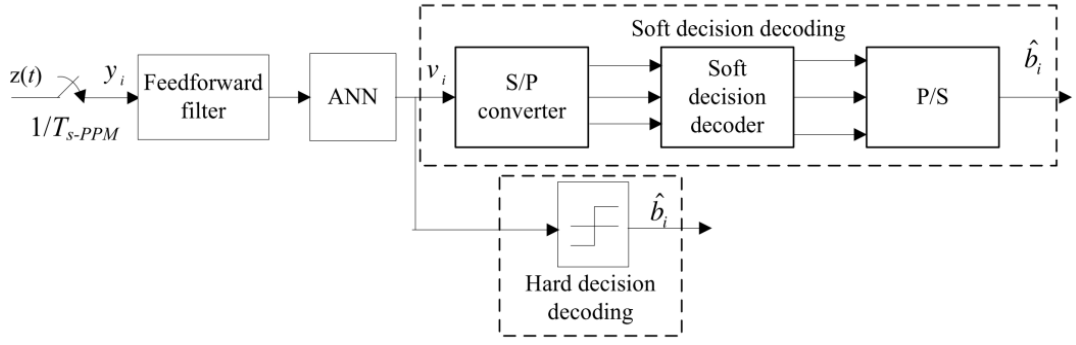


Figure 6.23: ANN based linear equalizer for soft and hard decoding PPM scheme.

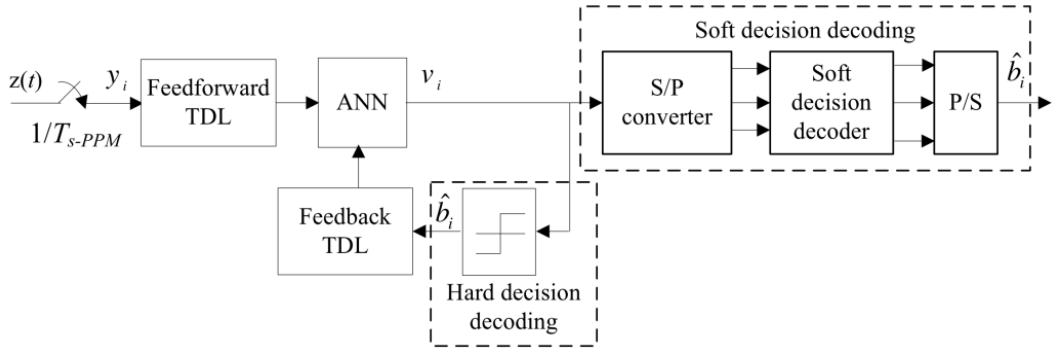


Figure 6.24: ANN based DFE for soft and hard decoding PPM scheme.

The NOPR to achieve a SER of 10^{-6} for the PPM hard decision decoding scheme with an ANN based adaptive linear equalizer for a range of D_T is shown in Figure 6.25. Also shown is the NOPR for the unequalized PPM. Equalized soft decoding offers improved performance compared to the hard decoding for all range of D_T and for all bit resolutions, though NOPR difference for the hard and soft decision decoding schemes decrease as the channel become more dispersive. Similar to the unequalized case, the NOPR for the equalized cases also shows an exponential growth. However, the gradients of the curves are significantly reduced and do not shows the infinite power penalties even at a D_T of 2. Unlike the unequalized cases where higher order PPM shows a sharp rise in the NOPR with the increasing value of D_T , equalized systems show almost similar profile for all bit resolutions with reduced increment in the power penalty. As expected, the reduction in NOPR for the equalizer system compared to the unequalized case increases with increasing value of D_T . For example, the reduction in NOPR for the equalized system compared to the unequalized case is 0 dB and ~ 7.3 dB at D_T values of 0.01 and 0.3, respectively for 4-PPM. However, the gain is larger for 8-PPM with ~ 9.6 dB difference at D_T of 0.3. Higher gain is achieved at higher values of D_T . However, comparison is not possible for the higher D_T values as the unequalized cases require very high NOPR.

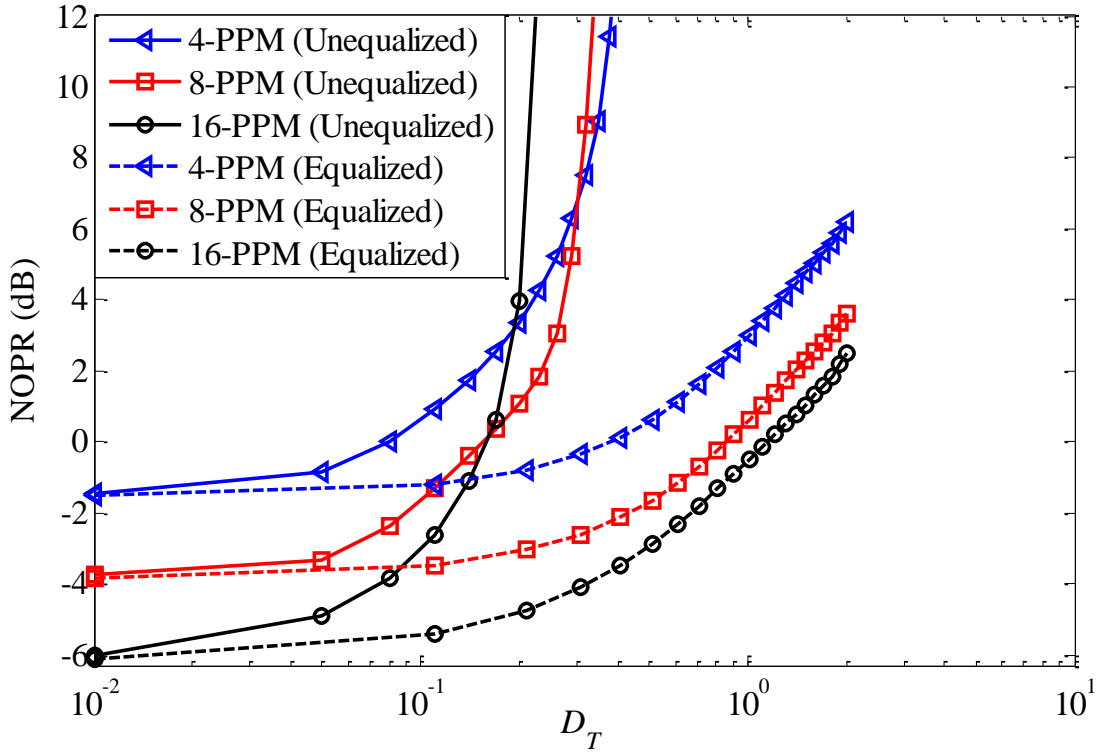


Figure 6.25: NOPR against the normalized delay spread D_T for unequalized and ANN based linear equalizer for PPM hard decision decoding scheme.

Further insight in the performance of equalized system can be achieved by observing the OPPs for different bit resolutions as shown in Figure 6.26. The OPP is calculated by subtracting the NOPR for the equalized system from the LOS system while keeping the modulation techniques and bit resolution the same. The curves show that OPP are the least and highest for the OOK system with the widest slot duration and 16-PPM with the shortest slot duration respectively. An interesting feature is that 4-PPM and 8-PPM show almost identical OPPs. Two factors are involved for the feature (a) the slot duration and (b) the probability of two consecutive pulses. Since 8-PPM has shorter pulse duration, the OPP should be higher than for 4-PPM. On the other hand due to longer symbol length, the probability of two consecutive pulses is significantly lower for 8-PPM compared to 4-PPM, hence the power penalty related to two consecutive pulses is higher for 4-PPM (note that avoiding two consecutive pulses can provide significant performance improvement as in DPIM [190]).

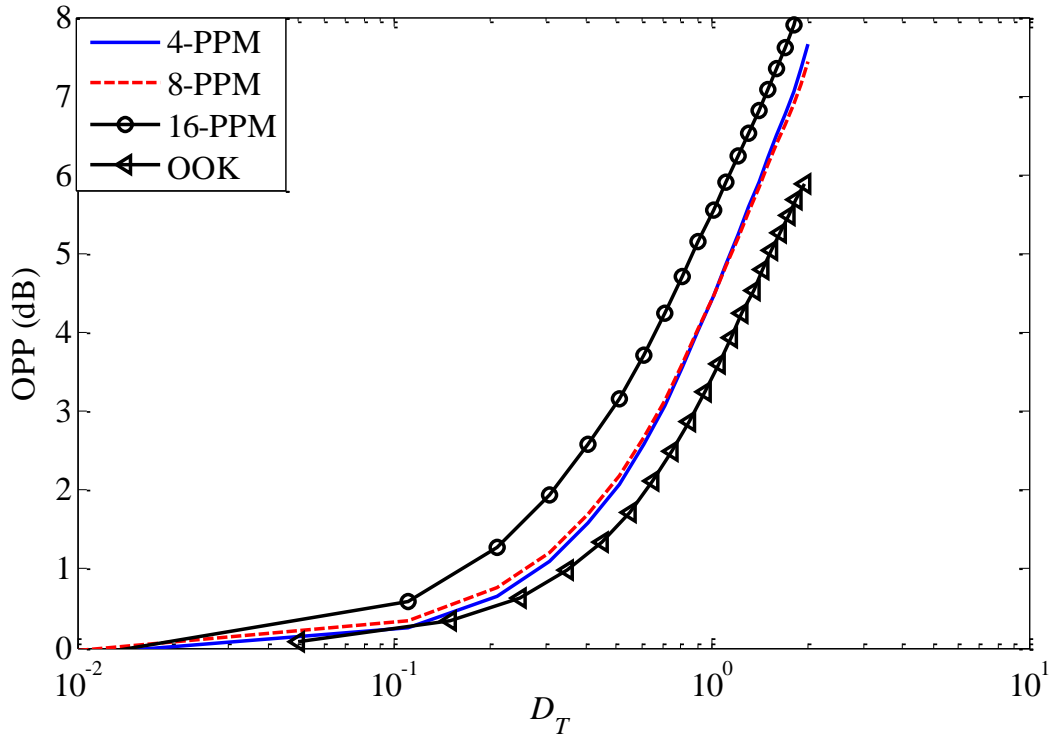


Figure 6.26: OPP against the normalized delay spread D_T for unequalized and ANN based linear equalizers for PPM with a hard decision decoding scheme.

The NOPR against D_T for the soft decision 4, 8 and 16-PPM with an ANN based adaptive linear equalizer is depicted in Figure 6.27. Also shown is the NOPR for the unequalized cases. As in other equalized cases, the equalized system illustrates a significantly improved performance compared to unequalized cases and showing no infinite NOPR for the D_T of 2. Since the soft decision decoding provides natural immunity to the ISI even without an equalizer, the reduction in NOPR using the equalizer is higher for the hard decision decoding. For example, the equalized system offers a reduction of ~ 7.3 dB and ~ 4 dB in NOPR for 4-PPM system at D_T of 0.3 for the hard and soft decision decoding schemes, respectively. It should be noted that higher gain in the equalized hard decision should not be interpreted as ineffectiveness of the equalizer for the soft decoding. Rather the soft decoding without an equalizer also provides some resistance to the ISI, meaning reduced gain with an equalizer. For example, the NOPRs for the unequalized 4-PPM at a D_T of 0.3 are ~ 6.9 dB and ~ 2.5 dB for the hard and soft decision decoding schemes, respectively. For the equalized systems, the NOPRs are ~ -0.42 dB and ~ -1.51 dB for the hard and soft decision decoding respectively. This clearly indicates that the soft decoding offer reduced NOPR for both the equalized and unequalized systems.

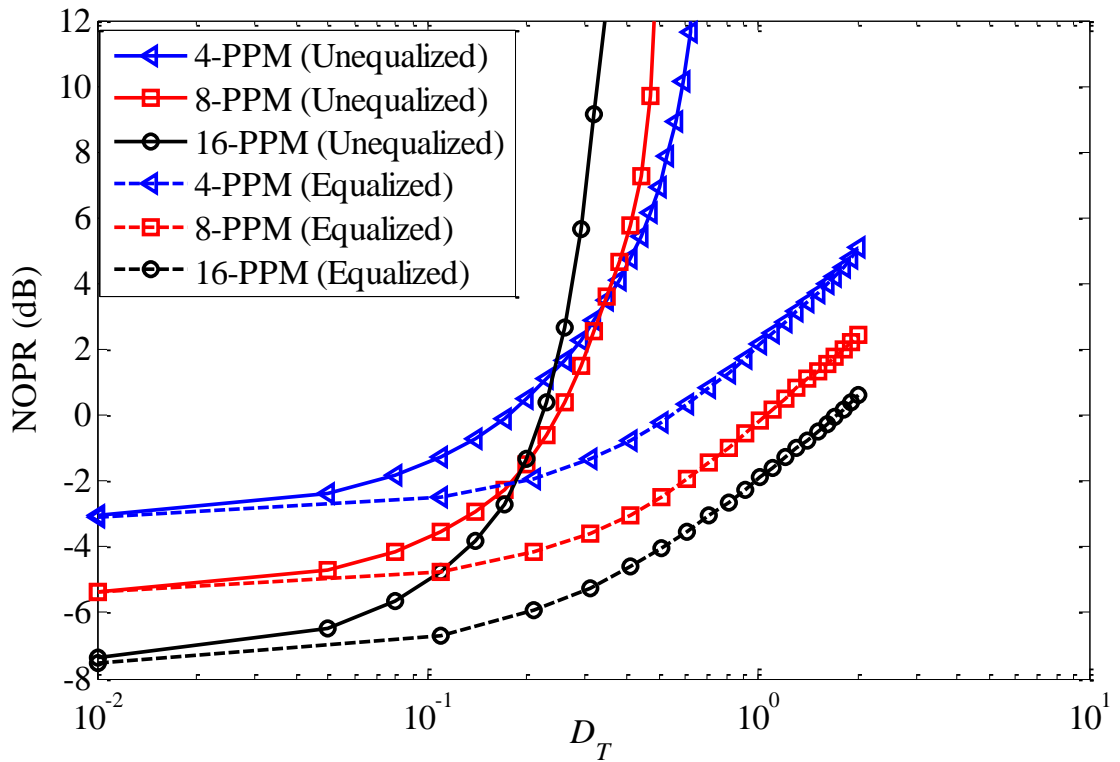


Figure 6.27: NOPR against the normalized delay spread D_T for unequalized and ANN based linear equalizers for PPM with a soft decision decoding scheme.

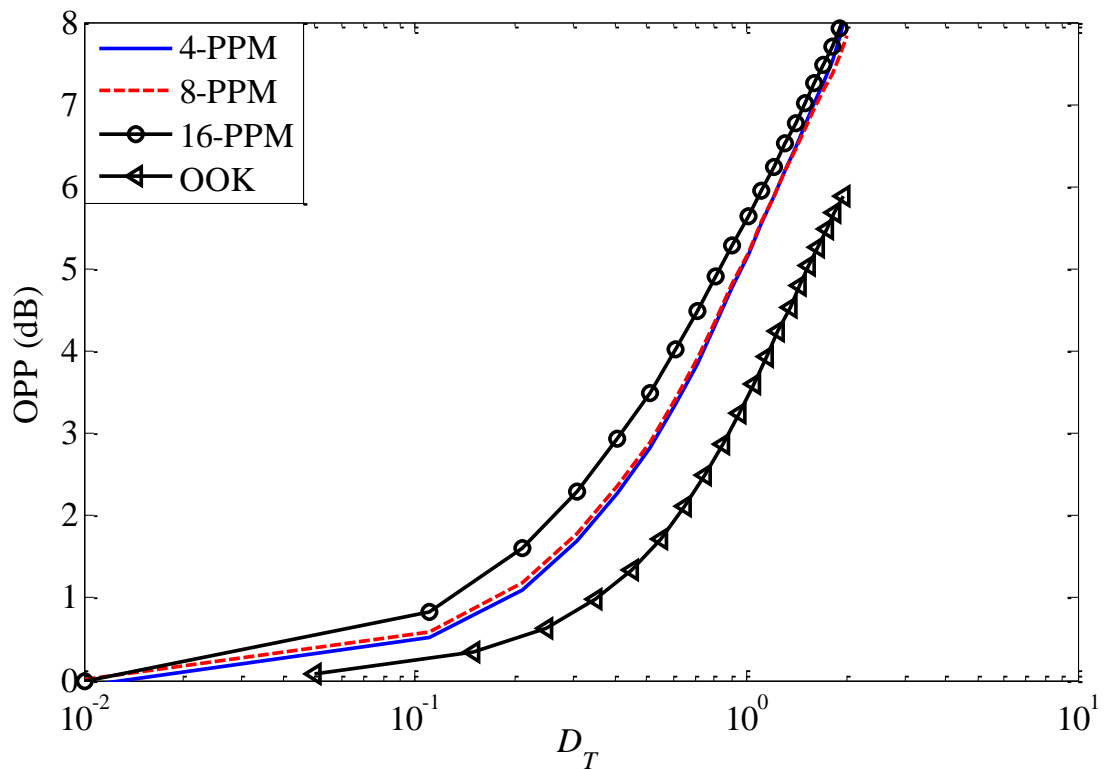


Figure 6.28: OPP against the normalized delay spread D_T for unequalized and ANN based linear equalizers for PPM with a soft decision decoding scheme.

The OPP for the equalized PPM system with the soft decision decoding for D_T of $[0, 2]$ is given in Figure 6.28. As in the case of hard decision decoding, the OPP is the highest for 16-PPM. However, the difference of OPPs between 4, 8 and 16-PPM is small and the OPP tends to approach the same value at higher value of D_T . As explained previously, the key roles are played by the power penalty due to the slot durations and the probability of two consecutive slots.

The comparative study of ANN based linear and DF equalizers for the PPM with a hard decision decoding scheme are carried out for different values of D_T and OPP versus D_T is demonstrated in Figure 6.29. Like the case of OOK, DFE provides a significant reduction in OPP compared to the linear equalizer only when the channel is highly dispersive, see Figure 6.29. The performance gain with DFE compared to the linear equalizer is apparent for $D_T > 0.2$ and the gain increases as the channel becomes more dispersive. The OPPs difference for the DF and linear equalizers are ~ 0.1 dB and ~ 0.6 dB for 16-PPM at D_T of 0.2 and 1, respectively. Like the linear equalizer case, the OPPs for the 4-PPM and 8-PPM are identical for DFEs. The simulation confirmed that DF soft decoding does not provide any improvement in performance compared to the hard decoding due to the hard decision decoding in feedback loop (see Figure 6.24) and hence is not reported here.

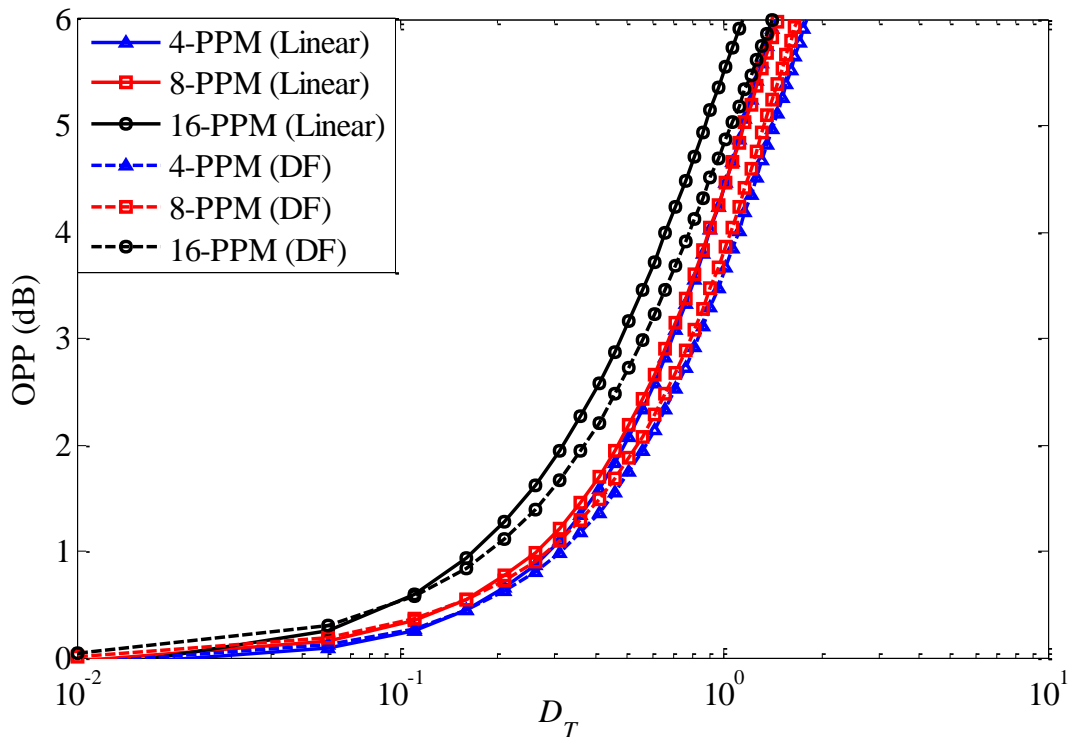


Figure 6.29: OPP versus the normalized delay spread D_T for ANN based linear and DF equalizers for PPM with a hard decision decoding scheme.

6.8.3 Equalized DPIM

The structures of the ANN based linear and DF equalizers for DPIM system are given in Figure 6.30 and Figure 6.31, respectively. The transmitter part and the channel are exactly the same as in Figure 6.6 and hence they are not duplicated here. The random binary data are first converted into a DPIM sequence and transmitted through a multipath channel. The received signal is sampled at the slot rate and the sample outputs are fed to the ANN through the TDLs. As in other case of adaptive equalizer, the ANN is first trained to estimate the channel prior to being utilized as an equalizer. The output of the equalizer is sliced to regenerate the DPIM sequences. Both linear and DF structures are studied. In the DF structure, the threshold output is fed back to the equalizer using additional TDLs, see Figure 6.31.

The NOPR to achieve a SER of 10^{-6} against the D_T for equalized 4, 8 and 16-DPIM with an ANN based linear equalizer is outlined in Figure 6.32. Also shown is the NOPR of the unequalized system. Similar to other equalized systems, ANN based equalizer shows a significant reduction in NOPR compared to the unequalized cases for $D_T > 0.1$. Equalization offers ~ 6 dB reduction in NOPR for 4-DPIM compared to the unequalized case at $D_T = 0.3$. Notice that it is not possible to completely remove the ISI and hence a nominal OPP occurs for the equalized case if $D_T < 0.1$ in comparison to the LOS channel. However higher OPP is visible at $D_T > 0.1$ and the OPP is ~ 6 dB at $D_T = 2$ for all cases.

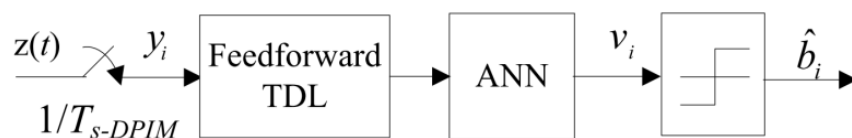


Figure 6.30: ANN based linear equalizer for DPIM scheme.

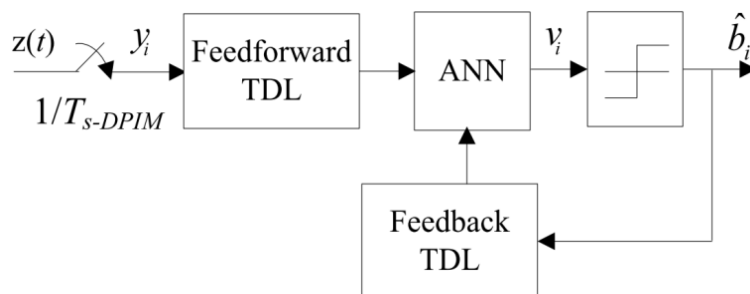


Figure 6.31: ANN based decision feedback equalizer for DPIM scheme.

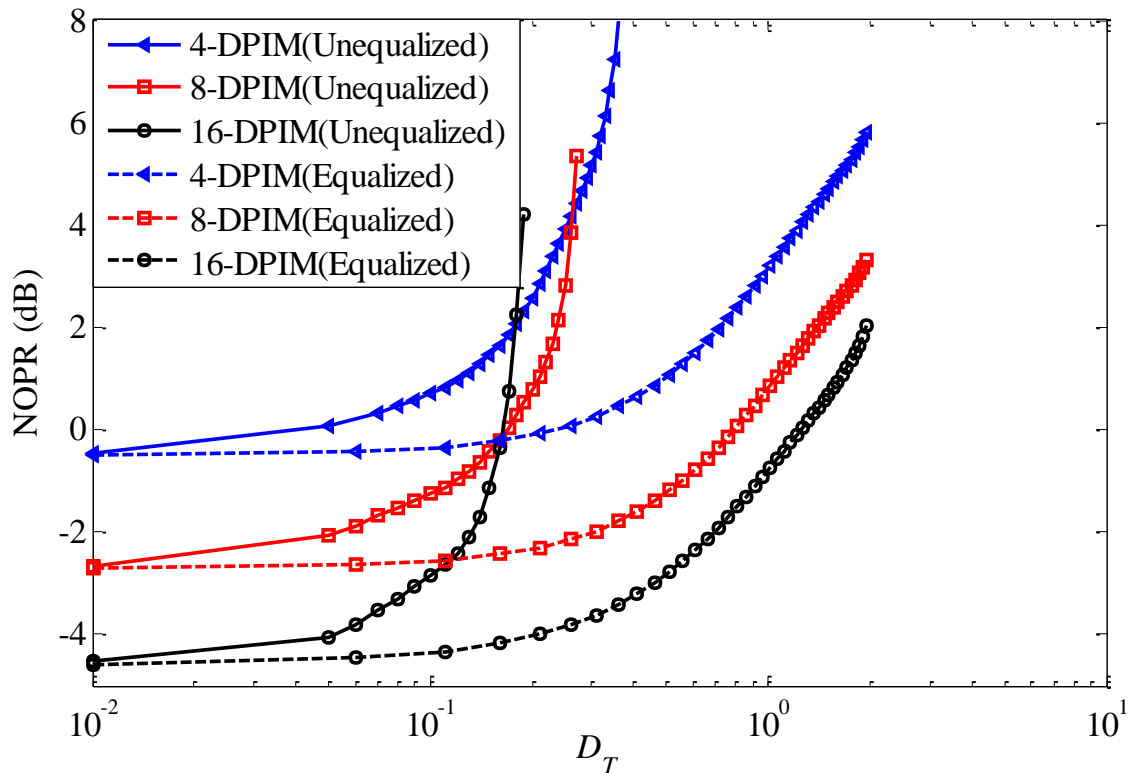


Figure 6.32: NOPR versus the normalized RMS delay spread for unequalized and linear ANN equalizers for the DPIM (OGS) scheme.

The OPP associated with dispersion in the ANN based linear and DF equalizer for DPIM scheme is depicted in Figure 6.33 for a range of D_T . It can be observed that the OPP for DPIM system increases exponentially with D_T though the gradient is much lower than the unequalized system. Unlike the case of PPM, the difference in the OPP is very marginal for all values of bit resolution and it is also closer to the OOK. This is due to the combined effect of two counter factors, the slot duration and probability of two consecutive slots. As a result, though the ISI due to the short slot duration is high for higher bit resolution, it is counter balanced by the lower probability of two consecutive slots. As in the previous cases, the DF structure provides improved performance compared to the linear structure for highly dispersive channel and a difference of ~ 0.6 dB is observed at D_T of 1.5.

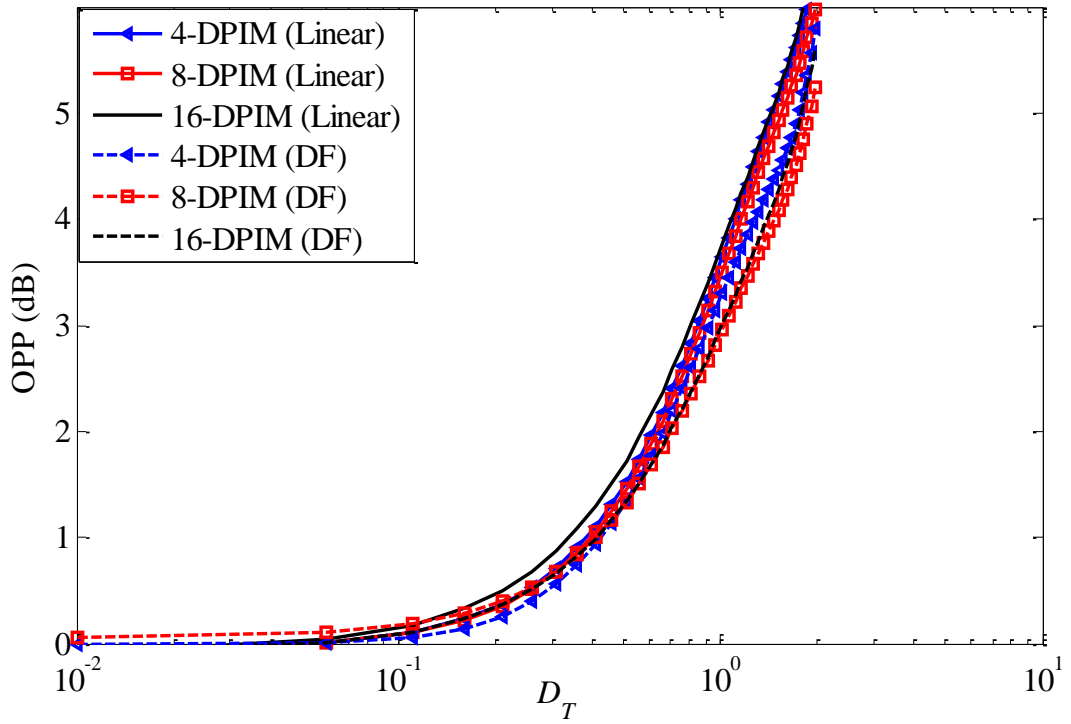


Figure 6.33: OPP against the normalized delay spread D_T for ANN based linear and DF equalizers for the DPIM scheme.

6.8.4 Comparative Study of the ANN and FIR Based Equalizers

The comparative studies of the linear and DF based equalizers based on the ANN and the traditional FIR filters are carried out in this section. To evaluate the performance of the traditional and the ANN based equalizers, the MSE is calculated between the equalizer outputs and the desired outputs. MSEs are calculated in identical channel conditions and hence can be used to measure for effectiveness of the equalizer. To calculate the MSE, 1000 random bits are transmitted through a diffuse channel with D_T of 2 at a data rate of 200 Mbps using the OOK modulation scheme. For the simplicity as well as for more comprehensive comparisons, the channel is assumed to be noise free and hence error in the equalizer outputs is solely due to dispersion in the channel. The noise free received sequence is used for training of the ANN and the traditional equalizer. The outputs of the equalizers are compared with the desired output to calculate MSEs. The resulting MSEs for both equalizers are given in Figure 6.34. The MSE for the traditional linear equalizer is in the range of 10^{-4} to 10^{-1} while for the ANN equalizer is in the range 10^{-8} to 10^{-4} . This indicates the effectiveness of the ANN as an equalizer compared to the traditional equalizer.

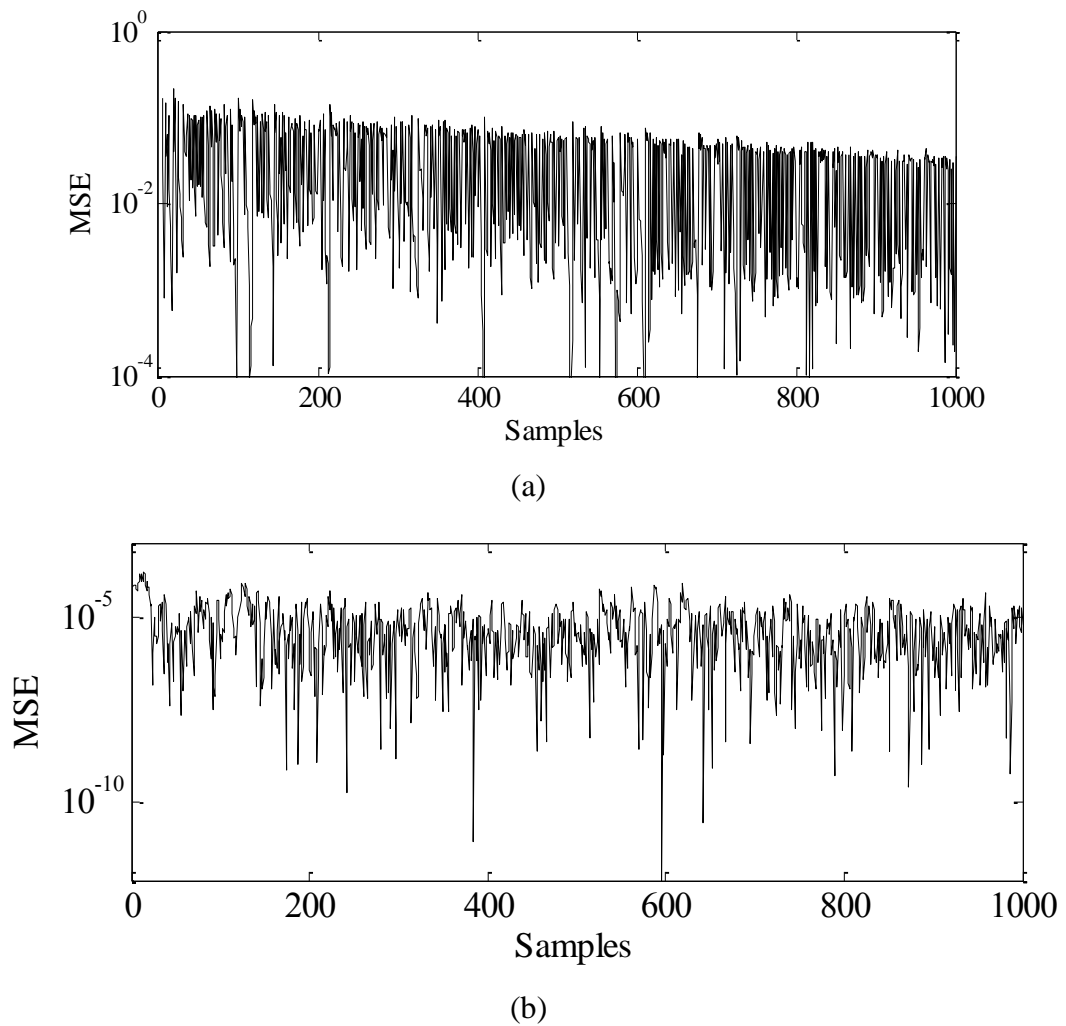


Figure 6.34: The MSE between the actual and target outputs from the linear equalizers for: (a) FIR filter equalizer, and (b) ANN equalizer.

The bit error probability of the ANN and the traditional linear equalizers for the OOK modulation scheme in a dispersive channel with D_T of 2 at a data rate of 200 Mbps is given in Figure 6.35. The figure reveals that the traditional linear equalizer can match the ANN based equalizer even in highly dispersive channel but the advantage of the ANN is in terms of reduced training length (TL). The simulation results show that the number of training symbols required for the traditional equalizer is significantly higher than that of the ANN equalizer especially in highly dispersive channel. BER performance indicates that the ANN trained using 200 bits offers almost identical performance to that of the traditional equalizer trained using 1000 bits for higher SNR values. Lower training length means reduced training time, less complexity and improved throughput.

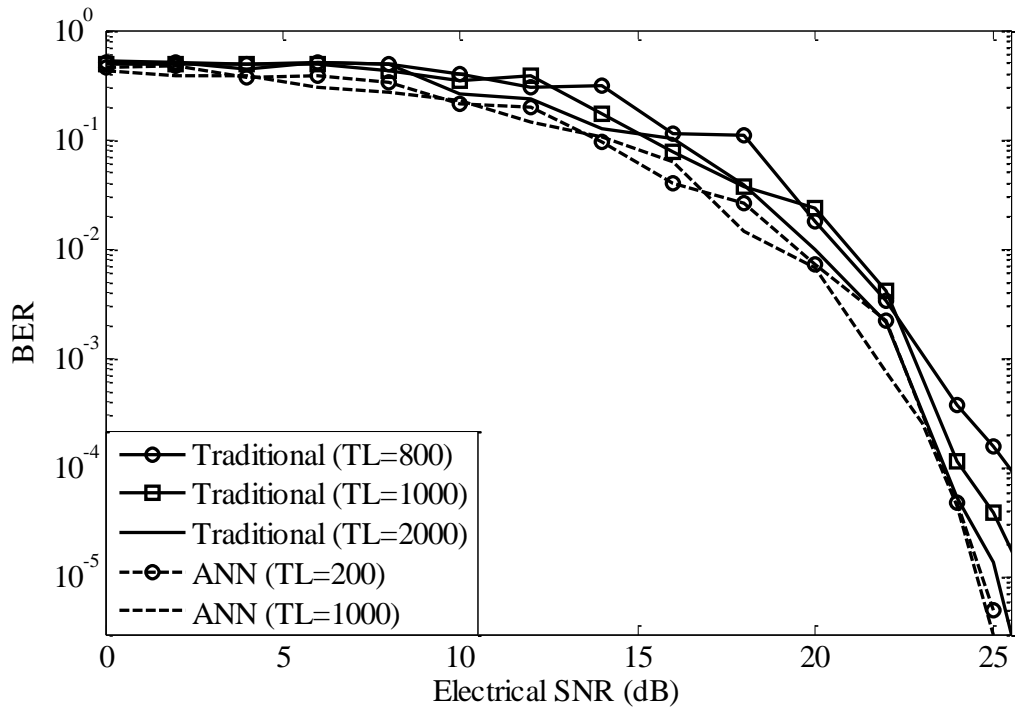


Figure 6.35: BER against the electrical SNR for the traditional and ANN linear equalizers for the OOK scheme at a data rate of 200 Mbps for a channel with D_T of 2 with different training lengths (TLs).

The bit error probability of the ANN and the traditional DFE for the OOK modulation scheme in a dispersive channel with D_T of 2 at a data rate of 200 Mbps is given in Figure 6.36. As with the linear equalizer, the DF ANN equalizer requires significantly lower training time compared to the traditional equalizer. It is found that the traditional DFE significantly is difficult to train in a highly dispersive channel and the LMS does not converge for almost all range of step sizes. Hence, a normalized LMS [285] is used to train the traditional equalizer. On the other hand, the entire training algorithms provide almost similar performance for the ANN based receiver with a training length of 500 matching the performance of the traditional equalizer with a training length of 2000. This also simplifies the ANN structure and parameter optimization compared to the traditional equalizers

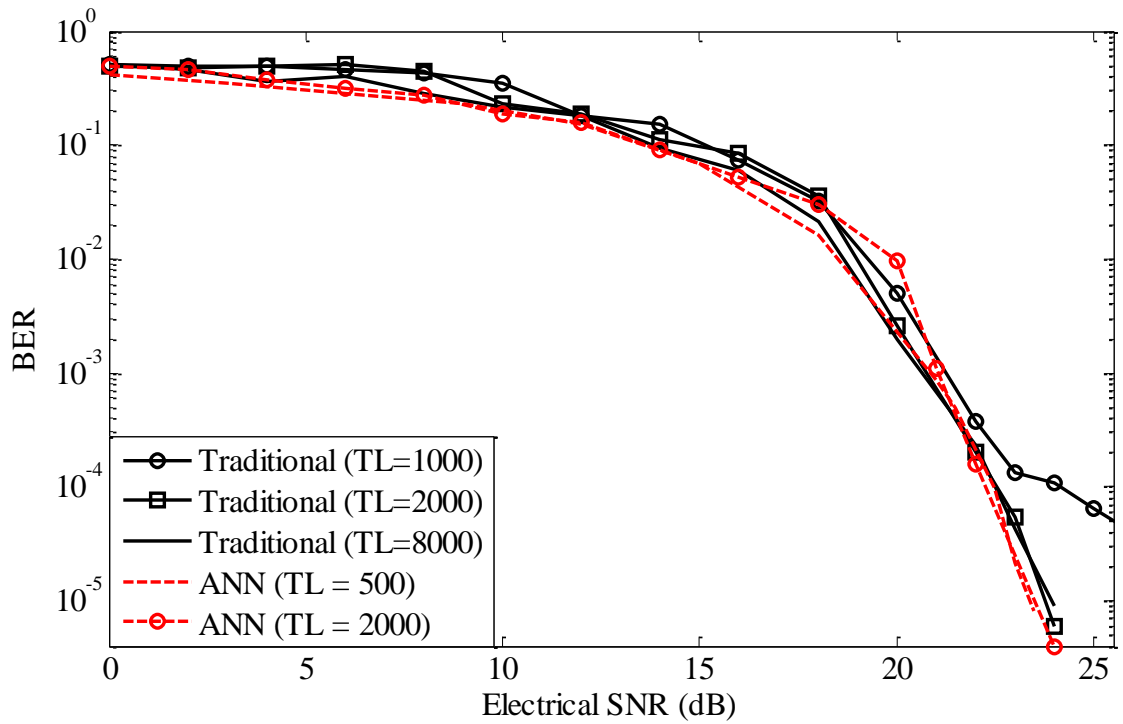


Figure 6.36: BER against the electrical SNR for the traditional and ANN DF equalizers for the OOK modulation scheme at a data rate of 200 Mbps for a channel with D_T of 2 with different training lengths

6.9 Summary

Artificial neural network based linear and decision feedback equalizers were proposed and studied for the dispersive indoor optical wireless channel. The unequalized studies showed that the NOPR to achieve a bit error probability of 10^{-6} increases significantly as the channel becomes more dispersive with irreducible power penalties for the $D_T > 0.5$ for the OOK system. The power penalty is more severe for modulation techniques with smaller slot durations. Hence the unequalized power penalty increment is the sharpest for 16-PPM. For PPM systems soft decision decoding offers a significant resistance to the ISI compared to the hard decision decoding. The soft decoding requires ~ 8.5 dB less NOPR compared to the hard decision decoding to achieve a SER of 10^{-6} at $D_T = 0.4$ for 4-PPM. Higher difference is noticeable for higher order of PPM. Similar to cases of OOK and PPM with a hard decision decoding scheme, the unequalized DPIM also shows an exponential increment in NOPR with D_T . Inclusion of guard slot(s) to avoid consecutive pulses in a DPIM scheme can provide resistance to the ISI. Further

reduction in NOPR for DPIM(1GS) in a diffuse channel can be achieved by implementing a hybrid decoding algorithm. The hybrid algorithm which is combination of hard and soft decision decoding schemes was proposed for decoding of DPIM(1GS) system showing an improved performance in a dispersive channel. However these techniques were not adequate in a highly dispersive channel to make the NOPR feasible for practical applications. Thus, an equalizer is incorporated in the dispersive channel.

In this study, the effectiveness of the feedforward backpropagation ANN for channel equalization in a diffuse indoor optical environment was investigated for OOK, PPM and DPIM systems. The ANN was first trained in a supervised manner to estimate the channel response and then used for equalization. It was observed that ANN is very effective in reducing the effect of ISI for all modulation techniques providing a significant reduction in NOPR compared to the unequalized systems. The equalized systems do not show any irreducible power penalty even for channel with D_T of 2 for all modulation techniques. The decision feedback structure offered improved performance compared to the linear equalizer structure for highly dispersive channel, though such improvement is not observed in the less dispersive channels. Due to the practical limitations, soft decision decoding feedback structure does not provide any improvement compared to the hard decoding for the PPM system. The OPP for the equalized system is the least for the OOK system closely followed by DPIM and PPM. 16-PPM showed the highest power penalty, whereas 4-PPM and 8-PPM showed almost identical power penalties. DPIM system also showed similar power penalties for all bit resolutions.

The comparative studies of the traditional finite impulse response filter based and the ANN based equalizer demonstrated that both can be effective in reducing the ISI in a dispersive channel. The traditional equalizer can match the performance of the ANN based equalizer for all channel conditions. The advantage of the ANN is on the easiness of training especially in a highly dispersive channel as well as a reduced training length. The simulation results showed that ANN requires a significantly reduced training length compared to the traditional equalizer structure. A reduced training length means reduced training time, less complexity and improved throughput.

Chapter 7 Discrete Wavelet Transform and Artificial Neural Network Based Receiver

7.1 Introductions

In the previous two chapters, the effects of interferences due to fluorescent light and multipath propagation in indoor OWC systems are studied by separately treating the FLI and the ISI. The receivers are designed to mitigate one of the factors in absence of the other. In a LOS channel, ISI is not present and hence a DWT based receiver is more than adequate. However, the ISI due to multipath propagation and FLI are present simultaneously in the diffuse environment. In Chapter 6, FLI is ignored when analysing the effect of multipath induced ISI with an equalizer. In this chapter, the combined effect of ISI and FLI with the DWT-ANN based receiver is presented. The studies in Chapters 5 and 6 showed that if a suitable mitigating technique is deployed, one of the interference (FLI or ISI) is the dominant source of system impairment. The power penalty due to the FLI is significantly higher even with the DWT at low data rates. The power penalty due to the FLI reduces to less than 1.5 dB for OOK and 0 dB for PPM at data rate >40 Mbps. However, the residual ISI causes significant power penalty even with an equalizer. The combined effect of the FLI and ISI can be significantly worse than the individual effect, even with mitigating techniques. This chapter explores the consequence of the FLI in diffuse link with DWT-ANN based receiver. An ANN based linear equalizer is deployed in conjunction with the DWT based denoising scheme. The performance of the DWT-ANN based receiver for different modulation techniques is given in details below.

7.1 OOK

Since the OPP due to FLI is significantly high for all data rates, an alleviating technique is always incorporated in the receiver. Thus, it is assumed throughout this chapter that the receiver integrates a DWT based denoising. To analyse the effect of FLI in a diffuse link, the NOPR for the OOK scheme to achieve a BER of 10^{-6} is calculated using a computer simulation for the unequalized system. The NOPR against D_T of $[0, 1]$ in an unequalized diffuse channel in the presence of FLI with DWT denoising is given in Figure 7.1 for data rates of 40, 120 and 200 Mbps. Also shown is the unequalized performance in the absence of the FLI. Since the NOPR without FLI is independent of data rates, a single NOPR curve represents the performance for all data rates. The figure reveals that the NOPR for the channel with FLI depends on data rates, with higher data rates requiring lower NOPR for the same value of D_T . OPP at 40 Mbps is significantly higher compared to that of 120 Mbps due to the fact that OPP due to the FLI is higher at lower data rates. Also, the OPP curve is the steepest for lower data rates while that of channel without FLI is the least sharp. The difference in NOPRs for the LOS link ($D_T = 0$) with/without FLI at 40 Mbps and 120 Mbps are ~ 2 dB and ~ 1 dB, respectively. However, the difference increases sharply with D_T to ~ 8 dB and ~ 2.8 dB at $D_T = 0.28$. This shows that the combined effect of the FLI and ISI is more severe than the individual effect.

The natural measure to mitigate the combined effect is to use a combination of ANN and DWT. The proposed DWT-ANN receiver design to reduce the combined effect of the FLI and ISI is given in Figure 7.2. The received signal is first denoised using DWT and then fed to the ANN for equalization. The descriptions of the DWT based denoising and the ANN based equalizer are given in Chapters 6 and 7, respectively and is not repeated here.

The NOPR in the presence of the FLI and ISI depend on the data rate and D_T , respectively. Thus, to fully understand the effect of one factor in the presence of another, NOPR are calculated under the conditions of (a) a fixed data rate for a range of D_T and (b) fixed value of D_T with varying data rates.

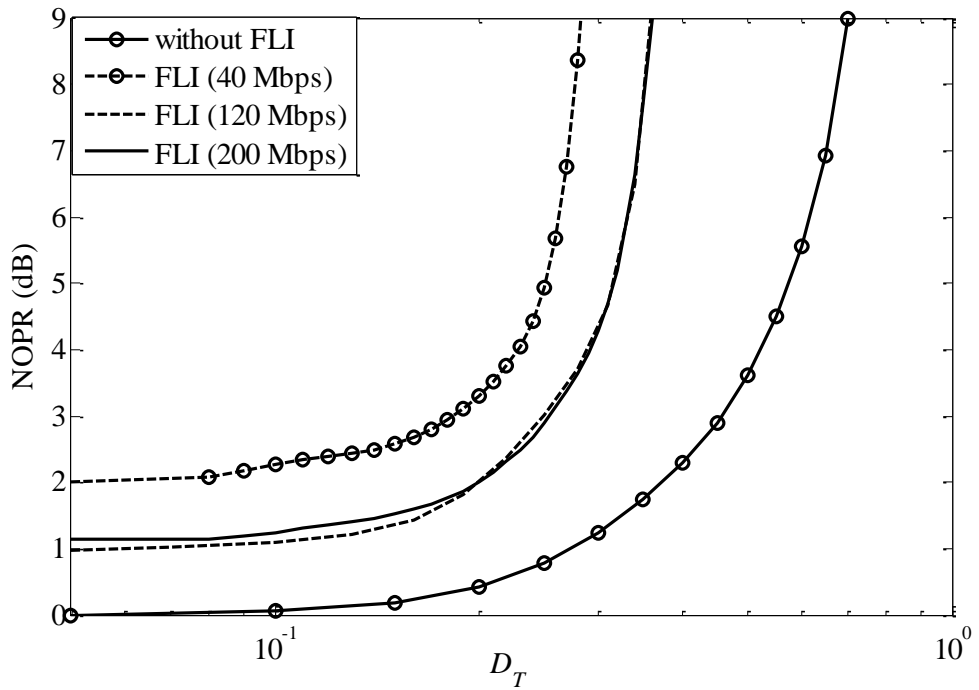


Figure 7.1: Unequalized NOPR against the normalized delay spread in presence/absence of FLI with/without the DWT based denoising scheme for data rates of 40, 120 and 200 Mbps.

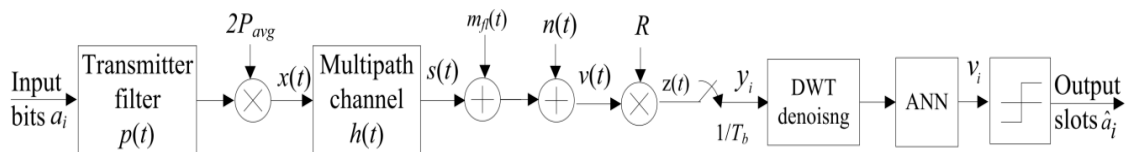


Figure 7.2: The block diagram of the DWT-ANN based receiver for OOK modulation scheme for an indoor OWC link.

The NOPR to achieve a BER of 10^{-6} for the DWT-ANN receiver in a diffuse indoor OWC channel with D_T of $[0, 2]$ in the presence of the FLI at data rates of 40, 120 and 200 Mbps is given in Figure 7.3. Also shown is the equalized performance in the absence of FLI. The NOPR for all cases show an exponential increment with D_T . In presence of the FLI, a data rate of 40 Mbps requires the highest NOPR and 120 and 200 Mbps show identical NOPR. Unlike the unequalized case, the differences in NOPR with and without FLI show little variation over a range of D_T . The difference in NOPR at 40 Mbps for the channel without and with FLI increases from 1.8 dB at $D_T = 0$ to 2.4 dB at $D_T = 2$. However, such increment is not observed at higher data rates. This indicates that combined OPP due to FLI and ISI for DWT-ANN receiver is roughly the summation of individual OPPs.

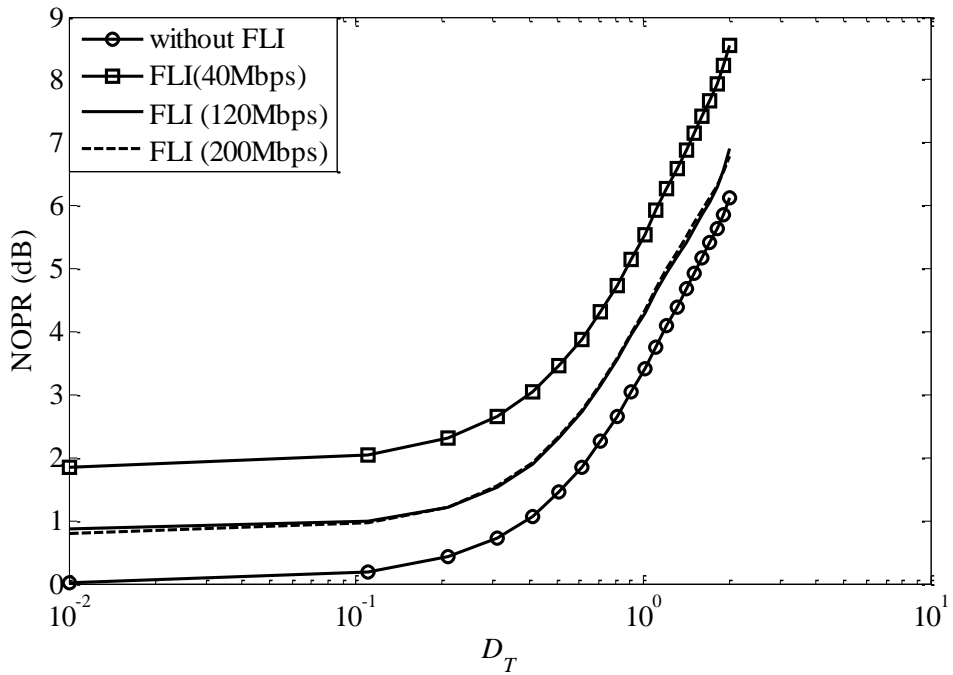


Figure 7.3: The NOPR for OOK against the normalized delay spread with/without FLI with the DWT-ANN receiver for data rates of 40, 120 and 200 Mbps.

To analyse the effect of the FLI in a diffuse channel, OPP is calculated for different data rates with a fixed value of D_T . The OPP for OOK system in presence of FLI with D_T of 0, 0.4, 1.2 and 2 at data rates of 20-200 Mbps for the DWT-ANN receiver is shown Figure 7.4. Also shown is the OPP for DWT based denoising with a threshold detector (without ANN) for a LOS link (see Chapter 5 for details). The OPP increases as the channel get more dispersive; channel with $D_T = 2$ showing the largest power penalty whereas LOS ($D_T = 0$) links show the least power penalty. For a fixed value of D_T , the OPP decreases with increasing data rates as power penalty due to FLI decreases with the increase of data rates. For the channel with D_T of 2, the OPP reduces from ~ 9.6 dB at a data rate of 20 Mbps to 6.8 dB at a data rate > 100 Mbps. There is little variation (< 0.5 dB) in the difference of OPPs for all range of data rates. It can be seen that the OPP of DWT-ANN receiver is less than that of DWT-threshold based receiver for a LOS link. A maximum difference of ~ 0.3 dB is observable with an average value of ~ 0.2 dB. This indicates that the threshold value of zero used for the DWT-threshold receiver is not the optimum. ANN with adaptability capability can adjust the threshold value, thus giving the optimum performance. To find the optimum threshold value, further analysis is necessary. Since the performance of the suboptimal threshold level of zero can provide performance close to optimum level, further analysis is not carried out to find the optimum threshold level.

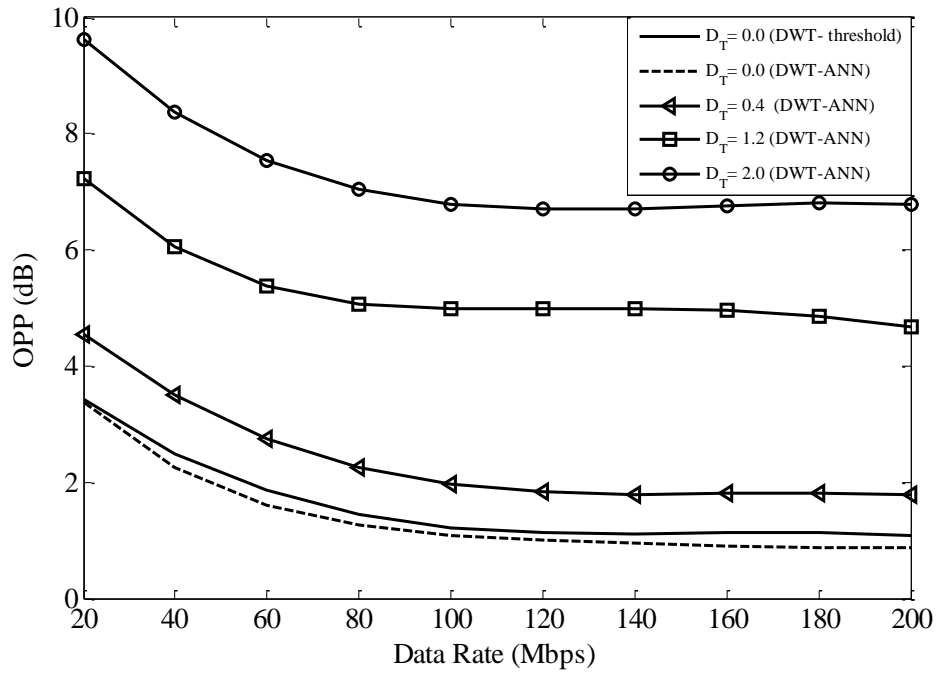


Figure 7.4: OPP versus the data rates (20-200 Mbps) for the DWT-ANN based receiver OOK scheme with the normalized delay spread values of 0, 0.4, 1.2 and 2 in presence of the FLI.

7.2 PPM

Unlike OOK, where significant power penalty incurs due to FLI even with denoising, the OPP for PPM soft decision decoding schemes with FLI reduces to zero above a data rate of 20 Mbps. Since power penalty due to ISI at low data rates is insignificant, DWT-ANN is not necessary to obtain the optimum performance for the soft decision decoding scheme. DWT based denoising at low data rates and ANN equalization at high data rates is sufficient to obtain the optimum performance. Though the power penalty due to FLI can effectively be eliminated using the DWT based denoising scheme for PPM hard decision decoding, a significant power penalty incurs if DWT is not incorporated. Hence, the DWT-ANN based receiver is suggested for the PPM hard decision decoding scheme. The block diagram of DWT-ANN based receiver for the PPM scheme is given in Figure 7.5. The receiver consists of a DWT denoising module followed by an ANN equalizer. The soft or hard decision decoding can be carried out to the equalized output, details of which can be found in the Section 2.8.1.2. As explained previously, the DWT-ANN based receiver is not necessary for the soft decision decoding scheme. Thus, here the study is focused on the DWT-ANN based receiver for PPM with hard decision decoding only.

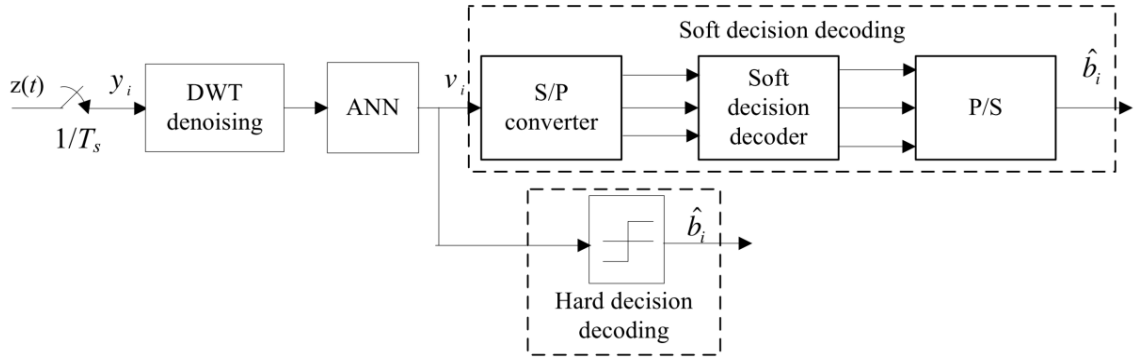


Figure 7.5: The block diagram of DWT-ANN based receiver for PPM hard and soft decision decoding scheme in diffuse indoor OWC in presence of FLI.

The OPP for the DWT-ANN receiver against D_T for 4-PPM in presence of FLI at data rates of 2 and 5 Mbps is given in Figure 7.6. The OPP of 4-PPM in a diffuse channel in absence of FLI is also shown for comparison. The OPP in presence of the FLI is identical to that of OPP without FLI at a data rate ≥ 5 Mbps. This shows that the effect of FLI can be completely removed in a diffuse channel for PPM schemes with a proper denoising technique. The dominating factor for the power penalty for the PPM scheme is ISI which increases exponentially even with an equalizer. In a diffuse channel, the OPP is higher at 2 Mbps than at 5 Mbps with a minimum difference of 1.5 dB. Practically speaking the OPP curve for 2 Mbps has little meaning at higher D_T values. The typical D_{rms} value for a normal room environment is 10-12 ns [95], which corresponds to D_T of 0.02 - 0.024 at a data rate of 2 Mbps. At this low value of D_T , the system acts almost like a LOS link with negligible OPP due to ISI (see Figure 7.6, OPP curve without FLI). D_T of 0.2 at 2 Mbps corresponds to D_{rms} value of 100 ns, which is not a realistic delay spread value for a practical channel. Hence, it is safe to say that ISI is the dominating cause of OPP for a diffuse channel even in the presence of intense FLI for the PPM scheme. The higher order of PPM scheme also shows similar profile.

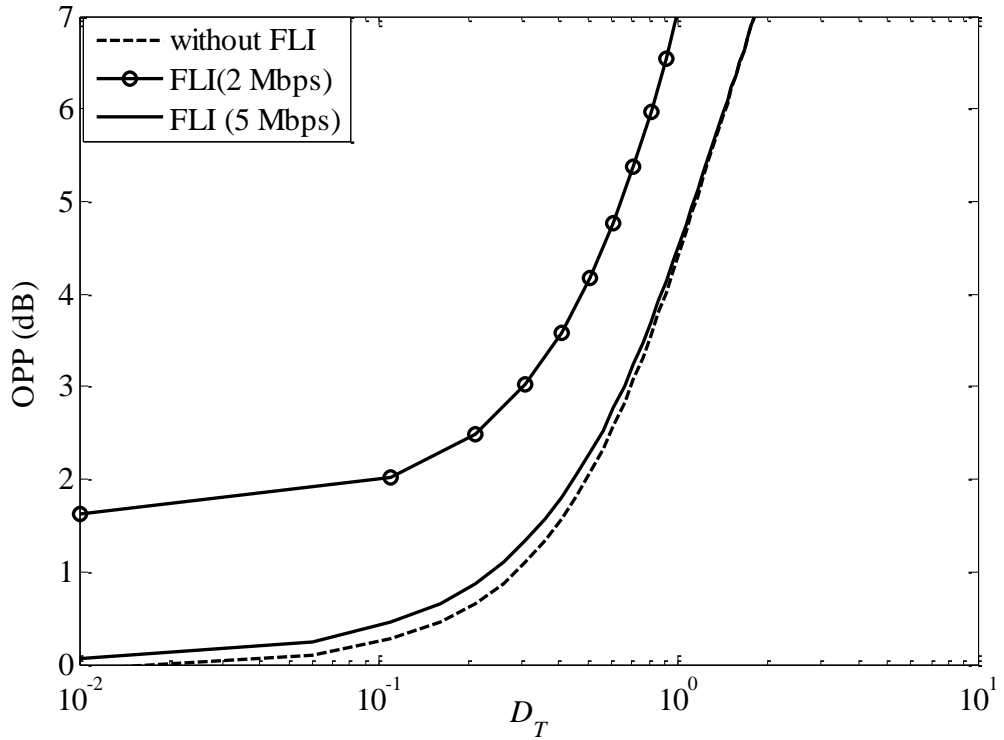


Figure 7.6: OPP for DWT-ANN receiver at SER of 10^{-6} against the D_T of $[0, 2]$ for 4-PPM with a hard decision decoding scheme in a diffuse channel with FLI at data rates of 2 and 5 Mbps.

7.3 DPIM

The performance of the DPIM scheme in a LOS link in presence of FLI with DWT denoising is intermediate between PPM and OOK. Similar performance profile is expected for DPIM in a diffuse link with lower order and higher orders DPIM showing performance similar to OOK and PPM respectively. The receiver design based on DWT-ANN for the DPIM scheme is demonstrated in Figure 7.7. The DPIM received signal corrupted by the FLI and ISI is first sampled at $1/T_{s-DPIM}$ followed by the DWT based denoising module. The denoised signal is then fed to ANN for equalization. The equalized output is sliced using a threshold value of 0.5 to regenerate DPIM symbol sequences. The detail of DWT based denoising and ANN based equalizer for the DPIM scheme is described in Chapters 5 and 6.

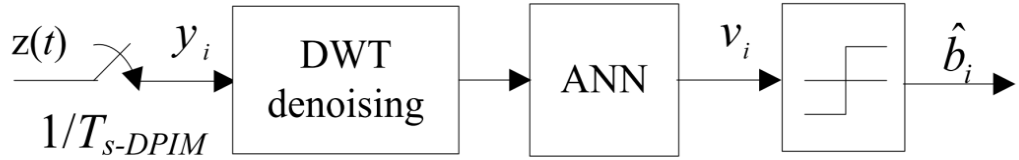


Figure 7.7: The block diagram of the DWT-ANN based receiver for the DPIM modulation scheme for effective removal of the FLI and channel equalization in an indoor OW link.

In order to fully understand the behaviour of DPIM in the presence of FLI, an investigation over a range of bit resolutions is necessary. The computer simulation is carried out to determine the OPP to achieve a SER of 10^{-6} in a diffuse link for 4 and 16-DPIM with the DWT-ANN based receiver. The results are shown in Figure 7.8 and Figure 7.9 for D_T of [0, 2]. As in the case of OOK, the difference in OPPs between the channel with and without FLI is observed in a dispersive channel for 4-DPIM. However, the DPIM scheme shows identical OPP profile above 40 Mbps. The differences in OPP for the channel with and without FLI are ~ 2.4 dB and ~ 3.1 dB at D_T of 0 and 2, respectively for a data rate of 10 Mbps. The differences are effectively reduced to lower values (0.5 dB at $D_T = 0$ and 1 dB at $D_T = 2$) at a data rate > 40 Mbps as the DWT based denoising scheme is more effective at higher data rates (see Section 5.5.3 for detail).

16-DPIM shows significantly different profile to 4-DPIM with much reduced power penalty. Similar to PPM, there is no difference in the OPP performance for the channel with and without FLI at a data rate > 20 Mbps. However, a small difference in OPP of ~ 0.5 dB can be observed between the channel with and without FLI at a data rate of 10 Mbps. This proves the effectiveness of the DWT-ANN based receiver in significantly enhancing the performance of all baseband modulation techniques with/without the FLI.

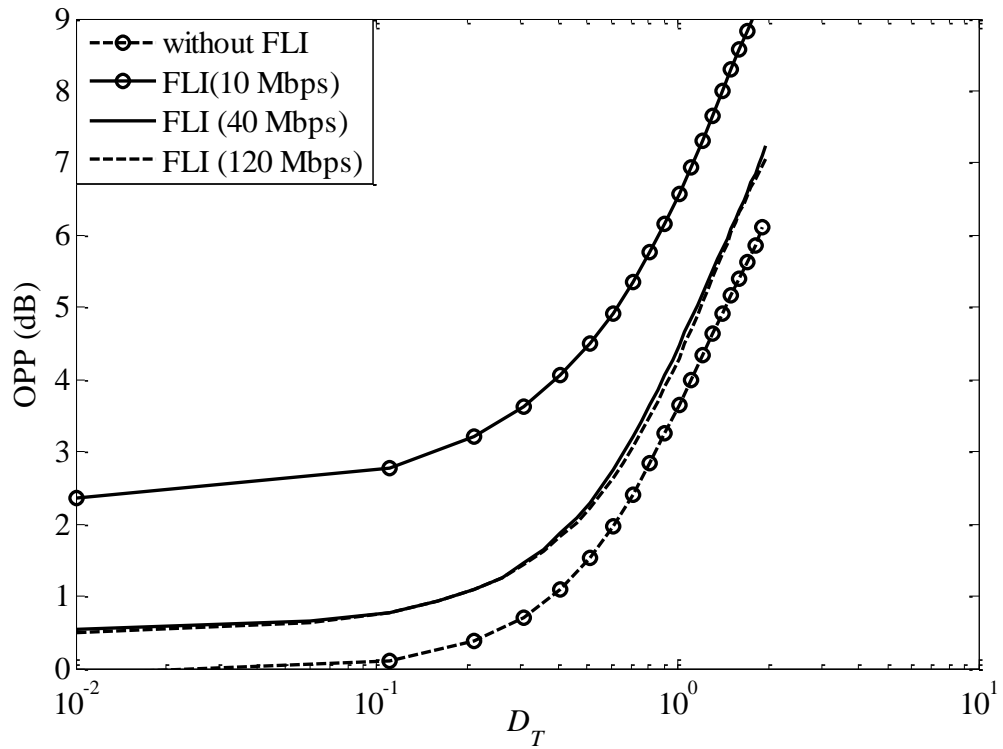


Figure 7.8: OPP for the DWT-ANN receiver at SER of 10^{-6} against the normalized delay spread of 0.01- 2 for 4-DPIM in presence of FLI at data rates of 10, 40 and 120 Mbps.

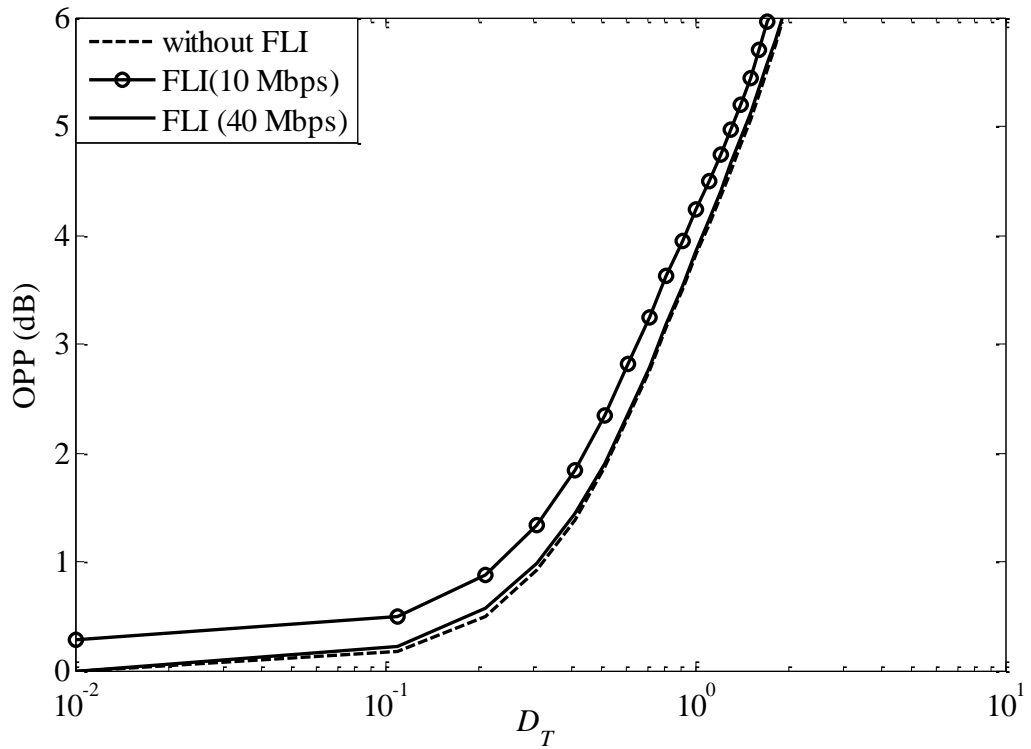


Figure 7.9: OPP for the DWT-ANN receiver at SER of 10^{-6} against the normalized delay spread of 0.01- 2 for 16-DPIM in presence of FLI at data rates of 10 and 40 Mbps.

7.4 Summary

This chapter provided a comprehensive study of the performance of baseband modulation techniques for the dispersive indoor OWC channel in the presence of FLI with the DWT-ANN based receiver. Depending on the modulation type, power penalty due to FLI or ISI can be significantly high. Mitigating techniques to remove either FLI or ISI is not effective to remove the effect of both factors. Hence, DWT based denoising and ANN equalization were proposed. It was shown that the DWT-ANN based receiver is very effective in reducing the power penalty due to the FLI and ISI irrespective of the modulation type. The comparative study of OOK in a diffuse link showed that difference in OPP for a channel with and without FLI decrease with increasing the data rate. However, above a certain data rate (120 Mbps in this case), the difference remains constant. A maximum difference in OPP of ~ 2.4 dB at $D_T = 2$ is observed for OOK at a data rate of 40 Mbps. The difference reduces to ~ 0.9 dB at a data rate ≥ 120 Mbps. For the channel with D_T of 2, the OPP reduces from ~ 9.6 dB at a data rate of 20 Mbps to 6.8 dB at a data rate of > 100 Mbps. Note that the OPP due to ISI in a multipath dispersive channel without FLI at D_T of 2 is ~ 6 dB. This proves the effectiveness of DWT-ANN based receiver to remove the FLI and ISI. Similar profile of OPP in dispersive channel with FLI is shown by 4-DPIM. However, the difference in OPP for channel with and without FLI is smaller for 4-DPIM compared to OOK with a maximum OPP of 1 dB at 40 Mbps. This is due to the fact that DWT is more effective in reducing the FLI in DPIM scheme.

The effect of FLI can be completely eliminated in PPM with the soft decision decoding scheme at data rates higher than 20 Mbps, thus removing the need for DWT denoising. A simple equalizer with soft decoding provides the optimum performance. However, for PPM with hard decision decoding, a significant power penalty occurs due to FLI and hence the DWT-ANN receiver has to be incorporated in a dispersive channel. Unlike the case of OOK, the performance of the DWT-ANN receiver in the presence of FLI can match the performance of channel without FLI. Since PPM has very small spectral components at the DC and low frequency components, DWT is very effective in removing the effect of FLI. This gives rise to the identical performance for PPM with the hard decision decoding scheme with/without FLI at a data rate greater than 5 Mbps. Similar performance profile was observed for 16-DPIM at a data rate of 20 Mbps or higher, thus illustrating the effectiveness of the DWT-ANN based receiver.

Chapter 8 Adaptive Decoding of Convolutional Code using Artificial Neural Network

8.1 Introductions

Viterbi algorithm is the optimum method for decoding convolutional code using the MLSD technique. However, complexity, delay and memory requirements associated with the Viterbi algorithm are relatively high and hence a sub-optimal decoding of convolutional code using ANN has been intensively studied [286-297]. The ANN, as an alternative to the Viterbi algorithm, has been suggested because of the low complexity, parallel processing, adaptability and fault tolerance capabilities. Though the performance of ANN as an error control decoder of block codes is comparable to the optimal decoder, the performance of ANN as convolutional decoder is far from being satisfactory [296]. A number of structures and approaches have been suggested to improve the performance of ANN as a convolutional decoder. They can broadly be classified into three classes: (i) feedforward network trained using the minimum Hamming distance codewords [294, 295], (ii) RNN with the iterative decoding [287, 291-293] and (iii) fixed-weight training-free ANN [294]. In the first approach, a feedforward ANN is trained to act as a decoder for $1/N$ rate convolutional code. The received signal is partitioned into a number of codewords using an overlapping sliding window. ANN is trained to identify errors in the received codeword and hence correctly decodes the transmitted bits from the noisy received signal. With the optimum training strategy, the performance of the ANN decoder can closely match that of the Viterbi decoder [295]. However, the limiting factor is the large training length which is impractical for real time applications [295].

The decoding problem is formulated as the noise energy function (NEF) minimization problem where the gradient descent algorithm (GDA) can be employed to solve the

problem [287, 291]. An RNN with iterative decoding is applied to decode $1/N$ convolutional code using the GDA. Error performance of RNN decoder is comparable to the Viterbi algorithm and performs extremely well for some specially structured convolutional codes [287]. However, the large number of iterations (as high as 100) required to ensure that ANN performs as well as the Viterbi algorithm [289] makes such scheme practically infeasible. In [294] ANN based convolutional decoder based on the “neuralization” of the Viterbi decoder is presented, where the connection weights of the ANN decoder are fixed to either +1 or -1. The ANN decoder structure is similar to the Viterbi decoder with performance matching that of the ideal Viterbi algorithm. However, the system is not adaptive and like the Viterbi decoder, a separate design is necessary for each encoder.

The quest for efficient structure, minimum iterations and practically feasible training length for the adaptive decoding of convolutional code is the motivation to suggest the MLP as an alternative to the Viterbi decoding. A ‘soft’ sliding block decoding method using ANN for convolutional code is proposed and investigated. This approach is loosely based on the block decoding algorithm [298]. However, instead of using a look up table, ANN is trained to decode a bit sequence from the received sequence. This approach makes the decoding more flexible and adaptive. Soft decoding of the convolutional code using Viterbi algorithm offers significant performance improvement compared to the hard decoding but at the cost of increased complexity [179]. Unlike the Viterbi algorithm, the ANN soft decoding does not incur any additional decoding complexity compared to the hard decoding. Hence soft decoding would be more relevant for practical applications. The following advantages can be outlined compared to the existing ANN based decoder: (i) a reduced training length compared to [295], (ii) performance close to the ‘soft’ decision Viterbi algorithm, (iii) similar performance to the RNN decoder with reduced computational complexity and with no iterations (which reduces decoding time), (iv) soft input soft output decoding method for improved performance and (v) adaptive decoding without need for a look-up table.

This chapter provides the ANN based decoding algorithm for convolutional code with performance comparisons with the Viterbi algorithm. A case study is provided to inspect effectiveness for decoding and equalization in a diffuse indoor OWC channel.

8.2 The Structure of ANN Decoder

The ANN decoder proposed here is based on the sliding block decoding introduced in [298]. The block diagram of discrete equivalent of digital communication system with convolutional encoder and decoder is shown in Figure 8.1. The transmitted bit sequence x_k are generated by applying convolutional encoding on the information bits a_k . The receiver incorporates a matched filter and a sampler. For simplicity, only the sample output y_k is shown in the figure. For the ‘hard’ decoding y_k is sliced using a threshold level to generate the binary sequence. For the ‘soft’ decoding, quantized values of y_k are presented to decoder. The convolutional decoder then estimates the transmitted bit sequence \hat{a}_k .

The Viterbi algorithm for convolutional code is described in detail in Chapter four. In this study, ANN decoder is considered. Though the task of the ANN decoder and the Viterbi decoder is the same, the working principle is completely different. The principle of Viterbi algorithm is to find a path in the Trellis that will minimize the path metrics between the received and valid bit sequences. The ANN decoder on the other hand works on the concept of the classifications. The ANN classifies the received signal into one of the two classes: binary ‘1’ or ‘0’ based on the observation vector. To clarify the concept, consider one portion of Trellis transition from the initial state p to another state q at a discrete time k (Figure 8.2). If a decoder can predict the state p or q with high reliability based on observation vectors, then it is very likely that the decoder can classify the received signal. Hence the task of decoder is to estimate these states with high reliability as well as to classify the received sequence to estimate a_k .

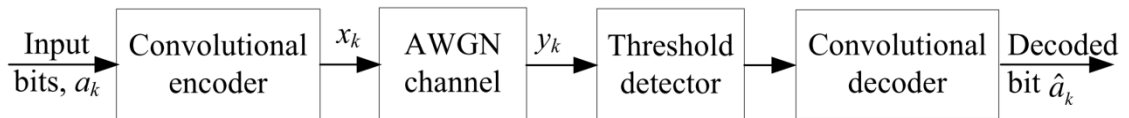


Figure 8.1: The block diagram of discrete equivalent of communication system with convolutional encoder and decoder.

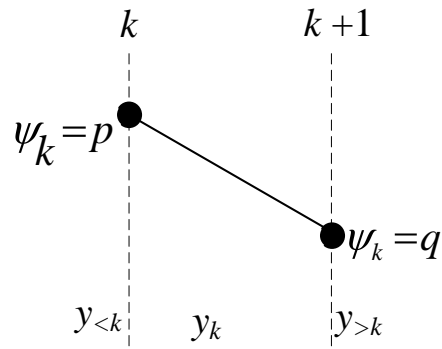


Figure 8.2: State transition diagram of convolutional code.

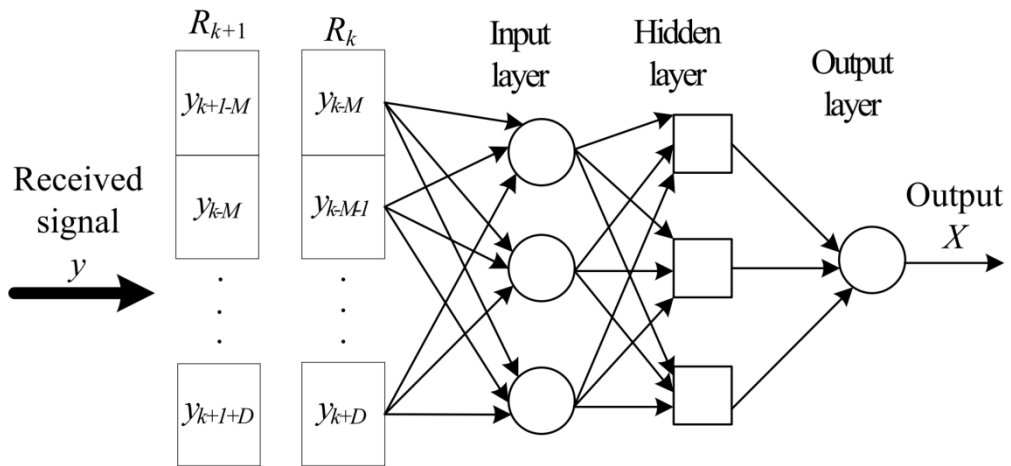


Figure 8.3: Schematic of ANN decoder with input codewords and output bits.

The schematic of ANN decoder is given in Figure 8.3. The received sequence $\{y_k : 1 < k < \infty\}$ are first sorted into overlapping W -codeword $R_k = \{y_{k-M}, y_{k-M-1}, \dots, y_k, \dots, y_{k+D}\}$, where $W = M + D$, M and D are called the memory and delay, respectively [298]. The W -codeword window sequence is fed to the ANN for estimating bits a_k that corresponds to the reference codeword. It must be pointed out that it is not necessary to use the central codeword as a reference and hence $M \neq D$. The window is shifted by one time unit with each decoding cycle. The ANN estimates the decoding bit based on the windowed input. In this decoding approach using the ANN; it is assumed that if the window size W is long enough and ANN is trained properly, the ANN can estimate a_k with a low probability of error. The effectiveness of the ANN decoder hence depends on a number of factors; the most important are the training length, the decoding window, the size of ANN and the training SNR. The optimization of the ANN parameter is discussed in the following section.

8.3 Optimization of ANN Parameters

In order to obtain optimum performance of ANN, there are a number of constraints that needs to be optimized. Computer simulations are carried out with the simulation parameters given in Table 8.1. The simulation results and optimum parameters for a $\frac{1}{2}$ convolutional encoder are discussed below.

8.3.1 Window Length and Decoding Position

The accuracy and system complexity of ANN decoder depends on the window length W . A short length window does not provide enough information for successful classification, where as a long window length increases the complexity without necessarily enhancing the performance. However, the difficulty arises in optimizing the window length as the performance also depends on number of other parameters including the training length, the number of neurons and training SNR. Rather than optimizing all parameters, the approach taken in this study is to optimize a unique parameter at a time.

Table 8.1 The simulation parameters for ANN decoder.

Parameters	Values
Window length W	4-9
Constraint length	3
Code rate	$\frac{1}{2}$
Generation vectors	[1 7]
ANN type	Feedforward backpropagation
No. of hidden layers	1
No. of neurons in hidden layer	$6W$
Transfer function	Log-sigmoid
Training SNR	3 -7 dB
Training length	1,000 -100,000

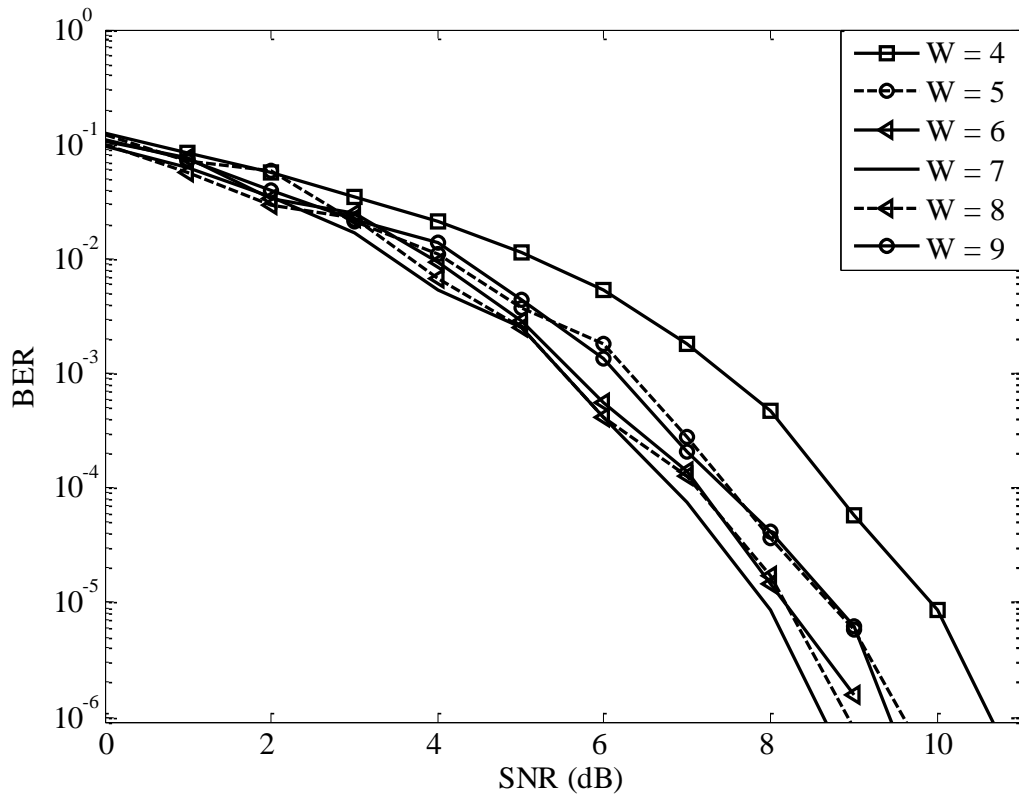


Figure 8.4: The BER against the SNR for an ANN decoder with a range of window lengths.

A number of simulations are carried out for $W = 4$ to 13 and for varying the memory M and delay D (see Figure 8.3). A training length of 50000 bits and $6W$ neurons in the hidden layer is deployed. For each combination of W and D , the performance of ANN decoder is simulated by varying the training SNR from 1 - 8 dB. The best BER performance for a range of SNR is determined for each W as depicted in Figure 8.4. The figure illustrates that the optimum performance is obtained when $W = 7$ with $W > 7$ showing marginally inferior performance. A shorter window length leads to significantly inferior BER performance. Smaller W will not provide enough information and the classification will be prone to error. A larger value of W means increased classification boundaries requiring extensive training for correct classification. To obtain similar performance to $W = 7$ for larger window length, the training length needs to be increased. The optimum performance for $W = 7$ is obtained at $D = 2$. The BER performance for $W = 8$ and for $W = 6$ is also close to $W = 7$.

8.3.2 Number of Neurons

The classification capability of ANN depends on the number of neurons in the hidden layer. Since a single layer with sufficient number of neurons is adequate for performance of any task, the optimum structure for ANN is obtained by varying number of neurons in the hidden layer. The BER performance against the SNR for ANN decoder with the number of neurons varying from $1W$ to $8W$ is given in Figure 8.5. It can be observed that a small number of neurons ($< 4W$) would provide a significantly inferior performance. However, employing higher number of neurons ($> 8W$) does not offer a superior performance. Since the task of optimization is to use as few neurons as possible without compromising in performance, $6W$ neurons will be adopted in this study for the ANN decoder.

8.3.3 Training SNR

The training is carried out by transmitting a predefined coded sequence through an AWGN channel. The noise is added to the training sequence in order to present the ANN decoder with all possible random error patterns that could occur during the transmission. The performance of the ANN decoder is very sensitive to the SNR. A small training SNR value could result in the Hamming distance between the transmitted and received codewords being greater than the minimum Hamming distance D_{hm} , thus leading to futile training. (Note: the maximum number of errors that a decoder can correct is $(D_{hm}-1)/2$; hence if the number of errors within the decoding window is greater than $(D_{hm}-1)/2$, the decoder cannot correct the errors). On the other hand, if the training SNR is very large, ANN will be provided with insufficient number of error patterns within the codewords, thus leading to less efficient training. This empirical observation clearly illustrates that ANN must be trained with the optimum training SNRs. Simulations are carried out to optimize the training SNR and results are given in Figure 8.6. The results show that SNR in the range of 2-5 dB is optimum for effective training with SNR = 2 dB showing slightly superior performance.

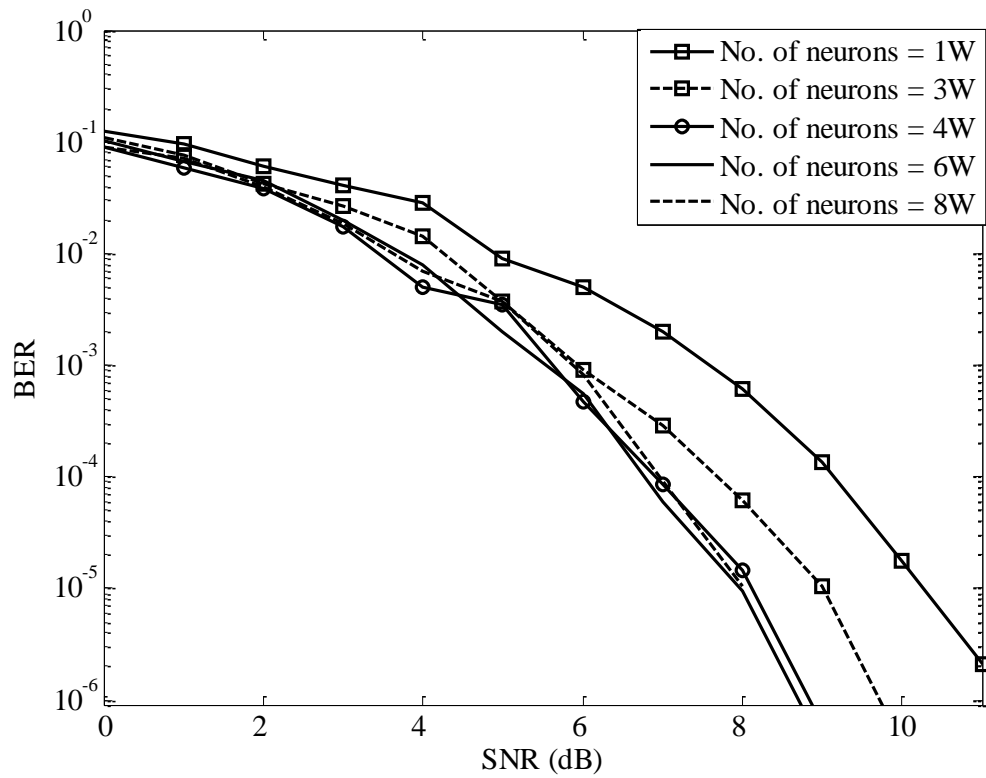


Figure 8.5: The BER against the SNR for an ANN decoder with varying number of neurons in the hidden layer.

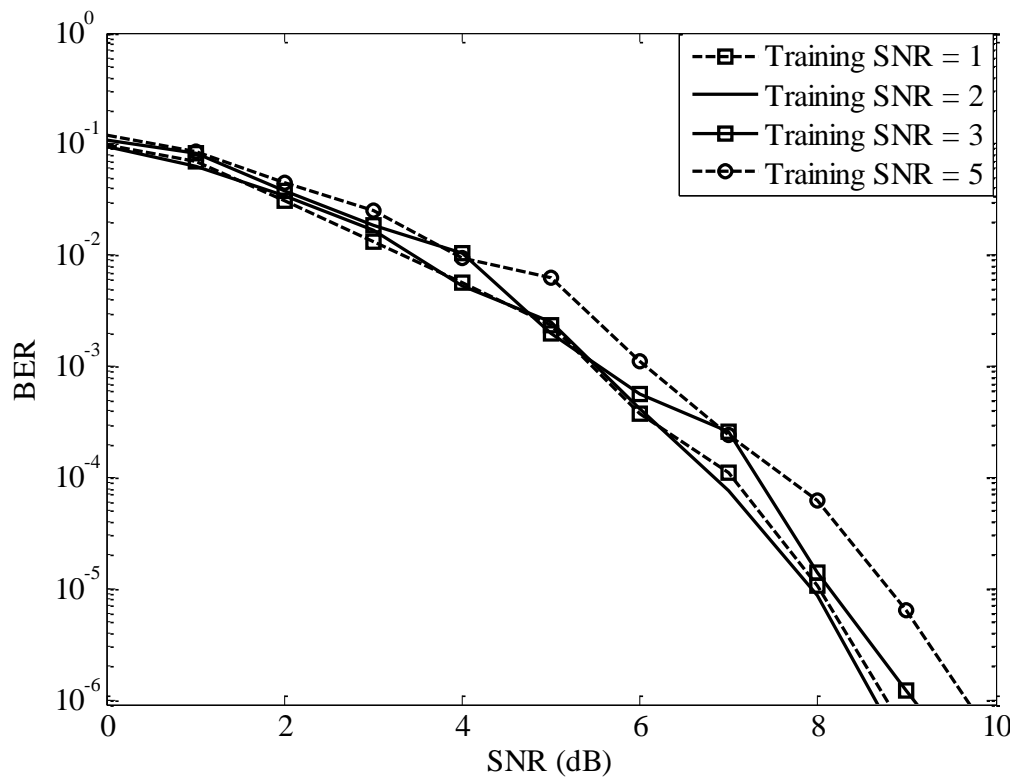


Figure 8.6: The BER against the SNR for an ANN decoder for a range of neurons in hidden layer.

8.3.4 Training Length

For the optimum performance of ANN decoder, the ANN should be provided with all possible error combination that may occur. Depending upon the window length and training SNR, the training length can vary. For the optimum window length of 7, the BER against the SNR for different training lengths is demonstrated in Figure 8.7. The results illustrate that a training length of 40000 is close to optimum. A training length greater than 40000 displays only a marginal improvement, which is apparent only for low values of SNR. A training length of 30000 offers only marginally inferior performance.

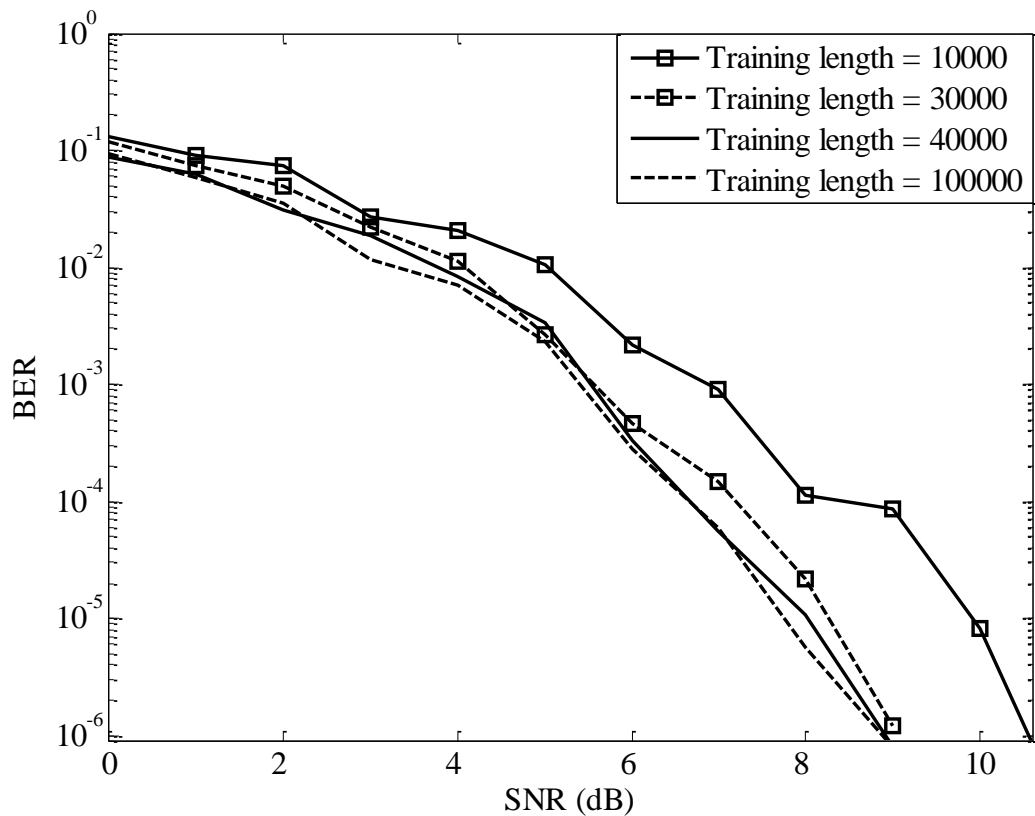


Figure 8.7: The BER against the SNR for an ANN decoder for a range of training length.

8.4 Comparative Study of ANN and Viterbi Decoder

Comparative studies of the BER performance of the ANN decoder against the optimum Viterbi decoder can quantify the effectiveness of the ANN decoder. Simulations are carried out to calculate the BERs for: (i) uncoded system, (ii) coded system with the Viterbi ‘hard’ and ‘soft’ decoding schemes and (iii) coded system with ANN ‘hard’ and ‘soft’ decoding schemes. The BER against the SNR for coded and uncoded systems are presented in Figure 8.8. As expected, the ‘soft’ decision decoding shows the best BER performance, whereas with the ‘hard’ decoding showing an improved performance compared to the uncoded system. The performance of the ANN and Viterbi decoder is identical for ‘hard’ decision decoding at low SNR values, though marginal performance improvement can be achieved with ANN at higher SNR values. The ‘soft’ Viterbi decoder offers improved performance compared to the ANN ‘soft’ decoder. However the difference in SNR at a BER of 10^{-6} is < 0.6 dB, indicating the effectiveness of the ANN decoder. Further improvement in the BER performance of ANN is suggested using the iterative decoding [287]. Since the improvement achieved by iterative decoding in this case is < 0.6 dB (provided that ANN can match the optimum performance of Viterbi ‘soft’ decoding), the iterative decoding does not provide a significant improvement for the proposed ANN decoder.

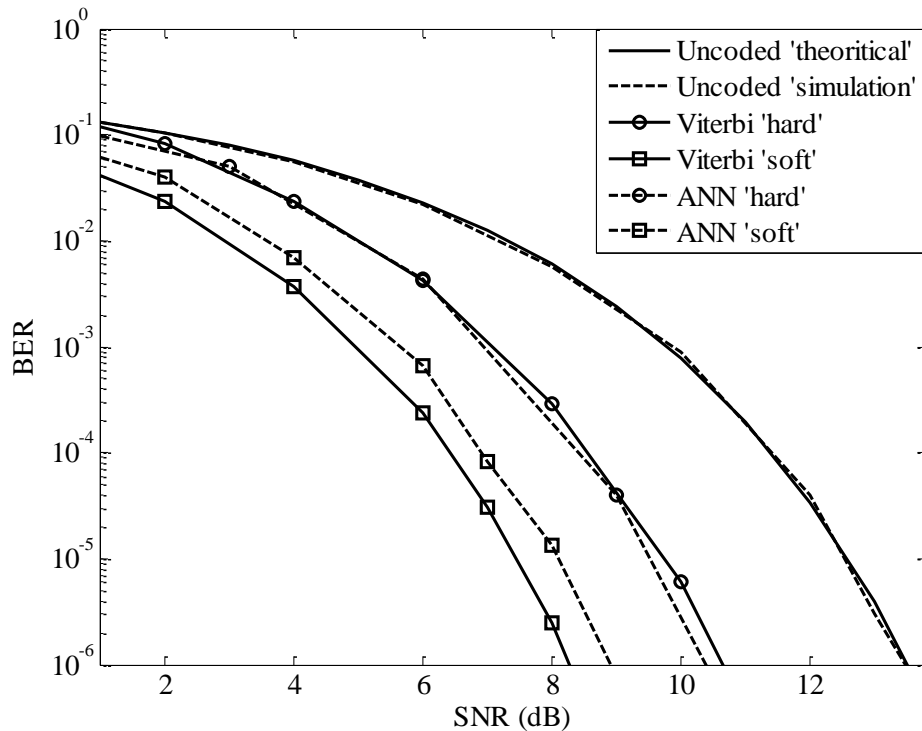


Figure 8.8: BER against the SNR for uncoded and convolutional coded systems with ANN and Viterbi ‘hard’ and ‘soft’ decoders in AWGN channel.

Though the performance is slightly inferior, ANN offers a number of advantages including ability to deal with analogue input signal without the need for quantization and a shorter length decoding window size. The decoding is done entirely based on the windowed received sequence, without the knowledge of the initial and final states, thus parallel decoding is possible. Furthermore, due to the soft input soft output strategies, one can extract reliability information that can be utilized to enhance the system performance. The reliability information can further be used for predicting the possible error position and for iterative decoding.

8.5 Performance of ANN Equalizer and ANN Decoder in Diffuse Indoor OWC Channels

Here, the ANN equalizer is proposed for compensating ISI in a dispersive OWC link as well as for error control to reduce the effect of AWGN noise. In fact, the equalizer and the error control are utilized in the receiver to improve the overall performance of the system. In principle, the equalization and decoding task can be combined as a single task. However, with many factors involved for optimum decoding and equalization, the resulting statistical relationship becomes thorny to manage in an efficient manner [299]. Hence, the equalization and decoding are carried out separately. The system block diagram of an ANN equalizer and an ANN decoder for an indoor OWC system is given in Figure 8.9. At the receiver, both the ANN equalizer and the ANN decoder are incorporated. It is not difficult to observe that the system given in Figure 8.9 is a combination of systems described in Figure 8.1 and Figure 6.16, the only difference being the inclusion of an interleaver/deinterleaver pair at the transmitter and receiver, respectively. The interleaver/deinterleaver pair randomizes the sequential error at the equalizer output, resulting in improved performance with application of error control coding.

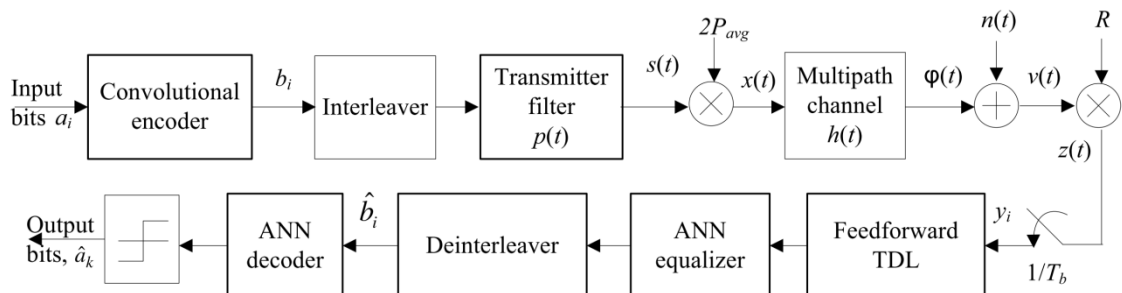


Figure 8.9: The block diagram of ANN based equalizer and decoder for diffuse indoor OWC channel.

The BER performance of an equalized system with and without an error control code in a dispersive channel with D_T of 1 is given in Figure 8.10. Since coding without equalization does not provide any system improvement in a dispersive channel, such system is not considered here. The benefit of using coding in conjunction with the equalizer is clearly demonstrated in the BER curves as SNR required to achieve a certain BER is the smallest for such systems (Figure 8.10). The equalizer compensates the ISI due to multipath propagation and the error control code minimizes the error due to the AWGN in the channel. Hence the overall performance is superior than using the equalizer and error control code separately. The application of the soft decoding offers a reduction in SNR of ~ 4 dB to achieve a BER of 10^{-6} compared to the equalizer system without the error control code. A performance difference of ~ 1.5 dB is noticeable between the ‘hard’ and ‘soft’ decision decoding schemes with ‘soft’ decision decoding offering an enhanced performance. The performance of the ANN and Viterbi ‘hard’ decoder matches each other. Similar to the previous cases, the Viterbi ‘soft’ decoding always outperforms the ANN ‘soft’ decoding.

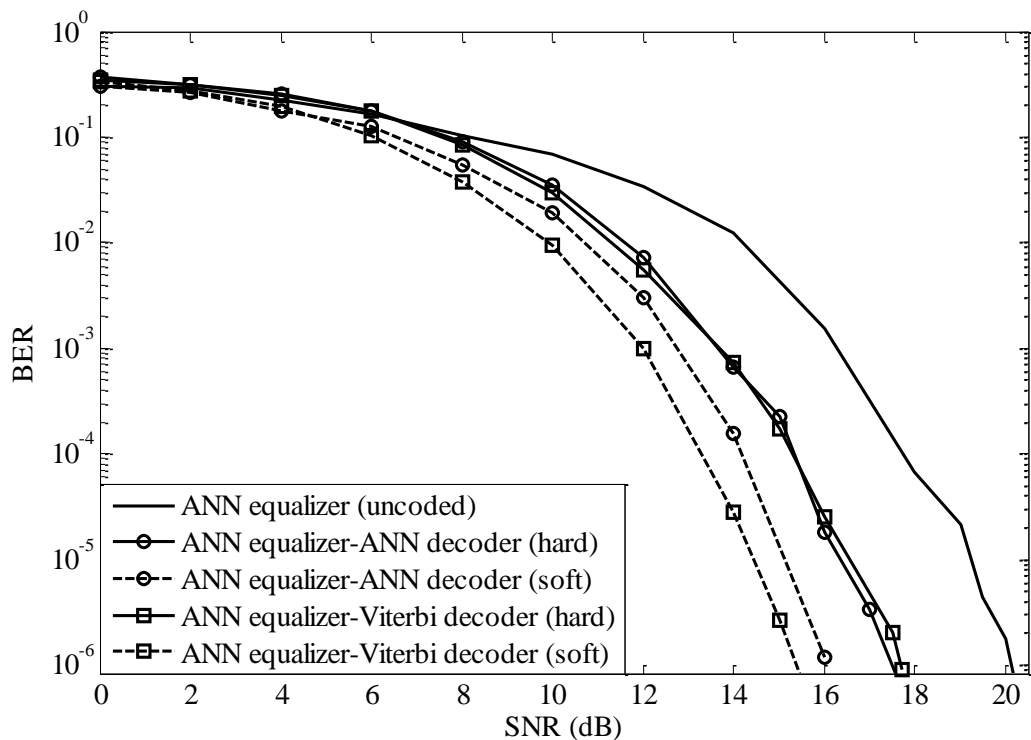


Figure 8.10: BER against the SNR for an ANN equalizer with ANN and Viterbi ‘hard’ and ‘soft’ decoders in a dispersive channel with D_T of 1.

To appreciate the effect of the interleaver, simulations are carried out in identical channel conditions using an identical equalizer and decoder but with and without the interleaver/deinterleaver pair. The BER performance against the SNR for such system is illustrated in Figure 8.11. The figure clearly demonstrates the advantage of using interleaver for both ‘soft’ and ‘hard’ decoding as a performance improvement of > 0.5 dB is achieved for ‘soft’ decoding and > 1 dB for ‘hard’ decoding. The interleaver randomizes the sequential error in the output of the equalizer; hence an improved performance can be achieved.

Further improvement using the iterative equalization and decoding can be achieved. However, the focus here is to prove the existence of adaptive decoding for the convolutional code. Further study is necessary to investigate the performance of ANN decoder with larger constraint length.

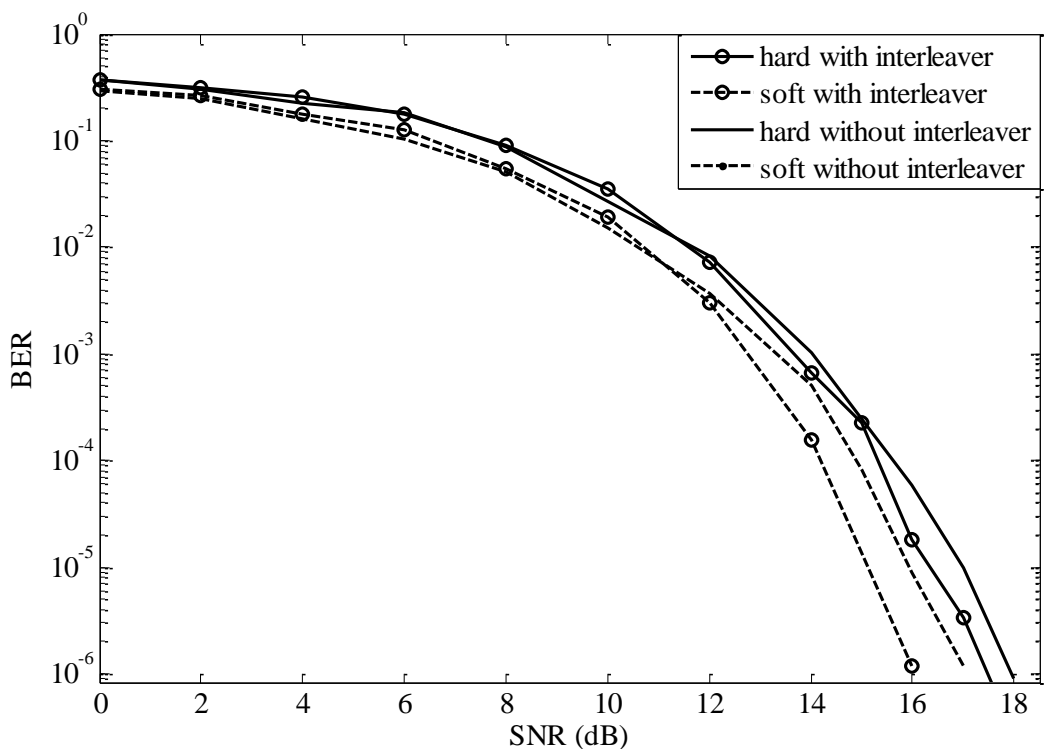


Figure 8.11: BER against the SNR for an ANN equalizer, ANN decoder with and without interleaver/deinterleaver pair in a dispersive channel with D_T of 1.

8.6 Summary

A ‘soft’ sliding block ANN decoder for the $\frac{1}{2}$ rate convolutional code was proposed and studied. Unlike Viterbi algorithm, where the decoder locates a path that minimizes the Hamming distance between the possible transmitted and received codewords, the ANN classifies the signal in a complex vector plane based on the observation vector. A two layered feedforward backpropagation ANN with the Log-sigmoid transfer function was trained for classification tasks. Simulations were carried out to optimize system parameters for the best performance and it was observed that a training length of 40000 bits with a decoding window of 7 trained at an SNR value of 2 dB would provide optimum performance. The comparative study with Viterbi decoder showed that ANN decoder outperforms the Viterbi ‘hard’ decoder. The Viterbi ‘soft’ decoder provides the best BER performance for the entire range of SNRs outperforming the ANN ‘soft’ decoder by a SNR value of 0.6 dB at the BER of 10^{-6} . The combination of the ANN equalizer and the ANN decoder was a very effective in improving overall system performance. A SNR reduction of ~ 4 dB was obtained using the ANN ‘soft’ decoder compared to uncoded equalized system in diffuse indoor OWC channels. Incorporating interleaver/deinterleaver pair at the transceiver can also enhance the performance with a potential gain of 1 dB using ‘soft’ decoding. Though the ANN decoder provides an improved performance compared to uncoded scheme and offers a number of advantages compared to Viterbi decoder, a further study and modification in the ANN structure is necessary to make the decoder practically realizable and efficient. In this Chapter, it was proved that ANN can act as a decoder for $\frac{1}{2}$ rate convolutional code with constraint length of 3. Due to time constraints, the ANN structure for constraint length greater than 3 was not investigated. Further study might be useful to generalize the ANN decoder for convolutional code.

Chapter 9 Hardware Realization

9.1 Introductions

The Chapters six, seven and eight introduced a number of techniques that can be used to reduce the effect of FLI and ISI. The wavelet based denoising significantly reduces the power penalty due to the FLI and the ANN can be an effective measure to reduce the power penalty due to ISI. The computer simulations were carried out to measure the effectiveness of the DWT-ANN receiver. In this chapter, the realization of such system in a digital signal processing (DSP) board is reported. The DSP is preferred over analogue components due to space, flexibility and ease of use. A small change in design parameters may results in complete rewiring of hard-wired analogue circuit, while the same effect can be achieved by changing few lines of code in a ROM or EPROM of DSP.

Matlab/Simulink Embedded IDE link [300] in combination with Texas instrument (TI) code composer studio (CCS) is used for rapid prototyping of the system. The system is implemented in DSK TMS320C6713 DSP board. TMS320C6713 is capable of floating-point operations with clock speed of 225 MHz [301]. Hence if the system could be successfully realized in the DSP board, any modern DSP board could be used for high speed operations. To verify the DSP results, output from the DSP board is imported to the host computer and compared with the Matlab output. Details of the DSP implementation with significant outputs are described in this chapter.

9.2 DWT Denoising in DSP

Though Matlab simulation provides a significant insight into working principle of DWT, to obtain a model close to practical cases, the Simulink is preferred. The Matlab and Simulink treat the boundary value conditions differently and hence significant differences can be observed in the initial output of DWT decomposition. Moreover, the filter delays are ignored in the Matlab. As a result, a working Simulink model of DWT denoising is necessary to implement the proposed system in DSP board. The Simulink model then can be converted into C-language which can be used to program the DSP board using the CCS.

The Simulink model of DWT based denoising is shown in Figure 9.1. The signal is first decomposed into a number of wavelet levels. The DWT decomposition is implemented using a filter bank (see Figure 9.2 (a)). Each level of decomposition is accomplished passing the signal thorough a HPF and a LPF. The output of the LPF is further decomposed using the similar filters until the desired level of decomposition is obtained. For denoising FLI, the output of LPF from the lowest level of decomposition filter is made zero as explained in Chapter 5, Section 5.5. The denoised signal is reconstructed by reversing the decomposition process as shown in Figure 9.2 (b). The reconstruction filter bank is exact mirror image of decomposition filter bank. It can be observed that a number of delays are used in the reconstruction process to account the filter delays. Filter delays are cumulative and depend on the order of LPF or HPF. Hence different delay values are required at different level of reconstruction (see Figure 9.2 (b)). In this study, the family of Daubechies mother wavelet (db8) is utilized with an order of 15. Hence the delay values are $15 \times 2^{(2i-1)}$, where $i \in \mathbb{Z} \ \& \ i > 0$.

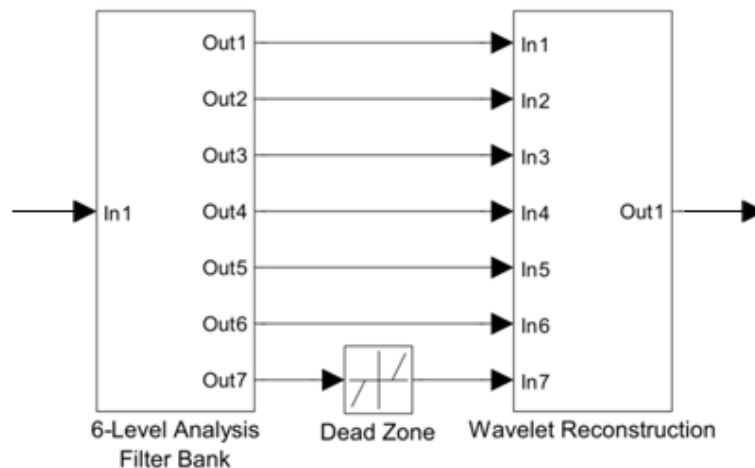


Figure 9.1: Simulink diagram of the DWT based denoising

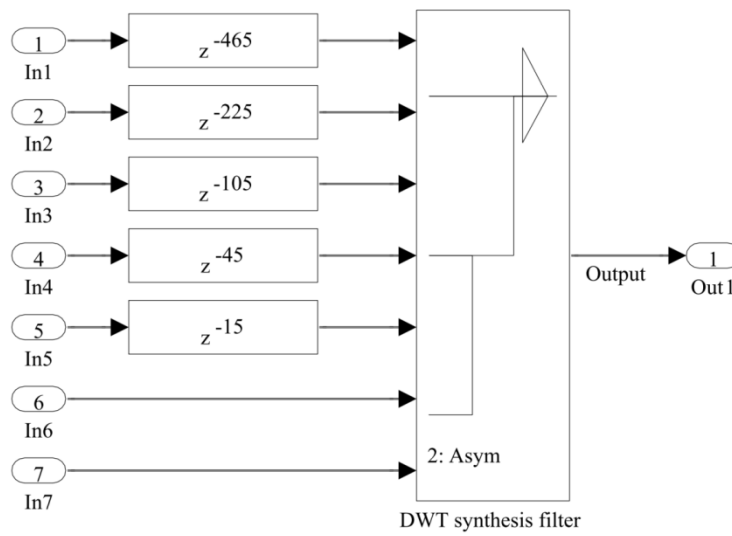
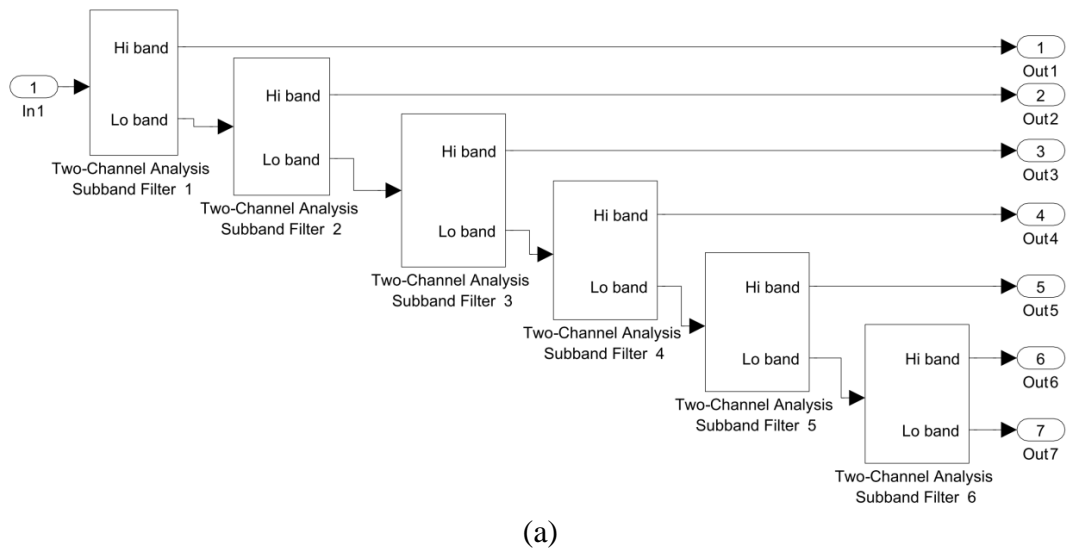


Figure 9.2: The block diagram of (a) DWT decomposition and (b) DWT reconstruction.

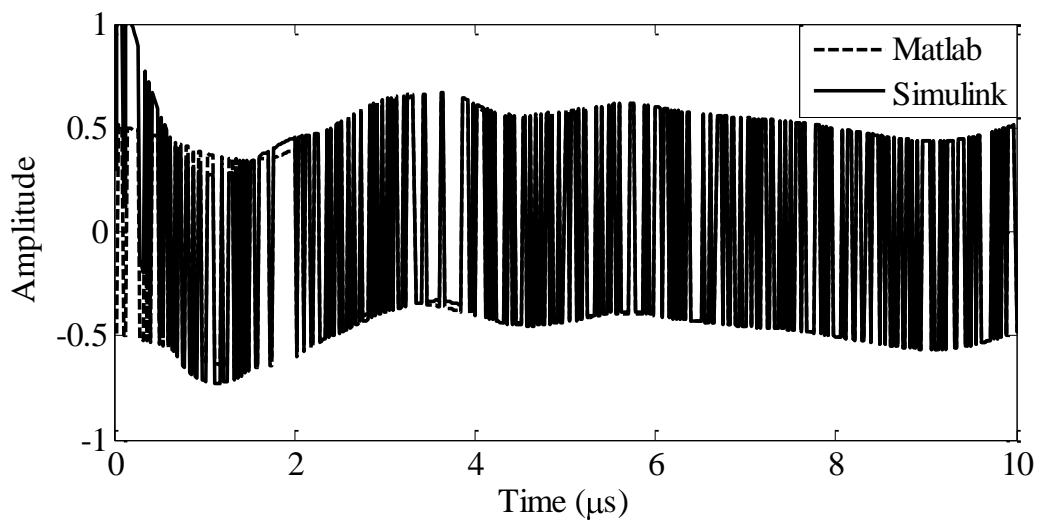


Figure 9.3: The received OOK signal at 50 Mbps in presence of FLI denoised using Matlab and Simulink

The OOK signal at 50 Mbps in presence of FLI denoised using Matlab and Simulink are given in Figure 9.3. For simplicity, the received signal is assumed to be free from any other form of noises and interference. For like to like comparisons, filter delay in the Simulink model is removed. Except for the initial phases of 0 - 0.5 μ s, the difference in the denoised signals are negligible. The differences in output at 0 - 0.5 μ s is observed as the boundary conditions are treated differently in Matlab and Simulink [302]. However, this study showed that the difference in initial outputs doesn't significantly affect the error probability of overall system.

The Simulink model can be converted into assembly code for the TMS320C6713 using Simulink and CCS. To verify the output from the DSP board, the real-time data exchange (RTDX) link is used to transfer data from DSP to computer. The received signal is denoised using DWT model given in Figure 9.1 and reconstructed using model given in Figure 9.2. The denoised signal is then fed back to host computer and DSP outputs are compared with Matlab outputs as shown in Figure 9.4. It should be noted here that the processing in the Matlab and DSP are independent of each other. The C-code for the DWT based denoising is given in Appendix A.

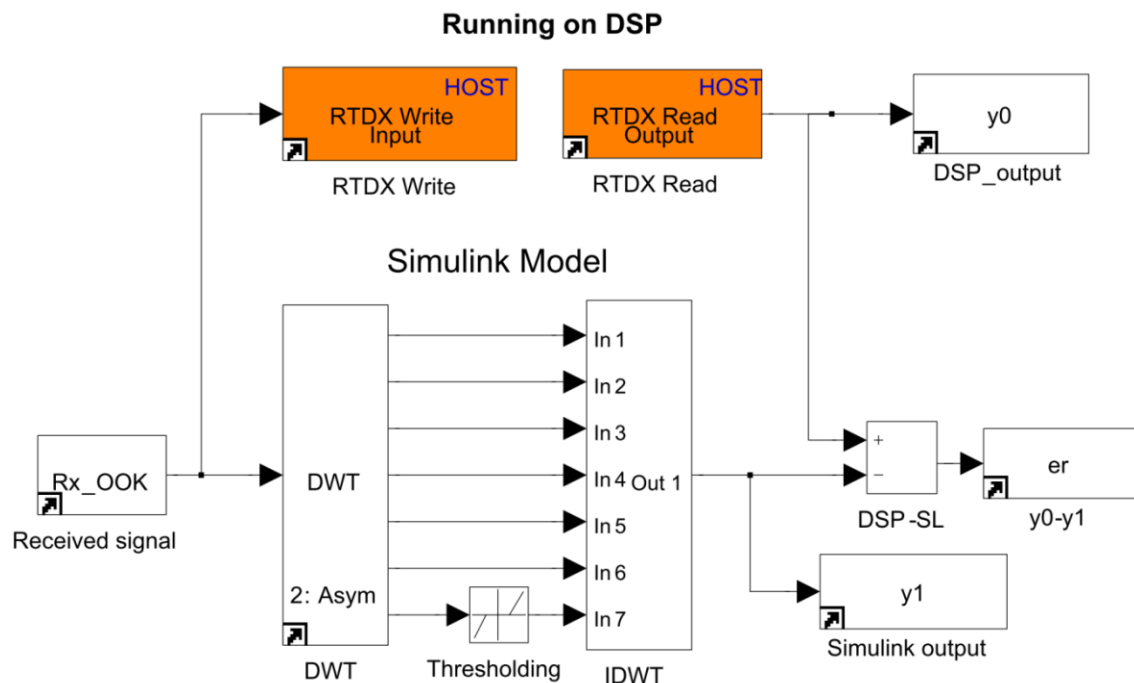


Figure 9.4: The Simulink model of DSP implementation of the DWT based denoising.

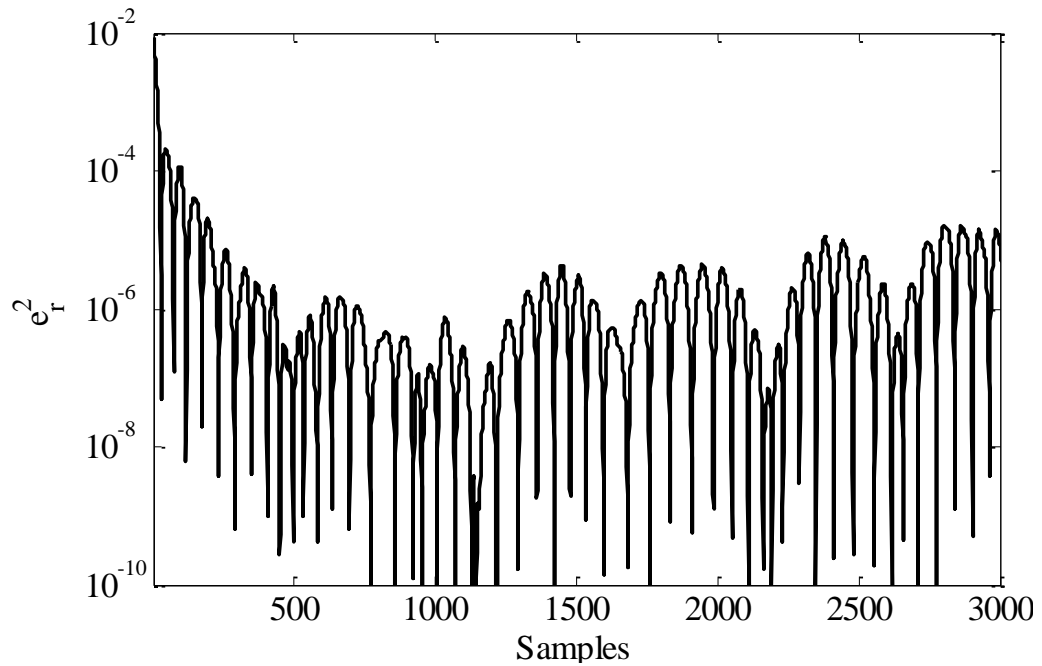


Figure 9.5: Square of error signal e_r between the DSP and Matlab denoised outputs against number of samples.

The error signal e_r is calculated by subtracting Matlab output with DSP output. The square of error signal for sample values is demonstrated in Figure 9.5. It can be observed that except for the initial phases, the error signal e_r is significantly low in the range of 10^{-6} . Since the denoised outputs are sliced using a threshold value of zero, the low value of e_r does not affect the error probability of the system. This provides evidence that the DWT based denoising can be successfully implemented in the DSP having capability of floating point operations.

9.3 ANN Based Equalizer in DSP

For the realization of ANN based equalizer, a similar approach is taken for DWT denoising is applied. The equalizer model is first realized in Simulink and the converted into assembly code for the TMS320C6713 using Simulink and CCS. The Simulink model of the ANN based DFE is given in Figure 9.6. For the simplicity of design, the number of feedforward and feedback TDLs, and the number of neurons in hidden layer is predefined and taken as six. The ANN is first trained in Matlab. The weight and bias

of the trained ANN is exported to the Simulink for rapid prototyping. The equalized outputs are sliced using a threshold level of 0.5. The resulting binary outputs are transferred to the host computer to calculate the BER. The C-code for the ANN based DFE is given in Appendix B.

The selection of equalized BER from Simulink model and DSP processing is tabulated in Table 9.1. It can be observed that the two results are strikingly similar for all range of SNR indicating the successful implementation of the ANN based DFE in the DSP board. The ANN based equalizer is implemented for a range of data rates and SNR values and found that the Simulink and the DSP outputs match each other for all scenarios. Since a slicer is applied to the ANN output, a minor difference in the output values in Simulink and DSP will not significantly changes the BER performance; leading to identical BER performance for all range of SNRs.

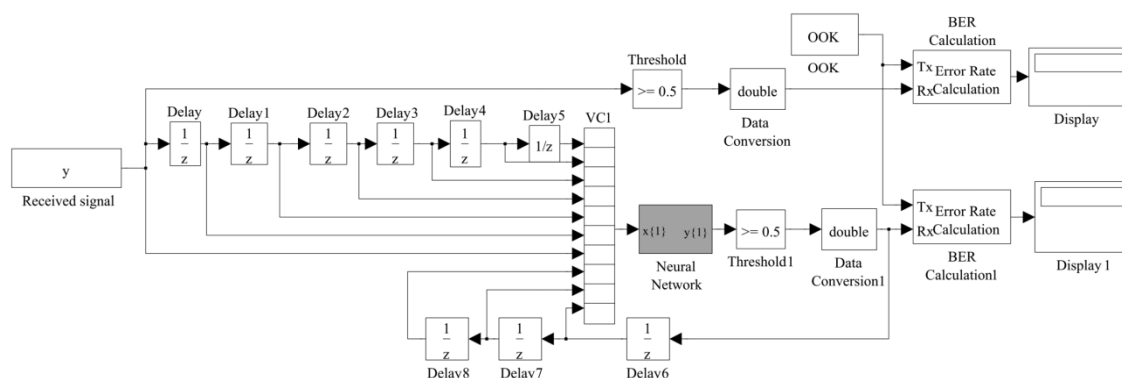


Figure 9.6 : Simulink model of ANN based DFE structure.

Table 9.1: The BER calculated using the Simulink model and DSP implementation.

SNR (dB)	BER(DSP)	BER(Simulink)
10	0.197	0.197
16	0.052	0.052
18	0.023	0.023
20	0.0012	0.0012

9.4 Summary

The realization of the proposed receiver based on DWT based denoising and ANN equalizer was achieved in TMS320C6713 DSB board. For the realization of the system, Simulink model of the proposed receivers were designed. The outputs from the Simulink and Matlab were compared and results showed that the outputs are fairly similar for DWT based denoising. The difference in the Simulink and the Matlab denoised outputs at the initial phase was due to difference in handling the boundary conditions. However, the difference did not make any changes in overall performance of the system. The comparative study of DSP and Matlab outputs showed the error signal was less than 10^{-6} indicating successful implementation of the DWT in DSP. Similar results were obtained for the ANN equalizer. In fact, the BERs obtained from the Simulink and the DSP processing were identical. This indicates that proposed receiver can be successfully implemented in DSP having capability of floating point operations.

Chapter 10 Conclusions and Future Works

10.1 Conclusions

The objective of research was to explore techniques to overcome challenges that hinder the full utilization of potential unlimited bandwidth in optical wavelength for wireless indoor personal communications. Three key challenges, namely the eye safety, fluorescent light interference and multipath induced intersymbol interference were taken into consideration. Their adverse affect in indoor optical wireless links were investigated and possible alleviation techniques were proposed. The comparative studies of existing and the proposed solutions were also carried out to recognize the possible benefit of proposed solutions.

Eye-safety is a critical issue which should be given an upmost priority in design consideration. Eye-safety limits the maximum average optical power that can be transmitted using a point source, thus limiting the link range. Wide beam area transmitter or holographic diffuse can be utilized to make the light source ocular safe. Alternatively, power efficient modulation techniques like PPM, DPIM and DH-PIM can be utilized to reduce transmitted power without necessarily compromising overall system reliability. Further, a suitable error control code can be used to reduce an SNR required to achieve a desired error probability.

The simplest method of improving reliability of communication system is by utilization of repetition code discussed in detail in Chapter 3. Bit repetition in which a bit is retransmitted predefined number of times for OOK and symbol repetition in which a symbol is retransmitted a number of times for PPM are effective measures which had been investigated in literature. The study took the repetition concept further and applied to a number of variable length modulation schemes like DPIM and DH-PIM. The DPIM

and DH-PIM schemes can be trade off for either the bandwidth or the power efficiencies and hence useful for indoor OWC system. However, difficulties in decoding of the repetition code arise due to non-fix symbol boundaries. A majority symbol decision process in which the symbol that is repeated the highest number of times is assumed to be valid symbol at the receiver. For the calculation of error probability for such decoding scheme, the average symbol length, the symbol error probability and error position needs to be taken into consideration. Expression for slot error probability of the variable symbol length modulation scheme with retransmission scheme was derived for retransmission rates of 3, 4 and 5 and given in details in Chapter 3, Section 3.4. The retransmission rate of greater than 5 is not recommendable due to significant reduction in throughput. The slot error probability of the retransmission scheme is directly proportional to the symbol error probability and inversely related to the average symbol length. Hence the retransmission scheme is more effective if average symbol length is less as it reduces the symbol error probability. Theoretically it is proven that the code gain is higher for higher retransmission rate as the slot error probability depends on the higher power of symbol error probability without repetition. The theoretical slot error probability of retransmission scheme is verified using computer simulation for 16-DH-PIM_{1&2}. The simulation showed excellent matching with the analytical error probability; confirming the validity of analysis. Though verified only for the DH-PIM system, it is expected that it will equally be valid for all variable modulation schemes. A code gain of ~ 2 dB and ~ 4 dB is obtained for retransmission rates of 3 and 5 at a slot error probability of 10^{-4} .

The retransmission scheme is effective, simple to implement without the need for additional transceiver. However, the penalty is a significant reduction in the data throughput. For example, to achieve a code gain of ~ 3 dB, the retransmission rate should be four, meaning a 300% overhead burden. Hence more effective convolutional code was the subject of Chapter 4. The convolutional code is not only very effective but also the only option for variable symbol length modulation techniques. The block code cannot be applied to these modulation schemes due to lack of fixed symbol boundaries. The convolutional code was applied to DPIM and DH-PIM schemes. The upper bound for error probability for coded sequence was derived and verified using computer simulation.

DH-PIM with a unique header pattern applied to the convolutional encoder results in a distinctive pattern. As a result, the state diagram and hence the error probability for convolutional coded DH-PIM is different from the general case. A new expression for upper bound for error probabilities of a $\frac{1}{2}$ rate convolutional encoder with constraint length of 3 was derived. The comparative studies of upper error bounds for DH-PIM and general case showed that for the same uncoded error probability, the convolutional coded DH-PIM should offer lower error probability. However, at lower error probability of $\leq 10^{-6}$, the upper bound for CC-DH-PIM and the general upper bound almost overlap. The predicted and simulated error probability for the CC-DH-PIM matched each other reasonably well providing the validity of theoretical analysis. The convolutional code provides significant reduction in SNR to achieve a certain error probability. The reduction in SNR increases with decreasing error probability. A code gain of ~ 4 dB is observed at a SER of 10^{-4} for DH-PIM_{1&2}. Comparative study of CC-DH-PIM₁ with other modulation scheme showed that it outperforms the uncoded PPM. However, coded PPM offers the best performance. The error probability of 16-CC-DH-PIM₂ is very close to the standard 16-DH-PIM₁, 16-CC-DH-PIM₂ requiring an additional SNR of 0.5 dB to achieve the same level of performance. Increasing the constraint length further reduces the SNR requirement. An additional ~ 2 dB code gain can be achieved at a SER of 10^{-5} using an encoder with constraint length of 7 compared to the encoder with constraint length of 3. Similar code gain was also observed for DPIM schemes. The reduction in SNR requirement means reduction in the average transmitted power. Hence the code gain due to the convolutional code can be used to increase the link length or trade off for the system performance.

The second challenge that was undertaken in this research was the interference due to artificial light sources. It is a unique challenge in the sense that the noise introduced by artificial light sources is periodic and can extend up to MHz range. Among the artificial light sources, the interference produced by fluorescent light driven by electronic ballasts possesses the most serious problem. The three popular modulations techniques OOK, PPM and DPIM were taken as subject of study and optical power requirement to achieve an error probability of 10^{-6} was evaluated under different conditions. The optical power requirements for all modulation schemes in presence of FLI were very high with almost a constant value irrespective of the data rates. For OOK, the optical power requirement was > 16 dB and for DPIM and PPM, the values depend on the bit resolution with higher bit resolution requiring less power. PPM with soft decision

decoding offered the highest immunity to the fluorescent light interference and optical power penalty is negligible even without any filter above the data rates > 20 Mbps. The immunity in PPM soft decision decoding is achieved as a sample value relative to other samples within a symbol is important, rather than the absolute values in other cases. The simplest method to reduce the FLI is by utilization of a HPF with suitable cut-off frequency. An alternative method based on DWT was investigated in this study. The fundamental concept of DWT based denoising is to separate the received signal into different bands of frequency using DWT decomposition and remove the band of signal that corresponds to the interference during reconstruction process. For the effective removal of the interference, the number of decomposition levels needed to be varied based on the data rate and the bit resolution. The optimum decomposition levels for OOK, PPM and DPIM schemes were determined for a range of data rates.

The DWT based denoising proved to be very effective in eliminating the effect of FLI at higher data rate. The optical power penalty due to the interference is effectively reduced to ~ 1.6 dB at 40 Mbps for OOK, which is a reduction of ~ 7.4 dB compared to the system without denoising. The power penalty is reduced further at higher data rates to a value of ~ 1.2 dB at 200 Mbps. The optical power penalty is always present for the OOK system due to spectral overlapping of interfering and modulating signal; as both have high spectral content near the DC value. For the modulating schemes with low spectral content near DC value like PPM, the power penalty due to the FLI can effectively be eliminated. Contrary to the OOK scheme, the power penalty is reduced to a null value using DWT based denoising for data rates of > 10 Mbps for 4-PPM and > 5 Mbps for 8 & 16-PPM with a hard decision decoding scheme. Since PPM with the soft decision decoding is immune to the FLI, the denoising does not provide any improvement for data rates > 20 Mbps. However, a marked improvement is observed at a lower data rate for all bit resolutions. DPIM was a special case in which the lower order of DPIM showed characteristic similar to OOK and higher order DPIM similar to PPM. The phenomenon is observed due to progressive reduction in spectral content near a DC value with increasing bit resolution. Though the DWT is very effective in reducing the effect of FLI for DPIM, it still leaves a power penalty of 0.7 dB for 4-DPIM at the data rates of > 40 Mbps. The power penalty is completely eliminated above the data rates of 30 Mbps for 16-DPIM.

Comparative studies of the HPF and DWT based denoising for effective removal of FLI were also carried out. The study showed that DWT has potential to outperform HPF with reduced complexity. The filter order for practical realization is also significantly reduced from a value of 2148 for HPF to 15 for DWT at 200 Mbps. This clearly indicates the advantage of DWT over HPF for effective denoising of FLI.

One of the most important challenges that hinder the full utilization of potential high bandwidth in the optical wavelength was the subject of Chapter 6. ISI due multipath propagation is critical at high data rates and can lead to a significant power penalty making such systems practically infeasible unless a compensation technique is incorporated at the receiver. The optical power penalty increases exponentially with the normalized delay spread and the OOK scheme is practically unrealizable above the normalized delay spread of 0.5. The ISI is more severe to the modulation scheme having smaller slot duration. It was observed that the soft decision decoding significantly improved the resistance to ISI compared to the hard decision decoding for the PPM scheme. A new hybrid decoding approach was proposed for DPIM(1GS). The hybrid approach combined the soft and hard decoding as soft decoding is not feasible for DPIM due to practical reasons. The hybrid approach offered a significant reduction in optical power requirement. However, the approach was not adequate to make diffuse system practically feasible at highly dispersive channel. The traditional approach of reducing the effect of ISI is utilization of an equalizing filter at the receiver. A new equalizing structure based on classification problem was proposed and the ANN was utilized as classification tool. A number of parameters for the ANN equalizer were optimized including number of neurons in the hidden layer, a training algorithm and a training length. Two architectures: the linear and the decision feedback were studied with later showing improved performance at a highly dispersive channel. Unlike the unequalized cases, the equalized systems did not show infinite power penalty even at a normalized delay spread of 2 indicating effectiveness of the proposed scheme. However, complete elimination of the ISI was not feasible and a small residual power penalty was observed for the equalized system. The power penalty was dependent on the normalized delay spread, modulation schemes and equalizer structures. A comparative study of the ANN based equalizer and traditional equalizer was also carried out. The mean square error for the ANN based equalizer is significantly lower than that of the traditional equalizer indicating a possible improvement. In fact, the ANN equalizer can match the

performance of traditional equalizer in all channel conditions with a reduced training length.

The combined effect of FLI and ISI was investigated in Chapter 7. The power penalty due to FLI with DWT denoising is more pronounced at low data rates while the ISI has severe effect only at high data rates. To compensate the combined effect of FLI and ISI, an DWT-ANN based receiver was proposed. The power penalty due to combined effects was found to be roughly the summation of individual power penalties. Identical performances were observed for PPM with a hard decision decoding scheme with and without FLI in a diffuse channel at a data rate greater than 5 Mbps. Similar performance profile was observed for 16-DPIM at a data rate of 20 Mbps or higher presenting evidence of the effectiveness of DWT-ANN based receiver to successfully eliminate FLI and ISI.

In Chapter 8, adaptive soft sliding decoding of convolutional code using ANN was studied. Though the Viterbi algorithm is the optimum for the convolutional code, a number of practical limitations caused to look for an alternative approach. The adaptive decoding scheme for an error control code was subject of interest as decoding does not require the knowledge of the encoder and hence offering possibility of adaptive encoding to obtain optimum performance in a given environment. A feedforward backpropagation ANN was used to decode the convolutional code. A number of ANN parameters including number of neurons, decoding window and training length were optimized for efficient training. With optimum parameters utilized for the ANN decoder, it was observed that ANN with a hard decision decoding structure can match the performance of the Viterbi hard decision decoding. However the Viterbi soft decision decoding offers the best performance outperforming the ANN soft decoding by > 0.6 dB. This signifies that the suboptimal ANN decoder can also be very effective convolutional decoder.

Finally, the practical realization of the DWT-ANN receiver was carried out using a DSP board and reported in Chapter 9. Rapid prototyping of the proposed receiver was carried out using the Matlab/Simulink and a code composer studio and practically realized in TMS320C6713 DSK DSP board. To verify the experimental results, the DSP output was transferred to the host computer in real time using RDTX and compared with the simulation results. The comparison showed that DSP board output differs only

marginally to simulation results. However the marginal difference does not change the overall error probability of the system. The output from the DSP board was obtained for different conditions and the results always verified the computer simulation, thus indicating a successful realization of the DWT-ANN receiver in the DSP board.

10.2 Future Works

Though extensive study of the DWT-ANN based receiver had been carried for a number of channel conditions, it is imperative to provide a list of further works that is necessary to make the system more efficient and effective as well as for guidelines in further research perspective. A number of encouraging results were obtained and some of the results need further investigation in order to comprehend.

The most important improvement can be obtained in the practical realization of the DWT-ANN. In this study, an offline training strategy in which the weight and the bias for ANN were determined by computer simulations was utilized. However, the online training strategy in which the ANN parameters are adjusted in the DSP board itself would be more practical for real time application. The offline training is a valid method for verification purposes only.

A brief study of combined decoding and equalization using the ANN was carried out in Chapter 8 showing effectiveness of the ANN based decoder and equalizer. A broader study is necessary to establish this approach. Further enhancement can be obtained by soft decoding of the convolutional code as well as iterative decoding. Turbo decoding and equalization using ANN can be a topic of further investigation though such study can be very challenging due to limited investigations so far.

The study of the ANN decoder for convolutional code was limited to a $\frac{1}{2}$ rate encoder. The ANN decoder showed promising outputs encouraging further investigations. It is an interesting prospect to design an ANN decoder for a puncture convolutional code. Furthermore, it is still too early to predict the effectiveness of the ANN decoder for the turbo code. A strategy needs to be developed for the information exchange between different nodes of the ANN decoder for iterative decoding of turbo decoding. The interleaver/deinterleaver pair used in turbo code can cause a serious problem in

decoding. Nonetheless, such study can be very useful to further understand the turbo code as well as to design adaptive decoder for turbo code if successful.

The constraint length utilised in this study for a convolutional encoder with an ANN decoder is three. However, a longer constraint length provides further code gain with the penalty of increased complexity. The ANN decoder is based on a classification problem. Hence longer constraint length means a larger decoding window and higher number of classification boundaries. This can lead to increase in the training length, and the number of hidden neurons. Due to limitation of scope, the study of ANN decoder is not carried out beyond the constraint length of 3. The ANN decoder for encoder with a constraint length of greater than 3 represents a new research project.

One of the key limitations of the study is the focus on the indoor wireless applications though the proposed receiver design could easily be adapted to any digital communications. Since the ANN has adaptability, in principle ANN based receiver should perform equally well in nonstationary environment. The receiver design can be easily adapted to outdoor free space optical communications where the link is frequently exposed to the adverse environmental conditions like rain, fog, smoke. The adaptability of the DWT-ANN based receiver in such environment is very important for practical applications and is a subject of future research.

Appendix A

Filter Coefficients of Wavelet Families [302, 303]

The filter coefficients of different mother wavelets (Daubechies db_i , $i=1,2,\dots,8$) for DWT analysis are given in the appendix. The wavelet name (e.g. $db1$ for first member of Daubechies wavelet) is given in first row with filter coefficients in corresponding column.

Table A.1: Filter coefficients of Daubechies wavelets

db1	db2	db3	db4	db5	db6	db7	db8	db9
0.7071067812	0.482962913145	0.332670552950963	0.230377813309	0.160102397974	0.111540743350	0.077852054085	0.054415842243	0.038077947364
0.7071067812	0.836516303737	0.806891509313336	0.714846570553	0.603829269797	0.494623890398	0.396539319482	0.312871590914	0.243834674613
	0.224143868042	0.459877502119332	0.630880767940	0.724308528438	0.751133908021	0.729132090846	0.675630736297	0.604823123690
	-0.129409522551	0.135011020010391	-0.027983769417	0.138428145901	0.315250351709	0.469782287405	0.585354683654	0.657288078051
		0.085441273882247	-0.187034811719	-0.242294887066	-0.226264693965	-0.143906003929	-0.015829105256	0.133197385825
		0.035226291882102	0.030841381836	-0.032244869585	-0.129766867567	-0.224036184994	-0.284015542962	-0.293273783279
			0.032883011667	0.077571493840	0.097501605587	0.071309219267	0.000472484574	-0.096840783223
			-0.010597401785	-0.006241490213	0.027522865530	0.080612609151	0.128747426620	0.148540749338
				-0.012580751999	-0.031582039317	-0.038029936935	-0.017369301002	0.030725681479
				0.003335725285	0.000553842201	-0.016574541631	-0.044088253931	-0.067632829061
					0.004777257511	0.012550998556	0.013981027917	0.000250947115
					-0.001077301085	0.000429577973	0.008746094047	0.022361662124
						-0.001801640704	-0.004870352993	-0.004723204758
						0.000353713800	-0.000391740373	-0.004281503682
							0.000675449406	0.001847646883
							-0.000117476784	0.000230385764
								-0.000251963189
								0.000039347320

Table A.2: Filter coefficients of Symlets wavelets (Sym2- Sym8)

Sym 2	Sym 3	Sym 4	Sym 5	Sym 6	Sym 7	Sym 8
0.482962913145	0.332670552951	0.032223100604	0.019538882735	-0.007800708325	0.010268 176709	0.001889950333
0.836516303737	0.806891509313	-0.012603967262	-0.021101834025	0.001767711864	0.004010 244872	-0.000302920515
0.224143868042	0.459877502119	-0.099219543577	-0.175328089908	0.044724901771	-0.107808 237704	-0.014952258337
-0.129409522551	-0.135011020010	0.297857795606	0.016602105765	-0.021060292512	-0.140047 240443	0.003808752014
	-0.085441273882	0.803738751807	0.633978963458	-0.072637522786	0.288629 631752	0.049137179674
	0.035226291882	0.497618667633	0.723407690402	0.337929421728	0.767764 317003	-0.027219029917
		-0.029635527646	0.199397533977	0.787641141030	0.536101 917092	-0.051945838108
		-0.075765714789	-0.039134249302	0.491055941927	0.017441 255087	0.364441894835
			0.029519490926	-0.048311742586	-0.049552 834937	0.777185751701
			0.027333068345	-0.117990111148	0.067892 693501	0.481359651258
				0.003490712084	0.030515 513166	-0.061273359068
				0.015404109327	-0.012636 303403	-0.143294238351
					-0.001047 384889	0.007607487325
					0.002681 814568	0.031695087811
						-0.000542132332
						-0.003382415951

Table A.3: Filter coefficients of Coiflet wavelets (Coif 1- Coif 4)

Coif 1	Coif 2	Coif 3	Coif 4	Coif 5
-0.072732619513	0.016387336464	-0.003793512864	0.000892313669	-0.000212080840
0.337897662458	-0.041464936782	0.007782596427	-0.001629492013	0.000358589688
0.852572020212	-0.067372554722	0.023452696142	-0.007346166328	0.002178236358
0.384864846864	0.386110066823	-0.065771911282	0.016068 943965	-0.004159358782
0.072732619513	0.812723635450	-0.061123390003	0.026682300156	-0.010131117521
-0.015655728135	0.417005184424	0.405176902410	-0.081266699681	0.023408156788
	-0.076488599079	0.793777222626	-0.056077313317	0.028168028974
	-0.059434418647	0.428483476378	0.415308407030	-0.091920010569
	0.023680171946	-0.071799821619	0.782238930921	-0.052043163181
	0.005611434819	-0.082301927107	0.434386056491	0.421566206733
	-0.001823208871	0.034555027573	-0.066627474263	0.774289603730
	-0.000720549445	0.015880544864	-0.096220442034	0.437991626216
		-0.009007976137	0.039334427123	-0.062035963969
		-0.002574517689	0.025082261845	-0.105574208714
		0.001117518771	-0.015211731528	0.041289208754
		0.000466216960	-0.005658286 687	0.032683 574270
		-0.000070983303	0.003751436157	-0.019761778945
		-0.000034599773	0.001266561929	-0.009164231163
			-0.000589020756	0.006764 185449
			-0.000259974552	0.002433373213
			0.000062339034	-0.001662863702
			0.000031229876	-0.000638131343
			-0.000003259680	0.000302259582
			-0.000001784985	0.000140541150
				-0.000041340432
				-0.000021315027
				0.000003734655
				0.000002063762
				-0.000000167443
				-0.000000095177

Table A.4: Filter coefficients of Biorthogonal Spline (Bior) wavelets

Bior 1.3	Bior 1.5	Bior 2.2	Bior 2.4
0.7071067812	0.7071067812	0.3535533906	0.3535533906
0.7071067812	0.7071067812	0.7071067812	0.7071067812
		0.3535533906	0.3535533906
-0.08838834765	0.01657281518		
0.08838834765	-0.01657281518	-0.1767766953	0.03314563037
0.7071067812	-0.121533978	0.3535533906	-0.06629126074
0.7071067812	0.121533978	1.060660172	-0.1767766953
0.08838834765	0.7071067812	0.3535533906	0.4198446513
-0.08838834765	0.7071067812	-0.1767766953	0.994368911
	0.121533978		0.4198446513
	-0.121533978		-0.1767766953
	-0.01657281518		-0.06629126074
	0.01657281518		0.03314563037

References

- [1] A. G. Bell, "On the production and reproduction of sound by light," *American Journal of Sciences*, vol. XX, no. 118, pp. 305 - 324, 1880.
- [2] J. S. Belrose, "Fessenden and Marconi: their differing technologies and transatlantic experiments during the first decade of this century," *International Conference on 100 Years of Radio*, London, UK, pp. 32-43, 1995.
- [3] F. R. Gfeller and U. Bapst, "Wireless in-house data communication via diffuse infrared radiation," *Proceedings of the IEEE*, vol. 67, no. 11, pp. 1474- 1486, 1979.
- [4] D. O'Brien, G. Parry, and P. Stavrinou, "Optical hotspots speed up wireless communication," *Nature Photonics*, vol. 1, no. 5, pp. 245-247, 2007.
- [5] C. Ta-Shing and M. Gans, "High speed infrared local wireless communication," *IEEE Communications Magazine*, vol. 25, no. 8, pp. 4-10, 1987.
- [6] A. M. Street, P. N. Stavrinou, D. C. O'Brien, and D. J. Edwards, "Indoor optical wireless systems - A review," *Optical and Quantum Electronics*, vol. 29, pp. 349-378, 1997.
- [7] D. Heatley, D. R. Wisely, and P. Cochrane, "Optical wireless: The story so far," *IEEE Communications Magazine*, vol. 36, no. 12, pp. 72-82, 1998.
- [8] P. S. Peter, L. E. Philip, T. D. Kieran, R. W. David, M. Paul, and W. David, "Optical wireless: a prognosis," *Proc. SPIE*, PA, USA, pp. 212-225, 1995.
- [9] M. D. Kotzin and A. P. van den Heuvel, "A duplex infra-red system for in-building communications," *36th IEEE Vehicular Technology Conference*, pp. 179-185, 1986.
- [10] R. L. Poulin, D. R. Pauluzzi, and M. R. Walker, "A multi-channel infrared telephony demonstration system for public access applications," *IEEE International Conference on Selected Topics in Wireless Communications*, pp. 286-291, 1992.
- [11] R. D. Wisely, "A 1 Gbit/s optical wireless tracked architecture for ATM delivery," *IEE Colloquium on Optical Free Space Communication Links*, London, UK, pp. 14/1-14/7, 1996.
- [12] A. Mihaescu, A. Songue, P. Besnard, O. Bouchet, and L. Qiang, "Reduced model channel method for impulse response: Characterization of indoor wireless optical channels," *CNSDSP*, pp. 544-547, 2008.
- [13] H.-S. Lee, "A photon modeling method for the characterization of indoor optical wireless communication," *Progress In Electromagnetics Research*, vol. PIER 92, pp. 121-136, 2009.
- [14] J. B. Carruthers and S. M. Carroll, "Statistical impulse response models for indoor optical wireless channels," *International Journal of Communication Systems*, vol. 18, no. 3, pp. 267-284, 2005.
- [15] G. W. Marsh and J. M. Kahn, "50-Mb/s diffuse infrared free-space link using on-off keying with decision-feedback equalization," *IEEE Photonics Technology letters*, vol. 6, no. 10, pp. 1268 - 1270, 1994.
- [16] G. W. Marsh and J. M. Kahn, "Performance evaluation of experimental 50-Mb/s diffuse infrared wireless link using on-off keying with decision-feedback equalization," *IEEE Transactions on Communications*, vol. 44, no. 11, pp. 1496-1504, 1996.
- [17] D. C. O'Brien, G. E. Faulkner, E. B. Zyambo, K. Jim, D. J. Edwards, P. Stavrinou, G. Parry, J. Bellon, M. J. Sibley, V. A. Lalithambika, V. M. Joyner, R. J. Samsudin, D. M. Holburn, and R. J. Mears, "Integrated transceivers for

- optical wireless communications," *IEEE Journal of Selected Topics in Quantum Electronics*, vol. 11, no. 1, pp. 173-183, 2005.
- [18] D. C. O'Brien, G. E. Faulkner, K. Jim, E. B. Zyambo, D. J. Edwards, M. Whitehead, P. Stavrinou, G. Parry, J. Bellon, M. J. Sibley, V. A. Lalithambika, V. M. Joyner, R. J. Samsudin, D. M. Holburn, and R. J. Mears, "High-speed integrated transceivers for optical wireless," *IEEE Communications Magazine*, vol. 41, no. 3, pp. 58-62, 2003.
- [19] M. D. A. Mohamed and S. Hranilovic, "Optical impulse modulation for indoor diffuse wireless communications," *IEEE Transactions on Communications*, vol. 57, no. 2, pp. 499-508, 2009.
- [20] T. Lueftner, C. Kroepl, M. Huemer, J. Hausner, R. Hagelauer, and R. Weigel, "Edge-position modulation for high-speed wireless infrared communications," *IEE Proceedings Optoelectronics*, vol. 150, no. 5, pp. 427-437, 2003.
- [21] U. Sethakaset and T. A. Gulliver, "Differential amplitude pulse-position modulation for indoor wireless optical communications," *EURASIP Journal on Applied Signal Processing*, vol. 2005, no. 1, pp. 3-11, 2005.
- [22] U. Sethakaset and T. A. Gulliver, "Performance of differential pulse-position modulation (DPPM) with concatenated coding over optical wireless communications," *IET communications*, vol. 2, no. 1, pp. 45-52, 2008.
- [23] Z. Ghassemlooy and N. M. Aldibbiat, "Multilevel digital pulse interval modulation scheme for optical wireless communications," *ICTON2006*, Nottingham, UK, pp. 149-153, 2006.
- [24] Z. Ghassemlooy and A. R. Hayes, "Digital pulse interval modulation for IR communication systems-a review," *International Journal of Communication Systems*, vol. 13, no. 7-8, pp. 519-536, 2000.
- [25] N. M. Aldibbiat, Z. Ghassemlooy, and R. McLaughlin, "Indoor optical wireless systems employing dual header pulse interval modulation (DH-PIM)," *International Journal of Communication Systems*, vol. 18, no. 3, pp. 285-305, 2005.
- [26] S. H. Khoo, E. B. Zyambo, G. Faulkner, D. C. O'Brien, D. J. Edwards, M. Ghisoni, and J. Bengtsson, "Eyesafe optical link using a holographic diffuser," *IEE Colloquium on Optical Wireless Communications*, London, UK, pp. 3/1-3/6, 1999.
- [27] Y. Jianping, C. K. C. George, and L. Tuan-Kay, "Holographic diffuser for diffuse infrared wireless home networking," *Optical Engineering*, vol. 42, no. 2, pp. 317-324, 2003.
- [28] M. R. Pakravan, E. Simova, and M. Kavehrad, "Holographic diffusers for indoor infrared communication systems," *International Journal of Wireless Information Networks*, vol. 4, pp. 259-274, 1997.
- [29] M. Wen, J. Yao, D. W. K. Wong, and G. C. K. Chen, "Holographic diffuser design using a modified genetic algorithm," *Optical Engineering*, vol. 44, no. 8, p. 085801, 2005.
- [30] K. L. Sterckx, J. M. H. Elmirghani, and R. A. Cryan, "Pyramidal fly-eye detection antenna for optical wireless systems," *Optical Wireless Communications (Ref. No. 1999/128), IEE Colloquium on*, pp. 5/1-5/6, 1999.
- [31] A. G. Al-Ghamdi and J. M. H. Elmirghani, "Performance evaluation of a pyramidal fly-eye diversity antenna in an indoor optical wireless multipath propagation environment under very directive noise sources," *Optoelectronics, IEE Proceedings -*, vol. 150, no. 5, pp. 482-489, 2003.
- [32] D. I. Shin, K. H. Shin, I. K. Kim, K. S. Park, T. S. Lee, S. I. Kim, K. S. Lim, and S. J. Huh, "Low-power hybrid wireless network for monitoring infant incubators," *Medical Engineering & Physics*, vol. 27, no. 8, pp. 713-716, 2005.

- [33] S. Williams, "IrDA: Past, present and future," *IEEE Personal Communications*, vol. 7, no. 1, pp. 11-19, 2000.
- [34] "Infrared Data Association Releases IrDA Global Market Report 2007," 2007, <http://irda.affiniscap.com/displaycommon.cfm?an=1&subarticlenbr=17>, last accessed date: 11 Oct. 2009.
- [35] "KDDI developed high-speed wireless data transmission technology for USB devices," http://en.gigazine.net/index.php?/news/comments/20090715_usb_wireless, last accessed date: 11 Oct. 2009.
- [36] S. Biswas, R. Tatchikou, and F. Dion, "Vehicle-to-vehicle wireless communication protocols for enhancing highway traffic safety," *IEEE Communications Magazine*, vol. 44, no. 1, pp. 74-82, 2006.
- [37] D. C. O'Brien, G. E. Faulkner, S. Zikic, and N. P. Schmitt, "High data-rate optical wireless communications in passenger aircraft: Measurements and simulations," *CNSDSP 2008*, pp. 68-71, 2008.
- [38] N. P. Schmitt, T. Pistner, C. Vassipoulis, D. Marinos, A. C. Boucouvalis, M. Nikolitsa, C. Aidinis, and G. Metaxas, "Diffuse wireless optical link for aircraft intra-cabin passenger communication," *Proc. Communications systems, networks and digital signal* pp. 625-628, 2006.
- [39] H. Kotake, S. Haruyama, M. Nakagawa, and K. Seki, "BER characteristic of ground-to-train communication system using free-space optics technology," *ICTON '07*, pp. 165-169, 2007.
- [40] S. Hagihira, M. Takashina, M. Mori, N. Taenaka, T. Mashimo, and I. Yoshiya, "Infrared transmission of electronic information via LAN in the operating room," *Journal of Clinical Monitoring and Computing*, vol. 16, no. 3, pp. 171-175, 2000.
- [41] "Safety of laser products - Part 1: Equipment classification and requirements ", IEC, report no: I. 60825-1:2001, 2007.
- [42] D. A. Rockwell and G. S. Mecherle, "Optical wireless: low-cost, broadband, optical access," SONA Communications Corporation, 2007.
- [43] J. M. Kahn and J. R. Barry, "Wireless infrared communications," *Proceedings of IEEE*, vol. 85, no. 2, pp. 265-298, 1997.
- [44] J. R. Barry, *Wireless Infrared Communications*. Boston: Kluwer Academic Publishers, 1994.
- [45] J. B. Carruthers, "Wireless infrared communications," Wiley Encyclopaedia of Telecommunications, 2002.
- [46] P. L. Eardley, D. R. Wisely, D. Wood, and P. McKee, "Holograms for optical wireless LANs," *IEE Proceedings Optoelectronics*, vol. 143, no. 6, pp. 365 - 369, 1996.
- [47] M. R. Pakravan, E. Simova, and M. Kavehrad, "Holographic diffusers for indoor infrared communication systems," *Global Telecommunications Conference*, London, UK, pp. 1608-1612, 1996.
- [48] P. Benitez, J. C. Minano, F. J. Lopez, D. Biosca, R. Mohedano, M. Labrador, F. Munoz, K. Hirohashi, and M. Sakai, "Eye-safe collimated laser emitter for optical wireless communications," *Optical Wireless Communications*, Boston, 2002.
- [49] W. Mengtao, Y. Jianping, W. K. W. Damon, and C. K. C. George, "Holographic diffuser design using a modified genetic algorithm," *Optical Engineering*, vol. 44, no. 8, pp. 085801-1-085801-8, 2005.
- [50] Z. Ghassemlooy, A. R. Hayes, N. L. Seed, and E. D. Kaluarachchi, "Digital pulse interval modulation for optical communications," *IEEE Communications Magazine*, vol. 36, no. 12, pp. 95-99, 1998.

- [51] A. R. Hayes, "Digital pulse interval modulation for indoor optical wireless communication systems," PhD thesis, Sheffield Hallam University, UK, 2002.
- [52] D. Shiu and J. M. Kahn, "Differential pulse position modulation for power-efficient optical communication," *IEEE Transaction on Communication*, vol. 47, no. 8, pp. 1201-1210, 1999.
- [53] T. Luftner, C. Kropl, R. Hagelauer, M. Huemer, R. Weigel, and J. Hausner, "Wireless infrared communications with edge position modulation for mobile devices," *IEEE - Wireless Communications*, vol. 10, no. 2, pp. 15-21, 2003.
- [54] Z. Yu, R. Green, and M. Leeson, "Multiple pulse amplitude and position modulation for the optical wireless channel," *10th Anniversary International Conference on Transparent Optical Networks*, Athens, pp. 193-196, 2008.
- [55] A. Tavares, R. L. Aguiar, R. T. Valadas, D. M. Santos, and A. M. Duarte, "Advanced technologies for infrared wireless indoor local area networks," *Proc International Conf. on Telecommunications - ConTEL*, Figueira da Foz, Portugal pp. 68-72, 2001.
- [56] K. Samaras, D. C. O'Brien, and D. J. Edwards, "Combination of repetition-coded PPM with SR-ARQ for wireless infra-red communication," *Electronics Letters*, vol. 34, no. 23, pp. 2199-2201, 1998.
- [57] T. Ozugur, M. Naghshineh, P. Kermani, C. M. Olsen, B. Rezvani, and J. A. Copeland, "Performance evaluation of L-PPM links using repetition rate coding," *The Ninth IEEE International Symposium on Personal, Indoor and Mobile Radio Communications*, pp. 698-702, 1998.
- [58] L. Shu, D. Costello, and M. Miller, "Automatic-repeat-request error-control schemes," *IEEE Communications Magazine*, *IEEE*, vol. 22, no. 12, pp. 5-17, 1984.
- [59] S. Rajbhandari, Z. Ghassemlooy, and N. M. Aldibbiat, "Slot error rate performance of DH-PIM with symbol retransmission for optical wireless links," *European Transactions on Telecommunications*, vol. 20, no. 2, pp. 217-225, 2009.
- [60] N. Kim and H. Park, "Low-complexity iterative equalisation and decoding for wireless optical communications," *IET Communications*, vol. 2, no. 1, pp. 61-65, 2008.
- [61] H. F. Rashvand, Y. Zeng, R. J. Green, and M. S. Leeson, "Look-up table error correcting multiple pulse PPM codes for wireless optical communication channels," *IET communications*, vol. 2, no. 1, pp. 27-34, 2008.
- [62] H. Kohsuke, O. Ikuo, and F. Chikato, "Iterative decoding of convolutional codes applied to separate coded PPM," *Electronics and Communications in Japan (Part I: Communications)*, vol. 86, no. 12, pp. 78-90, 2003.
- [63] H. Park, "Convolutional coded pulse-position modulation on wireless optical communication," *IEE Proceedings of optoelectronics*, vol. 148, no. 4, pp. 199-203 2001.
- [64] T. Ohtsuki, "Rate-adaptive indoor infrared wireless communication systems using repeated and punctured convolutional codes," *IEEE Communications Letters*, vol. 4, no. 2, pp. 56-58, 2000.
- [65] M. Matsuo, T. Ohtsuki, I. Sasase, and T. Udagawa, "Rate-adaptive indoor infrared wireless communication systems using punctured convolutional codes and adaptive PPM," *Electronics and Communications in Japan (Part I: Communications)*, vol. 84, no. 8, pp. 31-39, 2001.
- [66] K. Akhavan, M. Kavehrad, and S. Jivkova, "High-speed power-efficient indoor wireless infrared communication using code combining—Part II," *IEEE Transaction on Communications*, vol. 50, no. 9, pp. 1495-1502, 2002.

- [67] D. C. Lee and J. M. Kahn, "Coding and equalization for PPM on wireless infrared channels," *IEEE Transaction on Communication*, vol. 47, no. 2, pp. 255-260, 1999.
- [68] O. Tomoaki, "Performance analysis of indoor infrared wireless systems using PPM CDMA," *Electronics and Communications in Japan (Part I: Communications)*, vol. 85, no. 1, pp. 1-10, 2002.
- [69] S. Lee, J. M. KAHN, and M. D. Audeh, "Trellis-coded pulse-position modulation for indoor wireless infrared communications," *IEEE Transaction on Communications*, vol. 45, no. 9, pp. 1080-1087, 1997.
- [70] K. Harada, I. Oka, and C. Fujiwara, "Iterative decoding of convolutional codes applied to separate coded PPM," *Electronics and Communications in Japan (Part I: Communications)*, vol. 86, no. 12, pp. 78-90, 2003.
- [71] K. Akhavan, M. Kavehrad, and S. Jivkova, "High-speed power-efficient indoor wireless infrared communication using code combining—Part I," *IEEE Transactions on Communications*, vol. 50, no. 9, pp. 1495-1502, 2002.
- [72] Y.-B. Zhu, H.-X. Wang, and T.-Y. Zhang, "Analysis of error performance on Turbo coded FDPIM," *Optoelectronics Letters*, vol. 4, no. 4, pp. 287-291, 2008.
- [73] U. Sethakaset and T. A. Gulliver, "Marker codes to correct insertion/deletion errors in differential pulse-position modulation for wireless infrared communications," *IEEE Pacific Rim Conference on Communications, Computers and signal Processing*, pp. 181-184, 2005.
- [74] Z. Ghassemlooy and S. Rajbhandari, "Convolutional coded dual header pulse interval modulation for line of sight photonic wireless links," *IET-Optoelectronics*, vol. 3, no. 3, pp. 142-148, 2009.
- [75] S. Rajbhandari, Z. Ghassemlooy, and N. M. Aldibbiat, "Performance of convolutional coded dual header pulse interval modulation in infrared links," *PGNET2006*, Liverpool, UK, pp. 227-231 2006.
- [76] S. Rajbhandari, Z. Ghassemlooy, N. M. Aldibbiat, M. Amiri, and W. O. Popoola, "Convolutional coded DPIM for indoor non-diffuse optical wireless link," *The 7th IASTED International Conferences on Wireless and Optical Communications* Montreal, Canada, pp. 286-290, 2007.
- [77] A. J. C. Moreira, R. T. Valadas, and A. M. d. O. Duarte, "Characterisation and modelling of artificial light interference in optical wireless communication systems," *Proceedings of the 6th IEEE International Symposium on Personal, Indoor and Mobile Radio Communications*, Toronto, Canada, pp. 326 - 331, 1995.
- [78] A. J. C. Moreira, R. T. Valadas, and A. M. d. O. Duarte, "Performance of infrared transmission systems under ambient light interference," *IEE Proceedings -Optoelectronics*, vol. 143, no. 6, pp. 339-346, 1996.
- [79] A. J. C. Moreira, R. T. Valadas, and A. M. d. O. Duarte, "Optical interference produced by artificial light," *Wireless Networks*, vol. 3, no. 2, pp. 131-140, 1997.
- [80] R. Narasimhan, M. D. Audeh, and J. M. Kahn, "Effect of electronic-ballast fluorescent lighting on wireless infrared links," *IEE Proceedings - Optoelectronics*, vol. 143, no. 6, pp. 347-354, 1996.
- [81] A. C. Boucouvalas, "Indoor ambient light noise and its effect on wireless optical links," *IEE Proceedings - Optoelectronics*, vol. 143, no. 6, pp. 334-338, 1996.
- [82] A. J. C. Moreira, A. M. R. Tavares, R. T. Valadas, and A. M. Duarte, "Modulation methods for wireless infrared transmission systems: performance under ambient light noise and interference," *Proceedings of SPIE*, Philadelphia, U.S.A., pp. 226-237, 1995.
- [83] K. Samaras, D. C. O'Brien, A. M. Street, and D. J. Edwards, "BER performance of NRZ-OOK and Manchester modulation in indoor wireless infrared links,"

- International Journal of Wireless Information Networks*, vol. 5, no. 3, pp. 219-233, 1998.
- [84] K. K. Wong, T. O'Farrell, and M. Kiatweerasakul, "The performance of optical wireless OOK, 2-PPM and spread spectrum under the effects of multipath dispersion and artificial light interference," *International Journal of Communication Systems*, vol. 13, no. 7-8, pp. 551-557, 2000.
- [85] N. M. Aldibbiat and Z. Ghassemlooy, "Artificial-light-interference effects on indoor optical wireless links employing DH-PIM," *Journal of Optical Networking*, vol. 5, no. 2, pp. 103-106, 2006.
- [86] A. M. R. Tavares, R. T. Valadas, and A. M. d. O. Duarte, "Performance of wireless infrared transmission systems considering both ambient light interference and inter-symbol interference due to multipath dispersion," *Conference on Optical Wireless Communications*, Boston, U.S.A, pp. 82-93., 1998.
- [87] A. J. C. Moreira, R. T. Valadas, and A. M. Duarte, "Reducing the effects of artificial light interference in wireless infrared transmission systems," *Proceedings of IEE Colloquium on Optical Free Space Communication Links*, London, U.K, pp. 5/1-5/10., 1996.
- [88] S. Lee, "Reducing the effects of ambient noise light in an indoor optical wireless system using polarizers," *Microwave and Optical Technology Letters*, vol. 40, no. 3, pp. 228-230, 2004.
- [89] R. T. Valadas, A. M. R. Tavares, and A. M. Duarte, "Angle diversity to combat the ambient noise in indoor optical wireless communication systems," *International Journal of Wireless Information Networks*, vol. 4, no. 4, pp. 275-288, 1997
- [90] A. M. Street, K. Samaras, D. C. O'Brien, and D. J. Edwards, "Closed form expressions for baseline wander effects in wireless IR applications," *Electronics Letters*, vol. 33, no. 12, pp. 1060-1062, 1997.
- [91] Z. Ghassemlooy, "Investigation of the baseline wander effect on indoor optical wireless system employing digital pulse interval modulation," *IET Communications*, vol. 2, no. 1, pp. 53-60, 2008.
- [92] R. J. Dickenson, "Wavelet analysis and artificial intelligence for diffuse indoor optical wireless communication." PhD thesis, Northumbria University, 2007.
- [93] S. Rajbhandari, Z. Ghassemlooy, and M. Angelova, "Effective denoising and adaptive equalization of indoor optical wireless channel with artificial light using the discrete wavelet transform and artificial neural network," *Journal of Lightwave Technology*, vol. 27, no. 20, pp. 4493-4500, 2009.
- [94] S. Rajbhandari, Z. Ghassemlooy, and M. Angelova, "Wavelet transform-Neural network based receiver for DPIM in diffuse indoor optical wireless links in presence of artificial light interference," *IJEEE*, vol. 5, no. 2, pp. 102-111, 2009.
- [95] J. B. Carruthers and J. M. Kahn, "Modeling of nondirected wireless Infrared channels," *IEEE Transaction on Communication*, vol. 45, no. 10, pp. 1260-1268, 1997.
- [96] J. M. Kahn, W. J. Krause, and J. B. Carruthers, "Experimental characterization of non-directed indoor infrared channels," *IEEE Transactions on Communications*, vol. 43, no. 234, pp. 1613-1623, 1995.
- [97] M. D. Audeh, J. M. Kahn, and J. R. Barry, "Performance of pulse-position modulation on measured non-directed indoor infrared channels," *IEEE Transaction on Communications*, vol. 44, no. 6, pp. 654-659, 1996.
- [98] M. D. Audeh, J. M. Kahn, and J. R. Barry, "Decision-feedback equalization of pulse-position modulation on measured nondirected indoor infrared channels," *IEEE Transaction on Communications*, vol. 47, no. 4, pp. 500-503, 1999.

- [99] J. R. Barry, "Sequence detection and equalization for pulse-position modulation," *International Conference on Communication*, New Orleans, LA, pp. 1561-1565, 1994.
- [100] T. Komine, L. Jun Hwan, S. Haruyama, and M. Nakagawa, "Adaptive equalization for indoor visible-light wireless communication systems," *Asia-Pacific Conference on Communications*, pp. 294-298, 2005.
- [101] S. Haykin, "Adaptive digital communication receivers," *IEEE Communications Magazine*, vol. 38, no. 12, pp. 106- 114, 2002.
- [102] K. Burse, R. N. Yadav, and S. C. Shrivastava, "Nonlinear stationary channel equalization of QAM signals using multiplicative neuron model," *International Journal of Computer Science and Network Security*, vol. 9, no. 5, pp. 273-279, 2009.
- [103] J. C. Patra and N. R. N. Pal, "A functional link artificial neural network for adaptive channel equalization," *Signal Processing*, vol. 43, no. 2, pp. 181 - 195, 1995.
- [104] S. K. Padhy, S. P. Panigrahi, P. K. Patra, and S. K. Nayak, "Non-linear channel equalization using adaptive MPNN," *Applied Soft Computing*, vol. 9, no. 3, pp. 1016-1022, 2009.
- [105] S. Rajbhandari, Z. Ghassemlooy, and M. Angelova, "Bit error performance of diffuse indoor optical wireless channel pulse position modulation system employing artificial neural networks for channel equalisation," *IET Optoelectronics*, vol. 3, no. 4, pp. 169-179, 2009.
- [106] S. Rajbhandari, Z. Ghassemlooy, and M. Angelova, "Signal detection and adaptive equalization using a discrete wavelet transform - artificial neural network for OOK indoor optical wireless links," *16th ICEE2008*, Tehran, Iran, 2008.
- [107] L. Juan and E. Mutafungwa, "Rate adaptation of convolutional coded optical CDMA systems for improved goodput," *Optics Communications*, vol. 240, no. 4-6, pp. 315-327, 2004.
- [108] A. Garda-Zambrana and A. Puerta-Notario, "Rate-adaptive modulation techniques for indoor wireless infrared links at bit rates of wide dynamic range," *IEEE Vehicular Technology Conference*, pp. 2313-2317 vol.4, 2001.
- [109] K. Akhavan, M. Kavehrad, and S. Jivkova, "Adaptive-rate code combining for wireless infrared communications systems employing direction diversity," *Proceedings of 21st Century Military Communications Conference* Los Angeles, USA, pp. 75-79, 2000.
- [110] C. Long and M. Groth, "Bibliography of early optical (audio) communications," 2005, http://modulatedlight.org/Modulated_Light_DX/ModLightBiblio.html, last accessed date: 11th Oct.2009.
- [111] C. R. Lomba, R. T. Valadas, and A. M. Duarte, "Efficient simulation of the impulse response of the indoor wireless optical channel," *International Journal of Communication Systems*, vol. 13, no. 7-8, pp. 537-549, 2000.
- [112] N. M. Aldibbiat, "Optical wireless communication systems employing dual header pulse interval modulation (DH-PIM)." PhD thesis, Sheffield Hallam University, UK, 2001.
- [113] T. Lüftner, "Edge position modulation for wireless infrared communications ", PhD thesis, Friedrich-Alexander University, 2005.
- [114] H. Joshi, R. J. Green, and M. S. Leeson, "Multiple sub-carrier optical wireless systems," *ICTON 2008*, Athens, pp. 184-188, 2008.
- [115] O. Gonza'lez , R. Pe' rez-Jime' nez, S. Rodr'iguez, J. Rabada'n, and A. Ayala, "OFDM over indoor wireless optical channel," *IEE Proceedings - Optoelectronics*, vol. 152, no. 4, pp. 199-204, 2005.

- [116] P. Hyuncheol and J. R. Barry, "Modulation analysis for wireless infrared communications," *ICC '95*, Seattle, WA, USA, pp. 1182-1186, 1995.
- [117] R. McClellan and J. Metzler, "Designing the new MAN," <http://www.networkworld.com/research/2001/1105feat.html>, last accessed date: 11 Oct. 2009.
- [118] T. Miki, T. Ohya, H. Yoshino, and N. Umeda, "The overview of the 4th generation mobile communication system," *ICICS'05*, Singapore, pp. 1551-1555, 2005.
- [119] D. O'Brien, "Cooperation in optical wireless communications," *Cognitive wireless networks: Concepts, methodologies and visions inspiring the age of enlightenment of wireless communications*, F. H. P. Fitzek and M. D. Katz, Eds.: Springer, 2007, pp. 623-634.
- [120] D. C. O'Brien and K. Marcos, "Optical wireless communications within fourth-generation wireless systems " *Journal of Optical Networking*, vol. 4, no. 6, pp. 312-322, 2005.
- [121] D. C. O'Brien, M. Katz, P. Wang, K. Kalliojarvi, S. Arnon, M. Matsumoto, R. Green, and S. Jivkova, "Short-range optical wireless communications," *Wireless world research forum*, pp. 1-22.
- [122] A. Acampora, "Last mile by Laser." *Scientific American Magazine* 2002, <http://www.scientificamerican.com/article.cfm?id=last-mile-by-laser>, last accessed date: 11 Oct. 2009.
- [123] H. A. Willebrand and B. S. Ghuman, "Fiber optics without fiber," *Spectrum, IEEE*, vol. 38, no. 8, pp. 40-45, 2001.
- [124] C. C. Davis, I. I. Smolyaninov, and S. D. Milner, "Flexible optical wireless links and networks," *Communications Magazine, IEEE*, vol. 41, no. 3, pp. 51-57, 2003.
- [125] R. J. Green, H. Joshi, M. D. Higgins, and M. S. Leeson, "Recent developments in indoor optical wireless systems," *IET Communications*, vol. 2, no. 1, pp. 3-10, 2008.
- [126] E. Leitgeb, J. Bregenzer, P. Fasser, and M. Gebhart, "Free space optics - extension to fiber-networks for the "last mile"," *LEOS 2002*, pp. 459-460 vol.2, 2002.
- [127] A. G. Al-Ghamdi and J. M. H. Elmirghani, "Multiple spot diffusing geometries for indoor optical wireless communication systems," *International Journal of Communication Systems*, vol. 16, no. 10, pp. 909-922, 2006.
- [128] J. Hamkins and B. Moision, "Selection of modulation and codes for deep-space optical communications," *Proceedings of the SPIE*, vol. 5338, no. 123, pp. 123-130, 2004.
- [129] A. Shlomi, "Optimization of urban optical wireless communication systems," *IEEE Transactions on Wireless Communications*, vol. 2, no. 4, pp. 626-629, 2003.
- [130] K. Wilson and M. Enoch, "Optical communications for deep space missions," *IEEE Communications Magazine*, vol. 38, no. 8, pp. 134-139, 2000.
- [131] "Free space optics (FSO): An introduction", <http://www.free-space-optics.org>, last accessed date: 11 Oct. 2009.
- [132] "IrDA Market Report 2007", http://www.irda.org/associations/2494/files/Publications/IrDA_MR_TOC.pdf, last accessed date: 11 Oct. 2009.
- [133] D. M. Forin, G. M. Tosi Belleffi, F. Curti, N. Corsi, V. De Sanctis, V. Sacchieri, A. J. L. Teixeira, and G. Cincotti, "On field test of a wavelength division multiplexing free space optics transmission at very high bit rates," in *9th International Conference on Telecommunications*, 2007.

- [134] N. Cvijetic, D. Qian, and T. Wang, "10Gb/s Free-Space Optical Transmission using OFDM," *Conference on Optical Fiber communication/National Fiber Optic Engineers Conference, 2008*, San Diego, CA, pp. 1-3, 2008.
- [135] J. P. Conti, "What you see is what you send - [comms visible light]," *Engineering & Technology*, vol. 3, no. 19, pp. 66-69, 2008.
- [136] M. Kavehrad, "Broadband room service by light," *Scientific American Magazine*, pp. 82-87, 2007.
- [137] T. Komine and M. Nakagawa, "Fundamental analysis for visible-light communication system using LED lights," *IEEE Transactions on Consumer Electronics*, vol. 50, no. 1, pp. 100-107, 2004.
- [138] M. Hoa Le, D. O'Brien, G. Faulkner, Z. Lubin, L. Kyungwoo, J. Daekwang, and O. YunJe, "High-speed visible light communications using multiple-resonant equalization," *IEEE Photonics Technology Letters*, vol. 20, no. 14, pp. 1243-1245, 2008.
- [139] I. E. Lee, M. L. Sim, and F. W. L. Kung, "Performance enhancement of outdoor visible-light communication system using selective combining receiver," *IET Optoelectronics*, vol. 3, no. 1, pp. 30-39, 2009.
- [140] R. Ramirez-Iniguez, S. M. Idrus, and Z. Sun, *Optical wireless communications: IR for wireless connectivity*. NW: Auerbach Publications, 2008.
- [141] Z. Ghassemlooy and A. R. Hayes, "Optical wireless communication systems - Part I: Review."
- [142] G. W. Marsh and J. M. Kahn, "Channel reuse strategies for indoor infrared wireless communications," *IEEE Transactions on Communications*, vol. 45, no. 10, pp. 1280-1290, 1997.
- [143] P. Khoman and D. A. Johns, "A CMOS optical preamplifier for wireless infrared communications," *IEEE Transactions on Circuits and Systems II: Analog and Digital Signal Processing*, vol. 46, no. 7, pp. 852-859, 1999.
- [144] S. Hranilovic, *Wireless optical communication systems*. New York: Springer-Verlag New York Inc. , 2004.
- [145] A. P. Tang, J. M. Kahn, and K.-P. Ho, "Wireless infrared communication links using multi-beam transmitters and imaging receivers," *IEEE International Conference on Communications*, Dallas, USA, pp. 180-186 1996.
- [146] A. Sivabalan and J. John, "Improved power distribution in diffuse Indoor Optical Wireless systems employing multiple transmitter configurations," *Optical and Quantum Electronics*, vol. 38, no. 8, pp. 711-725, 2006.
- [147] K. L. Sterckx, "Optical wireless systems performance enhancement through an assessment of the channel impairments." PhD thesis, University of Wales Swansea, 2000.
- [148] V. Jungnickel, V. Pohl, S. Nonnig, and C. v. Helmolt, "A physical model of the wireless infrared communication channel," *IEEE Journal on Selected Areas in Communications*, vol. 20, no. 3, pp. 631-640, 2002.
- [149] N. Hayasaka and T. Ito, "Channel modeling of nondirected wireless infrared indoor diffuse link," *Electronics and Communications in Japan*, vol. 90, no. 6, pp. 9-19, 2007.
- [150] J. B. Carruthers and P. Kannan, "Iterative site-based modeling for wireless infrared channels," *IEEE Transactions on Antennas and Propagation*, vol. 50, no. 5, pp. 759-765, 2002.
- [151] C. R. Lomba, R. T. Valadas, and A. M. Duarte, "Propagation losses and impulse response of the indoor optical channel: A simulation package," *Mobile communications advanced systems and components* Berlin / Heidelberg: Springer, 1994, pp. 285-297.

- [152] J. B. Carruthers, S. M. Carroll, and P. Kannan, "Propagation modelling for indoor optical wireless communications using fast multi-receiver channel estimation," *IEE Proceedings- Optoelectronics*, vol. 150, no. 5, pp. 473-481, 2003.
- [153] J. R. Barry, J. M. Kahn, W. J. Krause, E. A. Lee, and D. G. Messerschmitt, "Simulation of multipath impulse response for indoor wireless optical channels," *IEEE Journal on Selected Areas in Communications*, vol. 11, no. 3, pp. 367 - 379, 1993.
- [154] X. Yang, M. Gong, H. Zhang, P. Yan, S. Zou, W. Jin, K. Zhang, F. Jiang, and Y. Meng, "Simulation of impulse response on IR wireless indoor channel with concentrator," *Proceedings of the SPIE*, vol. 4873, pp. 71-78, 2002.
- [155] R. P. Silvestre, P. J. Rafael, J. L. H. Francisco, B. G. H. Oswaldo, and J. A. A. Alejandro, "Reflection model for calculation of the impulse response on IR-wireless indoor channels using ray-tracing algorithm," *Microwave and Optical Technology Letters*, vol. 32, no. 4, pp. 296-300, 2002.
- [156] K. Smitha, A. Sivabalan, and J. John, "Estimation of channel impulse response using modified ceiling bounce model in non-directed indoor optical wireless systems," *Wireless Personal Communications*, vol. 45, no. 1, pp. 1-10, 2008.
- [157] F. J. Lopez-Hernandez, R. Perez-Jimeniz, and A. Santamaria, "Monte Carlo calculation of impulse response on diffuse IR wireless indoor channels," *Electronics Letters*, vol. 34, no. 12, pp. 1260-1262, 1998.
- [158] D. R. Biosca, P. Lopez, and J. L., "Generalization of Monte Carlo ray-tracing algorithm for the calculation of the impulse response on indoor wireless infrared channels," *Universidad, Ciencia y Tecnología*, vol. 9, no. 33, pp. 17-25, 2005.
- [159] A. Mihaescu and M. Ottesteanu, "Reduced size model method for diffuse optical indoor wireless channel characterization," *WSEAS Transactions on Communications*, vol. 5, no. 2, pp. 155-160, 2006.
- [160] S. Arumugam and J. John, "Effect of transmitter positions on received power and bandwidth in diffuse indoor optical wireless systems," *Optical and Quantum Electronics*, vol. 37, no. 1, pp. 1-14, 2007.
- [161] O. Gonzalez, S. Rodriguez, R. Perez-Jimenez, B. R. Mendoza, and A. Ayala, "Error analysis of the simulated impulse response on indoor wireless optical channels using a Monte Carlo-based ray-tracing algorithm," *IEEE Transactions on Communications*, vol. 53, no. 1, pp. 124- 130, 2005.
- [162] H. Hashemi, G. Yun, M. Kavehrad, and F. Behbahani, "Frequency response measurements of the wireless indoor channel at infrared frequencies," *IEEE International Conference on Communications*, New Orleans, LA, USA, pp. 1511-1515, 1994.
- [163] F. J. Lopez-Hernandez and M. J. Betancor, "DUSTIN: algorithm for calculation of impulse response on IR wireless indoor channels," *Electronics Letters*, vol. 33, no. 21, pp. 1804 - 1806, 1997.
- [164] V. Pohl, V. Jungnickel, and C. Helmolt, "A channel model for wireless infrared communication," *The 11th IEEE International Symposium on Personal, Indoor and Mobile Radio Communications, 2000*, vol. 1, pp. 297 - 303, 2000.
- [165] M. R. Pakravan and M. Kavehrad, "Indoor wireless infrared channel characterization by measurements," *IEEE Transactions on Vehicular Technology*, vol. 50, no. 2, pp. 1053-1073, 2001.
- [166] R. Perez-Jimenez, J. Berges, and M. J. Betancor, "Statistical model for the impulse response on infrared indoor diffuse channels," *Electronics letter*, vol. 33, no. 15, pp. 1298-1300, 1997.
- [167] S. M. Sze and K. K. Ng, *Physics of semiconductor devices* 3rd ed.: John Wiley & Sons Inc., 2007.

- [168] G. P. Agrawal *Fiber-Optic communication systems*, 3rd ed. NY: John Wiley & Sons, 2002.
- [169] V. Pohl, V. Jungnickel, and C. Helmolt, "Integrating-sphere diffuser for wireless infrared communication," *IEE Proceedings - Optoelectronics* vol. 147, no. 4, pp. 281-285, 2000.
- [170] D. A. Rockwell and G. S. Mecherle, "Wavelength selection for optical wireless communications systems," *Proc. of SPIE*, vol. 4530, pp. 27-35, 2001.
- [171] A. J. C. Moreira, R. T. Valadas, and A. M. O. Duarte, "Optical interference produced by artificial light," *Wireless Networks*, vol. 3, pp. 131-140, 1997.
- [172] K. Samaras, A. M. Street, D. C. O'Brien, and D. J. Edwards, "Error rate evaluation of wireless infrared links," *IEEE International Conference on Communications*, Atlanta, U.S.A, pp. 826-831, 1998.
- [173] K. K. Wong, T. O'Farrell, and M. Kiatweerasakul, "Infrared wireless communication using spread spectrum techniques," *IEE Proceedings - Optoelectronics*, vol. 147, no. 4, pp. 308-314, 2000.
- [174] J. R. Barry, "Wireless communication using non-directed infrared radiation," PhD thesis, University of California, 1992.
- [175] J. M. Kahn, P. Djahani, A. G. Weisbin, K. T. Beh, A. P. Tang, and R. You, "Imaging diversity receivers for high-speed infrared wireless communication," *IEEE Communications Magazine*, vol. 36, no. 12, pp. 88-94, 1998.
- [176] W. Hirt, M. Hassner, and N. Heise, "IrDA-VFIR(16Mbits/s): Modulation code and system design," *IEEE Personal Communications* vol. 8, no. 1, pp. 58 - 71, 2001.
- [177] I. Millar, M. Beale, B. Donoghue, K. W. Lindstrom, and S. Williams, "The IrDA standards for high-speed infrared communications," in *Hewlett-Packard Journal*, 1998.
- [178] L. W. Couch *Digital and Analog Communication Systems*, 6th ed.: Prentice Hall, 2001.
- [179] J. G. Proakis, *Digital communications*, Fourth ed. New York: McGraw-Hill, Inc., 2001.
- [180] Y. Fan and R. Green, "Comparison of pulse position modulation and pulse width modulation for application in optical communications," *Optical Engineering*, vol. 46, no. 6, pp. 065001-1-065001-7, 2007.
- [181] M. D. Audeh and J. M. Kahn, "Performance evaluation of L-pulse-position modulation on non-directed indoor infrared channels," *ICC '94*, New Orleans, LA, USA, pp. 660-664, 1994.
- [182] H. Chan, K. L. Sterckx, J. M. H. Elmirghani, and R. A. Cryan, "Performance of optical wireless OOK and PPM systems under the constraints of ambient noise and multipath dispersion," *IEEE Communications Magazine*, vol. 36, no. 12, pp. 83-87, 1998.
- [183] H. Park and J. R. Barry, "Performance of multiple pulse position modulation on multipath channels," *IEE Proceedings - Optoelectronics*, vol. 143, no. 6, pp. 360-364, 1996.
- [184] H. Sugiyama and K. Nosu, "MPPM: a method for improving the band-utilization efficiency in optical PPM," *Journal of Lightwave Technology*, vol. 7, no. 3, pp. 465-472, 1989.
- [185] U. Sethakaset and T. A. Gulliver, "MAP detectors for differential pulse-position modulation over indoor optical wireless communications," *IEICE Transactions on Fundamentals of Electronics, Communications and Computer Sciences*, vol. E89-A, no. 11, pp. 3148-3151, 2006.

- [186] S. Ubolthip and T. A. Gulliver, "Channel capacity of differential amplitude pulse-position modulation (DAPPM) over indoor optical wireless communications," *APCC '06*, Busan, pp. 1-5, 2006.
- [187] Y. Zengm, R. J. Green, S. Sun, and M. S. Leeson, "Tunable pulse amplitude and position modulation technique for reliable optical wireless communication channels," *Journal of Communications*, vol. 2, no. 2, pp. 22-28, 2007.
- [188] G. Cariolaro, T. Erseghe, and L. Vangelista, "Exact spectral evaluation of the family of digital pulse interval modulated signals," *Information Theory, IEEE Transactions on*, vol. 47, no. 7, pp. 2983-2992, 2001.
- [189] A. R. Hayes, Z. Ghassemlooy, N. L. Seed, and R. McLaughlin, "Baseline-wander effects on systems employing digital pulse-interval modulation," *IEE Proceedings - Optoelectronics* vol. 147, no. 4, pp. 295-300, 2000.
- [190] Z. Ghassemlooy, A. R. Hayes, and B. Wilson, "Reducing the effects of intersymbol interference in diffuse DPIM optical wireless communications," *IEE Proceedings-Optoelectronics*, vol. 150, no. 6, pp. 445 - 452, 2003.
- [191] X. Yang, M. Gong, H. Zhang, P. Yan, K. Zhang, W. Jin, F. Jiang, S. Zou, and Y. Meng, "The performance of DPIM with equalizer on diffuse optical wireless communications," *Proc. SPIE*, vol. 4911, no. 102, pp. 102-107, 2002.
- [192] N. M. Aldibbiat, Z. Ghassemlooy, and R. McLaughlin, "Error performance of dual header pulse interval modulation (DH-PIM) in optical wireless communications," *IEE Proceedings - Optoelectronics*, vol. 148, no. 2, pp. 91-96, 2001.
- [193] N. M. Aldibbiat, Z. Ghassemlooy, and R. McLaughlin, "Dual header pulse interval modulation for dispersive indoor optical wireless communication systems," *IEE Proceedings -Circuits, Devices and Systems*, vol. 149, no. 3, pp. 187-192, 2002.
- [194] Z. Ghassemlooy, W. O. Popoola, and N. M. Aldibbiat, "Equalised dual header pulse interval modulation for diffuse optical wireless communication system," *Mediterranean J. of Electronics and Communications*, vol. 2, no. 1, pp. 59-61, 2006.
- [195] N. M. Aldibbiat, Z. Ghassemlooy, and R. McLaughlin, "Spectral characteristics of dual header pulse interval modulation (DH-PIM)," *IEE Proceedings - Communications*, vol. 148, no. 5, pp. 280-286, 2001.
- [196] R. You and J. M. Kahn, "Average power reduction techniques for multiple-subcarrier intensity-modulated optical signals," *IEEE Transaction on Communications*, vol. 49, no. 12, pp. 2164-2171, 2001.
- [197] J. B. Carruthers and J. M. Kahn, "Multiple-subcarrier modulation for nondirected wireless infrared communication," *Selected Areas in Communications, IEEE Journal on*, vol. 14, no. 3, pp. 538-546, 1996.
- [198] R. Hui, B. Zhu, R. Huang, C. T. Allen, K. R. Demarest, and D. Richards, "Subcarrier multiplexing for high-speed optical transmission," *Journal of Lightwave Technology*, vol. 20, no. 3, pp. 417 - 427, 2002.
- [199] C. E. Shannon, "A mathematical theory of communication," *Bell System Technical Journal*, vol. 27, pp. 379-423, 1948.
- [200] C. Berrou and A. Glavieux, "Near optimum error correcting coding and decoding: Turbo codes " *IEEE Transactions on Communications*, vol. 44, no. 10, pp. 1261-1271, 1996.
- [201] T. K. Moon, *Error correction coding: Mathematical methods and algorithms* New Jersey: Wiley-Interscience (June 6, 2005) 2005.
- [202] D. J. C. MacKay and R. M. Neal, "Near Shannon limit performance of low density parity check codes," *Electronics Letters*, vol. 33, no. 6, pp. 457-458, 1997.

- [203] S.-Y. Chung, G. D. Forney, T. J. Richardson, and R. Urbanke, "On the design of low-density parity-check codes within 0.0045 dB of the Shannon limit," *IEEE Communications Letters*, vol. 5, no. 2, pp. 58-60, 2001.
- [204] T. J. Richardson, M. A. Shokrollahi, and R. L. Urbanke, "Design of capacity-approaching irregular low-density parity-check codes," *IEEE Trans. Inform. Theory*, vol. 47, no. 2, pp. 619-637, 2001.
- [205] J. Boutros, G. Caire, E. Viterbo, H. Sawaya, and S. Vialle, "Turbo code at 0.03 dB from capacity limit," *IEEE International Symposium on Information Theory*, p. 56 2002.
- [206] D. Mackenzie, "Take it to the limit," *New Scientist*, vol. 187, no. 2507, pp. 38-41, 2005.
- [207] S. Haykin, "Digital Communications," *Digital Communications* New York: John Wiley & Sons, 1988.
- [208] P. Sweeney, *Error control coding: From theory to practice*, 1 ed.: WileyBlackwell, 2002.
- [209] A. J. Viterbi, "Error bounds for convolutional codes and an asymptotically optimum decoding algorithm," *IEEE Transactions on Information Theory*, vol. 13, no. 2, pp. 260-269, 1967.
- [210] T. Wuth, E. Agrell, M. Karlsson, and M. Sköld, "Fiber communications using convolutional coding and bandwidth-efficient modulation," *Optics Express*, vol. 14, no. 2, pp. 542-555, 2006.
- [211] J. G. Proakis, *Digital communications*, Third ed. New York: McGraw-Hill, Inc., 1995.
- [212] D. Mackenzie, "Wavelets seeing the forest and the trees." National Academy of Sciences, 2001, <http://www.beyonddiscovery.org/content/view.txt.asp?a=1952>, last accessed date: 11 Oct. 2009.
- [213] B. B. Hubbard, *The world according to wavelets: The story of a mathematical technique in the making*. Wellesley, Massachusetts A K Peters 1996.
- [214] R. Polikar, "The engineer's ultimate guide to wavelet analysis: the wavelet tutorial," 2005, <http://users.rowan.edu/~polikar/WAVELETS/WTtutorial.html>, last accessed date: 11 Oct. 2009.
- [215] C. S. Burrus, R. A. Gopinath, and H. Guo, *Introduction to wavelets and wavelet transforms: A primer* New Jersey: Prentice Hall, 1998.
- [216] J. Li, "Image compression: The mathematics of JPEG 2000," *Modern Signal Processing*, vol. 46, pp. 185-221, 2003.
- [217] D. L. Donoho, I. M. Johnstone, G. Kerkycharian, and D. Picard, "Wavelet shrinkage: Asymptopia?," *Journal of the Royal Statistics Society*, vol. 57, pp. 301-337, 1995.
- [218] D. L. Donoho, "De-noising by soft-thresholding," *IEEE Transactions on Information Theory*, vol. 41, no. 3, pp. 613-627, 1995.
- [219] K. Chan and A. W. Fu, "Efficient time series matching by wavelets," *Proceedings of the 15th International Conference on Data Engineering* Sydney, Australia, pp. 126-133, 1999.
- [220] F. K. Chan, A. W. Fu, and C. Yu, "Haar wavelets for efficient similarity search of time-series: with and without time warping," *IEEE Transactions on Knowledge and Data Engineering*, vol. 15, no. 3, pp. 686- 705, 2003.
- [221] A. Grinsted, J. C. Moore, and S. Jevrejeva, "Application of the cross wavelet transform and wavelet coherence to geophysical time series," *Nonlinear Processes in Geophysics*, vol. 11, pp. 561-566, 2004.
- [222] S. Pittner and S. V. Kamarthi, "Feature extraction from wavelet coefficients for pattern recognition tasks," *International Conference on Neural Networks*, pp. 1484-1489, 1997.

- [223] A. K. Pradhan, S. K. Meher, and A. Routray, "Communication channel equalization using wavelet network," *Digital Signal Processing*, vol. 16, no. 4, pp. 445-452, 2006.
- [224] N. G. Prelcic, F. P. Gonzalez, and M. E. D. Jimenez, "Wavelet packet-based subband adaptive equalization," *Signal Processing*, vol. 81, no. 22, pp. 1641-1662, 2001.
- [225] R. E. Learned, H. Krim, B. Claus, A. S. Willsky, and W. C. Karl, "Wavelet packet-based multiple access communication," *Wavelet Applications in Signal and Image Processing II*, vol. 2303, pp. 246-259, 1994.
- [226] A. Jamin and P. Mahonen, "Wavelet packet modulation for wireless communications " *Wireless Communications and Mobile Computing*, vol. 5, no. 2, pp. 1-18, 2005.
- [227] A. R. Lindsey, "Wavelet packet modulation for orthogonally multiplexed communication," *IEEE Transactions on Signal Processing*, vol. 45, no. 5, pp. 1336-1339, 1997.
- [228] B. G. Negash and H. Nikookar, "Wavelet-based multicarrier transmission over multipath wireless channels," *IEE Electronics Letters*, vol. 36, no. 21, pp. 1787-1788, 2000.
- [229] M. Sablatash, J. H. Lodge, and C. J. Zarowski, "Theory and design of communication systems based on scaling functions, wavelets, wavelet packets and filter banks," *The 8th Intl. Conf. on Wireless Communication*, Alberta, Canada, pp. 640 - 659, 1996.
- [230] F. Doyis, M. Mondin, and F. Daneshgaran, "The modified Gaussian: a novel wavelet with low sidelobes with applications to digital communications," *IEEE Communications Letters*, vol. 2, no. 8, p. 208, 1998.
- [231] F. Daneshgaran and M. Mondin, "Symbol synchronization using wavelets," *Military Communications Conference*, San Diego, CA, USA, pp. 891-895, 1995.
- [232] J.-C. Pesquet, H. Krim, H. Carfantan, and J. G. Proakis, "Estimation of noisy signals using time-invariant wavelet packets," *The Twenty-Seventh Asilomar Conference on Signals, Systems and Computers*, CA, USA, pp. 31 - 34, 1993.
- [233] M. M. Akho-Zahieh and O. C. Ugweje, "Wavelet packet based MC/MCD-CDMA communication system," *Electronics Letters*, vol. 42, no. 11, pp. 644-645, 2006.
- [234] H. Zhang, H. H. Fan, and A. Lindsey, "Wavelet packet waveforms for multicarrier CDMA communications," *IEEE International Conference on Acoustics, Speech, and Signal Processing*, OH, USA, pp. III-2557- 2560, 2002.
- [235] H. Zhang, H. H. Fan, and A. Lindsey, "A wavelet packet based model for time-varying wireless communication channels," *IEEE Third Workshop on SPAWC Taiwan*, pp. 50-53, 2001.
- [236] M. Martone, "Wavelet-based separating kernels for array processing of cellular ds/cdma signals in fast fading," *IEEE Transaction on Communications*, vol. 48, no. 6, pp. 979-995, 2000.
- [237] X. Fernando, S. Krishnan, H. Sun, and K. Kazemi-Moud, "Adaptive denoising at infrared wireless receivers " *The International Society for Optical Engineering*, vol. 5074, pp. 199-207 2003.
- [238] S. Gracias and V. U. Reddy, "Wavelet packet based channel equalization," *Sadhana*, vol. 21, no. 1, pp. 75-89, 1996.
- [239] S. Mallat, *A wavelet tour of signal processing*, 2nd ed. San Diego: Academic Press, 1999.
- [240] J. P. Gazeau, "Wavelet analysis in signal and image processing," Northumbria University, 2007.

- [241] F. Liu, X. Cheng, J. Xu, and X. Wang, "Wavelet based adaptive equalization algorithm," *Global Telecommunications Conference 1997*, Phoenix, AZ, USA, pp. 1230-1234, 1997.
- [242] C. M. Leavey, M. N. James, J. Summerscales, and R. Sutton "An introduction to wavelet transforms: a tutorial approach," *Insight*, vol. 45, no. 5, pp. 344-353, 2003.
- [243] M. Misiti, Y. Misiti, G. Oppenheim, and J.-M. Poggi, *Wavelet Toolbox: User's Guide*. MA, USA: The MathWorks Inc. , 2008.
- [244] S. G. Mallat, "A theory for multiresolution signal decomposition: the wavelet representation," *IEEE Transactions on Pattern Analysis and Machine Intelligence*, vol. 11, no. 7, pp. 674 - 693, 1989.
- [245] G. Strang and T. Nguyen, *Wavelets and filter banks* 2ed.: Wellesley College, 1996.
- [246] R. Polikar, "The story of wavelets," *Physics and Modern Topics in Mechanical and Electrical Engineering*: World Scientific and Eng. Society Press, 1999, pp. 192-197.
- [247] . Valens, "A really friendly guide to wavelets," <http://pagesperso-orange.fr/polyvalens/clemens/wavelets/wavelets.html>, last accessed date: 11 Oct. 2009.
- [248] R. J. Dickenson and Z. Ghassemlooy "BER performance of 166 Mbit/s OOK diffuse indoor IR link employing wavelets and neural networks," *Electronics Letters*, vol. 40, no. 12, pp. 753 - 755, 2004.
- [249] J. R. Barry, E. A. Lee, and D. G. Messerschmitt, *Digital Communication* 3rd ed. Boston: Kluwer Academic Publishers 2003.
- [250] L. Hanzo, C. H. Wong, and M. S. Yee, "Neural network based equalization," *Adaptive wireless transceivers*: Wiley-IEEE Press, 2002, pp. 299-383.
- [251] P. Savazzi, L. Favalli, and v. Mecocci, "A suboptimal approach to channel equalization based on the nearest neighbor rule," *IEEE Journal on Selected Areas in Communications*, vol. 16, no. 9, pp. 1640-1648, 1998.
- [252] A. K. Tripathy and K. T. Raghavendra, "An efficient channel equalizer using artificial neural networks," *Neural Network World*, vol. 16, no. 4, pp. 357-368, 2006.
- [253] B. Lu and B. L. Evans, "Channel equalization by feedforward neural networks," *IEEE International Symposium on Circuits and Systems*, vol. 5, pp. 587 - 590 1999.
- [254] J. Choi, M. Bouchard, and T. H. Yeap, "Decision feedback recurrent neural equalization with fast convergence rate," *IEEE Transactions on Neural Networks*, vol. 16, no. 3, pp. 699-708, 2005.
- [255] R. Zayani, R. Bouallegue, and D. Roviras, "Adaptive predistortions based on neural networks associated with Levenberg-Marquardt algorithm for satellite down links," *EURASIP Journal on Wireless Communications and Networking* vol. 2008, no. 2008, pp. 1-15, 2008.
- [256] G. Forney, Jr., "Maximum-likelihood sequence estimation of digital sequences in the presence of intersymbol interference," *IEEE Transaction on Information Theory*, vol. 18, no. 3, pp. 363-378, 1972.
- [257] J. G. Proakis, M. Salehi, and G. Bauch, *Contemporary communication systems using Matlab*, 2 ed. Boston: PWS Publishing Company, 2003.
- [258] F. G. Stremler, *Introduction to communication systems*, 3 ed. Massachusetts: Prentice Hall, 1990.
- [259] A. K. Jain, M. Jianchang, and K. M. Mohiuddin, "Artificial neural networks: a tutorial," *Computer*, vol. 29, no. 3, pp. 31-44, 1996.

- [260] A. Nogueira, M. Rosario de Oliveira, P. Salvador, R. Valadas, and A. Pacheco, "Using neural networks to classify Internet users," *Advanced industrial conference on telecommunications/service assurance with partial and intermittent resources*, pp. 183-188, 2005.
- [261] A. N. Ramesh, C. Kambhampati, J. R. T. Monson, and P. J. Drew, "Artificial intelligence in medicine " *Annals of The Royal College of Surgeons of England*, vol. 86, no. 5, pp. 334-338(5), 2004.
- [262] H. B. Burke, "Evaluating artificial neural networks for medical applications," *International Conference on Neural Networks*, Houston, TX, USA, pp. 2494 - 2495, 1997.
- [263] S.-C. B. Lo, J.-S. J. Lin, M. T. Freedman, and S. K. Mun, "Application of artificial neural networks to medical image pattern recognition: detection of clustered microcalcifications on mammograms and lung cancer on chest radiographs " *The Journal of VLSI Signal Processing*, vol. 18, no. 3, pp. 263-274, 1998.
- [264] S. Walczak, "An empirical analysis of data requirements for financial forecasting with neural networks," *Journal of Management Information Systems*, vol. 17, no. 4, pp. 203-222, 2001.
- [265] Y. Fu and T. Chai, "Neural-network-based nonlinear adaptive dynamical decoupling control," *IEEE Transactions on Neural Networks*, vol. 18, no. 3, pp. 921-925, 2007.
- [266] G. Dorffner, "Neural networks for time series processing," *Neural Network World*, vol. 6, no. 4, pp. 447-468, 1996.
- [267] A. Patnaik, D. E. Anagnostou, R. K. Mishra, C. G. Christodoulou, and J. C. Lyke, "Applications of neural networks in wireless communications," *IEEE Antennas and Propagation Magazine*, vol. 46, no. 3, pp. 130-137, 2004.
- [268] D. MacKay, *Information theory, inference, and learning algorithms*, 1st ed. Cambridge, UK: Cambridge university press 2003.
- [269] K. Hornik, M. Stinchcombe, and H. White, "Multilayer feedforward networks are universal approximators," *Neural Networks*, vol. 2, no. 5, pp. 359 - 366 1989.
- [270] S. Haykin, *Neural networks: A comprehensive foundation*, 2nd ed. New Jersey, USA: Prentice Hall, 1998.
- [271] D. P. Mandic and J. A. Chambers, *Recurrent neural networks for prediction*: John Wiley and Sons Ltd., 2001.
- [272] L. Behera, S. Kumar, and A. Patnaik, "On adaptive learning rate that guarantees convergence in feedforward networks," *IEEE Transactions on Neural Networks*, vol. 17, no. 5, pp. 1116-1125, 2006.
- [273] A. Toledo, M. Pinzolas, J. J. Ibarrola, and G. Lera, "Improvement of the neighborhood based Levenberg-Marquardt algorithm by local adaptation of the learning coefficient," *IEEE Transactions on Neural Networks*, vol. 16, no. 4, pp. 988-992, 2005.
- [274] U. Windhorst and H. Johansson, *Modern techniques in neuroscience research*: Springer-Verlag Berlin and Heidelberg GmbH & Co., 1999.
- [275] R. P. Lippmann, "An introduction to computing with neural nets," *IEEE ASSP Magazine*, vol. 4, no. 2, pp. 4-22, 1987.
- [276] S. Haykin, "Neural networks expand SP's horizons," *IEEE Signal Processing Magazine*, vol. 13, no. 2, pp. 24-49, 1996.
- [277] R. W. Kirkland and D. P. Taylor, "Neural network channel equalization," *Neural networks in telecommunications*, B. Yuhua and N. Ansari, Eds. Boston Kluwer Academic Publishers, 1994, pp. 143-171.

- [278] I. Cha and S. A. Kassam, "Channel equalization using adaptive complex radial basis function networks," *IEEE Journal on Selected Areas in Communications*, vol. 13, no. 1, pp. 122-131, 1995.
- [279] K. A. Al-Mashouq and I. S. Reed, "The use of neural nets to combine equalization with decoding for severe intersymbol interference channels," *IEEE Transactions on Neural Networks*, vol. 5, no. 6, pp. 982 - 988, 1994.
- [280] W. Weng, R. Lin, and C. Huse, "The design of an SCFNN based nonlinear channel equalizer," *Journal of information science and engineering* vol. 21, pp. 695-709, 2005.
- [281] S. Sitharama Iyengar, E. C. Cho, and V. V. Phoha, *Foundations of wavelet networks and applications*, 1st. ed.: Chapman & Hall/CRC, 2002.
- [282] E. A. Martínez-Rams and V. Garcerán-Hernández, "Assessment of a Speaker Recognition System Based on an Auditory Model and Neural Nets," *IWINAC 2009*, Santiago de Compostela, Spain, pp. 488-498, 2009.
- [283] S. Trenn, "Multilayer Perceptrons: Approximation Order and Necessary Number of Hidden Units," *IEEE Transactions on Neural Networks*, vol. 19, no. 5, pp. 836-844, 2008.
- [284] H. Demuth, M. Beale, and M. Hagan, "Neural network toolbox 5 user's guide," The Mathworks, 2007, pp. 5-34-51.
- [285] S. Haykin, *Adaptive Filter Theory*. New Jersey, USA: Prentice Hall International, 2001.
- [286] M. Ibnkahla, "Applications of neural networks to digital communications: a survey," *Signal Processing*, vol. 20, no. 7, pp. 1185 - 1215, 2000.
- [287] S. M. Berber, "Soft output decision convolutional (SONNA) decoders based on the application of neural networks," *Engineering Applications of Artificial Intelligence*, vol. 21, pp. 1-13 2008.
- [288] J. Bruck and M. Blaum, "Neural networks, error-correcting codes, and polynomials over the binary n -cube," *IEEE Transactions on Information Theory*, vol. 35, no. 5, pp. 976-987, 1989.
- [289] S. M. Berber, P. J. Secker, and Z. Salcic, "Theory and application of neural networks for $1/n$ rate convolutional decoders," *Engineering Applications of Artificial Intelligence*, vol. 18, pp. 931-949, 2005.
- [290] M. Ibnkahla and J. Yuan, "A neural network MLSE receiver based on natural gradient descent: application to satellite communications," *EURASIP Journal on Applied Signal Processing*, vol. 2004, no. 1, pp. 2580 - 2591, 2004.
- [291] A. Hamalainen and J. Henriksson, "A recurrent neural decoder for convolutional codes," *IEEE International Conference on Communications*, Vancouver, BC, Canada, pp. 1305-1309, 1999.
- [292] S. Shouyu, Z. Junli, and Z. Qi, "A neural network approach to Viterbi algorithm based on MFA," *IEEE International Conference on Communications, Circuits and Systems and West Sino Expositions*, pp. 69-72, 2002.
- [293] S. Zoran, B. Stevan, and S. Paul, "FPGA prototyping of RNN decoder for convolutional codes," *EURASIP journal on applied signal processing*, vol. 2006, pp. 1-9, 2006.
- [294] X. Wang and S. B. Wicker, "An artificial neural net Viterbi decoder," *IEEE Transactions on Communications*, vol. 44, no. 2, pp. 165-171, 1996.
- [295] G. Marcone, E. Zincolini, and G. Orlandi, "An efficient neural decoder for convolutional codes," *European Transactions on Telecommunications*, vol. 6, no. 4, pp. 439-445, 1995.
- [296] W. R. Caid and R. W. Means, "Neural network error correcting decoders for block and convolutional codes," *Global Telecommunications Conference*, pp. 1028-1031, 1990.

- [297] L. Huazhang, Y. Dongfeng, C. Xinju, and L. Famai, "The neural decoder for convolutional codes on the mobile channel," *International Conference on Communication Technology*, Beijing, China, p. 5, 1998.
- [298] K.-H. Tzou and J. Dunham, "Sliding block decoding of convolutional codes," *IEEE Transactions on Communications*, vol. 29, no. 9, pp. 1401-1403, 1981.
- [299] R. Koetter, A. C. Singer, and M. Tüchler, "Turbo equalization," *IEEE Signal Processing Magazine*, vol. 21, pp. 67-80, 2004.
- [300] Mathworks, "Embedded IDE link™ CC 3 user's guide," 2009.
- [301] Texas Instrument, "TMS320c6713 floating point digital signal processor," 2005.
- [302] M. Misiti, Y. Misiti, G. Oppenheim, and J.-M. Poggi, "Wavelet Toolbox™ 4 User's Guide," 2008.
- [303] P. Getreuer, "Filter coefficients to popular wavelets," 2006, http://www.mathworks.com/matlabcentral/fileexchange/5502-filter-coefficients-to-popular-wavelets?controller=file_infos&download=true, last access date: 11 Oct. 2009.